TECHNISCHE UNIVERSITÄT WIEN

DISSERTATION

Search for Dark Energy and Modified Gravity with Tabletop Experiments

Ausgeführt zum Zwecke der Erlangung des akademischen Grades
eines Doktors der Naturwissenschaften
unter der Leitung von

Privatdoz. Dipl.-Ing. Dr.techn. Mario Pitschmann
E 141 - Atominstitut

eingereicht an der Technischen Universität Wien
Fakultät für Physik

von

Hauke Fischer, BSc BSc MSc
Matrikelnummer 01207049
Wien

September 30, 2024

Deutsche Kurzfassung der Dissertation

Skalarfelder sind sowohl durch die theoretische als auch die experimentelle Physik gut motiviert. Sie werden von höherdimensionalen Theorien wie der Stringtheorie vorhergesagt, erklären die Masse der Eichbosonen der schwachen Wechselwirkung und können dazu dienen, die kosmische Inflation anzutreiben oder Modelle für dunkle Materie oder dunkle Energie zu konstruieren.
Leichte Skalarfelder, wie sie häufig in der Kosmologie auftreten, können zu einer gravitationsähnlichen fünften Kraft führen. Die Existenz solcher Skalarfelder erfordert entweder äußerst schwache Kopplungen an Materie durch die Feinabstimmung von Parametern oder die Integration von Mechanismen, die das Fehlen beobachteter fünfter Kräfte erklären, um nicht im Widerspruch zu experimentellen Tests der Allgemeinen Relativitätstheorie zu stehen.

Der Fokus dieser Arbeit liegt auf Skalarfeldern mit einem sogenannten Screening-Mechanismus, wie ihn zum Beispiel das Chameleon-, Symmetron- oder Dilatonfeld besitzen. Diese Mechanismen sorgen dafür, dass die fünfte Kraft bei hohen Materiedichten unterdrückt wird, aber im Vakuum stark werden kann.

Tabletop Experimente im Vakuum sind besonders gut geeignet, um nach solchen Feldern zu suchen. Die Kombination ihrer sehr hohen Messgenauigkeit mit der Vakuumumgebung macht sie zu mächtigen Werkzeugen bei der Suche nach Skalarfeldern. Allerdings ist die theoretische Berechnung dieser Felder äußerst schwierig, da ihre Bewegungsgleichungen nichtlinear sind.

Der Hauptfokus dieser Arbeit liegt darauf, theoretische und numerische Methoden zu entwickeln, um Tabletop Experimente, die mit der TU Wien assoziiert sind, zu analysieren. Dazu gehören die Neutroneninterferometrie, Gravitationsresonanzspektroskopie (qBOUNCE) und das Casimir and Non-Newtonian Force Experiment (CANNEX). Diese Experimente wurden unter anderem mit dem Ziel aufgebaut, nach fünften Kräften zu suchen. Die Untersuchungen werden durch eine Analyse von Lunar Laser Ranging (LLR) ergänzt.

Ein wesentlicher Schwerpunkt dieser Arbeit liegt auf der Untersuchung des Dilatonmodells, das im Grenzfall starker Kopplung von der Stringtheorie erwartet wird.
Die entwickelten Methoden werden angewandt, um den Parameterraum des Dilaton-, Symmetron- und Chameleonfeldes einzuschränken und das experimentelle und theoretische Verständnis dieser Felder zu fördern.

Abstract

Scalar fields, ubiquitous in theoretical physics, hold significant promise both theoretically and experimentally. They arise in higher-dimensional frameworks like string theory and play pivotal roles in diverse phenomena, including endowing mass to weak interaction gauge bosons via the Higgs mechanism, driving cosmic inflation, and shedding light on enigmatic concepts such as dark matter and dark energy.

Of particular interest are light scalar fields, prevalent in cosmological contexts, which could potentially introduce a fifth force akin to gravity. However, stringent constraints from local gravity tests necessitate careful consideration. The existence of such scalar fields demands either exceedingly weak couplings to matter through fine-tuning or the incorporation of mechanisms that account for the absence of observed fifth forces.

This thesis focuses on scalar field theories equipped with screening mechanisms, exemplified by models like chameleon, symmetron, and environment-dependent dilaton fields. These mechanisms render the fifth force weak in dense environments while allowing its manifestation in low-density settings.

To explore these theories, vacuum tabletop experiments emerge as optimal tools due to their high precision and since they usually operate in vacuum. However, the nonlinear nature of the governing equations presents significant theoretical challenges.

The primary objective of this work is to develop theoretical and numerical techniques tailored for studying screened scalar fields within the framework of tabletop experiments, particularly those associated with TU Wien. These experiments, including neutron interferometry, gravity resonance spectroscopy (qBOUNCE), and the Casimir And Non-Newtonian force EXperiment (CANNEX), are suited to probe screened scalar fields. Additionally, an analysis of Lunar Laser Ranging (LLR) within this context is conducted.

A key focus lies on investigating the relatively less explored environment-dependent dilaton model, whose self-interaction potential naturally arises in the strong coupling limit of string theory.

The culmination of this research involves deriving parameter constraints for the environment-dependent dilaton, chameleon, and symmetron models, thereby contributing to a deeper understanding of screened scalar fields and their implications in theoretical and experimental physics.

Acknowledgments

I extend my heartfelt gratitude to all those who supported me throughout my PhD journey.

First and foremost, I owe a debt of gratitude to my supervisor Mario Pitschmann, the visionary behind this project. Mario's profound knowledge and diverse interests including quantum field theory, general relativity, cosmology, and experimental physics and his willingness to share his knowledge in numerous conversations enriched my understanding of physics immensely. However, it's Mario's exceptional conscientiousness that I hold in highest regard. His unwavering commitment to supporting his students is exemplified by his remarkable support. While few individuals respond to emails within hours, sometimes minutes, Mario consistently does so. Whenever I asked for a longer discussion with him, he would usually give me an appointment on the very same day, which I find very commendable. Beyond guiding me through my doctoral studies, he provided numerous ideas for my future academic pursuits and always truly supported me.

I also wish to express my appreciation to René Sedmik, a postdoctoral fellow at the TU Wien, who despite his demanding schedule with the CANNEX experiment, generously shared his expertise in numerical methods during the nascent stages of my research.

Furthermore, I am grateful to Christian Käding, a postdoctoral fellow in Mario's theory group. While always ready to share his expertise when I had questions, I am especially grateful to him for his dedication to completing our final publication during the last stages of my PhD when time constraints were pressing.

Michael Neunteufel, a postdoctoral researcher in mathematics at TU Wien, merits my sincere thanks for his willingness to engage in insightful discussions related to numerical methods, despite his own professional commitments.

Special acknowledgment goes to Joachim Bosina, currently a postdoctoral fellow at TU Wien, for his invaluable assistance with various logistical matters and tasks throughout my PhD journey.

I am also profoundly thankful to several other individuals whose scientific contributions have significantly enriched this work. I am pleased to offer a comprehensive listing of all scientific contributions in a dedicated chapter at the conclusion of my thesis.

Lastly, I am profoundly grateful to my wife, Nathalia Fischer, for her unwavering support and understanding throughout this challenging period. Her love and encouragement sustained me as we navigated the complexities of raising two young children while pursuing my doctoral studies. Without her steadfast support, balancing the demands of parenthood and academia would have been an insurmountable task.

Publications

The research of this thesis contributed to the following publications:

Published:

[1] Philippe Brax, **Hauke Fischer**, Christian Käding, and Mario Pitschmann.
The environment dependent dilaton in the laboratory and the solar system.
Eur. Phys. J. C, 82(10):934, 2022.

[2] **Hauke Fischer**, Christian Käding, René I.P. Sedmik, Hartmut Abele, Philippe Brax and Mario Pitschmann.
Search for environment-dependent dilatons.
Phys. Dark Univ., 43:101419, 2024.

[3] **Hauke Fischer**, Christian Käding, Hartmut Lemmel, Stephan Sponar and Mario Pitschmann.
Search for dark energy with neutron interferometry.
PTEP, 2024(2):023E02, 2024.

[4] Hamid Haghmoradi, **Hauke Fischer**, Alessandro Bertolini, Ivica Galić, Francesco Intravaia, Mario Pitschmann, Raphael Schimpl, and René I.P. Sedmik.
Force metrology with plane parallel plates: Final design review and outlook.
Physics, 6:690–741, 3 2024.

[5] **Hauke Fischer,** Christian Käding and Mario Pitschmann.
Screened Scalar Fields in the Laboratory and the Solar System.
Universe, 10:297, 2024.

[6] **Hauke Fischer,** and René I.P. Sedmik.
Numerical methods for scalar field dark energy in table-top experiments and lunar laser ranging.
arXiv:2401.16179, 2024.
accepted by JCAP

Contents

Conventions

The following conventions are used throughout this thesis:

1. The Minkowski metric is defined as $\eta_{\mu\nu} = \text{diag}(1, -1, -1, -1)$.
2. Unless explicitly stated otherwise, $\hbar$ and c are set to 1.
3. The reduced Planck mass is defined as $m_{\text{pl}} := \sqrt{\frac{\hbar c}{8\pi G}} \simeq 2.435 \times 10^{21}$ MeV.
4. For two four-vectors a, b, the operation $a_\mu b^\mu$ is defined as $a_0 b^0 + a_1 b^1 + a_2 b^2 + a_3 b^3$.
5. A dot over a function ($\dot{\phi}$) refers to a time derivative.
6. Experimental vacuum densities are denoted by ρ_V, and material densities are represented by ρ_M.
7. ϕ_V denotes the potential minimum of a scalar field within vacuum, while ϕ_M signifies the minimum within material.

1. Introduction

According to our current understanding, our universe consists of approximately 5 % baryonic matter, 27 % dark matter and 68 % dark energy [7]. Despite their prevalence, the nature of dark matter and dark energy remains largely elusive, with indications that they interact only weakly, if at all, with Standard Model particles. The energy distribution of the universe is commonly quantified by the parameter $\Omega := \rho/\rho_c$, where ρ represents the average energy density of the universe and ρ_c denotes the critical density required for a flat universe (further discussed in Section 2.1). Notably, the measured value of Ω aligns closely with unity [7], implying that the observable universe exhibits flatness—a characteristic that would not be observed without the influence of dark matter and dark energy.

While baryonic matter is observable directly, the existence of dark matter is inferred through various phenomena, including the flat rotation curves of spiral galaxies [8], the gravitational lensing effects of massive structures like galaxies, the high velocities of individual galaxies within clusters [9], the rapid formation of gravitationally bound structures [10, 11], and other empirical observations (for a comprehensive review, see [12]). In each instance, the presence of dark matter is necessary to account for the unexpectedly strong gravitational effects, surpassing those predicted solely by visible matter.

Dark energy, in contrast, is primarily linked to the accelerated expansion of the universe and, unlike dark matter, exhibits an extremely uniform distribution while exerting gravitational repulsion. Notably, observations of Type Ia supernovae have provided compelling evidence for the ongoing accelerated expansion of our universe [13–15]. Further support for the existence of dark energy has been garnered from observations of the cosmic microwave background radiation (CMB) [16–18] and the presence of Baryonic Acoustic Oscillations in the large-scale correlation function of galaxy surveys [19–21]. Dark energy is often associated with the concept of vacuum energy. The simplest model capable of describing cosmic acceleration posits a cosmological constant Λ_0, representing an intrinsic energy of the vacuum.

While the ΛCDM (Λ for the cosmological constant and CDM for cold dark matter) model of cosmology is sometimes referred to as the standard model of cosmology [22], it leaves several questions unanswered.

The idea of cosmic inflation, originally proposed by Alan Guth [23], addresses two of these questions. The Ω parameter, measured to be approximately 1, implies a flat universe, however, general relativity (GR) also allows for $\Omega > 1$ (indicating positive overall curvature) or $\Omega < 1$ (indicating negative overall curvature), with no a priori reason for it to be precisely 1. Additionally, if the universe were to start with $\Omega \neq 1$, it would quickly deviate from this value. The second issue, known as the horizon problem, arises from the remarkable uniformity in the temperature of the universe in all directions, which seems inconsistent with the ΛCDM cosmology where not all regions could have interacted sufficiently to reach temperature equilibrium [24]. Both problems are ultimately fine-tuning problems: if the initial conditions of the universe were such that matter had identical temperatures everywhere and the universe was precisely flat, the ΛCDM model would require no extension. However, in the theory of cosmic inflation the potential energy of a decaying scalar field could trigger a brief period of exponential expansion prior to the ΛCDM epoch. In this theory, the observable universe emerged from a tiny patch of space that had ample time to reach temperature equilibrium and underwent exponential expansion to become significantly larger. This rapid expansion naturally leads to a universe approaching flatness and possessing a highly uniform temperature. Cosmic inflation also provides insight into the origin of initial density fluctuations present in the CMB, which subsequently evolve into the large-scale structure of the universe [25,26]. The Planck Collaboration has concluded that 'the Planck results

offer powerful evidence in favor of simple inflationary models' [27].

Another fine-tuning issue arises from the extremely small value of $\Lambda_0 \sim 10^{-120}\, m_{\mathrm{pl}}^4$ [28,29] within the ΛCDM cosmology, which lacks an explanation. Λ_0 is typically associated with the energy of the vacuum and should theoretically receive contributions from the zero-point energy of quantum fields. However, estimates suggest that the contribution of quantum fields is approximately 60 orders of magnitude larger than the observed value of Λ_0, however, this depends on the chosen ultraviolet cutoff for the SM. Postulating a bare cosmological constant, independent of quantum fields and capable of canceling their contributions to 60 decimal places, necessitates remarkable fine-tuning [29]. Given the success of cosmic inflation theory, it's natural to consider whether the current accelerated expansion of the universe might also be driven by the potential energy of a scalar field. This approach to dark energy is sometimes referred to as quintessence [29, 30]. Alternatively, it's possible that the value of Λ_0 is inherently zero, and its observed small value could be explained by a scalar field approaching its potential energy value of zero at a later stage in the universe's evolution.

Scalar fields have significant motivation beyond potential cosmological applications. A prominent example is the Higgs field, postulated to explain the non-vanishing mass of weak interaction gauge bosons [31–33]. The discovery of the Higgs boson [34] confirms the existence of scalar fields in nature.

Another motivation for anticipating new scalar fields stems from their prediction by various modifications of GR. Modifying GR arises from several potential motivations. While quantum physics typically describes phenomena at very small scales and encompasses the strong and electroweak forces, gravity, as described by GR, is primarily associated with large-scale phenomena such as planets, solar systems, galaxies, and cosmology. In most scenarios, it suffices to apply either quantum physics or GR independently. However, in extreme situations like black holes [35], neither gravity nor quantum physics can be ignored: gravity cannot be neglected due to its significant mass, and quantum physics becomes essential because matter is compressed into a tiny region, necessitating a quantum description. Consequently, extensive efforts have been directed towards finding a deeper theory of quantum gravity that deviates from GR (see [36] for a review). One early modification of GR, explored by Albert Einstein himself, is known as Kaluza-Klein theory [37], which aims to unify electromagnetism with gravity—albeit classically—in a five-dimensional spacetime. The additional fourth spatial dimension is compactified to form a small cylinder. In this theory, the metric possesses five additional degrees of freedom (in five spacetime dimensions, the metric has 15 independent components; in four dimensions, it has 10 due to symmetry). While 10 degrees of freedom correspond to the familiar four-dimensional spacetime metric, four components can be associated with the electromagnetic four-potential. The remaining component acts as a scalar field in an effective four-dimensional theory. Similarly, other higher-dimensional theories such as string theory, which rely on the compactification of high-dimensional spaces, naturally predict new scalar degrees of freedom in an effective four-dimensional spacetime theory [38]. Other modifications of GR that predict new scalar degrees of freedom include $f(R)$ gravity [39], where the Ricci scalar in the Einstein-Hilbert action is replaced with a function of R, and Brans-Dicke theory [40], which introduces a new scalar field into the Einstein-Hilbert action to permit a spacetime-dependent value of the gravitational constant G.

While there is ample motivation to expect new scalar degrees of freedom, the discovery of the accelerated expansion of the universe is particularly intriguing because a scalar field capable of driving cosmic expansion would need to be extraordinarily light (see Section 2.1). Consequently, it would introduce a new long-range force that should be detectable in solar system tests and tabletop experiments. With stringent solar system tests of GR provided by Lunar Laser Ranging (LLR) [41], the absence of any observed fifth forces can only be reconciled by an extraordinarily

weak coupling of the scalar field to matter.

A different approach, which allows for gravitational strength coupling without violating existing constraints, was introduced with the chameleon scalar field [42] (for further discussion, see Section 3.2). This field has a mass that depends on the matter density of its environment. In high-density regions, the mass increases, rendering the field short-ranged and 'screened', while in low-density regions, the field becomes long-ranged and would lead to an appreciable new force. This concept has ignited a new branch of research into screening mechanisms and the detection of screened scalar fields. Additional screening mechanisms have been discovered and can generally be classified into three categories [29]: increasing the mass in dense environments, such as the chameleon; decreasing the coupling to matter in dense environments, as exemplified by symmetrons [43] (discussed in Section 3.3); and kinetic screening and Vainshtein screening, where the kinetic term in the Lagrangian is modified (or additional terms are added), suppressing kinetics in dense environments, leading to a short range. An example of this is galileons [44, 45], which are not the focus of this thesis.

References [46–49] investigated whether symmetron fields could also account for phenomena typically associated with particle dark matter. They concluded that the anomalous rotation curves of spiral galaxies might be attributed to the fifth force of a symmetron field and its energy contribution to galaxies. Similarly, symmetrons may explain gravitational lenses that are too strong to be accounted for by GR and baryonic matter. It has long been known that rotation curves of galaxies can be derived from modifications of gravity that do not postulate the existence of particle dark matter. A well-known alternative possibility is to modify Newton's laws of motion for extremely small accelerations, an idea known as Modified Newtonian Dynamics (MOND) [50, 51]. A relativistic generalization of MOND is known as TeVes [52], a tensor-vector-scalar field theory. Clearly, no screened scalar field theory to date can explain all the lines of evidence for dark matter without introducing particle dark matter. Nonetheless, the possibility remains that they may contribute to the solution of the dark matter problem, which serves as additional motivation to explore them.

Screened scalar fields exhibit certain generic features, such as the suppression of the fifth force in dense environments and large objects. This suppression occurs because the fields couple only to a thin shell beneath the object's surface, a phenomenon known as the thin-shell effect [53]. Consequently, if such fields exist, high-precision tabletop experiments are expected to be more sensitive to them than astrophysical measurements. This increased sensitivity arises because, in smaller scale experiments, the thin-shell effect is less pronounced, shorter ranges can be probed, and the experiments are conducted in a vacuum where the force experiences less suppression. However, despite these qualitative expectations, determining which experiment is most sensitive to screened scalar fields requires a rigorous analysis dependent on the specific model parameters. Thus, tabletop experiments should be viewed as complementary to astrophysical measurements.

To date, various tabletop experiments have been employed to probe fifth forces associated with screened scalar fields and derive constraints on the parameters of these models. These experiments include atom interferometry [54–58], Eöt-Wash experiments [59, 60], gravity resonance spectroscopy [61–64], atomic precision measurements [65], neutron interferometry [66], CASIMIR experiments [67–70], and more. Additional investigations using Bose-Einstein condensate interferometry have been suggested and could significantly enhance the search for chameleons and symmetrons [71] (see also Ref. [72] for further exploration of screened scalar fields in the context of Bose-Einstein condensates).

In addition to laboratory tests, several astrophysical analyses have been undertaken (refer to [53, 73] for a comprehensive review). However, these endeavors have thus far failed to detect any positive effects associated with screened scalar fields.

The Atominstitut of the Technische Universität Wien presents an ideal environment for the investigation of screened scalar fields, owing to its affiliation with various high-precision tabletop experiments designed to probe new physics. Notably, the qBOUNCE experiment [74–76], which utilizes gravity resonance spectroscopy, along with neutron interferometry, have been employed in the quest to uncover the chameleon field [66, 77–79]. Furthermore, qBOUNCE has extended its scope to investigate the symmetron field [63, 64].

In addition, the Casimir And Non-Newtonian Force Experiment (CANNEX) stands out as a dedicated endeavor, conceived from its inception to be adept at detecting, among other things, fifth forces linked with screened scalar fields [80]. Currently, scientists at the Atominstitut are actively engaged in assembling this experiment (a detailed introduction of these experiments is provided in Section 5). Notably, prospective constraints on the parameters governing the chameleon and symmetron fields have already been calculated [81, 82].

This thesis is part of a collaborative effort between experimental physicists associated with the Technische Universität Wien and theoretical physicists. It encompasses several overarching objectives:

One primary goal is to conduct a thorough investigation into the relatively underexplored environment-dependent dilaton model. This model holds stronger theoretical motivations compared to the chameleon or symmetron models, as its potential naturally emerges in the strong coupling limit of string theory [83–85]. Moreover, it has been proposed as a potential candidate for dark energy. However, despite its theoretical promise, this model has received comparatively less attention than the chameleon or symmetron models, and as of yet, parameter constraints are lacking.

Another significant aim is to enhance both the theoretical and numerical analyses for deriving experimental constraints applicable to the qBOUNCE, CANNEX, and neutron interferometry experiments across various models. Additionally, the objective includes deriving constraints from LLR [86, 87]. This endeavor seeks to bolster our understanding of the fundamental physics underlying these experiments and advance our capability to derive meaningful constraints that contribute to broader scientific knowledge.

This thesis is organized as follows:

Section 2 provides a brief exploration of the role of a cosmological constant and discusses how scalar fields could potentially drive the accelerated expansion of the universe. This investigation is followed by a concise introduction to the general framework of scalar-tensor theories investigated within this thesis.

Section 3 is mainly dedicated to the introduction of the environment-dependent dilaton model. This Section delves into its parameter-dependent screening mechanisms, parameter symmetries, and further investigates its potential as a dark energy candidate. Brief introductions to the symmetron and chameleon models are also provided.

Section 4 discusses suitable techniques for simulating any of the explored models for arbitrary parameters. Special attention is given to the environment-dependent dilaton field, which presents unique numerical challenges due to its exponential self-coupling. Additionally, a robust numerical method for solving the stationary Schrödinger equation in the presence of a screened scalar field is presented. These methods allow bypassing analytical approximations to the equations of motion and avoiding a perturbative treatment when solving the stationary Schrödinger equation.

In Section 5, each of the studied experiments is introduced in detail, and the theoretical framework necessary for computing scalar field constraints developed. The amalgamation of these results to derive the final constraints is elucidated.

Section 6 discusses the experimental constraints obtained using the methods outlined in this thesis. Constraints are derived for the following scenarios:

1. Dilaton field constraints from neutron interferometry, *q*BOUNCE, LLR and CANNEX, the latter only prospective.

2. Symmetron field constraints from neutron interferometry, *q*BOUNCE and CANNEX, the latter only prospective. The *q*BOUNCE and CANNEX constraints are a re-analysis of existing constraints, marked by significant methodological improvements compared to previous analyses.

3. Chamelon field constraints from *q*BOUNCE and CANNEX, the latter only prospective. The *q*BOUNCE and CANNEX constraints are a re-analysis of existing constraints, marked by significant methodological improvements compared to previous analyses. However, prospective CANNEX constraints for the case $n = 1$ and varying Λ are investigated for the first time.

The substantial methodological advancements made in this thesis compared to existing analyses are exemplified in Section 6.2.2 and Section 6.2.3.

In Section 7, the findings are summarized.

I wish to acknowledge that the results presented in this thesis encompass contributions beyond my own. A comprehensive breakdown of the specific contributions made by my collaborators will be provided in the Section 8.

2. Summary of Scalar-Tensor theories

In Subsection 2.1, the discussion briefly covers how scalar fields can potentially drive the accelerated expansion of the universe. It begins with an examination of the role of a cosmological constant and explores how a scalar field might emulate its effects.

Moving on to Subsection 2.2, the broader concept of scalar-tensor theories is introduced, which serves as the theoretical framework throughout this thesis.

2.1. Scalar field dark energy

This Subsection is largely based on [88], but some results were also taken from [24, 29] for a brief cosmological motivation for investigating scalar fields. Notably, the discussion on the Klein-Gordon field in Section 2.1.2 is not covered in these references; it has been included solely for illustrative purposes.

2.1.1. The cosmological constant

The cosmological constant Λ_0 serves as a parameter within Einstein's field equations:

$$R_{\mu\nu} - \frac{1}{2} g_{\mu\nu} R = \frac{1}{m_{\mathrm{pl}}^2} T_{\mu\nu} + \Lambda_0 g_{\mu\nu}, \tag{2.1.1}$$

where $R_{\mu\nu}$ denotes the Ricci Tensor, R the Ricci Scalar, $g_{\mu\nu}$ the space-time metric, and $T_{\mu\nu}$ the energy-momentum tensor of matter. By comparing the cosmological constant term with the energy-momentum tensor of a perfect fluid [89]:

$$T_{\mu\nu} = (p + \rho) u_\mu u_\nu - p g_{\mu\nu}, \tag{2.1.2}$$

where ρ represents the energy density of the fluid, p denotes its pressure, and u_μ its four-velocity, it is evident that the cosmological constant can be viewed as a perfect fluid with:

$$\begin{aligned} \rho_{\Lambda_0} &= m_{\mathrm{pl}}^2 \Lambda_0, \\ p_{\Lambda_0} &= -m_{\mathrm{pl}}^2 \Lambda_0 \\ w_{\Lambda_0} &:= \frac{p_{\Lambda_0}}{\rho_{\Lambda_0}} = -1. \end{aligned} \tag{2.1.3}$$

In the last line, the parameter w was introduced, quantifying the pressure-to-energy density ratio. Notably, a cosmological constant is characterized by $w_{\Lambda_0} = -1$, differing from non-relativistic matter with $w = 0$, while relativistic matter (such as photons and neutrinos) is characterized by $w = \frac{1}{3}$. To understand how a cosmological constant can accelerate the expansion of the universe, a brief discussion is provided on how the evolution of the universe depends on its energy content.

On large scales, the universe can be approximately described by a FLRW (Friedmann-Lemaître-Robertson-Walker) metric, compatible with the cosmological principle of isotropy and spatial homogeneity. In spherical coordinates (with angles θ and Φ), the line element is given by:

$$dl^2 = dt^2 - a_S^2(t) \Big(\frac{dr^2}{1 - kr^2} + r^2 (d\theta^2 + \sin^2\theta d\Phi^2) \Big). \tag{2.1.4}$$

Here, $a_S(t)$ represents the scale factor describing the universe's expansion, $k \in \{-1, 0, 1\}$ distinguishes between negatively curved, flat, or positively curved universes, and r is defined to be temporally constant, with expansion solely described by $a_S(t)$. Modeling the energy content of the universe as a perfect fluid with density ρ and pressure p, one can use Eq. (2.1.4) as an Ansatz for Einsteins Field Equations. Assuming the rest frame of matter ($u_\mu = \delta_{0i}$), this Ansatz results in the Friedman equations, describing the evolution of $a_S(t)$ over time:

$$\frac{3}{a_S^2}\left(\dot{a}_S^2 + k\right) = \frac{\rho}{m_{\text{pl}}^2} + \frac{\rho_{\Lambda_0}}{m_{\text{pl}}^2}, \tag{2.1.5}$$

$$\frac{\ddot{a}_S}{a_S} = -\frac{(\rho + 3p)}{6m_{\text{pl}}^2} + \frac{\rho_{\Lambda_0}}{3m_{\text{pl}}^2}. \tag{2.1.6}$$

Notably, the latter equation indicates that a universe dominated by the energy contribution of Λ_0 experiences $\ddot{a}_S > 0$, thus expanding at an accelerated rate. It is conventional to use Eq. (2.1.5) to define the critical energy density ρ_c for a flat universe ($k = 0$):

$$\rho_c(t) := 3H^2(t)m_{\text{pl}}^2. \tag{2.1.7}$$

Here, the Hubble parameter $H(t)$ is defined as $H(t) := \dot{a}_S(t)/a_S(t)$. Introducing

$$\Omega_{\Lambda_0} := \frac{\rho_{\Lambda_0}}{\rho_c}, \tag{2.1.8}$$

allows to express the current energy density of Λ_0 as

$$\rho_{\Lambda_0} = 3\Omega_{\Lambda_0}H_0^2 m_{\text{pl}}^2 \simeq 2.51 \times 10^{-35}\ \text{MeV}^4. \tag{2.1.9}$$

Here, $\Omega_{\Lambda_0} \simeq 0.685$ and H_0 represents the Hubble parameter at present [7].

2.1.2. Scalar fields mimicking a cosmological constant

The origin of the cosmological constant remains a mystery. One possible explanation is that the vacuum energy, associated with this constant, arises from a scalar field.

An important insight is that, similar to a cosmological constant, scalar fields can also be envisioned as perfect fluids. This is apparent when observing the energy-momentum tensor of a scalar field ϕ with a potential energy density $V(\phi)$:

$$T^\phi_{\mu\nu} = \partial_\mu\phi\partial_\nu\phi - g_{\mu\nu}\left(\frac{1}{2}\partial_\alpha\partial^\alpha\phi - V(\phi)\right). \tag{2.1.10}$$

Comparing this to Eq. (2.1.2), a scalar field can be conceptualized as a perfect fluid with the following components:

$$\begin{aligned} u_\mu &= (\partial_\alpha\phi\partial^\alpha\phi)^{-\frac{1}{2}}\partial_\mu\phi \\ p_\phi &= \frac{1}{2}\partial_\alpha\phi\partial^\alpha\phi - V(\phi) \\ \rho_\phi &= \frac{1}{2}\partial_\alpha\phi\partial^\alpha\phi + V(\phi). \end{aligned} \tag{2.1.11}$$

Hence, if $p_\phi = -\rho_\phi$ the scalar field effectively behaves as a cosmological constant. Considering a homogeneous scalar field, which aligns with the observed homogeneity of the universe on large scales, leads to:

$$w_\phi = \frac{\frac{1}{2}\dot{\phi}^2 - V(\phi)}{\frac{1}{2}\dot{\phi}^2 + V(\phi)}. \tag{2.1.12}$$

In order for the scalar field to act as a cosmological constant with $w_\phi \simeq -1$ it must slowly evolve over time ($\frac{1}{2}\dot{\phi}^2 \ll V(\phi)$). The slow-roll condition is coupled to the dynamics of the scalar field, which - assuming a FLRW background - is determined by

$$\ddot{\phi} + 3H\dot{\phi} + V_{,\phi}(\phi) = 0. \tag{2.1.13}$$

To serve as the source of dark energy, with $V(\phi) = 3\Omega_{\Lambda_0} H_0^2 m_{\rm pl}^2$, the scalar field's mass must be exceptionally light ($|m| \lesssim H_0 \simeq 10^{-33}$)eV to evolve suitably slowly. For elucidation, a simplified example is presented. More rigorous investigations are provided in Refs. [90–92].

A Klein-Gordon field with $V(\phi) = \frac{m^2}{2}\phi^2$ needs to fulfill $\phi = \sqrt{6\Omega_{\Lambda_0}} H_0 m_{\rm pl}/m$ to act as dark energy at present. From the slow-roll condition, it follows that $|\dot{\phi}| \ll \sqrt{6\Omega_{\Lambda_0}} H_0 m_{\rm pl}$. If $m \gg H_0$, Hubble friction loses effectiveness at the present moment:

$$\frac{3H_0\dot{\phi}}{V_{,\phi}(\phi)} \ll \frac{3H_0}{m} \ll 1. \tag{2.1.14}$$

Resultantly, the field behaves akin to a free harmonic oscillator. Hence

$$\frac{\frac{1}{2}\dot{\phi}^2}{V(\phi)} = \frac{\sin^2\big(m(t-t_c)\big)}{\cos^2\big(m(t-t_c)\big)}. \tag{2.1.15}$$

Here, t_c denotes a constant necessitating determination from initial conditions. Violation of the slow-roll condition occurs rapidly on cosmological timescales if $m \gg H_0$, with the scalar field oscillating at frequency m. Hence, $|m| \leq H_0$ is essential. A light scalar field could induce a long-ranged force if directly coupled to matter, necessitating screening mechanisms for compatibility with solar system tests of GR.

Unlike a true cosmological constant, the behavior of the scalar field typically varies with space-time. Given dark energy's enigmatic origin as just one motivation for exploring scalar fields, further exploration is deferred, and interested readers are directed to the comprehensive reviews in Ref. [29, 53] regarding scalar fields in the context of dark energy.

2.2. Scalar-Tensor theories

This Section offers a concise overview of the theoretical framework underlying the scalar field models investigated in this thesis. The foundation of this summary is drawn from Ref. [93]. For detailed mathematical proofs of the formulas presented, readers are directed to the cited reference.

The scalar field theories explored in this thesis are defined by the following general action [94]:

$$S = \int d^4x\,\sqrt{-g}\left(-\frac{m_{\rm pl}^2}{2}\,R + \frac{1}{2}\,\partial_\mu\phi\,\partial^\mu\phi - V(\phi)\right) + \int d^4x\,\sqrt{-\tilde{g}}\,\mathcal{L}_{\rm SM}(\tilde{g}_{\mu\nu}, \psi_i). \tag{2.2.16}$$

In this context, $V(\phi)$ represents the self-interaction potential of the scalar field ϕ, while $\tilde{g}_{\mu\nu} = A^2(\phi)g_{\mu\nu}$ denotes the Weyl-rescaled metric. The symbol R stands for the Ricci scalar, and $m_{\rm pl}$ is the reduced Planck mass. Importantly, matter is minimally coupled to $\tilde{g}_{\mu\nu}$ rather than $g_{\mu\nu}$. The Lagrangian density $\mathcal{L}_{\rm SM}$ incorporates the Standard Model (SM) fields ψ_i. This action extends the Einstein-Hilbert action of GR [95] (where $A(\phi) = 1$) by introducing a non-minimal coupling of the scalar field to the metric through a conformal factor $A(\phi)$.

Two distinct frames are typically distinguished: The first frame is the Einstein frame, where the Ricci-scalar term in the action of GR remains unchanged (with no scalar field), and the action is fully expressed by $g_{\mu\nu}$:

$$S = \int d^4x\sqrt{-g}\Big(-\frac{m_{\rm pl}}{2}R + \frac{1}{2}\partial_\mu\phi\partial^\mu\phi - V(\phi)\Big) + \int d^4x\sqrt{-g}A^4(\phi)\mathcal{L}_{\rm SM}\big(A^2(\phi)g_{\mu\nu}, \psi_i\big). \quad (2.2.17)$$

In the Jordan frame, the matter component of the action adopts the identical form as in GR, albeit with the modification that $g_{\mu\nu}$ is replaced by $\tilde{g}_{\mu\nu}$. The entire action is then expressed exclusively in terms of $\tilde{g}_{\mu\nu}$:

$$S = \int d^4x\sqrt{-\tilde{g}}A^{-2}(\phi)\Big(-\frac{m_{\rm pl}}{2}\tilde{R} + \frac{1}{2}\kappa^2(\phi)\tilde{\partial}_\mu\phi\tilde{\partial}^\mu\phi - A^{-2}(\phi)V(\phi)\Big) + \int d^4x\sqrt{-\tilde{g}}\mathcal{L}_{\rm SM}\big(\tilde{g}_{\mu\nu}, \psi_i\big), \quad (2.2.18)$$

with

$$\kappa^2(\phi) = 1 - \frac{3}{2}m_{\rm pl^2}\Big(\frac{d\ln A^{-2}(\phi)}{d\phi}\Big)^2. \quad (2.2.19)$$

It is important to observe that quantities denoted with a tilde correspond to values expressed in terms of the Jordan metric. For instance, $\tilde{\partial}_\mu\phi\tilde{\partial}^\mu\phi := \tilde{g}^{\mu\nu}\partial_\mu\phi\partial_\nu\phi$. In the subsequent discussion, some of the physical implications in these two distinct frames will be briefly examined.

2.2.1. The Jordan frame

In the Jordan frame, the Weyl-rescaling induces transformations:

$$\begin{aligned} g_{\mu\nu} \to \tilde{g}_{\mu\nu} &= A^2(\phi)g_{\mu\nu} \\ g^{\mu\nu} \to \tilde{g}^{\mu\nu} &= \frac{1}{A^2(\phi)}g^{\mu\nu}, \\ \sqrt{-g} \to \sqrt{-\tilde{g}} &= A^4(\phi)\sqrt{-g}, \\ dl \to d\tilde{l} &= A(\phi)dl. \end{aligned} \quad (2.2.20)$$

This implies that locally, all lengths and times are rescaled by a factor of $A(\phi)$, while leaving all angles invariant. This conformal rescaling affects densities and pressures but leaves masses unchanged:

$$\begin{aligned} m_0 &\to m_0, \\ \rho_0 &\to \tilde{\rho} = \frac{1}{A^3(\phi)}\rho_0 \\ p_0 &\to \tilde{p} = \frac{1}{A^3(\phi)}p_0, \end{aligned} \quad (2.2.21)$$

where the index 0 refers to quantities before re scaling. Similarly, $u^\mu = \frac{dx^\mu}{dl}$ implies:

$$u^\mu \to \tilde{u}^\mu = \frac{1}{A(\phi)} u^\mu$$
$$u_\mu \to \tilde{u}_\mu = A(\phi) u_\mu.$$

Since $\tilde{g}_{\mu\nu}$ is minimally coupled to matter, the covariant divergence of the stress-energy tensor is zero:

$$\tilde{\nabla}_\mu \tilde{T}^{\mu\nu} = 0. \tag{2.2.22}$$

Thus, in the Jordan frame, several physical quantities undergo rescaling. Point particles move along geodesics of $\tilde{g}_{\mu\nu}$ due to minimal coupling, and there is no fifth force from the scalar field. The equations of motion for $\tilde{g}_{\mu\nu}$ and ϕ could, in principle, be derived from the action in the Jordan frame, but they would not adopt a familiar form due to the substantial modifications compared to the Einstein-Hilbert action.

2.2.2. The Einstein frame

The Einstein frame exhibits a closer resemblance to GR, as evidenced by the forthcoming equations of motion. This frame is the preferred choice for subsequent analyses; therefore, a more in-depth investigation is provided. The transformations in the Einstein frame leave the following quantities unchanged

$$\begin{aligned} g_{\mu\nu} &\to g_{\mu\nu} \\ \sqrt{-g} &\to \sqrt{-g} \\ dl &\to dl \\ u^\mu &\to u^\mu. \end{aligned} \tag{2.2.23}$$

However, the mass, matter density, and pressure of matter depend on the scalar field:

$$\begin{aligned} m_0 &\to m = A(\phi) m_0 \\ \rho_0 &\to \rho = A(\phi) \rho_0 \\ p_0 &\to p = A(\phi) p_0. \end{aligned} \tag{2.2.24}$$

In the Einstein frame, the equations of motion for the metric assume a familiar form:

$$R_{\mu\nu} - \frac{1}{2} g_{\mu\nu} R = \frac{1}{m_{pl}^2} (T^\phi_{\mu\nu} + T_{\mu\nu}), \tag{2.2.25}$$

where

$$T^\phi_{\mu\nu} = \partial_\mu \phi \partial_\nu \phi - g_{\mu\nu} \big(\frac{1}{2} \partial_\alpha \partial^\alpha \phi - V(\phi) \big). \tag{2.2.26}$$

The equations of motion of ϕ are

$$\Box\phi + V_{\text{eff},\phi} = 0, \tag{2.2.27}$$

where

$$V_{\text{eff}}(\phi) = V(\phi) + \big(A(\phi) - 1\big)\rho \tag{2.2.28}$$

in the non-relativistic limit. The combined energy-momentum tensor of the scalar field and matter maintains covariant conservation:

$$\nabla^\mu(T^\phi_{\mu\nu} + T_{\mu\nu}) = 0. \tag{2.2.29}$$

However, individual conservation does not hold:

$$\begin{aligned}\nabla^\mu T_{\mu\nu} &= \partial_\nu\big(\ln\, A\big)T,\\ \nabla^\mu T^\phi_{\mu\nu} &= -\partial_\nu\big(\ln\, A\big)T.\end{aligned} \tag{2.2.30}$$

This implies the presence of a fifth force in the Einstein frame. The force acting on a point particle with mass m is given by:

$$f^\mu_\phi = m\Big(\partial^\mu\big(\ln\, A\big) - \partial_\alpha\big(\ln\, A\big)u^\alpha u^\mu\Big). \tag{2.2.31}$$

In the non-relativistic limit, which is used in this thesis, this expression simplifies

$$\vec{f}_\phi = -m\vec{\nabla}\ln\, A(\phi) \simeq -m\vec{\nabla}A(\phi) = -\beta(\phi)\frac{m}{m_{pl}}\vec{\nabla}\phi, \tag{2.2.32}$$

where the full coupling to matter is defined as:

$$\beta(\phi) = m_{\text{pl}}\frac{dA(\phi)}{d\phi}. \tag{2.2.33}$$

The calculation assumed $A(\phi) \simeq 1$, which is fulfilled for all models under considerations in this thesis. The force given in Eq. (2.2.32) bears a resemblance to the Newtonian gravitational force law, with a distinctive feature—unlike being directly proportional to the gradient of ϕ, it involves a coupling function β to matter that varies with the value of ϕ. For further details, see Ref. [93].

3. Screened scalar fields investigated in this thesis

Subsection 3.1 provides a detailed exploration of the environment-dependent dilaton field, an aspect that has not been thoroughly investigated prior to this work. The symmetron and chameleon field are introduced in Subsections 3.2-3.3.

3.1. The environment-dependent dilaton field

The environment-dependent dilaton field [83–85] is conceptualized as a scalar-tensor theory with the following expressions [73]:

$$A(\phi) = 1 + A_2 \frac{\phi^2}{2m_{\rm pl}^2} + \mathcal{O}\left(\frac{\phi^3}{m_{\rm pl}^3}\right),$$
$$V(\phi) = V_0 e^{-\lambda\phi/m_{\rm pl}}. \tag{3.1.34}$$

Here, V_0 represents a constant energy density, A_2 is a dimensionless coupling constant to matter, and λ is a numerical constant. The effective potential in the non-relativistic limit is then given by

$$V_{\rm eff}(\phi;\rho) = V_0 e^{-\lambda\phi/m_{\rm pl}} + A_2\rho\frac{\phi^2}{2m_{\rm pl}^2}. \tag{3.1.35}$$

An illustrative example is presented in Fig. 3.1.1.

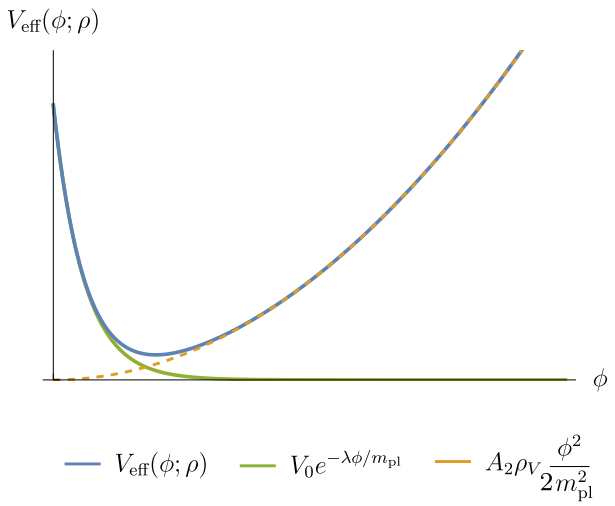

Fig. 3.1.1: Illustration of the effective potential of the environment-dependent dilaton field

This model finds motivation in the string dilaton χ within the strong coupling limit, where $V(\chi) \to 0$ as $\chi \to \infty$. $V(\chi)$ is asymptotically expanded as follows:

$$V(\chi) = \tilde{V}_0 e^{-\chi} + \mathcal{O}(e^{-2\chi}). \tag{3.1.36}$$

In Ref. [83], it is assumed that the coupling to matter reaches a minimum at a large value χ_0, and is given by

$$A(\chi) - 1 \propto (\chi - \chi_0)^2. \tag{3.1.37}$$

Under certain assumptions, the model considered here can be derived from the string dilaton by defining $\phi := \frac{m_{\rm pl}}{\lambda}(\chi - \chi_0)$, as elaborated in [93]. Throughout this thesis, the environment-dependent dilaton model defined in Eq. (3.1.34) is treated as an effective field theory, always adhering to the condition

$$A_2 \frac{\phi^2}{2m_{\rm pl}^2} < 0.1 \tag{3.1.38}$$

to ensure that couplings to matter of higher order can be neglected. The selection of 0.1 as the cutoff value may appear somewhat arbitrary; alternatively, one could opt for a different threshold that is sufficiently small compared to one. This particular value was chosen because it is the largest order of magnitude estimate that is smaller than one. However, it has been checked that all results obtained in this thesis are insensitive to the specific value chosen for the cutoff. Subsequent Subsections will establish general properties of the environment-dependent dilaton field. Henceforth, the term "environment-dependent dilaton field" is abbreviated as "dilaton field."

3.1.1. Potential minimum, dilaton mass and full coupling to matter

The potential minimum ϕ_ρ for the dilaton field is determined by the equation:

$$V_{{\rm eff},\phi}(\phi_\rho; \rho) = 0. \tag{3.1.39}$$

A short calculation shows [1]

$$\phi_\rho = \frac{m_{\rm pl}}{\lambda} W\left(\frac{\lambda^2 V_0}{A_2 \rho}\right). \tag{3.1.40}$$

Here, the Lambert W function [96] is employed, defined as the inverse function of xe^x. As W is a monotonically increasing function, it follows that if $\rho_1 < \rho_2$, then $\phi_{\rho_1} > \phi_{\rho_2}$.

This implies that the dilaton field experiences greater suppression in denser environments. The mass μ_ρ of the dilaton field is expressed as:

$$\mu_\rho = \sqrt{V_{{\rm eff},\phi\phi}(\phi_\rho; \rho)} = \frac{1}{m_{\rm pl}} \sqrt{\lambda^2 V_0 e^{-\lambda\phi_\rho/m_{\rm pl}} + A_2\rho}. \tag{3.1.41}$$

The full coupling to matter, denoted as $\beta(\phi)$, is given by:

$$\beta(\phi) = A_2 \frac{\phi}{m_{\rm pl}}. \tag{3.1.42}$$

3.1.2. The three parameter regions, screening mechanisms and parameter symmetries

This Subsection demonstrates the natural division of the dilaton model's parameter space into three distinct regions, each characterized by unique physical behaviors:

The small λ region, the intermediate λ region, and the large λ region, as illustrated in Fig. 3.1.2. This thesis adopts a parameter-agnostic approach, investigating the entire 3D parameter space that satisfies the minimal requirement of not violating the cutoff condition (3.1.38). Deriving parameter-agnostic constraints maximizes the amount of information obtained. Importantly, it will become evident throughout this Section that the dilaton model exhibits various approximate parameter symmetries, making it generally impossible to assign physical meaning to individual parameters. Therefore, excluding parameters from subsequent analyses would be arbitrary.

With this approach, the parameters considered are determined solely by the sensitivity of the experiments under scrutiny. Subsequent experimental analyses reveal that the experiments can probe the dilaton parameters for values up to $A_2 \sim 10^{60}$, $\lambda \sim 10^{32}$, and $V_0 \sim 10^{10^{24}}$ MeV^4 within the large λ region. This is why extremely large values of V_0 are considered in this thesis. In Section 3.1.4, it is clarified that this large value of V_0 is an artifact of the chosen parameterization and has no physical consequences.

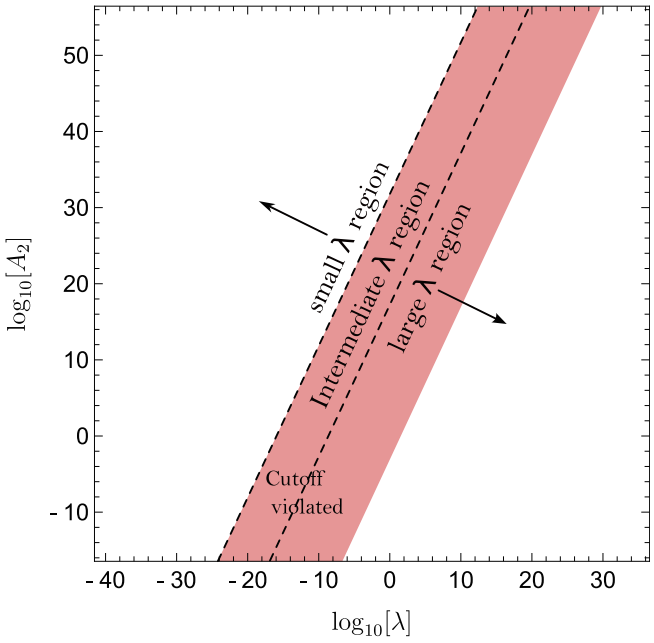

Fig. 3.1.2: This is an example of the three parameter regions for $V_0 = 10$ MeV^4 and $\rho_V = 10^{-15}$ MeV^4. The model is only defined for the small and large λ regions, because the intermediate λ region violates (3.1.38). ϕ has been set to ϕ_V to evaluate the red region where the cutoff is violated.

The small λ region Keeping V_0, A_2 and ρ fixed, λ can always be chosen small enough such that:

$$\frac{\lambda^2 V_0}{A_2 \rho} \ll 1, \tag{3.1.43}$$

defining the small λ region. Employing $W(x) \simeq x$ for small x, the following approximations hold within this region:

Exact expression	ϕ_ρ	$e^{-\lambda\phi_\rho/m_{\rm pl}}$	μ_ρ	$\beta(\phi_\rho)$
Approximation	$m_{\rm pl}\,\frac{\lambda V_0}{A_2\rho}$	1	$\frac{\sqrt{A_2\rho}}{m_{\rm pl}}$	$\frac{\lambda V_0}{\rho}$

Table 1: Approximations for the small λ region

This indicates a pronounced dependence of both the matter coupling $\beta(\phi_\rho)$ and field mass μ_ρ on matter density. Thus, two screening mechanisms manifest strongly within this parameter region: the chameleon effect, where the mass increases in dense environments and hence the range decreases, and a suppression of the coupling to matter.

Parameter symmetry:

Moreover, there is an approximate parameter symmetry within the dilaton model in this region. The equations of motion,

$$\begin{aligned}\Box\phi &= \frac{\lambda}{m_{\rm pl}}V_0 e^{-\lambda\phi/m_{\rm pl}} - A_2\rho\frac{\phi}{m_{\rm pl}^2}\\ &\simeq \frac{\lambda}{m_{\rm pl}}V_0 - A_2\rho\frac{\phi}{m_{\rm pl}^2},\end{aligned} \tag{3.1.44}$$

depend solely on the product $V_0\lambda$ and not on the individual values of V_0 and λ. Since neither of these parameters contributes to the full coupling of matter, the fifth force of the dilaton field also depends solely on the product $V_0\lambda$. This parameter symmetry was further substantiated through numerical evaluations.

The intermediate λ region The intermediate λ region is characterized by $\frac{\lambda^2 V_0}{A_2\rho} \simeq 1$. Serving as a boundary between the small and large λ regions, this domain is mostly undefined in the experimentally accessible values of V_0 due to a violation of the cutoff condition (3.1.38):

$$A_2\frac{\phi_\rho^2}{2m_{\rm pl}^2} \simeq \frac{A_2}{2\lambda^2}W(1)^2 < 0.1, \tag{3.1.45}$$

which implies an upper bound on V_0:

$$V_0 < \frac{0.2}{W(1)^2}\rho \simeq 0.6\rho. \tag{3.1.46}$$

Consequently, the model is only well-defined in this region for exceedingly small values of V_0. It's worth noting that in subsequent investigations, experiments primarily exhibit sensitivity when $V_0/\rho \gg 1$, rendering detailed exploration of this region unnecessary.

The large λ region The large λ region is characterized by the condition $\frac{\lambda^2 V_0}{A_2\rho} \gg 1$. The expression

$$V_{{\rm eff},\phi}(\phi_\rho;\rho) = 0, \tag{3.1.47}$$

implies

$$e^{-\lambda\phi_\rho/m_{\rm pl}} = \frac{W\left(\frac{\lambda^2 V_0}{A_2\rho}\right)}{\frac{\lambda^2 V_0}{A_2\rho}}. \tag{3.1.48}$$

Using $W(x) \simeq \ln(x)$ for large x [96] results in the following approximations that are valid in the large λ region:

Exact expression	ϕ_ρ	$e^{-\lambda\phi_\rho/m_{\rm pl}}$	μ_ρ	$\beta(\phi_\rho)$
Approximation	$\frac{m_{\rm pl}}{\lambda}\ln\left(\frac{\lambda^2 V_0}{A_2\rho}\right)$	$\ln\left(\frac{\lambda^2 V_0}{A_2\rho}\right)/\frac{\lambda^2 V_0}{A_2\rho} \ll 1$	$\frac{1}{m_{\rm pl}}\sqrt{A_2\rho\ln\left(\frac{\lambda^2 V_0}{A_2\rho}\right)}$	$\frac{A_2}{\lambda}\ln\left(\frac{\lambda^2 V_0}{A_2\rho}\right)$

Table 2: Approximations for the large λ region

Hence, in the large λ region, the full coupling to matter predominantly depends logarithmically on ρ, while the mass approximately exhibits a square root dependence on ρ. Hence, the field primarily screens by the chameleon mechanism in this parameter region.

Parameter symmetry:

As highlighted earlier in this Section, the ratio V_0/ρ typically assumes values significantly larger than A_2 and λ within experimentally accessible parameters. Consequently, for the majority of the experimentally accessible parameter space:

$$\ln\left(\frac{V_0}{\rho}\right) \gg \ln\left(\frac{\lambda^2}{A_2}\right), \tag{3.1.49}$$

which permits further simplification:

Exact expression	ϕ_ρ	μ_ρ	$\beta(\phi_\rho)$
Approximation	$\frac{m_{\rm pl}}{\lambda}\ln\left(\frac{V_0}{\rho}\right)$	$\frac{1}{m_{\rm pl}}\sqrt{A_2\rho\ln\left(\frac{V_0}{\rho}\right)}$	$\frac{m_{\rm pl}}{\lambda}\ln\left(\frac{V_0}{\rho}\right)$

Table 3: Approximations for the large λ region, assuming (3.1.49)

These relationships imply an approximate parameter symmetry in this paramter region: The quantities ϕ_ρ and μ_ρ primarily depend on $A_2 \ln(V_0/\rho)$, rather than on the individual values of V_0 and A_2. Furthermore, the force acting on a point particle with mass m also follows this symmetry:

$$\begin{aligned}\vec{f}_\phi &= -\beta(\phi)\,\frac{m}{m_{\rm pl}}\,\vec{\nabla}\phi \\ &\simeq -\beta(\phi_M)\,\frac{m}{m_{\rm pl}}\,\vec{\nabla}\phi \\ &= -\beta(\phi_M)\,\frac{m}{m_{\rm pl}}\,\vec{\nabla}\delta\phi,\end{aligned} \tag{3.1.50}$$

where $\delta\phi := \phi(\vec{x}) - \phi_M$. Here, $\phi \simeq \phi_M$ has been utilized for $V_0 \to \infty$, as is evident from $\phi_M \leq \phi(x) \leq \phi_V$ (see Appendix A) and Eq. (3):

$$\left|\frac{\phi_V - \phi_M}{\phi_V + \phi_M}\right| \to 0\,, \text{ for } V_0 \to \infty. \tag{3.1.51}$$

Given that $\beta(\phi_M)$ follows the $A_2 \ln(V_0/\rho)$ symmetry, it remains to demonstrate that this holds true for $\delta\phi$. Employing

$$V_{\text{eff},\phi}(\phi_M;\rho_M) = 0 \;\Leftrightarrow\; \frac{\lambda V_0}{m_{\text{pl}}} e^{-\lambda\phi_M/m_{\text{pl}}} = \frac{\beta(\phi_M)\rho_M}{m_{\text{pl}}} \tag{3.1.52}$$

yields

$$\begin{aligned}\Box\delta\phi &= \frac{\beta(\phi_M)\rho_M}{m_{\text{pl}}} e^{-\lambda\delta\phi/m_{\text{pl}}} - \frac{\beta(\phi_M+\delta\phi)\rho}{m_{\text{pl}}} \\ &\simeq \frac{\beta(\phi_M)\rho_M}{m_{\text{pl}}} e^{-\lambda\delta\phi/m_{\text{pl}}} - \frac{\beta(\phi_M)\rho}{m_{\text{pl}}},\end{aligned} \tag{3.1.53}$$

thus confirming that $\delta\phi$ shares the parameter dependence with $\beta(\phi_M)$.

3.1.3. The dilaton as a source of dark energy

This Subsection explores the possibility of the dilaton field to serve as the exclusive source of dark energy. The viability of this scenario varies across the three parameter regions, necessitating separate investigations for each case. Since the Weyl factor exclusively couples to the matter density rather than the scalar field itself, the focus is on dilaton field parameters that satisfy

$$V_{\text{eff}}(\phi_{\rho_{\text{matter}}};\rho_{\text{matter}}) = \rho_{\Lambda_0}, \tag{3.1.54}$$

where ρ_{Λ_0} represents the energy density associated with dark energy, while

$$\rho_{\text{matter}} = 3\Omega_{\text{matter}} m_{\text{pl}}^2 H_0^2 = \frac{\Omega_{\text{matter}}}{\Omega_{\Lambda_0}}\rho_{\Lambda_0} \simeq 0.46\rho_{\Lambda_0}, \tag{3.1.55}$$

is the average density of matter in the observable universe. This approach neglects possible quantum corrections to the potential.

The small λ region In this parameter region, the dilaton's effective potential energy holds the potential to supply sufficient energy for driving the cosmological acceleration. Specifically, in the small λ region

$$V_0 \geq \rho_{\text{matter}} \Rightarrow V_{\text{eff}}(\phi_{\rho_{\text{matter}}};\rho_{\text{matter}}) \simeq V_0. \tag{3.1.56}$$

This is evident from

$$\begin{aligned}V_{\text{eff}}(\phi_{\rho_{\text{matter}}};\rho_{\text{matter}}) &= V_0 + \rho_{\text{matter}} A_2 \frac{\phi^2_{\rho_{\text{matter}}}}{2m_{\text{pl}}^2} \\ &= V_0\big(1 + \frac{\rho_{\text{matter}}}{V_0} A_2 \frac{\phi^2_{\rho_{\text{matter}}}}{2m_{\text{pl}}^2}\big) \simeq V_0,\end{aligned} \tag{3.1.57}$$

where the cutoff condition has been utilized as well as $V_0 \geq \rho_{\text{matter}}$. As a special case, it is noteworthy that in the small λ region, V_0 can conveniently be set to ρ_{Λ_0} to scrutinize the dilaton as a potential source of dark energy.

The intermediate λ region Within this parameter region, the dilaton field falls short in supplying the required energy for the ongoing cosmological acceleration. This limitation becomes apparent when examining

$$\begin{aligned} V_{\text{eff}}(\phi_{\rho_{\text{matter}}}; \rho_{\text{matter}}) &\simeq V_0 e^{-W(1)} + \rho_{\text{matter}} A_2 \frac{\phi_\rho^2}{2m_{\text{pl}}^2} \\ &\lesssim 0.44 \rho_{\text{matter}} \ll \rho_{\Lambda_0}. \end{aligned} \tag{3.1.58}$$

Here, Eq. (3.1.38) and Eq. (3.1.46) have been utilized. Consequently, the potential energy stored in the scalar field is insufficient to fuel the current cosmological acceleration.

The large λ region Within this parameter region, the dilaton field also lacks the potential energy required to drive the cosmological acceleration. The following inequality is established:

$$V_{\text{eff}}(\phi_\rho; \rho) \lesssim 0.1\rho. \tag{3.1.59}$$

Importantly, this inequality holds for any arbitrary ρ and has physical implications beyond the dilaton's role as dark energy. Therefore, the following derivation is maintained in a general form.

The defining property of ϕ_ρ:

$$V_{\text{eff},\phi}(\phi_\rho; \rho) = 0 \;\Leftrightarrow\; \frac{\lambda V_0}{m_{\text{pl}}} e^{-\lambda\phi_\rho/m_{\text{pl}}} = \frac{A_2 \phi_\rho \rho}{m_{\text{pl}}^2}, \tag{3.1.60}$$

implies:

$$\begin{aligned} V(\phi_\rho) &= V_0 e^{-\lambda\phi_\rho/m_{\text{pl}}} \\ &= A_2 \rho \frac{\phi_\rho^2}{m_{\text{pl}}^2} \frac{1}{W(\frac{\lambda^2 V_0}{A_2 \rho})} < \frac{0.2}{W(\frac{\lambda^2 V_0}{A_2 \rho})} \rho. \end{aligned} \tag{3.1.61}$$

The last step utilized Eq. (3.1.38). Consequently,

$$\begin{aligned} V_{\text{eff}}(\phi_\rho; \rho) &= V_0 e^{-\lambda\phi_\rho/m_{\text{pl}}} + A_2 \rho \frac{\phi_\rho^2}{2m_{\text{pl}}^2} \\ &< 0.1 \Big(1 + \frac{2}{W(\frac{\lambda^2 V_0}{A_2 \rho})}\Big) \rho \simeq 0.1\rho. \end{aligned} \tag{3.1.62}$$

In the final step, the defining property $\frac{\lambda^2 V_0}{A_2 \rho} \gg 1$ of the large λ region has been used, which implies $W(\frac{\lambda^2 V_0}{A_2 \rho}) \gg 1$. Hence, in the large λ region, the potential energy of the dilaton field is insufficient to drive the cosmological acceleration alone.

3.1.4. The physical meaning of the dilaton's parameters

As demonstrated, various parameter symmetries emerge in different regions, leading to dilaton forces that solely depend on either $V_0\lambda$ or $A_2\ln(V_0/\rho)$. Consequently, attempting to assign distinct physical interpretations to these parameters is contrived.

Moreover, the exceptionally large values that V_0 can assume within the large λ region in experimentally relevant parameter spaces are artifacts of the parameterization; the parameter V_0 usually lacks inherent physical significance. This viewpoint is supported by two considerations:

Firstly, the parameter symmetry within this region implies that the logarithm of V_0/ρ, significantly smaller than V_0/ρ, exerts a comparable physical effect to A_2.

Furthermore, from the analysis in Eq. (3.1.59), it becomes evident that, regardless of the value of V_0, the entire potential energy of the dilaton field— an actual physical quantity—remains bounded by $\sim 0.1\ \rho$. (This bound only applies to the large λ region, where experiments can probe V_0 values up to $10^{10^{24}}$ MeV^4)

3.2. The chameleon field

A scalar-tensor theory that has garnered significant attention is the chameleon field [42]. Formally, it can be defined by:

$$\begin{aligned} V(\phi) &= \frac{\Lambda^{n+4}}{\phi^n}, \\ A(\phi) &= e^{\phi/M_c} \simeq 1 + \frac{\phi}{M_c}, \end{aligned} \tag{3.2.63}$$

where M_c is a coupling constant to matter of dimension mass, Λ is a constant energy density and $n \in \mathbb{Z}^+ \cup 2\mathbb{Z}^- \backslash \{-2\}$ determines the power of the self-interaction potential. The effective potential is then given by:

$$V_{\text{eff}}(\phi;\rho) = \frac{\Lambda^{n+4}}{\phi^n} + \rho\frac{\phi}{M_c}. \tag{3.2.64}$$

An example is illustrated in Fig. 3.2.1.

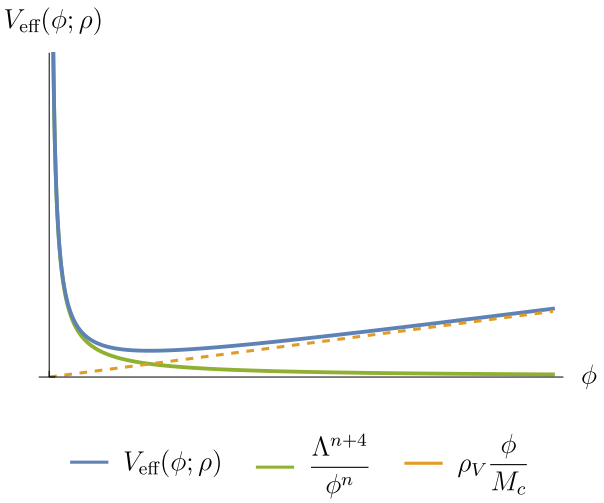

Fig. 3.2.1: This is an illustration of the effective potential of the chameleon field for $n > 0$.

Similar to the dilaton field, the condition

$$\frac{\phi}{M_c} < 0.1, \tag{3.2.65}$$

is employed to disregard couplings to higher orders in numerical calculations[1].

The potential minimum, mass, and full coupling to matter of the chameleon are expressed as [53]:

$$\begin{aligned} \phi_\rho &= \left(\frac{nM_c\Lambda^{n+2}}{\rho}\right)^{\frac{1}{n+1}}, \\ \mu_\rho &= n(n+1)\Lambda^{n+4}\left(\frac{\rho}{nM_c\Lambda^{n+4}}\right)^{\frac{n+2}{n+1}}, \\ \beta(\phi) &= \frac{m_{\text{pl}}}{M_c}. \end{aligned} \tag{3.2.66}$$

Given that the mass is a monotonically increasing function of ρ, chameleons experience an increase in mass in dense environments, resulting in an effectively short-ranged force in such cases and, consequently, a weakened associated force. This mechanism might allow the chameleon to evade constraints from local tests of gravity.

3.3. The symmetron field

The symmetron field is characterized by [43]:

[1] While technically not mandatory, this constraint is imposed as parameters where $\frac{\phi}{M_c} \gg 1$ have already been ruled out by numerous experiments (see, e.g., [53, 73]). Such values would lead to pronounced deviations from GR, lacking sufficient motivation. The use of a linear coupling to matter is common and simplifies several calculations.

$$V(\phi) = -\frac{\mu^2}{2}\phi^2 + \frac{\lambda_S}{4}\phi^4,$$
$$A(\phi) = 1 + \frac{\phi^2}{2M^2} + \mathcal{O}\left(\frac{\phi^3}{M^3}\right), \tag{3.3.67}$$

resulting in an effective potential:

$$V_{\text{eff}}(\phi;\rho) = \frac{1}{2}\left(\frac{\rho}{M^2} - \mu^2\right)\phi^2 + \frac{\lambda_S}{4}\phi^4. \tag{3.3.68}$$

The condition

$$\frac{\phi^2}{2M^2} < 0.1, \tag{3.3.69}$$

is used to allows to neglect couplings to higher order. For the symmetron field, it is customary to distinguish between the symmetric phase and the broken symmetry phase. The following definitions and formulas are standard, and can, e.g., be found in [61].

3.3.1. The symmetric phase

The symmetric phase is defined by:

$$\rho \geq M^2\mu^2. \tag{3.3.70}$$

In this phase, the effective potential exhibits a unique minimum at $\phi = 0$ (see Fig. 3.3.1 for an example). The mass and full coupling to matter of the field are given by:

$$\mu_\rho = \sqrt{\frac{\rho}{M^2} - \mu^2},$$
$$\beta(\phi) = m_{\text{pl}}\frac{\phi}{M^2}. \tag{3.3.71}$$

Given that ϕ seeks to minimize its potential, the coupling to matter is driven towards 0 in the symmetric phase. This phenomenon constitutes the screening mechanism associated with the symmetron field. Additionally, it is worth noting that the symmetron also becomes short-ranged - akin to the chameleon field - in high-density regions, as is evident from the condition $\rho \geq M^2\mu^2$ and the dependence of the field's mass on ρ.

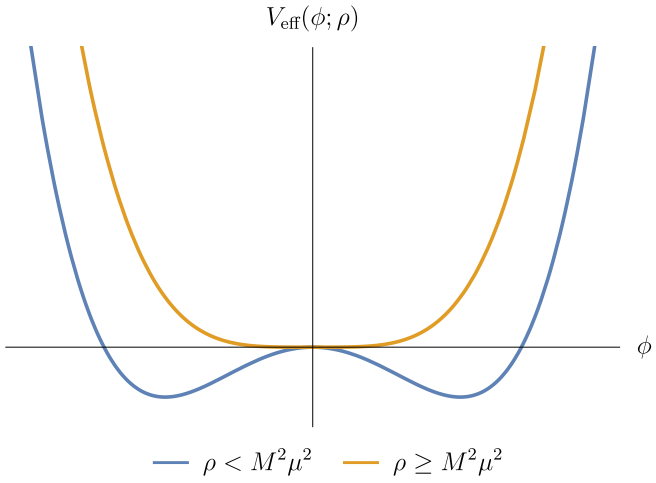

Fig. 3.3.1: This is an illustration of the symmetron potential in its two distinct phases.

3.3.2. The broken symmetry phase

The broken symmetry phase is defined by:

$$\rho < M^2\mu^2. \tag{3.3.72}$$

In this phase, the potential exhibits two distinct local minima, as depicted in Fig. 3.3.1. The potential minimum and mass of the field are given by:

$$\begin{aligned} \phi_\rho &= \pm\sqrt{\frac{\mu^2}{\lambda} - \frac{\rho}{\lambda M^2}}, \\ \mu_\rho &= \sqrt{2\left(\mu^2 - \frac{\rho}{M^2}\right)}. \end{aligned} \tag{3.3.73}$$

The full coupling to matter is still given by Eq. (3.3.71), but since the field is not driven to 0 anymore, there can be an appreciable coupling to matter, and the field can unscreen.

4. Numerical methods and scalar field simulations

To accurately compute the impact of a scalar field on an experiment, it is imperative to solve its equations of motion within the experimental setup. Due to the inherent non-linearity of the scalar fields considered, this usually necessitates numerical simulations. This Section elucidates the numerical methodologies employed for this purpose, forming the cornerstone for subsequent Sections. Throughout this thesis, the focus remains solely on static scalar fields.

The principal objective revolves around deriving parameter constraints for any model under scrutiny, demanding robust numerical techniques capable of effectively handling arbitrary parameters.

Inspired by the actual geometries of the experiments, scalar fields are computed for the following scenarios:

1. **One mirror geometry**: This configuration, utilized in modeling the neutron mirror within the qBOUNCE experiment, assumes the scalar field's dependence solely on the z coordinate. An infinitely extended neutron mirror with density ρ_M resides at $z < 0$, with a vacuum region above it having density ρ_V. The differential equation to be solved is:

$$\frac{d^2\phi}{dz^2} = V_{\text{eff},\phi}(\phi;\rho). \tag{4.0.74}$$

   The boundary condition is that the field minimizes its potential asymptotically: ϕ approaches ϕ_V as z tends towards infinity, and ϕ approaches ϕ_M as z tends towards negative infinity.

2. **Two mirror geometry**: This geometry, employed in computing the pressure within the CANNEX experiment, similarly assumes the scalar field's dependence only on the z direction. Here, a vacuum region exists for $|z| < d$ with density ρ_V, flanked by two infinitely extended mirrors placed at $|z| > d$, possessing density ρ_M. The differential equation to be solved mirrors that of the one mirror geometry, albeit with boundary conditions $\phi \to \phi_M$ as $|z| \to \infty$.

3. **Spherical geometry**: This setup, utilized in computing scalar fields for LLR, envisions a sphere with density ρ_M situated at $r < R$, surrounded by a vacuum region with density ρ_V for $r > R$. Exploiting spherical symmetry, the equation to solve becomes:

$$\frac{d^2\phi}{dr^2} + \frac{2}{r}\frac{d\phi}{dr} = V_{\text{eff},\phi}(\phi;\rho). \tag{4.0.75}$$

   Boundary conditions[2] are specified as $\frac{d\phi}{dr}(0) = 0$ and $\phi \to \phi_V$ as $r \to \infty$.

4. **Cylinder cross Section geometry:** For an infinitely long cylinder with density ρ_V for $r < d$ and ρ_M for $r > d$, the z dependence of the field can be neglected and it is sufficient to compute the cross section by solving

$$\frac{d^2\phi}{dr^2} + \frac{1}{r}\frac{d\phi}{dr} = V_{\text{eff},\phi}(\phi;\rho), \tag{4.0.76}$$

[2] Strictly speaking, the expression $\frac{d\phi}{dr}|_{r=0} = 0$ does not qualify as a boundary condition, as $r = 0$ does not represent a physical boundary. In Cartesian coordinates, no conditions are necessary at $\vec{x} = \vec{0}$. The necessity for an additional condition at $r = 0$ arises as an artifact of adopting spherical coordinates. In the context of spherical coordinates, it becomes imperative to set the first derivative to 0 at $r = 0$ to prevent $\frac{2}{r}\frac{d\phi}{dr}$ from diverging to infinity at $r = 0$. This condition is also necessary to ensure the spherical symmetry of the solution.

where boundary conditions are specified as $\frac{d\phi}{dr}(0) = 0$ and $\phi \to \phi_M$ as $r \to \infty$. This geometry will only be employed for code tests.

5. **Cylindrical geometry**: This geometry, employed in modeling the vacuum and air chamber for neutron interferometry, necessitates solving:

$$\left[\frac{1}{r}\frac{\partial}{\partial r}\left(r\frac{\partial}{\partial r}\right) + \frac{\partial^2}{\partial z^2}\right]\phi(r,z) = V_{\text{eff},\phi}(\phi;\rho)\,. \tag{4.0.77}$$

Here, the density is characterized by:

$$\rho(r,z) := \begin{cases} \rho_V & \left(r \le d\right) \wedge \left(-\frac{L}{2} < z < \frac{L}{2}\right) \\ \rho_M & \text{else} \end{cases} \tag{4.0.78}$$

where L denotes the chamber length and d denotes the inner radius. The boundary conditions are:

$$\phi(r,z) = \phi_M, \text{ if } \left(r = d+\delta\right) \vee \left(z = \frac{L}{2}+\delta\right) \vee \left(z = -\frac{L}{2}-\delta\right), \tag{4.0.79}$$

where δ represents half the thickness of the cylinder shell (typically around 5 mm in the experiment). Here, the logical and $\wedge$, as well as the logical or $\vee$ have been used. At $r = 0$ the condition $\frac{\partial\phi}{\partial r} = 0$ is required.

In the context of *q*BOUNCE, an additional requirement is to solve the stationary Schrödinger equation in the presence of a scalar field:

$$-\frac{1}{2m_n}\frac{d^2\psi_n(z)}{dz^2} + \Big(m_n g z + \mathfrak{Q}_X U_X(z)\Big)\psi_n(z) = E_n\psi_n(z), \tag{4.0.80}$$

where the precise expression for the scalar field induced potential $\mathfrak{Q}_X U_X(z)$ is derived in the theory chapter and provided in Eq. (5.3.231).

While various authors have successfully simulated chameleon and symmetron fields (cf. [56, 66, 67, 97–106]), the environment dependent dilaton field is less explored. No group has yet derived parameter constraints for this model, and simulations in experimental settings remain unachieved. Existing cosmological N-body simulations (cf. [102, 107]) are limited to specific parameters, utilizing a uniform finite difference method for discretizing equations of motion, which proves unsuitable for general parameters.

This Section primarily discusses the numerical methods employed to derive parameter constraints in the studied models, with a specific focus on the unique numerical challenges posed by the dilaton field and their resolution.

In Section 4.1, the exploration begins by deriving the exact two mirror solution for the environment-dependent dilaton model, under the simplifying assumption of $\rho_V = 0$. This foundational step ensures the availability of exact solutions for all models examined in this thesis, which is crucial to test the reliability of the numerical algorithms employed.

Sections 4.2 and 4.3 delve into the intricacies of why standard machine precision calculations (typically 16 digits) often fall short in accurately computing the dilaton and symmetron fields for arbitrary parameters. These challenges are thoroughly addressed, and the strategies employed to overcome them are outlined.

In Section 4.4, the algorithm utilized to solve the equations of motion for one- and two mirror geometries, for a spherical geometry and the cylinder cross section geometry, is elucidated. Moreover, Section 4.5 is dedicated to detailing the approach to full cylinder simulations.

Finally, in Section 4.6, the numerical methodology employed to solve the stationary Schrödinger equation is presented.

4.1. The exact two mirror solution with $\rho_V = 0$

In this Section, the exact dilaton solution within a vacuum region confined between two infinitely extended plates having a density of ρ_M is derived. These plates are situated at $z < -d$ and $z > d$, mimicking the geometric setup of the CANNEX experiment. It is noteworthy that the decision to derive an exact solution for this particular geometry is motivated by the absence of exact solutions for the geometries pertinent to other experiments explored in this thesis.

To formulate the one dimensional equation of motion, the dilaton field's Eq. (5.4.234) is reexpressed as

$$\frac{d^2\phi}{dz^2} = V_{\text{eff},\phi}(\phi;\rho) = -\frac{\lambda}{m_{\text{pl}}} V_0 e^{-\lambda\phi/m_{\text{pl}}} + A_2\rho\frac{\phi}{m_{\text{pl}}^2}. \tag{4.1.81}$$

The objective is to find a solution that approaches ϕ_M as $|z| \to \infty$. In a region of homogeneous density ρ, multiplying Eq. (4.1.81) by ϕ' and integrating over z results in:

$$\frac{1}{2}\left(\frac{d\phi}{dz}\right)^2 = V_{\text{eff}}(\phi;\rho) + c, \tag{4.1.82}$$

where c is a constant that has to be determined from boundary conditions or symmetry considerations.

4.1.1. Solution inside the vacuum region

Inside the vacuum region with $\rho_V = 0$ Eq. (4.1.82) simplifies to

$$\frac{1}{2}\left(\frac{d\phi}{dz}\right)^2 = V_0 e^{-\lambda\phi(z)/m_{\text{pl}}} - V_0 e^{-\lambda\phi_0/m_{\text{pl}}}. \tag{4.1.83}$$

Here, the choice of the integration constant ensures $\phi'(0) = 0$, maintaining symmetry of the field solution in the experimental setup. The quantity ϕ_0 is defined as $\phi(0)$ and $u(z)$ is defined through the relationship:

$$\phi(z) = \phi_0 - \frac{m_{\text{pl}}}{\lambda}\ln\big(u(z)\big), \tag{4.1.84}$$

implying $u(0) = 1$. This leads to the equation:

$$\frac{m_{\text{pl}}^2}{\lambda^2}\frac{\big(u'(z)\big)^2}{2u(z)^2} = V_0 e^{-\lambda\phi_0/m_{\text{pl}}}\big(u(z) - 1\big). \tag{4.1.85}$$

Defining

$$\alpha := \sqrt{2V_0}\frac{\lambda}{m_{\text{pl}}} e^{-\lambda\phi_0/(2m_{\text{pl}})}, \tag{4.1.86}$$

Eq. (4.1.85) can be expressed as:

$$\frac{\big(u'(z)\big)^2}{u^2(z)(u(z)-1)} = \alpha^2. \tag{4.1.87}$$

Next, Eq. (4.1.87) is solved within the range $-d \leq z \leq 0$. In this interval, the dilaton field ϕ exhibits an upward trend, reaching its local maximum at $z = 0$. Consequently $\phi'(z) \geq 0$. This, in turn, implies that $u'(z) \leq 0$ as indicated by Eq. (4.1.84). Integrating the equation yields:

$$\int_z^0 \frac{u'(s)}{\sqrt{u^2(s)\big(u(s)-1\big)}} ds = \alpha z. \tag{4.1.88}$$

Introducing the variable $y(s) := \sqrt{u(s)-1}$, the integral transforms to:

$$2\int_{\sqrt{u(z)-1}}^0 \frac{1}{1+y^2} dy = \alpha z. \tag{4.1.89}$$

Solving this expression for $u(z)$ yields:

$$u(z) = 1 + \tan\left(\frac{\alpha}{2} z\right)^2. \tag{4.1.90}$$

By analogous reasoning, one can ascertain that the obtained expression for $u(z)$ also satisfies Eq. (4.1.87) in the interval $0 \leq z \leq d$. Consequently, the full solution in between the plates can be written as:

$$\phi(z) = \phi_0 - \frac{m_{\mathrm{pl}}}{\lambda} \ln\left[1 + \tan\left(\frac{\alpha}{2} z\right)^2\right]. \tag{4.1.91}$$

4.1.2. Boundary conditions and definition of ϕ_0

The obtained solution introduces the parameter ϕ_0, which needs determination through boundary conditions. Inside the mirrors, Eq. (4.1.82) reduces to:

$$\frac{1}{2}\left(\frac{d\phi}{dz}\right)^2 = V_{\mathrm{eff}}(\phi; \rho_M) - V_{\mathrm{eff}}(\phi_M; \rho_M), \tag{4.1.92}$$

where integration constant must be selected to ensure the derivative approaches zero for $|z| \to \infty$. The demand for the derivative's continuity at $|z| = d$ results in an equation for $\phi_d := \phi(|d|)$. Equating (4.1.92) and (4.1.83) at $|z| = d$ yields:

$$\phi_d = \sqrt{\frac{2m_{\mathrm{pl}}^2}{A_2 \rho_M}\Big(V_{\mathrm{eff}}(\phi_M, \rho_M) - V_0 e^{-\lambda\phi_0/m_{\mathrm{pl}}}\Big)}, \tag{4.1.93}$$

where the positivity of the dilaton field has been utilized. Equating (4.1.93) with (4.1.91) at $|z| = d$ results in an implicit equation defining ϕ_0 as the root of $\mathrm{Eqn}(\phi_0)$:

$$\mathrm{Eqn}(\phi_0) := \phi_0 - \frac{m_{\mathrm{pl}}}{\lambda}\ln\left[1+\tan\left(\frac{\alpha}{2}d\right)^2\right] - \sqrt{\frac{2m_{\mathrm{pl}}^2}{A_2\rho_M}\left(V_{\mathrm{eff}}(\phi_M,\rho_M) - V_0 e^{-\lambda\phi_0/m_{\mathrm{pl}}}\right)}\,.$$

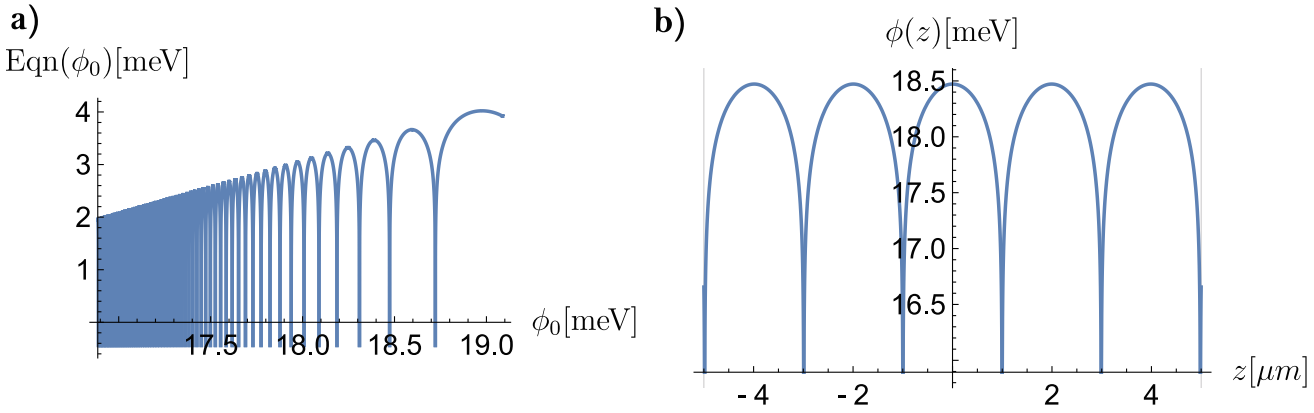

Fig. 4.1.1: **a)** Eqn(ϕ_0) is plotted for $V_0 = 10$ MeV^4, $\lambda = 10^{31}$ and $A_2 = 10^{40}$ for a plate separation of 10 μm.
b) The incorrect solution $\phi_0 \simeq 18.5$ meV is plottet, this solution has poles at $z \simeq \pm 1$ μm and $z \simeq \pm 3$ μm according to Eq. (4.1.91) and is hence not a legitimate solution of the differential equation.

Due to the periodicity of the tangent function, multiple solutions for ϕ_0 may exist, as exemplified in Fig. 4.1.1. However, considering that $\phi(z)$ must be defined on the domain $-d \leq z \leq d$ and $\tan(x)$ is undefined for $x = \pi/2 + n\pi$ and $n \in \mathbb{Z}$, the correct solution must satisfy $\alpha d < \pi$, establishing a lower bound on ϕ_0:

$$\phi_0 > \frac{2m_{\mathrm{pl}}}{\lambda}\ln\left(\frac{\lambda\sqrt{2V_0}d}{\pi m_{\mathrm{pl}}}\right), \tag{4.1.94}$$

where Eq. (4.1.86) has been employed. For the examined dilaton parameters, only one solution compatible with this lower bound was found. This solution is instrumental in verifying the accuracy of the proposed methods for solving the equations of motion. Although the numerical algorithm must work for $\rho_V > 0$, applying it to the case of $\rho_V = 0$ and comparing it with an exact solution provides a powerful consistency check. Furthermore, when ϕ_0 does not closely approach ϕ_V, the derived solution serves as an excellent approximation for the more realistic scenario where $\rho_V > 0$. This also allows the use of the analytical solution with $\rho_V = 0$ to test numerical algorithms under more realistic conditions. This observation becomes apparent when examining the region near the potential minimum ϕ_ρ defined by $V_{\mathrm{eff},\phi}(\phi_\rho;\rho) = 0$. Near ϕ_ρ, the following approximation, deduced from Eq. (4.1.81), holds:

$$\frac{\lambda}{m_{\mathrm{pl}}}V_0 e^{-\lambda\phi/m_{\mathrm{pl}}} \simeq A_2\rho\frac{\phi}{m_{\mathrm{pl}}^2}. \tag{4.1.95}$$

Deep within the mirror, the field is suppressed to ϕ_M, leading both terms on the right-hand side (RHS) of Eq. (4.1.81) to contribute roughly equally to the differential equation. As the field transitions into the vacuum region, the linear term undergoes a sudden suppression by several orders of magnitude due to $\rho_V \ll \rho_M$. Consequently, the exponential term begins to dominate Eq. (4.1.81). The field advances toward its new potential minimum, and it is only in proximity to ϕ_V that the linear term ceases to be suppressed, as indicated by Eq. (4.1.95). Therefore, as long as $\phi_0 \ll \phi_V$, the linear term can be disregarded within the vacuum region, which is equivalent to setting $\rho_V = 0$.

It is noteworthy that the obtained solution remains applicable to models featuring a distinct Weyl-rescaling function $A(\phi)$, as long as $V(\phi)$ remains unchanged. As a consequence of setting $\rho_V = 0$, the Weyl-rescaling no longer manifests in the differential equation between the mirrors. Any alteration in $A(\phi)$ would solely require adjustments to the implicit equation governing ϕ_0.

In the following, an explicit demonstration will be provided for which parameters this solution also approximates the case where $\rho_V > 0$, and it will be compared to the approximate two mirror solution derived in Appendix C.

4.1.3. Analysing the accuracy of the two mirror solutions

While the derived solution is exact for $\rho_V = 0$, making it suitable as a benchmark for numerical algorithms, the case where $\rho_V = 2.28 \times 10^{-20}$ MeV^4 corresponds to the lowest possible vacuum density of the CANNEX experiment. In this Section, it will be shown that, for a significant portion of the relevant parameter space, either the exact two mirror solution with $\rho_V = 0$ or the approximate two mirror solution (derived in Appendix C) with arbitrary ρ_V serves as an extremely accurate solution for the exact equation with $\rho_V = 2.28 \times 10^{-20}$ MeV^4. Due to the approximate parameter symmetries of the dilaton model, the analysis primarily focuses on a fixed value of $V_0 = 10$ MeV^4. The specific value of $V_0 = 10$ MeV^4 is arbitrary and the obtained results in this Section would only be marginally affected by increasing it by a factor 10^{10^6} or even much more as becomes evident in the derived constraints in Section 6.1. This specific value was chosen primarily because the investigated experiments quickly loose their sensitivity for $V_0/\text{MeV}^4 \ll 1$ making V_0 values close to 1 MeV^4 a natural choice.

To assess the accuracy of the solutions, the relative residual (RS) is defined as:

$$\text{RS}(\phi, z) := \frac{\left|\frac{d^2\phi}{dz^2}(z) + \frac{\lambda}{m_{\text{pl}}} V_0 e^{-\frac{\lambda\phi(z)}{m_{\text{pl}}}} - \frac{A_2\rho(z)}{m_{\text{pl}}^2}\phi(z)\right|}{\max\left\{\left|\frac{d^2\phi}{dz^2}(z)\right|, \left|\frac{\lambda}{m_{\text{pl}}} V_0 e^{-\frac{\lambda\phi(z)}{m_{\text{pl}}}}\right|, \left|\frac{A_2\rho(z)}{m_{\text{pl}}^2}\phi(z)\right|\right\}}. \tag{4.1.96}$$

This definition has previously been employed to assess the accuracy of numerical chameleon solutions [98]. For an exact solution $\text{RS}(\phi, z) = 0$, whereas for a random function ϕ, $\text{RS}(\phi, z) \sim 1$. Fig. 4.1.2 illustrates that the exact two mirror solution is an exceptionally accurate approximation for the case $\rho_V = 2.28 \times 10^{-20}$ MeV^4 when $A_2 < 10^{45}$ within the large λ region. For larger values of A_2, the dilaton range is so short that ϕ would reach ϕ_V inside the vacuum region, contradicting the assumption $\rho_V = 0$, which is necessary for the analytical solution to be accurate.

Conversely, within the small λ region, the approximate two mirror solution derived in Appendix C with arbitrary ρ_V is practically exact throughout the entire parameter region, as demonstrated in Fig. 4.1.3. This is attributed to the fact that the approximate solution is based on linearizing the equations of motion. Given that, in the small λ region, the real equations of motion are linear to a very good approximation (see Eq. (3.1.44)), any linearization yields a practically exact solution.

In the following Subsection an appropriate algorithm to solve the differential equations of motion of the dilaton field is introduced and numerical challenges and their resolutions are summarized. The accuracy of these methods is also verified for the chameleon and symmetron field.

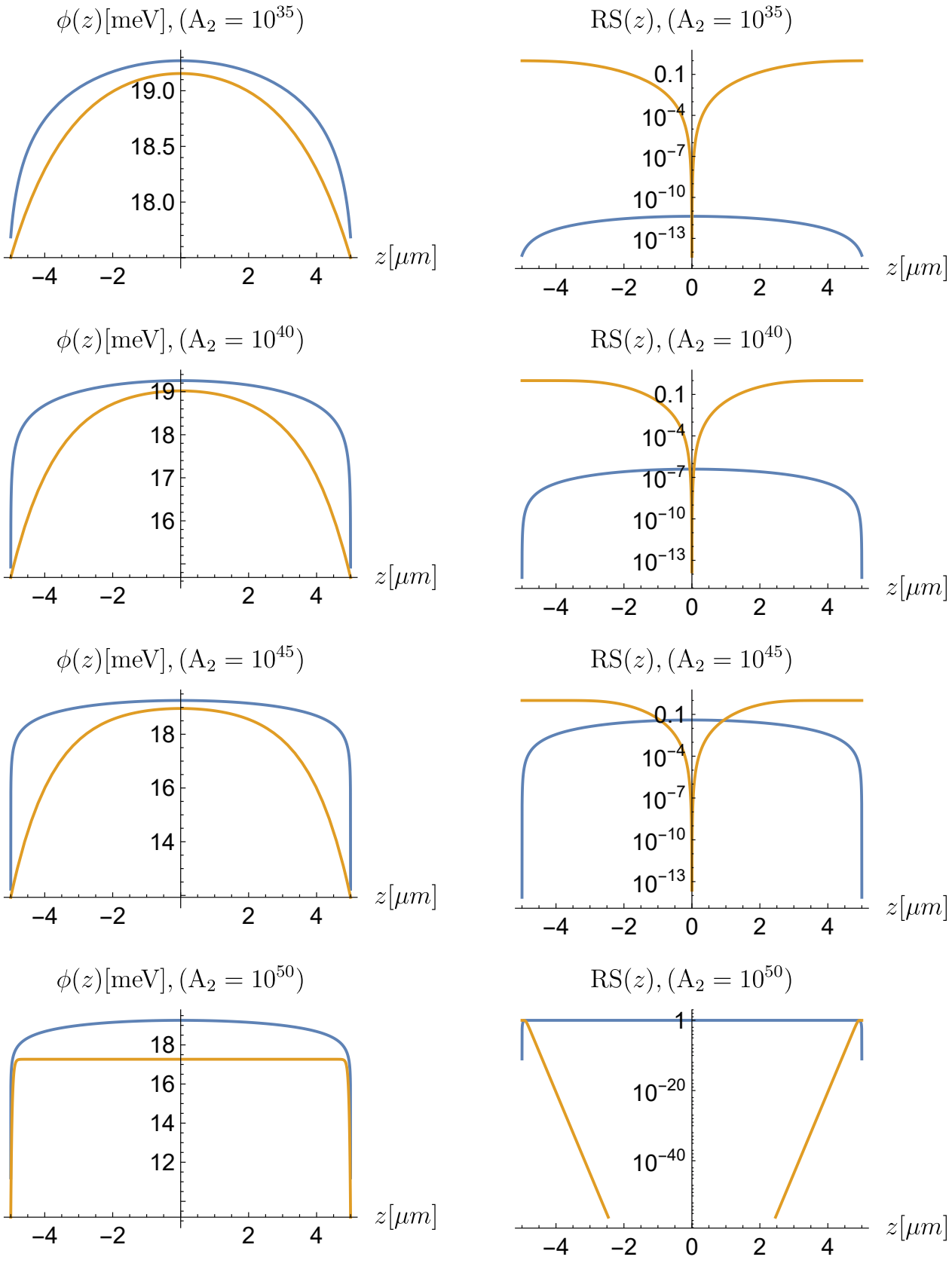

Fig. 4.1.2: The comparison involves the approximate two mirror solution (depicted in orange) with $\rho_V = 2.28 \times 10^{-20}$ MeV^4 and the exact two mirror solution (depicted in blue) with $\rho_V = 0$. Their relative residuals are illustrated, considering parameters $V_0 = 10$ MeV^4 and $\lambda = 10^{31}$. The figure highlights the value of A_2. The chosen parameters are directly relevant to the investigation of experimental constraints, see Fig. 4.2.1.

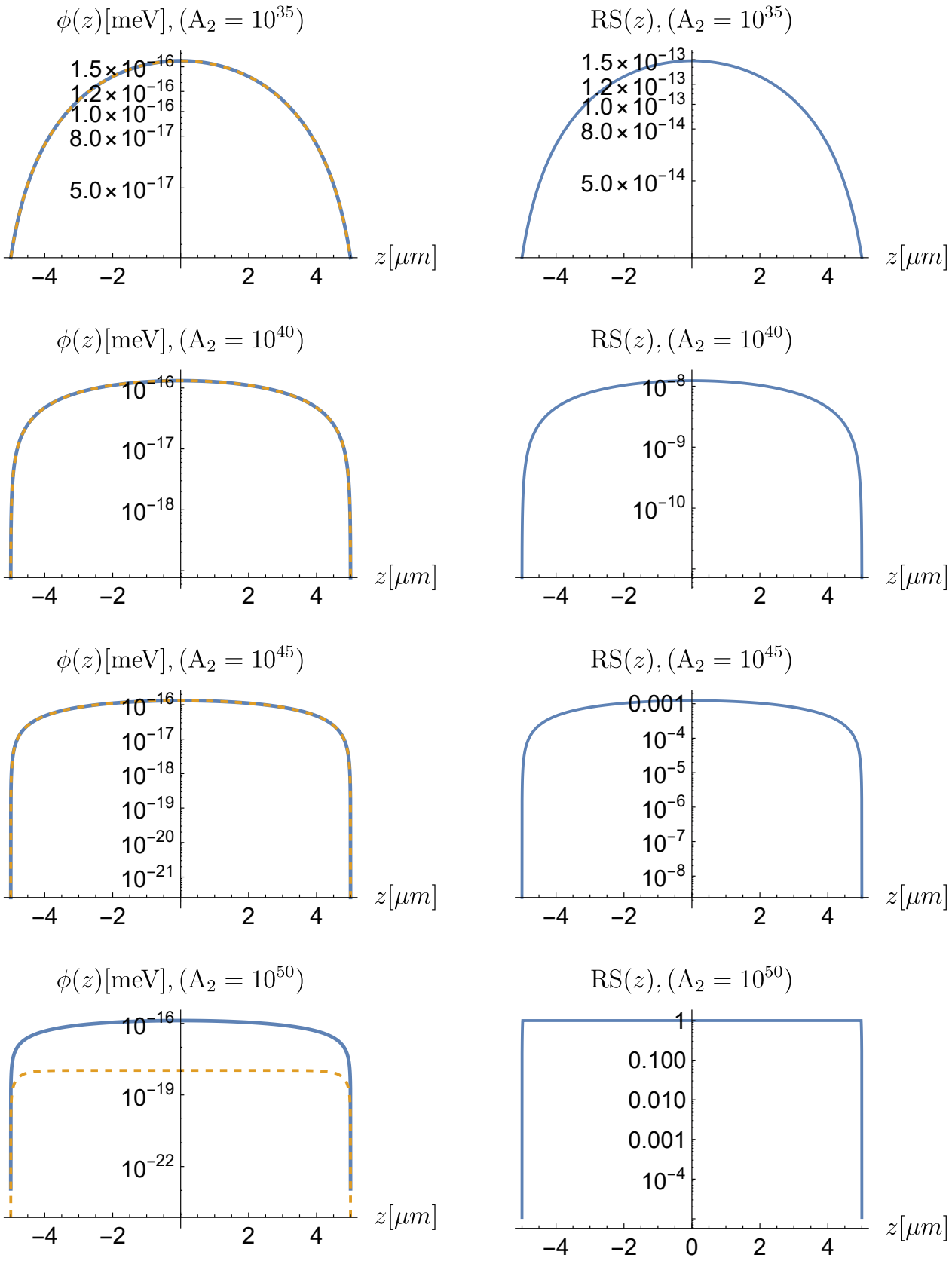

Fig. 4.1.3: The comparison involves the approximate two-mirror solution (depicted in orange) with $\rho_V = 2.28 \times 10^{-20}$ MeV^4 and the exact two mirror solution (depicted in blue) with $\rho_V = 0$. Their relative residuals are illustrated, considering parameters $V_0 = 10$ MeV^4 and $\lambda = 10^{-10}$. The figure highlights the value of A_2. For the approximate two mirror solution RS(z) is so extremely small ($\sim 10^{-100}$) that it is rounded to zero and not displayed in a logarithmic plot. The chosen parameters are directly relevant to the investigation of experimental constraints, see Fig. 4.2.1.

4.2. Precision Challenges of the dilaton field

This Section delves into precision challenges and their resolution within the context of the environment-dependent dilaton model, specifically within the experimentally relevant parameter space outlined in Fig. 4.2.1. The determination of experimentally relevant parameters is inherently post hoc: regions of parameters leading to measurable physical effects are computed. These results allow to determine the accessible—and consequently relevant—parameter volume for individual experiments. Although a detailed derivation is reserved for Section 6.1, the accessible parameter volume is presented here without discussion, because the robustness of numerical algorithms has to be guaranteed for these parameters.

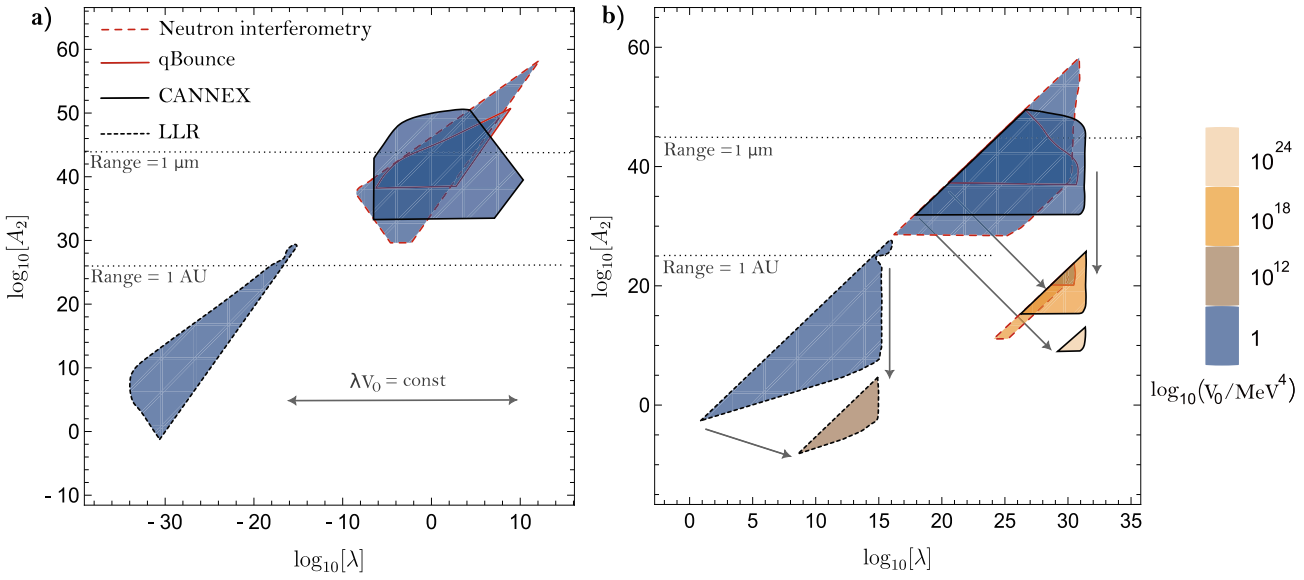

Fig. 4.2.1: The filled areas show which parameters of the dilaton model can be constraint by experiments. **a)** In the case of small λ, the physical outcomes are solely reliant on the product $V_0\lambda$, rendering the individual values of V_0 and λ irrelevant. Consequently, as V_0 grows, the constraint areas shift towards smaller λ values while maintaining their original shapes. **b)** Arrows depict how constraint regions evolve with increasing values of V_0. For a comprehensive explanation see Section 6.1. Figure published in Ref. [5]

4.2.1. Phenomenologically relevant parameter space

The model's parameter space can be broadly divided into three regimes, as detailed in Section 3.1.2:

- For small λ (Figure 4.2.1 left), the equation of motion is given to a very good approximation by

$$\Box\phi = \frac{\lambda}{m_{\rm pl}} V_0 e^{-\lambda\phi/m_{\rm pl}} - A_2\rho\frac{\phi}{m_{\rm pl}^2} \simeq \frac{\lambda}{m_{\rm pl}} V_0 - A_2\rho\frac{\phi}{m_{\rm pl}^2}. \tag{4.2.97}$$

  These are linear equations of motion, allowing for exact solutions for various geometries, see Appendix C. The parameter region characterized by small λ is found to be numerically straightforward and is hence only briefly explored in this thesis.

- For intermediate values of λ, the model becomes undefined due to the violation of condition (3.1.38).
- For large λ (see Figure 4.2.1 right), the dilaton field exhibits strong exponential self-coupling, resulting in highly nonlinear equations of motion where

$$e^{-\lambda\phi/m_{\rm pl}} \ll 1. \tag{4.2.98}$$

The parameter V_0 can take values as large as $V_0 = 10^{10^{24}}$ MeV^4 in the phenomenologically relevant parameter region, presenting significant numerical challenges, which are further discussed in the next Subsection.

4.2.2. Computing functions for very large values of V_0

Computing the effective potential

Handling large values of V_0 presents computational challenges, including potential overflows and underflows. For instance, the product

$$V_0 e^{-\lambda\phi/m_{\rm pl}} \tag{4.2.99}$$

may yield physically meaningful results, but individual values of V_0 and $e^{-\lambda\phi/m_{\rm pl}}$ can become excessively large or small, leading to underflows in the exponential. To mitigate this, the parameter $\gamma := \log_{10}(V_0/\text{MeV}^4)$ is introduced, enabling the effective potential to be expressed as

$$e^{\left(-\lambda\phi/m_{\rm pl}+\gamma\ln(10)\right)}\text{MeV}^4 + \frac{A_2\rho}{2m_{\rm pl}^2}\phi^2, \tag{4.2.100}$$

effectively averting underflows. Functions involving γ must be reformulated to prevent internal overflows.

Computing the potential minimum

A crucial instance is the computation of the potential minimum:

$$\phi_\rho = \frac{m_{\rm pl}}{\lambda} W\left(\frac{\lambda^2 V_0}{A_2\rho}\right) = \frac{m_{\rm pl}}{\lambda} W\left(\frac{\lambda^2 e^{\gamma\ln(10)}\text{MeV}^4}{A_2\rho}\right). \tag{4.2.101}$$

Here, $e^{\gamma\ln(10)}$ can lead to an overflow. This can be avoided by employing an asymptotic expansion of Lambert's W function [96]:

$$\begin{aligned} W(x) &= \ln(x) - \ln\ln(x) + \sum_{k=0}^{\infty}\sum_{m=1}^{\infty} c_{km}\big[\ln\ln(x)\big]^m\big[\ln(x)\big]^{-k-m}, \\ c_{km} &= \frac{1}{m!}(-1)^k \begin{bmatrix} k+m \\ k+1 \end{bmatrix}, \end{aligned} \tag{4.2.102}$$

where $\begin{bmatrix} k+m \\ k+1 \end{bmatrix}$ denotes the Stirling cycle number of the first kind. To lowest order, cancellation of $\ln(e^{\gamma\ln(10)}) = \gamma\ln(10)$ results in

$$\phi_\rho \simeq \frac{m_{\rm pl}}{\lambda}\Big(\gamma\ln(10) + \ln(\frac{\lambda^2\text{MeV}^4}{A_2\rho})\Big), \tag{4.2.103}$$

but higher-order correction terms of W can be added as well. In my implementation I employed Mathematica [108] to expand $W(x)$ to a sufficiently high order and simplify it analytically to

$$W(x) \simeq \ln(x) - \ln\ln(x) + \frac{\ln\ln(x)}{\ln(x)} + \frac{\big[-2+\ln\ln(x)\big]\ln\ln(x)}{2\ln(x)^2} + \frac{\ln\ln(x)\big[6-9\ln\ln(x)+2\ln\ln(x)^2\big]}{6\ln(x)^3} =: g(x). \tag{4.2.104}$$

I then ensured that the relative difference between $W(x)$ (computed exactly with Mathematica) and $g(x)$ is less than 10^{-28} for $\gamma \geq 10^6$ (this is only at the threshold of $\gamma = 10^6$, for $\gamma = 10^{24}$ the difference would be much smaller). For larger γ values, I exclusively used $g(x)$ instead of $W(x)$ and employed the analytical replacement

$$\ln(e^{\gamma \ln(10)}) = \gamma \ln(10), \tag{4.2.105}$$

to circumvent overflows. While the $\gamma-$parameterization has been used in numerical calculations, the text will stick to the V_0 parameterization, since this is how the model was originally defined.

The need to go beyond machine precision

The following numerical challenge arises when dealing with large values of V_0 due to the inherent limitation of machine precision calculations, typically accurate up to 15-16 digits on contemporary 64-bit machines. This level of precision often proves inadequate for obtaining physically meaningful results. Consider a static field in a vacuum chamber with density ρ_V, surrounded by material walls with density ρ_M. The field is governed by the inequality (a proof of this claim is provided in Appendix A):

$$\phi_M \leq \phi(x) \leq \phi_V. \tag{4.2.106}$$

For the maximum value of $V_0 \sim 10^{10^{24}}$ MeV^4 in the context of tabletop experiments, the relative difference between ϕ_V and ϕ_M is approximately expressed as:

$$2\frac{\phi_V - \phi_M}{\phi_V + \phi_M} \simeq \frac{\ln\left(\frac{\rho_M}{\rho_V}\right)}{\log_{10}(V_0/\text{MeV}^4)\ln(10)} \simeq 10^{-23}. \tag{4.2.107}$$

ρ_M has been assumed to be roughly 10 orders of magnitude larger than ρ_V in table top experiments. Consequently, $\phi(x) = \phi_M = \phi_V$ to machine precision, providing no meaningful physical information. Therefore, solving the equations of motion directly requires significantly higher precision, which most software cannot provide, and this increased precision also comes at a higher computational cost. The next Subsection introduces a method to circumvent calculations beyond machine precision.

4.2.3. Circumventing the need for high precision calculations

Machine precision calculations suffice for V_0 values up to approximately $10^{10^{12}}$ MeV^4; however, for V_0 values surpassing this threshold, higher precision becomes essential. This Section presents a resolution to this issue by reformulating the dilaton field as follows:

$$\phi(x) = \phi_M + \delta\phi(x). \tag{4.2.108}$$

Here, $|\delta\phi(x)| \ll |\phi_M|$ denotes a small value that primarily influences only the less significant digits of ϕ for large V_0 but significantly affects the dilaton force $\vec{f}_\phi$. Accordingly, the force is expressed as:

$$\vec{f}_\phi = -\beta(\phi)\frac{m}{m_{\rm pl}}\vec{\nabla}\phi = -\beta(\phi)\frac{m}{m_{\rm pl}}\vec{\nabla}\delta\phi. \tag{4.2.109}$$

Failing to isolate $\delta\phi$ and computing ϕ directly with machine precision would lead to the incorrect result $\phi(x) = \phi_M$, and hence $\vec{\nabla}\phi = 0$. Recalling the differential equation of ϕ:

$$\Box\phi = \frac{\lambda V_0}{m_{\rm pl}}e^{-\lambda\phi/m_{\rm pl}} - \frac{A_2\rho}{m_{\rm pl}^2}\phi, \tag{4.2.110}$$

the differential equation of $\delta\phi$ is given by:

$$\Box\delta\phi = \frac{\lambda V_0}{m_{\rm pl}}e^{-\lambda(\phi_M+\delta\phi)/m_{\rm pl}} - \frac{A_2\rho}{m_{\rm pl}^2}(\phi_M + \delta\phi). \tag{4.2.111}$$

Using Eq. (3.1.52) allows to recast the previous equation:

$$\Box\delta\phi = \frac{\beta(\phi_M)\rho_M}{m_{\rm pl}}e^{-\lambda\delta\phi/m_{\rm pl}} - \frac{\beta(\phi_M+\delta\phi)\rho}{m_{\rm pl}}. \tag{4.2.112}$$

Importantly, implementing Eq. (4.2.110) directly at machine precision can result in the rounding:

$$\begin{aligned}\Box\phi &\sim 0,\\ e^{-\lambda\phi/m_{\rm pl}} &\sim e^{-\lambda\phi_M/m_{\rm pl}},\end{aligned} \tag{4.2.113}$$

leading to completely incorrect results. These roundings are avoided analytically by implementing Eq. (4.2.112) instead. Note that the rounding $\frac{\beta(\phi_M+\delta\phi)\rho}{m_{\rm pl}} \simeq \frac{\beta(\phi_M)\rho}{m_{\rm pl}}$ does not affect the leading digits of $\frac{\beta(\phi_M+\delta\phi)\rho}{m_{\rm pl}}$ and is hence unproblematic. Section 4.4.3 serves to validate the legitimacy of this approach.

Next, the discussion briefly turns to the symmetron field, highlighting its inherent precision issues as well. Following this, the numerical algorithms utilized to solve the scalar field equations of motion will be discussed.

4.3. Precission challenges in Symmetron field computations

While the primary focus remains on numerically investigating the dilaton field, it is crucial to recognize that precision challenges extend beyond this specific field. Particularly, when examining parameters that place the symmetron field within its symmetry broken phase inside materials, precision becomes an inevitable concern.

Consider a scenario where chamber walls exhibit a density ρ_M while surrounded by a vacuum density ρ_V, resulting in the symmetron field persisting in its symmetry-broken phase even inside the walls. The potential minima are defined as follows:

$$\phi_V = \pm\sqrt{\frac{\mu^2}{\lambda} - \frac{\rho_V}{\lambda M^2}},$$
$$\phi_M = \pm\sqrt{\frac{\mu^2}{\lambda} - \frac{\rho_M}{\lambda M^2}}. \tag{4.3.114}$$

Keeping other parameters constant, it becomes apparent that their relative difference vanishes asymptotically:

$$2\left|\frac{\phi_M - \phi_V}{\phi_M + \phi_V}\right| \to 0, \quad \text{as } M \to \infty, \tag{4.3.115}$$

reflecting the behavior observed in the dilaton field for large values of V_0. Consequently, variations in fields become exceedingly minute for very large values of M, rendering them indiscernible with machine precision. In contrast to the dilaton field, only CANNEX and qBOUNCE are sensitive to parameter values where this becomes a concern. Since the associated geometries of these two experiments are one-dimensional, I have developed my own code for these experiments capable of arbitrary precision computation, effectively resolving these precision challenges. The transformation of the equations of motion for the dilaton field is still essential for cylinder simulations associated with neutron interferometry. The underlying algorithm is detailed in the following.

4.4. Solving one dimensional equations of motion

Solving for scalar fields in static configurations entails solving the partial differential equation:

$$\frac{d^2\phi}{dx^2} + \frac{d^2\phi}{dy^2} + \frac{d^2\phi}{dz^2} = V_{\text{eff},\phi}(\phi;\rho). \tag{4.4.116}$$

Eq. (4.4.116) is explicitly tackled for one and two mirror geometries, a spherical configuration and the cross section of an infinitely extented cylinder. These geometries are pertinent to qBOUNCE, CANNEX, LLR, and neutron interferometry respectively. The full cylinder geometry, also relevant to neutron interferometry, will be discussed separately.

The geometries in this Section are encapsulated by the following differential equation:

$$\frac{d^2\phi}{ds^2} + \Gamma\frac{2}{s}\frac{d\phi}{ds} = V_{\text{eff},\phi}(\phi;\rho). \tag{4.4.117}$$

Here, $s = r$ for spherical and cylindrical geometries. For one and two mirror geometries $s = z$, respectively. The parameter Γ takes the value 0 for one and two mirrors, 0.5 for the cross section of a infinitely extended cylinder and 1 for a sphere. The primary challenge in solving Eq. (4.4.117) stems from the extreme slopes of the dilaton field, as depicted in Fig. (4.4.3). The dilaton field exhibits significant variations at scales as small as 10 fm for experimentally accessible parameters. Achieving an accurate and uniform discretization would necessitate over 10^8 grid points in the vacuum region alone, rendering it computationally unfeasible.

4.4.1. Non-uniform finite difference method

Addressing the challenge of steep slopes necessitates the adoption of a non-uniform mesh within the simulation interval. While the FEM is a common choice for accommodating an arbitrary mesh (see e.g., [109]), this Section opts for non-uniform finite difference methods (FDMs) due to their simpler implementation, which is particularly advantageous for the straightforward geometries under consideration. The presented method, in case of the one and two mirror geometries, can be seen as a special case of the FEM, which is demonstrated in Appendix B.5.

Initially, the continuous simulation interval $[a, b]$ is discretized into grid points $s_0 = a, ..., s_{N+1} = b$. Here, a and b typically represent cutoffs. For instance, in the context of the one mirror solution, a and b are selected such that the field naturally relaxes towards its asymptotic boundary conditions ϕ_M within the mirror and ϕ_V within the vacuum region.

Defining

$$\begin{aligned} h_i &:= s_{i+1} - s_i \\ \phi_i &:= \phi(s_i), \\ \phi_i' &:= \frac{d\phi}{ds}(s_i), \\ \phi_i'' &:= \frac{d^2\phi}{ds^2}(s_i), \end{aligned} \tag{4.4.118}$$

a second-order Taylor expansion yields:

$$\begin{aligned} \phi_{i+1} &= \phi_i + \phi_i' h_i + \frac{\phi_i''}{2} h_i^2 + \mathcal{O}(h_i^3) \\ \phi_{i-1} &= \phi_i - \phi_i' h_{i-1} + \frac{\phi_i''}{2} h_{i-1}^2 + \mathcal{O}(h_{i-1}^3). \end{aligned} \tag{4.4.119}$$

Neglecting higher order terms, approximations of ϕ_i' and ϕ_i'' are defined as solutions to:

$$\begin{pmatrix} h_i & h_i^2/2 \\ -h_{i-1} & h_{i-1}^2/2 \end{pmatrix} \cdot \begin{pmatrix} \phi_i' \\ \phi_i'' \end{pmatrix} \approx \begin{pmatrix} \phi_{i+1} - \phi_i \\ \phi_{i-1} - \phi_i \end{pmatrix},$$

resulting in:

$$\phi_i'' \approx \frac{2(\phi_{i+1} - \phi_i)}{h_i(h_i + h_{i-1})} - \frac{2(\phi_i - \phi_{i-1})}{h_{i-1}(h_i + h_{i-1})}, \tag{4.4.120}$$

$$\phi_i' \approx \frac{h_i(\phi_i - \phi_{i-1})}{h_{i-1}(h_i + h_{i-1})} + \frac{h_{i-1}(\phi_{i+1} - \phi_i)}{h_i(h_i + h_{i-1})}. \tag{4.4.121}$$

These approximations extend the standard central difference scheme to non-uniform grids [110] and maintain second-order accuracy if $h_i = h_{i-1}$. Substituting Eqs. (4.4.120)–(4.4.121) into Eq. (4.4.117) results in the discretized differential equation:

$$\frac{2(\phi_{i+1} - \phi_i)}{h_i(h_i + h_{i-1})} - \frac{2(\phi_i - \phi_{i-1})}{h_{i-1}(h_i + h_{i-1})} + \Gamma \frac{2}{s_i} \left[\frac{h_i(\phi_i - \phi_{i-1})}{h_{i-1}(h_i + h_{i-1})} + \frac{h_{i-1}(\phi_{i+1} - \phi_i)}{h_i(h_i + h_{i-1})} \right] - V_{\text{eff},\phi}(\phi_i, \rho_i) = 0. \tag{4.4.122}$$

Appendix B.3 outlines how this system of equations is solved.

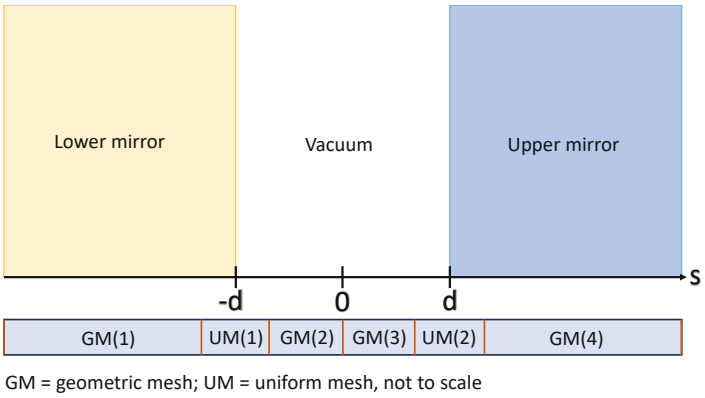

Fig. 4.4.1: Sketch for mesh construction, not to scale. Figure published in [6].

4.4.2. Mesh construction

The crucial task lies in appropriately choosing $s_0, ..., s_{N+1}$ to accurately capture the behavior of the scalar fields under consideration, as discussed in the following.

Uniform meshes:

In the vicinity of material surfaces at $s = -d$ and $s = d$ (referred to as UM(1) and UM(2) in Figure 4.4.1), a highly refined yet uniform mesh is established with a small spacing parameter D. Specifically, for $s = d$, this mesh comprises $2N_1 + 1$ points defined as follows:

$$\begin{aligned} s_i &:= d + iD, \text{ for } i = 0, ..., N_1, \\ s_{N_1+i} &:= d - iD, \text{ for } i = 1, ..., N_1. \end{aligned} \tag{4.4.123}$$

Geometric mesh:

To reduce the total number of mesh points, the small uniform meshes at the surfaces are connected with a mesh of exponentially increasing s_i. This facilitates a smooth transition from material boundaries, where fine spacing is crucial, to the center of homogeneous regions, allowing for a coarser grid. Taking GM(3) in Figure (4.4.1) as an example, the mesh is constructed as follows: Initially, the mesh boundaries are set at $a := d - N_1 D > 0$ and $b := 0$, as the scalar field exhibits the weakest slope in the middle of the vacuum region, justifying a coarser grid. The number of points within this mesh, denoted as N_2, is fixed. An exponential parameter $\delta > 1$ determines the positions of all other points:

$$\begin{aligned} s_0 &:= a \\ s_i &:= s_{i-1} - D\delta^{i-1}, \text{ i=1, ..., } N_2 - 1. \end{aligned} \tag{4.4.124}$$

To ensure $s_{N_2-1} = b$, δ has to be determined by solving:

$$\sum_{i=1}^{N_2-1} D\delta^{i-1} = D\frac{1-\delta^{N_2-1}}{1-\delta} = |b-a|. \tag{4.4.125}$$

Full mesh for the considered geometries

The full mesh is crafted by merging uniform and geometric meshes, as depicted in Figure 4.4.1. The final outcome for a two mirror geometry is illustrated in Figure 4.4.2. For one mirror,

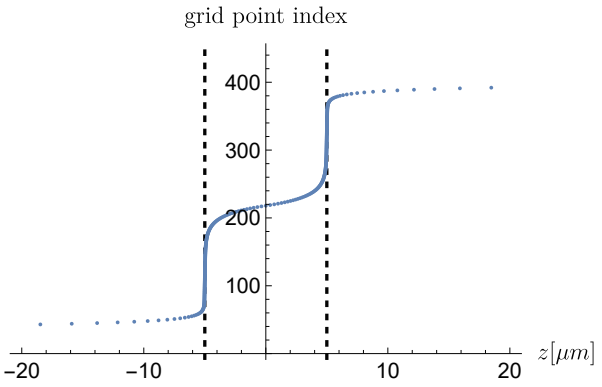

Fig. 4.4.2: This illustration provides an example of the grid construction realizing grid spacings between 1 nm and 19 mm with only ~ 430 points. The dotted lines mark the surfaces of the mirror. The mesh parameters are $D_1 = D_2 = 1$ nm, $N_1 = N_2 = 80$ and $N_3 = 30$.

spherical and cylindrical geometries, it suffices to construct only GM(1), UM(1), and GM(2). In contrast, for a two mirror geometry, owing to the symmetry of the setup, GM(3), UM(2), and GM(4) are selected as the mirror image counterparts of GM(1), UM(1), and GM(2). This brings the total number of parameters needed to define the mesh to 5: two spacing parameters D_1 and D_2, along with the parameters N_1 and N_2 dictating the number of points in the geometric meshes, as well as N_3 to determine the number of points for the uniform meshes. In the majority of cases examined, opting for $D_1 = D_2$ and $N_1 = N_2$ yielded highly satisfactory numerical results, thereby streamlining the parameter-setting process.

4.4.3. Testing the algorithm for the two mirror solution of the dilaton field

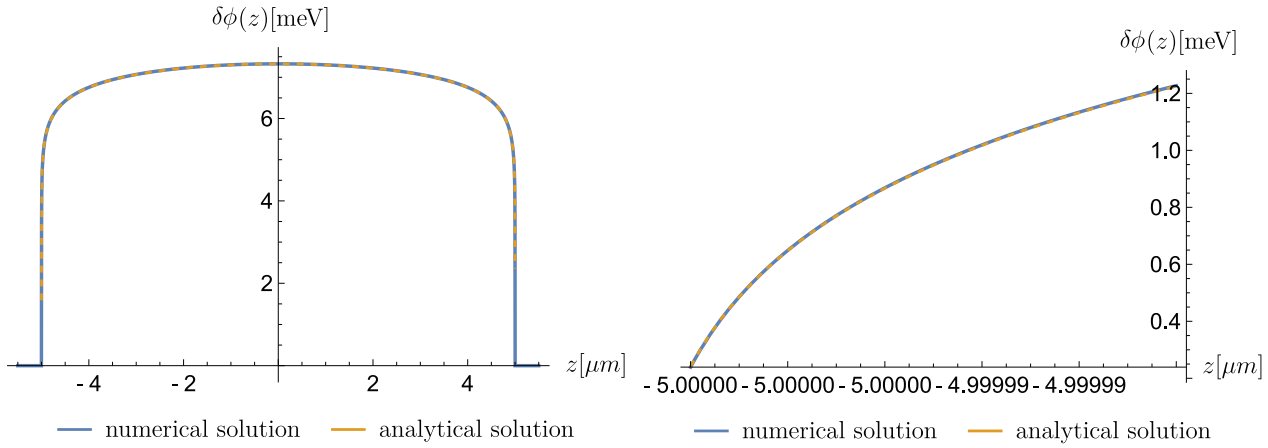

Fig. 4.4.3: The dilaton field defined in Eqs. (4.1.91) and (4.2.108) is plotted for $V_0 = 10$ MeV^4, $A_2 = 10^{45}$, $\lambda = 10^{31}$, $\rho_M = 1.083 \times 10^{-5}$ MeV^4 and $d = 5$ μm and compared to the solution of the numerical algorithm. The mesh parameters are $D_1 = D_2 = 10$ fm, $N_1 = N_2 = 80$ and $N_3 = 30$. For the given parameters $\phi_M \simeq 11.9$ meV. Figure published in [6].

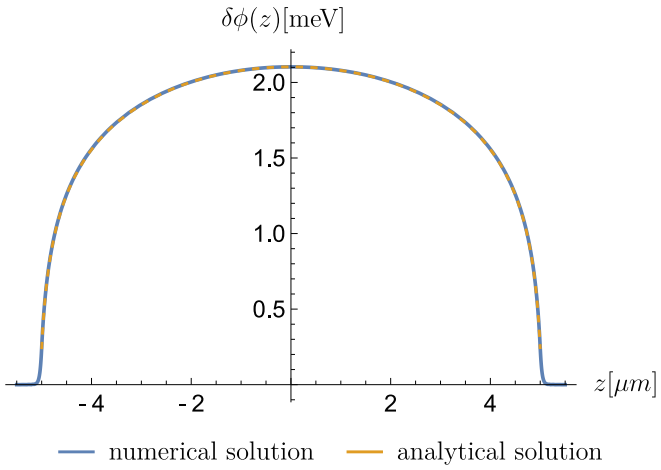

Fig. 4.4.4: The dilaton field defined in Eq. (4.1.91) and Eq. (4.2.108) is plotted for $V_0 = 10^{10^{24}}$ MeV^4, $A_2 = 10^{13}$, $\lambda = 10^{31}$, $\rho_M = 1.083 \times 10^{-5}$ MeV^4 and $d = 5$ μm and compared to the solution of the numerical algorithm. The mesh parameters are $D_1 = D_2 = 1$ nm, $N_1 = N_2 = 80$ and $N_3 = 30$. For the given parameters $\phi_M \simeq 5.61 \times 10^{23}$ meV. Figure published in [6].

The accuracy of the proposed algorithms is validated for scenarios involving extreme slopes in Figure 4.4.3 and an exceedingly large value of V_0 in Figure 4.4.4. The differential equation (4.2.112) for $\delta\phi$ is solved using the proposed algorithm, defining

$$V_{\text{eff}}(\delta\phi) := \frac{\beta(\phi_M)}{\lambda}\rho_M e^{-\lambda\delta\phi/m_{\text{pl}}} + \beta\left(\phi_M + \frac{\delta\phi}{2}\right)\rho\frac{\delta\phi}{m_{\text{pl}}}. \tag{4.4.126}$$

Numerical field solutions where computed with standard machine precision (16 digits), while the corresponding analytical solution for $V_0 = 10^{10^{24}}$ MeV^4 had to be computed with much higher precision (at least $\sim$ 30 digits) for comparison. The analytical and numerical solution closely match even inside extreme slopes. Since the analytical solution assumes $\rho_V = 0$, a numerical solution is mandatory for a realistic analysis of CANNEX and other experiments, where this restriction may not hold in general.

In Fig. 4.4.5, a comparison between the more realistic scenario with $\rho_V = 2.28 \times 10^{-20}$ MeV^4 and the analytical solutions is presented across a broader range of parameter combinations. As anticipated, the numerical algorithm and the approximate two mirror solution with $\rho_V = 2.28 \times 10^{-20}$ MeV^4 exhibit strong alignment in the small λ region ($\lambda = 10^{-5}$ in the figure), while the numerical algorithm remains in agreement with the analytically exact solution with $\rho_V = 0$ up to $A_2 = 10^{45}$. This consistency corroborates the earlier analysis outlined in Section 4.1.3.

4.4.4. Testing the algorithm for the two mirror solution of the symmetron and chameleon fields

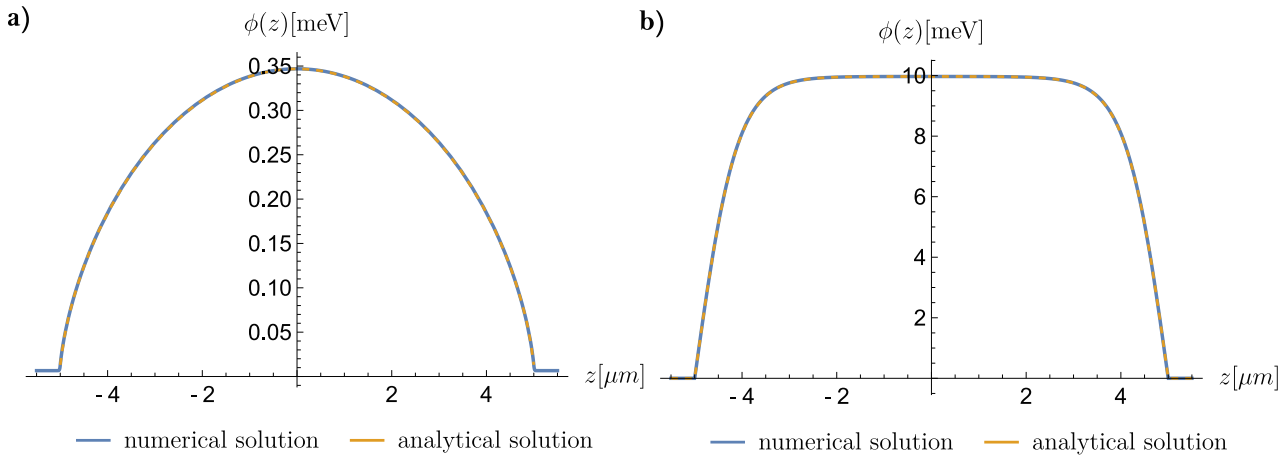

Fig. 4.4.6: **a)** The analytically exact two mirror solutions for the chameleon field for the parameters $n = 1,\ \beta = 4.1 \times 10^5$ and $\Lambda = 2.4 \times 10^{-9}$ is plotted alongside the solution of the numerical algorithm. **b)** The analytically exact two mirror solutions for the symmetron field for the parameters $\mu = 10^{-6.5}$ MeV, $M = 10^{-3.2}$ MeV and $\lambda = 10^3$ is plotted alongside the solution of the numerical algorithm. The experimental parameters were set to $\rho_M = 1.083 \times 10^{-5}$ MeV^4, $\rho_V = 0$ and $d = 5\ \mu$m. The mesh parameters are $D_1 = D_2 = 1$ nm, $N_1 = N_2 = 80$ and $N_3 = 30$. Figure published in [6].

The code has also been compared to the exact analytical solutions available for the symmetron and chameleon models [61, 111], see Figure 4.4.6. While the analytically exact solutions for the chameleon field are specifically applicable for $n = 1$, the numerical algorithm can compute the field for arbitrary parameters. In the code, the analytical solution was compared to the proposed algorithm for many more parameters, consistently showing the same level of agreement.

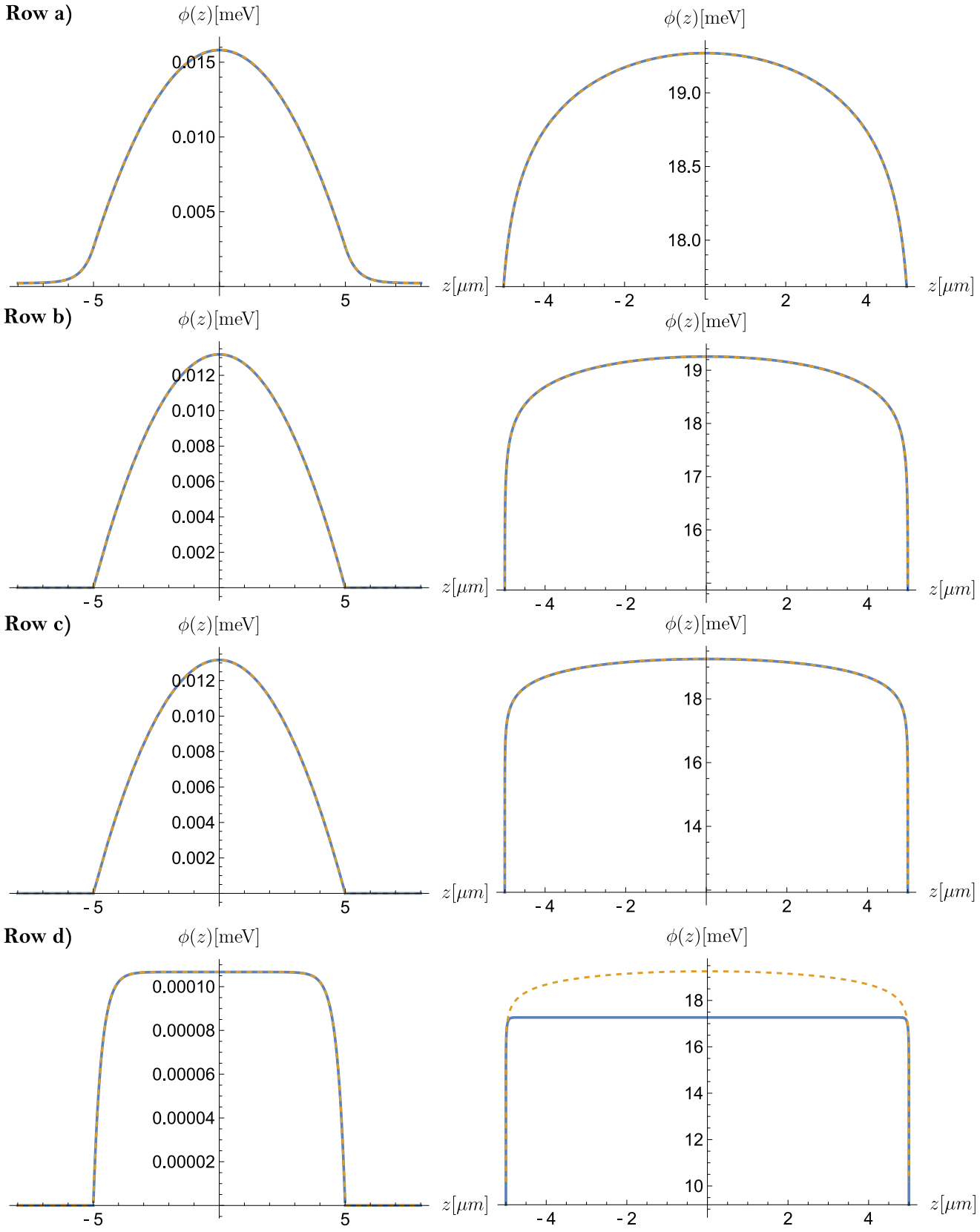

Fig. 4.4.5: V_0 is held constant at 10 MeV^4 for all comparisons. **Left column**: The analytical approximate two mirror solution (dashed yellow) is compared against the numerical solution (blue) for a fixed value of $\lambda = 10^{-5}$. **Right column**: The analytical exact two mirror solution with $\rho_V = 0$ (dashed yellow) is contrasted with the numerical solution (blue) for a fixed value of $\lambda = 10^{31}$. The parameter A_2 remains fixed at 10^{35} in **Row a)**, 10^{40} in **Row b)**, 10^{45} in **Row c)**, and 10^{50} in **Row d)**. Additionally, $\rho_V = 2.28 \times 10^{-20}$ MeV^4 and $\rho_M = 1.083 \times 10^{-5}$ MeV^4.

4.4.5. Testing for cylindrical and spherical geometries

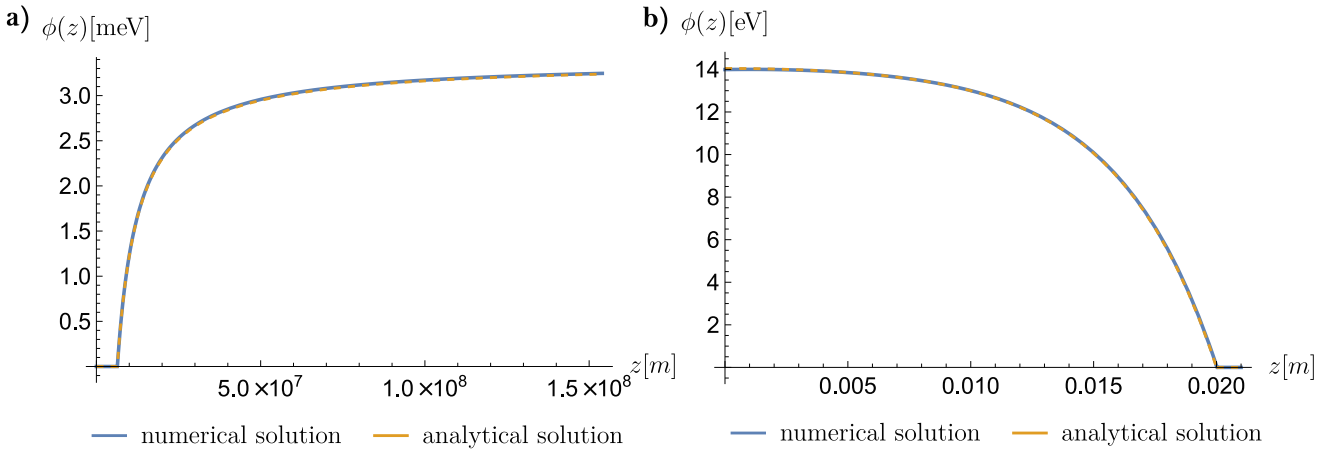

Fig. 4.4.7: **a)** The analytical solution for a sphere is compared to the numerical algorithm, for $V_0 = 10$ MeV^4, $A_2 = 10^{20}$ and $\lambda = 10^{-24}$. The densities are given by $\rho_V = 7.21 \times 10^{-29}$ MeV^4, $\rho_M = 2.37 \times 10^{-5}$ MeV^4. **b)** The analytical solution for a the cross section of a cylinder is compared to the numerical algorithm, for $V_0 = 10$ MeV^4, $A_2 = 10^{38}$ and $\lambda = 10^{-5}$. The densities are given by $\rho_V = 1.69 \times 10^{-16}$ MeV^4, $\rho_M = 1.1 \times 10^{-5}$ MeV^4.

The code was tested to ensure it can reproduce the known one mirror solution [61] for the symmetron field. While analytically exact solutions of the investigated scalar fields for spheres and cylinder cross sections remain elusive, inside the small λ region, the dilaton differential equation becomes linear and can be explicitly solved for both geometries, see Appendix C. The numerical algorithm and the approximate analytical solutions match in this scenario. An example is shown in Figure 4.4.7.

4.5. Numerical methods for simulating a cylinder

In the preceding Section, a method for solving one dimensional differential equations using a FDM has been developed. However, in Appendix B.5, it is demonstrated that this method can also be interpreted as a special case of the FEM for both one and two mirror geometries. Now, within the context of neutron interferometry, the task is to solve the differential equation for a cylinder with two degrees of freedom (r, z), as described in Equation (4.0.77).

There are two natural avenues to extend the method for one-dimensional equations of motion to a cylindrical geometry. One could either adhere to the FDM interpretation of the previous Section and apply Eq. (4.4.118) to each partial derivative individually, or opt for a two dimensional FEM approach.

The FEM, akin to the non-uniform FDM, allows for arbitrary discretization, making it optimal for screened scalar field simulations. Its versatility surpasses that of non-uniform finite difference schemes for higher-dimensional geometries, as it is better equipped to simulate arbitrary shapes. Figure 4.5.1 illustrates how a cylinder is divided into triangles for discretization, allowing for arbitrary distribution of degrees of freedom (points where the edges of different triangles intersect), which is only possible with the FEM and not FDMs.

I have chosen to utilize the FEM for cylindrical geometries for two reasons:

Firstly, Mathematica's built-in FEM code can be adapted to suit cylinder simulations relevant to neutron interferometry, thereby significantly reducing coding efforts. Secondly, the FEM proves superior when investigating more intricate geometries; hence, investigations based on the FEM can be easier generalized to other problems in the future.

However, the built-in Mathematica code is hampered by significant limitations. While I managed to address some of these limitations through manual modifications tailored to neutron interferometry, the code still falls short when it comes to deriving parameter constraints for other experiments explored in this work. Consequently, custom code had to be developed from the ground up for these additional experiments, a process detailed in the preceding Section.

Section 4.5.1 will provide an overview of integrating the FEM within the context of screened scalar fields. Following this, Section 4.5.2 will address the unreliability of Mathematica's nonlinear solver, while Section 4.5.3 will outline my manual interventions to rectify these limitations. In Section 4.5.4, mesh construction and initial guesses for Newton's method are detailed, the non-uniqueness of symmetron solutions is demonstrated, and several code tests discussed.

Section 4.5.5 concludes by addressing the remaining limitations of the code and clarifying why it is not applicable to the other experiments considered in this thesis.

4.5.1. Summary of the FEM for screened scalar fields

This Subsection provides a brief summary of the FEM applied to screened scalar fields. The following is a straight forward generalization of the FEM applied to the chameleon field [98] or the Poisson equation [112]. The discussion begins with the differential equation:

$$\Delta\phi = V_{\text{eff},\phi}(\phi;\rho), \tag{4.5.127}$$

on a domain $\hat{\Omega}$, with mixed Dirichlet and Neumann boundary conditions

$$\begin{aligned} \phi &= \phi_D \text{ on } \partial\hat{\Omega}_D, \\ \vec{\nabla}\phi\cdot\vec{n} &= g \text{ on } \partial\hat{\Omega}_N, \\ \partial\hat{\Omega} &= \partial\hat{\Omega}_D \dot{\cup} \partial\hat{\Omega}_N. \end{aligned} \tag{4.5.128}$$

The equation is multiplied by a test function φ_i and partially integrated:

$$\begin{aligned} &-\int_{\hat{\Omega}} \vec{\nabla}\phi\vec{\nabla}\varphi_i d^3x + \int_{\partial\hat{\Omega}} \vec{\nabla}\phi\cdot\vec{n}\varphi_i dS - \int_{\hat{\Omega}} V_{\text{eff},\phi}(\phi;\rho)\varphi_i d^3x \\ =&-\int_{\hat{\Omega}} \vec{\nabla}\phi\vec{\nabla}\varphi_i d^3x + \int_{\partial\hat{\Omega}_N} g\varphi_i dS - \int_{\hat{\Omega}} V_{\text{eff},\phi}(\phi;\rho)\varphi_i d^3x = 0, \end{aligned} \tag{4.5.129}$$

where homogeneous Dirichlet boundary conditions have been assumed for simplicity[3].

The last equation applied to all test functions is the weak form of the differential equation[4]. The finite element discretization works based on choosing a finite amount of basis functions φ_i and using an approximation of ϕ expressed as a linear combination of φ_i.

[3] Non-homogeneous Dirichlet boundary conditions are implemented by choosing an arbitrary smooth function $\hat{\phi}$ that fullfills the boundary conditions and making the Ansatz $\phi = \hat{\phi} + \delta$. Plugging this into the differential equation results in a differential equation with homogenous dirichlet conditions for δ that can then be solved as described.

[4] The weak derivative is a mathematical concept replacing the regular derivative. It involves multiplying a function by an arbitrary test function and partially integrating the result. This approach sometimes allows functions that aren't differentiable in the traditional sense to become differentiable.

Geometrically, the basis functions can be identified with the values assigned to the nodes within the FEM mesh, as illustrated in Fig. 4.5.1.

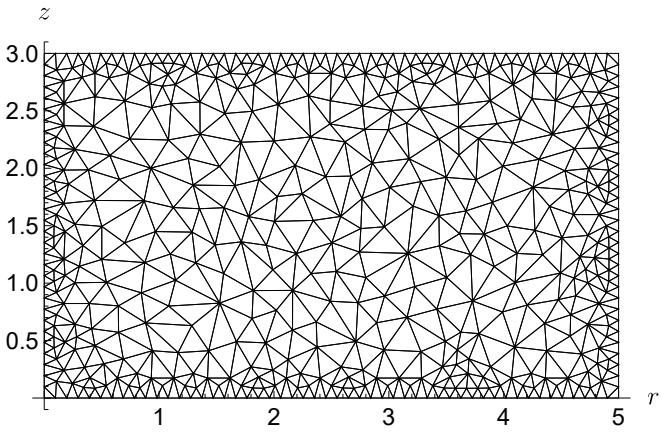

Fig. 4.5.1: This is an example of a FEM mesh for a cylinder. Each node corresponds to a basis function that is 1 at one of the nodes and continuously falls of to 0 at the surrounding nodes. For a detailed explanation I refer to the main text.

Within the domain $\hat{\Omega}$, the nodes are designated as $\vec{x}_1, ..., \vec{x}_N$, and each basis function φ_i is defined to assume a value of 1 at node i and 0 at all other nodes:

$$\varphi_i(\vec{x}_j) = \delta_{ij}. \tag{4.5.130}$$

A common choice in two dimensions is to use triangle basis functions: A triangle has three nodes and a linear function in two dimensions is specified by exactly three points. Hence, a basis function is uniquely defined by demanding it to be 1 at one node of the triangle an 0 at the others. Notably, unlike finite difference methods, these basis functions can aptly represent geometric shapes such as triangles, making them well-suited for effectively approximating complex domains.

The discretized version of the differential equation reads

$$-\sum_{j=1}^{N} \phi_j \Big(\int_{\hat{\Omega}} \vec{\nabla}\varphi_j \vec{\nabla}\varphi_i d^3x \Big) + \int_{\partial\hat{\Omega}_N} g\varphi_i dS - \int_{\hat{\Omega}} V_{\text{eff},\phi}\Big(\sum_{k=1}^{N} \phi_k\varphi_k; \rho \Big)\varphi_i d^3x = 0, \text{ for } i = 1, ..., N, \tag{4.5.131}$$

where ϕ_k corresponds to the value at $\vec{x}_k$ of the FEM approximation of ϕ. Defining

$$\mathbf{F} : \mathbb{R}^N \to \mathbb{R}^N \tag{4.5.132}$$

with

$$\mathbf{F}_i(\phi_1, ..., \phi_N) := -\sum_{j=1}^{N} \phi_j \Big(\int_{\hat{\Omega}} \vec{\nabla}\varphi_j \vec{\nabla}\varphi_i d^3x \Big) + \int_{\partial\hat{\Omega}_N} g\varphi_i dS - \int_{\hat{\Omega}} V_{\text{eff},\phi}\Big(\sum_{k=1}^{N} \phi_k\varphi_k; \rho \Big)\varphi_i d^3x, \tag{4.5.133}$$

the goal is to solve

$$\mathbf{F}(\phi_1, ..., \phi_N) = 0, \tag{4.5.134}$$

which corresponds to a root fining problem on $\mathbb{R}^N$. In order to solve this system, a non-linear solver needs to be employed. A standard choice is Newton's method or variants thereof [113], which is also what is used by Mathematica. To apply a Newton iteration, the Jacobian of $\mathbf{F}$ has to be computed. One obtains

$$J_{\mathbf{F},ij} = \frac{\partial \mathbf{F}_i}{\partial \phi_j} = -\int_{\hat{\Omega}} \vec{\nabla}\varphi_j \vec{\nabla}\varphi_i d^3x - \int_{\hat{\Omega}} V_{\text{eff},\phi\phi}\Big(\sum_{k=1}^{N} \phi_k \varphi_k; \rho\Big)\varphi_j \varphi_i d^3x. \tag{4.5.135}$$

Assuming an initial guess of $\phi^{(0)} := (\phi_1^{(0)}, ..., \phi_N^{(0)})$, the Newton iterations are given by

$$\mathbf{F}(\phi^{(n-1)}) + J_{\mathbf{F}}(\phi^{(n-1)})(\phi^{(n)} - \phi^{(n-1)}) = 0, \tag{4.5.136}$$

which is the linear system of equation that has to be solved at the n'th iteration.

In summary the FEM applied to screened scalar fields involves the solution of a root-finding problem on $\mathbb{R}^N$, where the goal is to find $\phi_1, ..., \phi_N$ that satisfy $\mathbf{F}(\phi_1, ..., \phi_N) = 0$. Next, it will be shown that the non-linear solver in Mathematica's FEM implementation is unreliable, and an explanation will be provided on how this issue was addressed.

4.5.2. Convergence problems with Mathematica's nonlinear solver

While Mathematica's NDSolve includes functionality for solving nonlinear differential equations using the FEM, it unfortunately exhibits unreliability in certain cases. Fig. 4.5.2 shows a solution returned by Mathematica's NDSolve, without triggering any error messages, for a two mirror geometry with $\rho_V = 0$. A comparison with the known exact solution reveals a substantial discrepancy, highlighting the inaccuracies in the obtained result. Furthermore, for more intricate geometries, such as the cylinder geometry, NDSolve often fails to provide any solution.

After a thorough investigation, the root of the problem has been identified:

The nonlinear solver in Mathematica does not effectively monitor convergence. This conclusion arises from the observation that, as discussed in the preceding Subsection, solving the differential equation ultimately leads to a nonlinear system of equations. To initiate the Newton iterations, an initial guess must be specified. In NDSolve, this can be provided using the 'initial seeding' option. In Fig. 4.5.2, the trivial seed $\phi = \phi_M$ has been used. Denoting the incorrectly returned solution by Mathematica as ϕ_2, upon restarting NDSolve, this time with the guess ϕ_2 instead of ϕ_M, the solution returned, denoted as ϕ_3, again proves incorrect, albeit slightly different from ϕ_2. Iterating this process eventually converges to the correct solution, indistinguishable from the exact solution.

Despite specifying the most stringent convergence criteria (these can be controlled with the accuracy goal and precision goal option in NDSolve), Mathematica's NDSolve terminates Newton's iteration prematurely for some unknown reason. I brought this issue to Mathematica's attention through their official forum[5], but as of now, a proper response has not been received. The workaround of repeatedly restarting NDSolve, although effective in some cases, is far from ideal, often resulting in no solution at all. Notably, Mathematica's FEM exhibits reliability for linear

problems but encounters challenges in handling nonlinear problems. In the following Section, the approach to address and resolve this problem will be outlined.

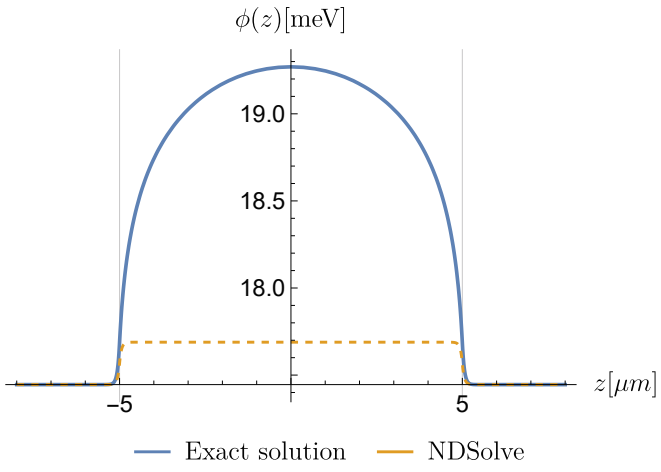

Fig. 4.5.2: The analytically exact solution is compared to the output of Mathematica's inbuilt function NDSolve, which was returned without error-messages. The parameters are $V_0 = 10$ MeV^4, $A_2 = 10^{35}$ and $\lambda = 10^{31}$. The densities are given by $\rho_V = 0$, $\rho_M = 1.08 \times 10^{-5}$ MeV^4.

4.5.3. Replacing Mathematica's nonlinear solver

The key insight that allows for the resolution of NDSolve's convergence issues with minimal effort lies in recognizing that the nonlinear solver can be decoupled from NDSolve, making it easily replaceable. This realization is underpinned by the following analytical understanding:

There exist two approaches to apply Newton's method for solving the differential equation:

$$\Delta\phi = V_{\text{eff},\phi}(\phi;\rho). \tag{4.5.137}$$

The first approach involves initially applying the FEM to the nonlinear differential equation, transforming it into an $N-$dimensional root-finding problem, which is then solved using Newton's method on $\mathbb{R}^N$, as discussed in Section 4.5.1.

Reference [114] highlights another method where Newton's method is directly applied in the function space before discretization, and notes that both approaches are often equivalent. Beginning with an initial guess function $\phi_f^{(0)}(\vec{x})$ (where subscript f was added to avoid confusion with the definition below Eq. (4.5.135)) for the field, the differential equation is linearized around this guess function to first order. The resulting solution serves as an improved guess for the subsequent iteration. This process generates a sequence of functions $\phi_f^{(0)}$, ...$\phi_f^{(n)}$, where $\phi_f^{(n)}$ is defined as the solution of the *linear* differential equation:

$$\Delta\phi_f^{(n)}(\vec{x}) = V_{\text{eff},\phi_f}\left(\phi_f^{(n-1)}(\vec{x});\rho(\vec{x})\right) + V_{\text{eff},\phi\phi}\left(\phi_f^{(n-1)}(\vec{x});\rho(\vec{x})\right)\left(\phi_f^{(n)} - \phi_f^{(n-1)}\right). \tag{4.5.138}$$

The significant advantage of the second approach is that NDSolve can be employed solely for solving the linear differential equations (4.5.138), which is reliable, while developing an independent nonlinear solver. The norm $||\phi_f||_2$ is defined as:

[5] This message can be found here: https://mathematica.stackexchange.com/questions/278396/convergence-problems-non-linear-fem

$$||\phi_f||_2 := \sqrt{\sum_{i=1}^{N} \phi_f^2(\vec{x}_i)}, \tag{4.5.139}$$

and these linear differential equations are iteratively solved using NDSolve until the condition

$$\frac{||\phi_f^{(n)} - \phi_f^{(n-1)}||_2}{||\phi_f^{(n-1)}||_2} < \epsilon, \tag{4.5.140}$$

is satisfied, where ϵ is a small value (typically set to at least 10^{-10}, but smaller for extreme parameters). This approach effectively decouples the nonlinear convergence issue from NDSolve, leading to a more robust solution strategy. The discussion is closed by explicitly demonstrating the equivalence of both Newton's methods:

The equivalence of both Newton's methods

Beginning with the differential equation:

$$\Delta\phi_f^{(n)}(\vec{x}) = V_{\text{eff},\phi}\Big(\phi_f^{(n-1)}(\vec{x}); \rho(\vec{x})\Big) + V_{\text{eff},\phi\phi}\Big(\phi_f^{(n-1)}(\vec{x}); \rho(\vec{x})\Big)\left(\phi_f^{(n)} - \phi_f^{(n-1)}\right), \tag{4.5.141}$$

its weak form is derived by multiplying with a test function and employing partial integration:

$$\begin{aligned} &-\int_{\hat{\Omega}} \vec{\nabla}\phi_f^{(n)}\vec{\nabla}\varphi_i d^3x + \int_{\partial\hat{\Omega}_N} g\varphi_i dS - \int_{\hat{\Omega}} \Big(V_{\text{eff},\phi}\big(\phi_f^{(n-1)}; \rho\big) \\ &+ V_{\text{eff},\phi\phi}\big(\phi_f^{(n-1)}; \rho\big)(\phi_f^{(n)} - \phi_f^{(n-1)})\Big)\varphi_i d^3x = 0. \end{aligned} \tag{4.5.142}$$

Here, $\phi_f^{(n-1)}$ represents the FEM solution from the previous iteration. Expressing both $\phi_f^{(n-1)}$ and $\phi_f^{(n)}$ in the FEM basis ($\phi_f^{(n-1)} = \sum_{k=1}^{N} \phi_k^{(n-1)}\varphi_k$, $\phi_f^{(n)} = \sum_{k=1}^{N} \phi_k^{(n)}\varphi_k$) results in:

$$\begin{aligned} &-\sum_{j=1}^{N} \phi_j^{(n)}\Big(\int_{\hat{\Omega}} \vec{\nabla}\varphi_j\vec{\nabla}\varphi_i d^3x\Big) + \int_{\partial\hat{\Omega}_N} g\varphi_i dS - \int_{\hat{\Omega}} V_{\text{eff},\phi}\big(\sum_{k=1}^{N} \phi_k^{(n-1)}\varphi_k; \rho\big)\varphi_i d^3x \\ &-\sum_{l=1}^{N}\Big(\int_{\hat{\Omega}} V_{\text{eff},\phi\phi}\big(\sum_{k=1}^{N} \phi_k^{(n-1)}\varphi_k; \rho\big)\varphi_l\varphi_i d^3x\Big)(\phi_l^{(n)} - \phi_l^{(n-1)}) = 0. \end{aligned} \tag{4.5.143}$$

Rearranging the equation yields:

$$\begin{aligned} &-\sum_{j=1}^{N} \phi_j^{(n-1)}\Big(\int_{\hat{\Omega}} \vec{\nabla}\varphi_j\vec{\nabla}\varphi_i d^3x\Big) + \int_{\partial\hat{\Omega}_N} g\varphi_i dS - \int_{\hat{\Omega}} V_{\text{eff},\phi}\big(\sum_{k=1}^{N} \phi_k^{(n-1)}\varphi_k; \rho\big)\varphi_i d^3x \\ &-\sum_{l=1}^{N}\Big(\int_{\hat{\Omega}} \vec{\nabla}\varphi_l\vec{\nabla}\varphi_i d^3x + \int_{\hat{\Omega}} V_{\text{eff},\phi\phi}\big(\sum_{k=1}^{N} \phi_k^{(n-1)}\varphi_k; \rho\big)\varphi_l\varphi_i d^3x\Big)(\phi_l^{(n)} - \phi_l^{(n-1)}) = 0. \end{aligned}$$

By using equations (4.5.135) and (4.5.133), this can be represented more succinctly as:

$$\mathbf{F}_i(\phi^{(n-1)}) + \sum_{l=1}^{N} J_{\mathbf{F},il}(\phi^{(n-1)})(\phi_l^{(n)} - \phi_l^{(n-1)}) = 0, \tag{4.5.144}$$

or in matrix notation:

$$\mathbf{F}(\phi^{(n-1)}) + J_{\mathbf{F}}(\phi^{(n-1)})(\phi^{(n)} - \phi^{(n-1)}) = 0, \tag{4.5.145}$$

which is identical to (4.5.136), using $\phi^{(n)} = (\phi_1^{(n)}, ..., \phi_N^{(n)})$. The explanation proceeds by detailing the construction of the mesh and verifying that the code works.

4.5.4. Mesh construction, code tests and initial guesses

In the preceding Subsections, a nonlinear FEM was outlined, relying on two crucial components.

Firstly, constructing an appropriate mesh is essential. This involves creating two one-dimensional grids: one for the radial points $r_0, ..., r_{N_1}$, representing the cross section of the cylinder, and the other for the axial points $z_0, ..., z_{N_2}$, indicating the cylinder's length. By employing these separate one-dimensional grids, as detailed in Section 4.4.2, a suitable two-dimensional grid can be defined. This grid is characterized by the points $\{(r_i, z_j) \mid 0 \leq i \leq N_1,\ 0 \leq j \leq N_2\}$. Fig. 4.5.3 provides an illustration of such a FEM grid. This construction ensures that the discretization is very fine close to material boundaries, while being coarser in other regions.

As expounded upon in Section 5.5.2, exploration revealed that neutron interferometry fails to yield new constraints for the chameleon field. Consequently, deep dives into chameleon simulations of cylinder geometries were not pursued. Subsequently, various tests conducted to validate the precision of the proposed method for the dilaton and symmetron fields are scrutinized. Additionally, deliberation on the suitability of different initial guesses for Newton's method is provided.

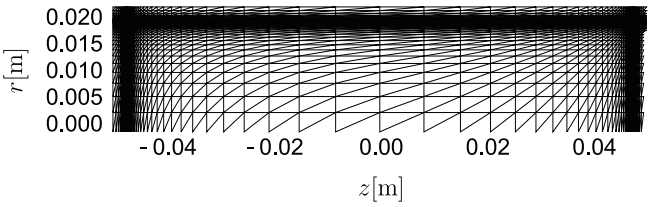

Fig. 4.5.3: The figure depicts an example of a FEM mesh that was used for cylinder simulations.

Code tests for the dilaton field

Initiating Newton's method with the trivial guess $\phi = \phi_M$ ensures convergence across all relevant parameters. The focus lies in exploring parameters inspired by the constraint volume, as discussed in Section 6, which stems from neutron interferometry. Thus, the simulations are tailored exclusively to these parameters.

For large values of A_2, an analytical short-range approximation is employed which makes simulations unnecessary, this will be elaborated on in detail in Section 5.2.2. Consequently, simulations and code testing are limited to $10^{28} \leq A_2 \leq 10^{36}$ for $V_0 = 10$ MeV^4 within the large λ region, for larger values of A_2 the short range approximation becomes highly accurate, as shown in Fig.

5.2.3. In the small λ region at $V_0 = 10$ MeV^4, $10^{30} \leq A_2 \leq 10^{40}$ needs to be considered. For the extreme scenario of $V_0 = 10^{10^{18}}$ MeV^4, simulations must robustly handle $10^{12} \leq A_2 \leq 10^{20}$.

The code underwent three tests:

Firstly, it was confirmed that the relative residual (RS) quickly decreases as the mesh is refined. The RS is defined as:

$$\mathrm{RS}(r,z) := \frac{\left|\frac{\partial^2\phi}{\partial z^2}(r,z) + \frac{\partial^2\phi}{\partial r^2}(r,z) + \frac{1}{r}\frac{\partial\phi}{\partial r}(r,z) + \frac{\lambda}{m_{\mathrm{pl}}}V_0 e^{-\frac{\lambda\phi(r,z)}{m_{\mathrm{pl}}}} - \frac{A_2\rho(r,z)}{m_{\mathrm{pl}}^2}\phi(r,z)\right|}{\max\left\{\left|\frac{\partial^2\phi}{\partial z^2}(r,z)\right|, \left|\frac{\partial^2\phi}{\partial r^2}(r,z)\right|, \left|\frac{1}{r}\frac{\partial\phi}{\partial r}(r,z)\right|, \left|\frac{\lambda}{m_{\mathrm{pl}}}V_0 e^{-\frac{\lambda\phi(r,z)}{m_{\mathrm{pl}}}}\right|, \left|\frac{A_2\rho(r,z)}{m_{\mathrm{pl}}^2}\phi(r,z)\right|\right\}}. \quad (4.5.146)$$

The exact solution corresponds to RS=0, whereas a random solution typically yields RS$\sim$1. Fig. 4.5.6 demonstrates that refining the mesh decreases RS to values significantly below 1.

Secondly, it was ensured that solutions converge rapidly as the mesh refines. As illustrated in Fig. 4.5.7, solutions from a coarse mesh with 12996 nodes and a finer mesh with 98596 nodes exhibit agreement to at least one part in 1000, often more.

To further validate the code, physical insight was leveraged by comparing it against known correct solutions. Particularly, the dilaton field at the center of the cylinder ($z = 0$) is minimally affected by the cylinder's top and bottom, as seen in Fig. 4.5.4-4.5.5. This observation allows for the approximation of the differential equation at $z = 0$ as:

$$\begin{aligned}
&\frac{\partial^2}{\partial r^2}\phi(r,0) + \frac{\partial^2}{\partial z^2}\phi(r,0) + \frac{1}{r}\frac{\partial}{\partial r}\phi(r,0) - V_{\mathrm{eff},\phi}\Big(\phi(r,0);\rho(r,0)\Big) \\
&\quad\simeq \frac{\partial^2}{\partial r^2}\phi(r,0) + \frac{1}{r}\frac{\partial}{\partial r}\phi(r,0) - V_{\mathrm{eff},\phi}\Big(\phi(r,0);\rho(r,0)\Big) \\
&\quad= 0. \qquad (4.5.147)
\end{aligned}$$

The reliable solution of this equation using the FDM in Section 4.4 has been demonstrated. Thus, the accuracy of the simulations away from the cylinder's ends for various parameter combinations is explicitly verified, as depicted in Figs. 4.5.8-4.5.9.

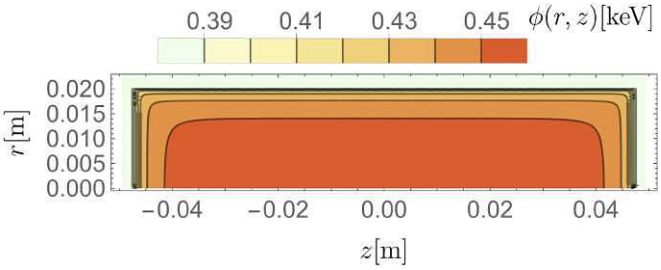

Fig. 4.5.4: The dilaton field is shown for the parameters $V_0 = 10$ MeV^4, $A_2 = 10^{30}$, and $\lambda = 10^{26.6}$.

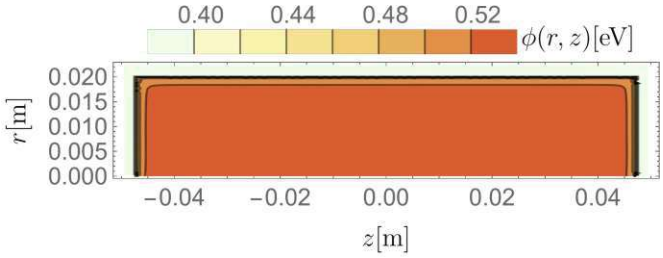

Fig. 4.5.5: The dilaton field is shown for the parameters $V_0 = 10$ MeV^4, $A_2 = 10^{36}$, and $\lambda = 10^{29.6}$.

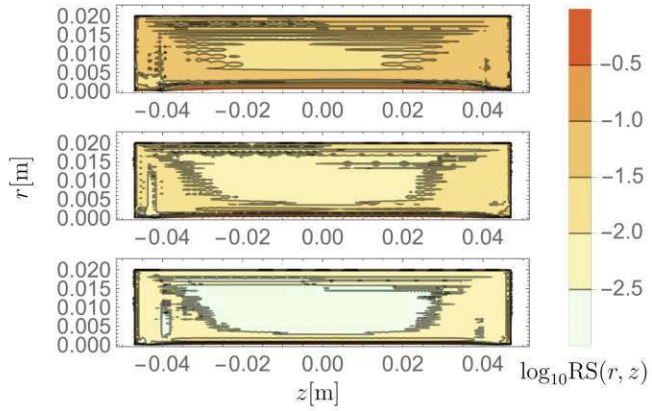

Fig. 4.5.6: The relative residuals are shown for three simulations, characterized by the parameters $V_0 = 10$ MeV^4, $A_2 = 10^{30}$, and $\lambda = 10^{26.6}$. Throughout all simulations, the mesh parameters remained consistent: the minimum distance between two points was fixed at 0.472 nm in the z direction and 0.182 nm in the r direction, without any additional uniform meshes around material surfaces. In the first simulation, the N parameters, as elaborated in Section 4.4.2, were all set to 30; for the second simulation, they were increased to 50, and for the third simulation, to 80. The meshes consisted of 12996, 37636, and 98596 nodes, respectively.

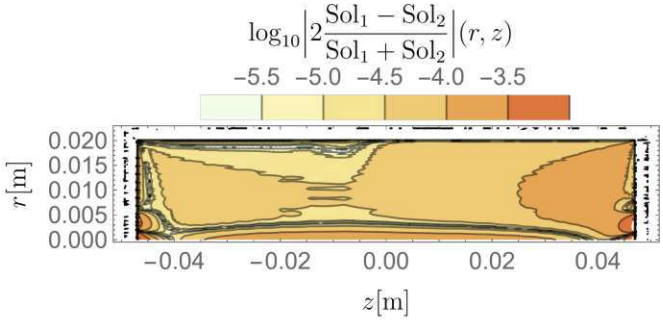

Fig. 4.5.7: The solutions obtained from the finest and coarsest meshes depicted in Fig. 4.5.6 are compared.

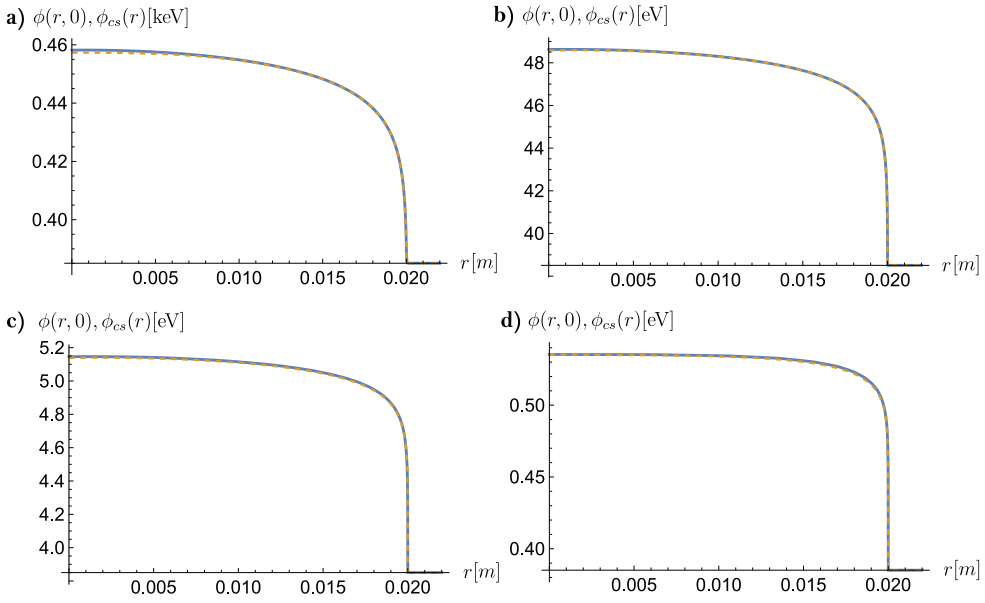

Fig. 4.5.8: A comparison between the simulation of the full cylinder at $z = 0$ (shown in blue) to the cross sectional simulation of an infinitely long cylinder using the FDM (depicted in dashed orange) is shown. The parameters for comparison are as follows: **a)** $V_0 = 10$ MeV^4, $A_2 = 10^{30}$, and $\lambda = 10^{26.6}$. **b)** $V_0 = 10$ MeV^4, $A_2 = 10^{32}$, and $\lambda = 10^{27.6}$. **c)** $V_0 = 10$ MeV^4, $A_2 = 10^{34}$, and $\lambda = 10^{28.6}$. **d)** $V_0 = 10$ MeV^4, $A_2 = 10^{36}$, and $\lambda = 10^{29.6}$.

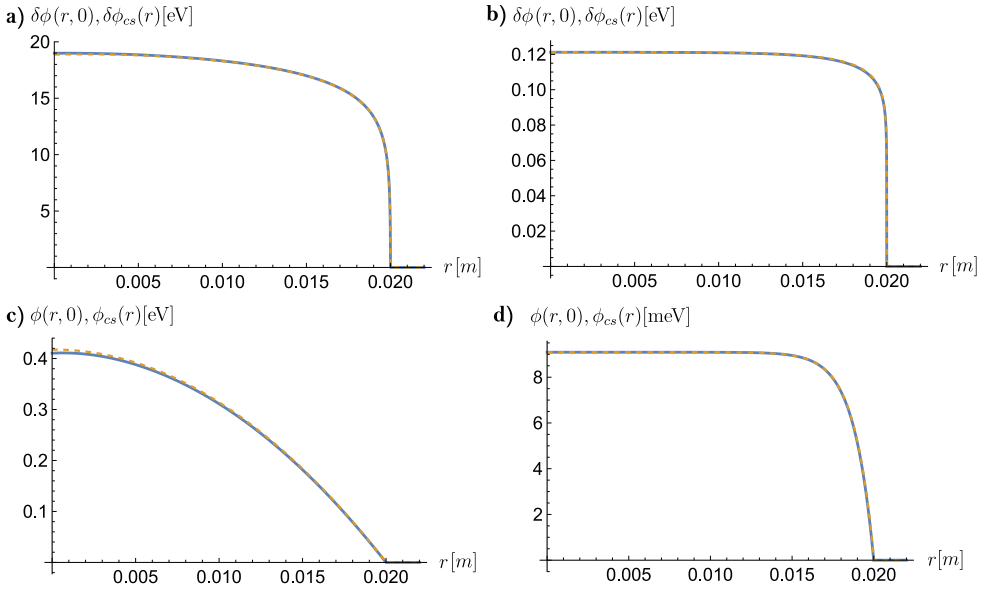

Fig. 4.5.9: A comparison of the simulation of the full cylinder at $z = 0$ (shown in blue) to the cross sectional simulation of an infinitely long cylinder using the FDM (depicted in dashed orange) is shown. Cases **a)** and **b)** show $\delta\phi(r, z)$. The parameters for comparison are as follows: **a)** $V_0 = 10^{10^{18}}$ MeV^4, $A_2 = 10^{15}$, and $\lambda = 10^{27.3}$. **d)** $V_0 = 10^{10^{18}}$ MeV^4, $A_2 = 10^{20}$, and $\lambda = 10^{29.7}$. **c)** $V_0 = 10$ MeV^4, $A_2 = 10^{35}$, and $\lambda = 10^{-7.4}$. **d)** $V_0 = 10$ MeV^4, $A_2 = 10^{39}$, and $\lambda = 10^{-7.2}$.

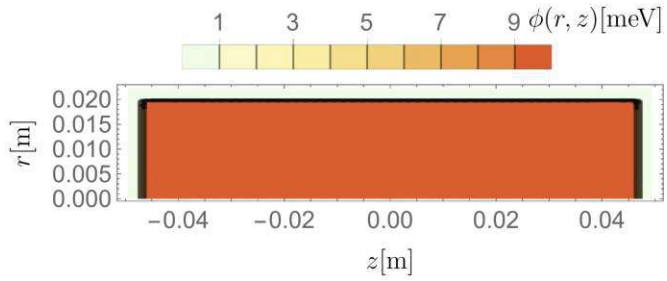

Fig. 4.5.10: The figure depicts a simulation of the symmetron field for the parameters $\mu = 1$ meV, $M = 10^{-1}$ GeV, and $\lambda_S = 10^{-2}$.

Code tests for the symmetron field

In contrast to the approach taken for the dilaton field, constraints for the symmetron field were exclusively derived from the short-range approximation (Eq. 5.2.223). Section 5.5.2, delves into why this approach suffices. Consequently, achieving high precision in simulations is not as imperative as it is for the dilaton field.

Code tests are therefore confined to a fixed parameter value of $\mu = 1$ meV, which represents the smallest value for which constraints were derived (corresponding to the largest symmetron ranges for which constraints were derived). For larger values of μ (resulting in shorter symmetron ranges), the approximation becomes increasingly accurate, obviating the need for simulations altogether. Similar to the dilaton field, it is demonstrated that the cylindrical cross section FDM simulation matches the full simulation at $z = 0$. Additionally, owing to the rapid attainment of its vacuum expectation value (VEV) within the chamber (refer to Fig. 4.5.10), there is negligible variation in the r direction at $r = 0$. Consequently, at $r = 0$, one can approximate:

$$\begin{aligned}
&\frac{\partial^2}{\partial r^2}\phi(0,z) + \frac{\partial^2}{\partial z^2}\phi(0,z) + \frac{1}{r}\frac{\partial}{\partial r}\phi(0,z) - V_{\text{eff},\phi}\Big(\phi(0,z);\rho(0,z)\Big) \\
&\quad\simeq \frac{\partial^2}{\partial z^2}\phi(z,0) - V_{\text{eff},\phi}\Big(\phi(z,0);\rho(z,0)\Big) \\
&\quad= 0.
\end{aligned} \tag{4.5.148}$$

This differential equation coincides with the one for the two mirror solution. Consequently, the two mirror solution with a plate distance of 9.4 cm (corresponding to the cylinder's length) should align with cylinder simulation at $r = 0$. Both tests were conduced, as depicted in Fig. 4.5.11, and excellent agreement between the FDM and the FEM is observed.

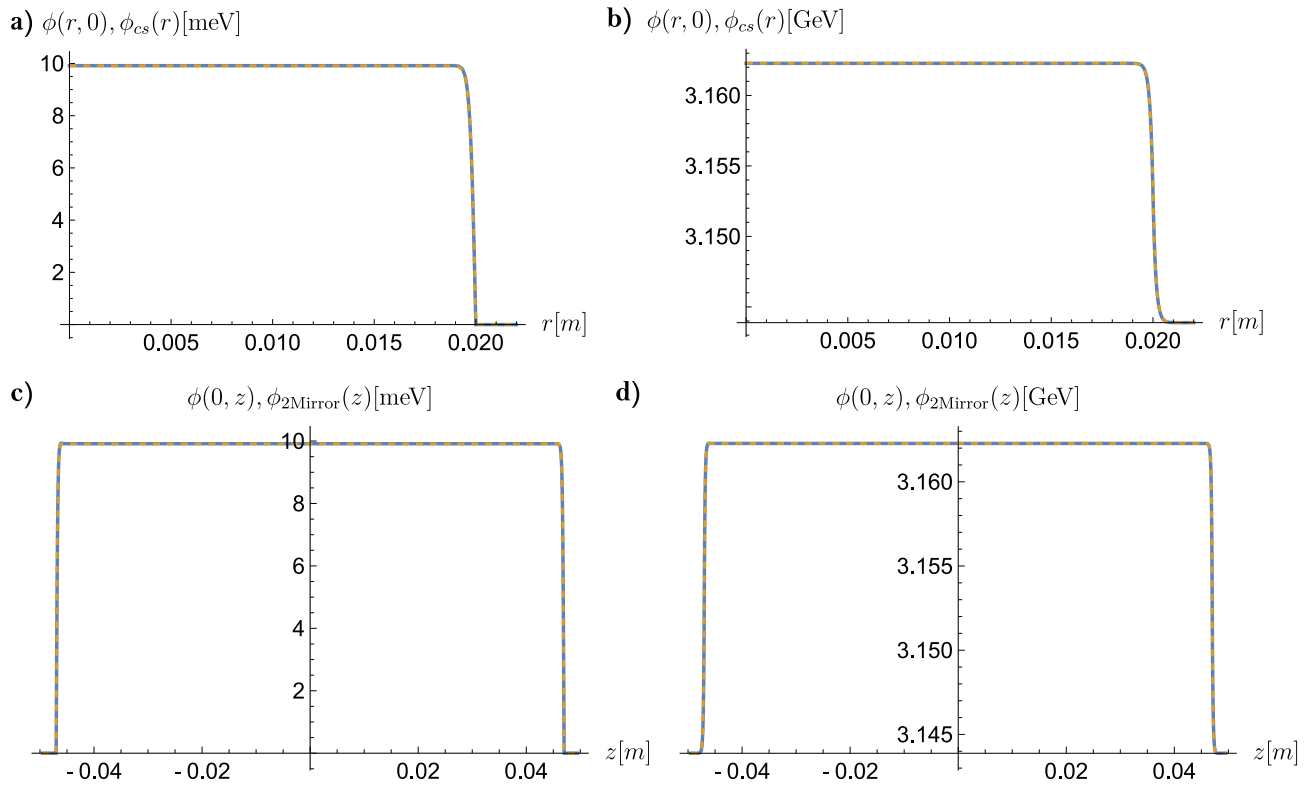

Fig. 4.5.11: This is a comparison between the simulation of the full cylinder at $z = 0$ (blue) and the cross sectional simulation of an infinitely long (Fig. **a)** and **b)**), or the two-mirror simulation (Fig. **c)** and **d)**) using the FDM (dashed orange). The parameters for comparison are as follows: **a)** $\mu = 1$ meV, $M = 10^{-1}$ GeV, and $\lambda_S = 10^{-2}$. **b)** $\mu = 1$ meV, $M = 10^{4.5}$ GeV, and $\lambda_S = 10^{-25}$. **c)** $\mu = 1$ meV, $M = 10^{-1}$ GeV, and $\lambda_S = 10^{-2}$. **d)** $\mu = 1$ meV, $M = 10^{4.5}$ GeV, and $\lambda_S = 10^{-25}$.

Initial guess and non-uniqueness of symmetron field solutions

Developing an appropriate initial guess for symmetron field simulations presents a challenge not encountered with the dilaton field, because the static equations of motion typically lack a unique solution. Examining the differential equation

$$\frac{\partial^2}{\partial r^2}\phi(r,z) + \frac{1}{r}\frac{\partial}{\partial r}\phi(r,z) + \frac{\partial^2}{\partial z^2}\phi(r,z) - \left(\frac{\rho}{M^2} - \mu^2\right)\phi(r,z) - \lambda\phi^3(r,z) = 0, \tag{4.5.149}$$

reveals that when the symmetron is in its symmetric phase within the cylinder shell, the potential minimum is $\phi_M = 0$. In such cases, the trivial solution $\phi(r,z) = 0$ satisfies the boundary conditions. However, as depicted in Fig. 4.5.10, non-trivial solutions complying with the same boundary conditions also exist. Moreover, it's evident that if ϕ is a solution of Eq. (4.5.149), then $-\phi$ is also a solution. In their study, Ref. [61] demonstrated that in the two mirror geometry, there can generally exist multiple static solutions with an increasing number of local extrema (nodes), all adhering to the boundary conditions.

In the subsequent discussion, three non-trivial solutions for identical symmetron parameters are deliniated, elucidating the method employed for their computation.

First solution:
The most straightforward solution entails the determination of a solution manifesting only one node. The qualitative behavior of this solution approximates the linearization of the differential equation around its potential minimum:

$$\left[\frac{1}{r}\frac{\partial}{\partial r}\left(r\frac{\partial}{\partial r}\right)+\frac{\partial^2}{\partial z^2}\right]\phi(r,z)=V_{\text{eff},\phi\phi}\big(\phi_\rho(r,z)\big)\big(\phi(r,z)-\phi_\rho(r,z)\big). \tag{4.5.150}$$

Here, $\phi_\rho(\vec{x})$ is defined as the positive potential minimum of ϕ assuming a density $\rho(\vec{x})$:

$$V_{\text{eff},\phi}\big(\phi_\rho(\vec{x}),\rho(\vec{x})\big)=0. \tag{4.5.151}$$

Therefore, to compute the actual symmetron solution with one node, one can initially solve Eq. (4.5.150) and utilize the solution as an initial guess for Newton's method. This approach typically converges to the desired solution, as illustrated in Fig. 4.5.12.

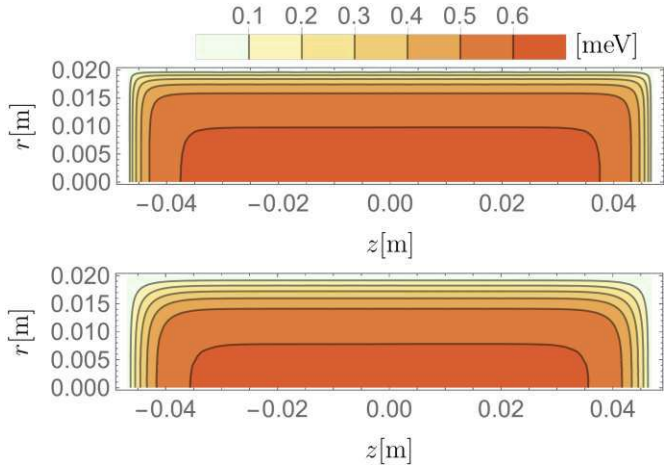

Fig. 4.5.12: The figure shows a symmetron simulation for the parameters $\mu = 6.1\times10^{-5}$ eV, $\lambda_S = 10^{-2}$ and $M = 10^3$ GeV. The top solution denotes the intitial guess that was used for Netwon's method, the bottom solution is the converged symmetron solution.

Second solution:
Securing a solution with two nodes typically involves some trial and error, as a reliable converging seed is not readily found. In the exemplification provided in Fig. 4.5.13, a step function was employed that is close to the positive VEV for negative z values ($\phi = 0.7\ \phi_V$), and close to the negative VEV for positive z values ($\phi = -0.7\ \phi_V$), while maintaining 0 within the shell.

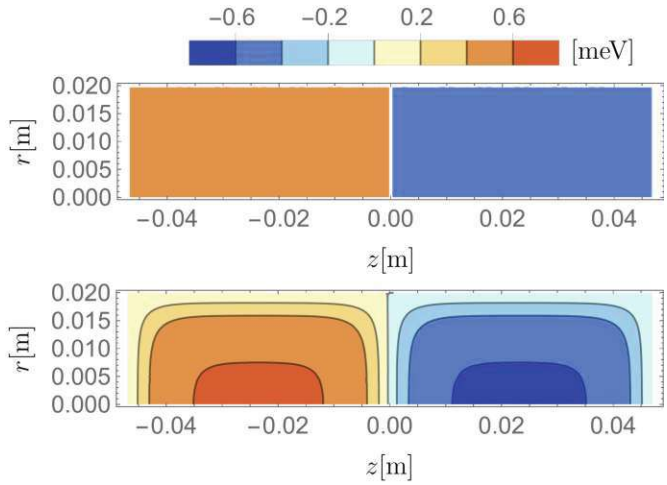

Fig. 4.5.13: The figure shows a symmetron simulation for the parameters $\mu = 6.1\times10^{-5}$ eV, $\lambda_S = 10^{-2}$ and $M = 10^3$ GeV. The top solution denotes the intitial guess that was used for Netwon's method, the bottom solution is the converged symmetron solution.

Third solution:
A third solution was identified via the following procedure: Initially, a multiple node solution was sought for an infinitely long cylinder by solving

$$\frac{\partial^2}{\partial r^2}\phi(r) + \frac{1}{r}\frac{\partial}{\partial r}\phi(r) - \left(\frac{\rho}{M^2} - \mu^2\right)\phi(r) - \lambda\phi^3(r) = 0, \tag{4.5.152}$$

utilizing a similar one-dimensional step function as employed for the second solution. Through trial and error, it was found that extending this equation to non-physical negative r and imposing the boundary conditions $\phi(r) = \phi_M$ for large and small r facilitated the convergence to a non-trivial solution. The solution for this step, alongside the initial guess, is depicted in Fig. 4.5.14.

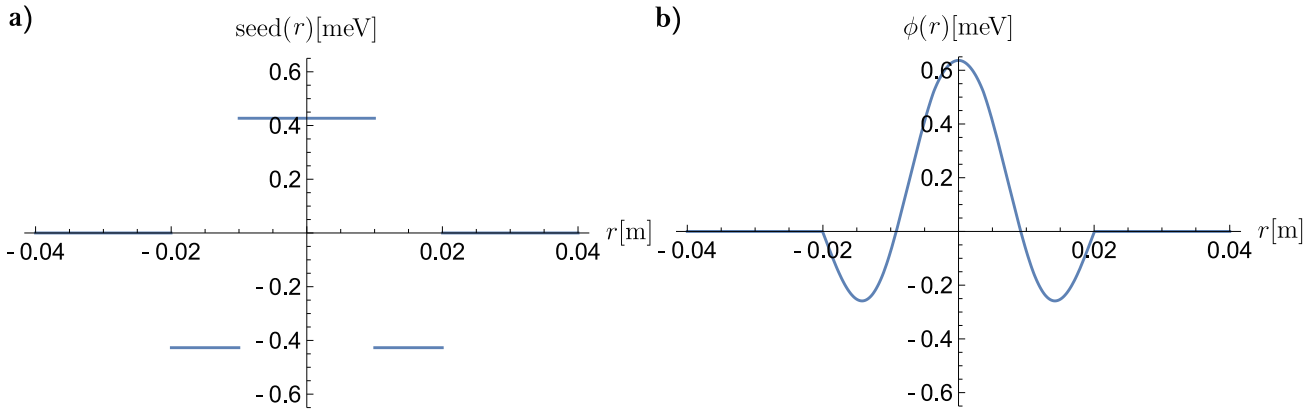

Fig. 4.5.14: The figure shows a symmetron simulation for the cross section of a cylinder for the parameters $\mu = 6.1 \times 10^{-5}$ eV, $\lambda_S = 10^{-2}$ and $M = 10^3$ GeV.
a) denotes the initial guess that was used for Netwon's method, and **b)** the converged symmetron solution.

Subsequently, the multiple node solution $\phi(r)$ for the cross section was utilized to formulate the following initial guess for the entire cylinder:

$$\text{Seed}(r,z) := \begin{cases} \phi(r)\big(L-2|z|\big), & (r<d)\wedge(|z|<\frac{L}{2}) \\ 0, & \text{else.} \end{cases} \tag{4.5.153}$$

This initial guess ultimately converged to a third non-trivial symmetron solution, as evidenced in Fig. 4.5.15.

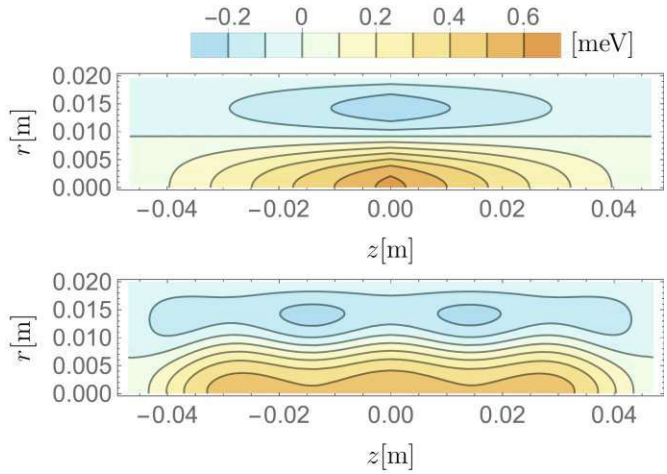

Fig. 4.5.15: The figure shows a symmetron simulation for the parameters $\mu = 6.1\times10^{-5}$ eV, $\lambda_S = 10^{-2}$ and $M = 10^3$ GeV. The top solution denotes the intitial guess that was used for Netwon's method, the bottom solution is the converged symmetron solution.

It's noteworthy that a well-founded initial guess alone does not ensure convergence to a multiple node solution. The same guess may converge or diverge depending on the FEM mesh. The quest to find these solutions entailed an arduous and unsystematic procedure. It took me approximately 1.5 working days to uncover all of the displayed solutions. Without prior knowledge of these solutions, identifying a suitable initial guess that leads to convergence proves challenging, and each simulation typically spans several minutes, rendering the process of experimenting with numerous seeds time-consuming.

A natural inquiry arises regarding the existence of further solutions. While it is plausible that additional solutions exist, the analytical one-dimensional two mirror analysis [61] that prompted the aforementioned search has indicated that higher node solutions only materialize for larger values of μ, wherein the field exhibits greater curvature. Given that the final solution fails to approach its VEV at ±0.61 meV, one can speculate that all multiple node solutions with cylinder symmetry have been exhausted for the given parameters. Since the symmetron does not have to follow the symmetries of the chamber, it is possible that solutions without cylinder symmetry exist, which would require to solve the full three dimensional equation of motion. Nonetheless, as the non-uniqueness of symmetron solutions does not constitute the primary focus of this PhD thesis, this was not explored in detail.

The physical interpretation of the discovered solutions will be elaborated upon in Section 5.5.2.

4.5.5. Remaining limitations

While the nonlinear FEM has shown efficacy in neutron interferometry, its utility in deriving parameter constraints for the CANNEX, qBOUNCE, and LLR experiments is constrained by two

primary factors:

Firstly, the analytical short-range approximation utilized in neutron interferometry, derived in Section 5.2.2, confines cylinder simulations to parameters that correspond to moderate curvature. However, when attempting to simulate fields with extreme curvatures, the necessity for increasingly finer mesh resolutions becomes prohibitive. Mathematica's FEM encounters difficulties with such extreme mesh constructions, often resulting in error messages and an inability to produce solutions.

Secondly, a notable limitation of Mathematica's FEM is its precision, capped at only 16 digits. Although a workaround to address precision issues concerning the dilaton field has been developed, similar challenges persist for the symmetron field, especially with extreme parameters requiring higher precision. In contrast, the FDM code that was developed for the other experiments operates with arbitrary precision, alleviating concerns related to precision.

In essence, neutron interferometry stands as the sole experiment that circumvents the necessity to simulate fields with extreme curvature or parameters due to the short-range approximation that is further discussed in Section 5.2.2.

It's important to note that these limitations stem from the implementation of Mathematica, rather than from the FEM itself. It has been demonstrated that the FDM implementation of the one and two mirror geometry is a special case of the FEM (see Appendix B.5). My FDM (or FEM) code reliably handles extreme meshes and parameters without encountering limitations. However, Mathematica's FEM struggles where my FEM succeeds, highlighting an implementation issue on Mathematica's part. Similarly, I believe that while the FEM is generally more suitable for arbitrary geometries, an implementation tailored to the challenges of screened scalar fields is necessary.

The focus will now shift to the remaining task of solving the stationary Schrödinger equation in the presence of a scalar field.

4.6. Numerical method to solve the one dimensional Schrödinger equation

This Subsection elaborates on the approach employed to solving the stationary Schrödinger equation. This need arises when calculating the energy shifts induced by the scalar field in *q*BOUNCE. As detailed in Section 5.3.3, the aim is to find solutions to:

$$-\frac{1}{2m_n}\frac{d^2\psi_n(z)}{dz^2} + \Big(m_n g z + \mathfrak{Q}_X U_X(z)\Big)\psi_n(z) = E_n\psi_n(z). \tag{4.6.154}$$

Here, $U_X(z) := m_n\Big(A_X\big(\phi(z)\big) - 1\Big)$ represents the scalar field induced potential experienced by a test particle due to the neutron mirror. The factor $\mathfrak{Q}_X$ accounts for the screening of the neutron, m_n is the neutron mass, g denotes the Newtonian gravitational acceleration, and $X \in \{\mathrm{D}, \mathrm{S}, \mathrm{C}\}$ stands for the dilaton, symmetron, and chameleon, respectively. These equations are derived and elaborated upon in Section 5.3.

To solve this equation, boundary conditions for ψ must be specified. The same boundary conditions as those used in prior *q*BOUNCE analyses involving the symmetron and chameleon field [63, 64, 76] are employed, which consistently assumed:

$$\begin{aligned} &\psi(0) = 0, \\ &\psi(z) \to 0, \quad \text{as } z \to \infty. \end{aligned} \tag{4.6.155}$$

The approximations are justified by the experimental observations that Ultra-cold neutrons are confined within the gravitational potential of the Earth and are reflected by the neutron mirror.

It's worth noting that previous derivations of qBOUNCE constraints of the symmetron and chameleon models have exclusively relied on perturbation theory up to the first order [63,64,76]. A subsequent analysis has validated the accuracy of perturbation theory for the chameleon field [79], however, there isn't a comparable investigation for the symmetron field.

Contrary to this, my investigations in this work have revealed that deriving constraints from perturbation theory is inaccurate for both the dilaton and symmetron fields, while confirming its accuracy for the chameleon field. This examination is detailed in Appendix B.6.

For this reason, the aim is to solve Eq. (4.6.154) numerically, enabling a comprehensive non-perturbative treatment. Two analytical approaches are briefly reviewed in Sections 4.6.1-4.6.2, which are only applicable to specific parameters. These methods will serve as benchmarks for the more general numerical treatment in Section 4.6.3.

4.6.1. Energy shifts from perturbation theory

The application of perturbation theory serves as an initial estimate for scalar field-induced energy shifts. The first-order contribution of scalar fields to the resonance frequency shift, as described by perturbation theory, is expressed as (see e.g. [115]):

$$\delta E_{pq} = \mathfrak{Q}_X \int_{-\infty}^{\infty} dz U_X(z) \left(|\psi_p^{(0)}(z)|^2 - |\psi_q^{(0)}(z)|^2 \right). \tag{4.6.156}$$

Here, $\psi_p^{(0)}$ represents the p'th eigenstate in the unperturbed scenario, with its formulas outlined in Eq. (5.3.228). Heuristically, one expects perturbation theory to be applicable if [6]

$$\mathrm{pert}(n) := \left| \frac{E_n - E_n^{(0)}}{E_n^{(0)}} \right| \ll 1, \tag{4.6.157}$$

for the n value under consideration. This allows to compare a numerical solution of the Schrödinger equation to perturbation theory as long as $\mathrm{pert}(n) \ll 1$, for $n \in \{1, 3, 4\}$, which corresponds to the experimentally investigated energy states.

4.6.2. Energy shifts from effective g

If the scalar field exhibits long-range behavior, it can be Taylor expanded across the extent of the wave function:

$$U_X(z) = U_X(0) + \frac{dU_X}{dz}(0) z + \frac{d^2U_X}{dz^2}(0) \frac{z^2}{2} + \mathcal{O}(z^3). \tag{4.6.158}$$

[6] This is not a precise condition for the validity of perturbation theory. A rigorous treatement is found in [115], for instance. However, the focus of this thesis does not lie in an exhaustive exploration of perturbation theory; rather, focuses on a numerical solution of the Schrödinger equation. I have observed that this simplified condition serves as a reliable indicator for perturbation theory's alignment with non-perturbative numerical methods, especially after redefining scalar field potentials via the transformation $U_X(z) \to U_X(z) - U_X(0)$. Such a redefinition, permissible due to the inherent ambiguity in the definition of potentials by an additive constant, ensures that both the scalar field and the mgz term equate to 0 at $z = 0$, facilitating meaningful comparison.

To neglect nonlinear terms, the following condition is imposed:

$$\left| \frac{\frac{d^2U_X}{dz^2}(0)\frac{z^2}{2}}{\frac{dU_X}{dz}(0)z} \right| < 0.1. \tag{4.6.159}$$

This implies

$$\Rightarrow |z| < 0.2 \left| \frac{\frac{dU_X}{dz}(0)}{\frac{d^2U_X}{dz^2}(0)} \right| =: z_{\max}. \tag{4.6.160}$$

If $z_{\max}$ effectively exceeds the wave function's extent, the Schrödinger equation in the presence of the scalar field can be simplified to:

$$-\frac{1}{2m_n}\frac{d^2\psi_n(z)}{dz^2} + m_n g_{\text{eff}} z \psi_n(z) = E_n \psi_n(z), \tag{4.6.161}$$

where g_{eff} is defined as:

$$g_{\text{eff}} := g + \frac{\mathfrak{Q}_X}{m_n}\frac{dU_X}{dz}(0). \tag{4.6.162}$$

Consequently, the Schrödinger equation assumes a form identical to the unperturbed Newtonian case, with the substitution $g \to g_{\text{eff}}$. Exact solutions for wave functions and energies can be computed straightforwardly by replacing $g \to g_{\text{eff}}$ in the analytical Newtonian solutions provided in Eq. (5.3.228). The extent of the first and fourth energy states is consistently smaller than $\sim 10\ \tilde{z}_0$, where $\tilde{z}_0$ corresponds to z_0 in Eq. (5.3.228). Hence, after the substitution $g \to g_{\text{eff}}$, ensuring

$$z_{\max} > 10\ \tilde{z}_0 \tag{4.6.163}$$

guarantees the accuracy of this approach.

Within this approach, only the potential and its first two derivatives need to be known at $z = 0$. These expressions are functions of the field and its first two derivatives at $z = 0$, and they can be computed analytically. The derivation of these values naturally emerges from the formulation of the pressure formula in the CANNEX experiment, as detailed in Section 5.4.2 and can hence be found in this Section.

This method allows for testing numerical algorithms in the non-perturbative regime.

4.6.3. Numerical solution of the Schrödinger equation

To precisely compute energy shifts across a range of parameters, employing a numerical approach becomes essential. The task involves solving the stationary Schrödinger equation to determine the eigenvalues and eigenstates of the Hamiltonian. In order to devise a numerical algorithm, the Hamiltonian is initially discretized into an $N \times N$ matrix, which is then numerically diagonalized.

I have adopted a methodology outlined in Ref. [116], which utilizes the same non-uniform FDM I employed for scalar field simulations. This approach permits arbitrary discretization of the simulation interval. Here's an elucidation of the method:

Initially, the simulation interval [0, cutoff] is discretized into $z_0 = 0, ..., z_{N+1} =$ cutoff. The cutoff must be sufficiently large to ensure the wave functions naturally decay sufficiently to 0 before reaching the cutoff. Thus, the discretized stationary Schrödinger equation takes the form:

$$-\frac{1}{2m_n}\Big(\frac{2(\psi_{i+1}-\psi_i)}{h_i(h_i+h_{i-1})}-\frac{2(\psi_i-\psi_{i-1})}{h_{i-1}(h_i+h_{i-1})}\Big)+V_i\psi_i=E\psi_i, \tag{4.6.164}$$

where $V_i = \mathfrak{Q}_X U_X(z_i) + m_n g z_i$. This yields the discrete Hamiltonian matrix, A, given by:

$$A_{ij}=\begin{cases}-\frac{1}{2m_n}\frac{2}{h_i(h_i+h_{i-1})} & \text{, if } j=i+1\\ -\frac{1}{2m_n}\frac{2}{h_{i-1}(h_i+h_{i-1})} & \text{, if } j=i-1,\\ \frac{1}{2m_n}\big(\frac{2}{h_i(h_i+h_{i-1})}+\frac{2}{h_{i-1}(h_i+h_{i-1})}\big)+V_i & \text{, if } j=i,\\ 0 & \text{, else .}\end{cases} \tag{4.6.165}$$

Boundary conditions ($\phi_0 = \phi_{N+1} = 0$) need to be handled similarly to the scalar field equations of motion described in Appendix B.4.1. The matrix A is tridiagonal, but only symmetric on a uniform grid due to:

$$\begin{aligned}A_{i+1,i}&=-\frac{1}{2m_n}\frac{2}{h_i(h_{i+1}+h_i)},\\ A_{i,i+1}&=-\frac{1}{2m_n}\frac{2}{h_i(h_i+h_{i-1})}.\end{aligned} \tag{4.6.166}$$

To restore symmetry, A is recast as:

$$A_{ij}=\begin{cases}-\frac{1}{2m}\frac{1}{h_i}\frac{1}{L_i^2} & \text{, if } j=i+1\\ -\frac{1}{2m}\frac{1}{h_{i-1}}\frac{1}{L_i^2} & \text{, if } j=i-1,\\ \frac{1}{2m_n}\big(\frac{2}{h_i(h_i+h_{i-1})}+\frac{2}{h_{i-1}(h_i+h_{i-1})}\big)+V_i & \text{, if } j=i,\\ 0 & \text{, else .}\end{cases} \tag{4.6.167}$$

where

$$L_i^2 := \frac{h_i+h_{i-1}}{2}. \tag{4.6.168}$$

M is defined as the diagonal matrix with L_i^2 on the diagonal, and B as:

$$\begin{aligned}B&=MA, \text{or}\\ B_{ij}&=L_i^2 A_{ij}.\end{aligned} \tag{4.6.169}$$

Since A is tridiagonal and M is diagonal, B is also tridiagonal and symmetric. This transformation allows to convert the discrete eigenvalue problem:

$$A\psi = E\psi, \tag{4.6.170}$$

where $\psi = (\psi_1, ..., \psi_N)$, into a symmetric problem. M is expressed as $M = LL$, where L is a diagonal matrix with L_i on the diagonal. For an eigenvector of A with eigenvalue E, one obtains:

$$B\psi = MA\psi = EM\psi = ELL\psi. \tag{4.6.171}$$

Multiplying with L^{-1} from the left and defining $\Phi = L\psi$ yields:

$$L^{-1}BL^{-1}L\psi = L^{-1}BL^{-1}\Phi = E\Phi, \tag{4.6.172}$$

or

$$H\Phi = E\Phi, \tag{4.6.173}$$

where $H = L^{-1}BL^{-1}$. Since B is symmetric and L is diagonal, H is also symmetric ($H^T = L^{-1,T}B^TL^{-1,T} = L^{-1}BL^{-1} = H$).

Hence, H is diagonalized to obtain the eigenvectors for A as:

$$\psi = L^{-1}\Phi, \tag{4.6.174}$$

which represents the discrete energy state approximation of the Hamiltonian.

Mathematica's eigensystem function was used to compute all eigenvectors and eigenvalues and sort them by magnitude. This allows for an easy extraction of the desired eigenenergy and eigenstate.

A cutoff was applied, typically at 100 μm, to ensure accurate computation of unperturbed wave functions. However, a smaller cutoff is used if the scalar field compresses the wave function into a smaller region. Due to significant differences in the shapes of wave functions and scalar fields, using the same mesh for solving the stationary Schrödinger equation as for scalar field simulations is generally unsuitable. Therefore, the following strategy was adopted to discretize the stationary Schrödinger equation:

In scenarios where the scalar field induces weak perturbations, a single uniform grid capable of resolving Newtonian energy states suffices. Conversely, in cases of extreme perturbations, a single uniform grid that captures the initial slope of the scalar field is adequate. For intermediate scenarios, two uniform grids can be merged: one with a very small step-size and small extent to capture the initial slope of the scalar field, and another with a larger step-size and a larger extent to capture the Newtonian potential. This approach consistently yields excellent results.

4.6.4. Code tests for solving the stationary Schrödinger equation

To ensure algorithmic precision, a series of tests were conducted.

Initially, the ability to recover the analytically known eigenenergies and eigenstates of the Newtonian problem was verified. Defining $\Delta E_{pk} := E_p - E_k$, comparisons were focused on the experimentally measured quantities ΔE_{13} and ΔE_{14}. The comparison between the exact solutions and the code output is presented in Fig. 4.6.1.

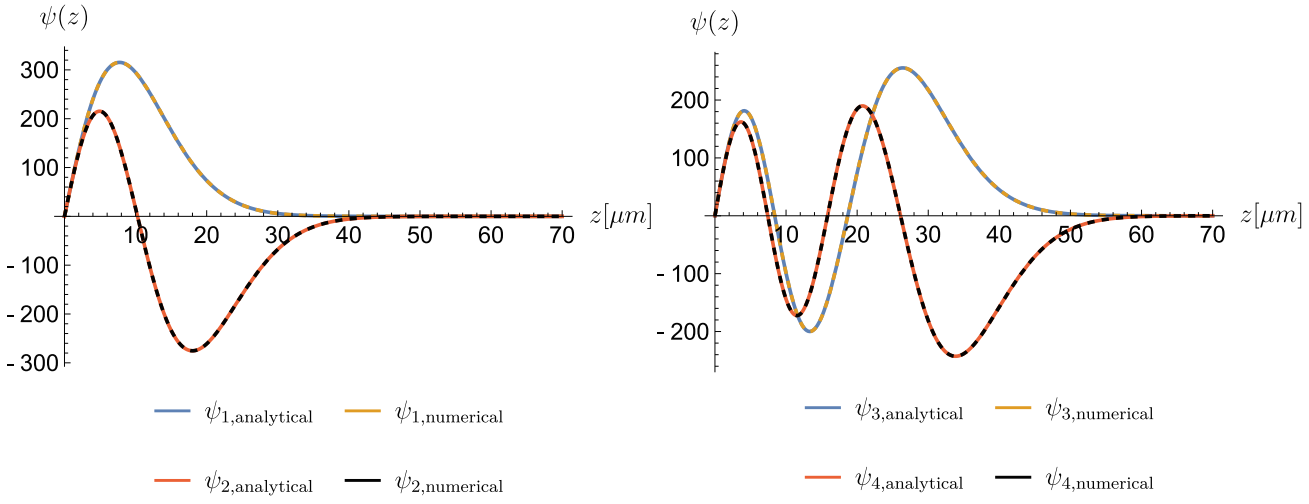

Fig. 4.6.1: The figure shows a comparison between the numerical algorithm and the exact solution, for the first four energy states in the absence of any scalar field. For the energy differences one finds: $|(\Delta E_{13,\text{analytical}} - \Delta E_{13,\text{numerical}})/\Delta E_{13,\text{analytical}}| = 1.5 \times 10^{-4}$, $|(\Delta E_{14,\text{analytical}} - \Delta E_{14,\text{numerical}})/\Delta E_{14,\text{analytical}}| = 1.8 \times 10^{-4}$, for a uniform mesh with cut-off 100 μm and 500 points.

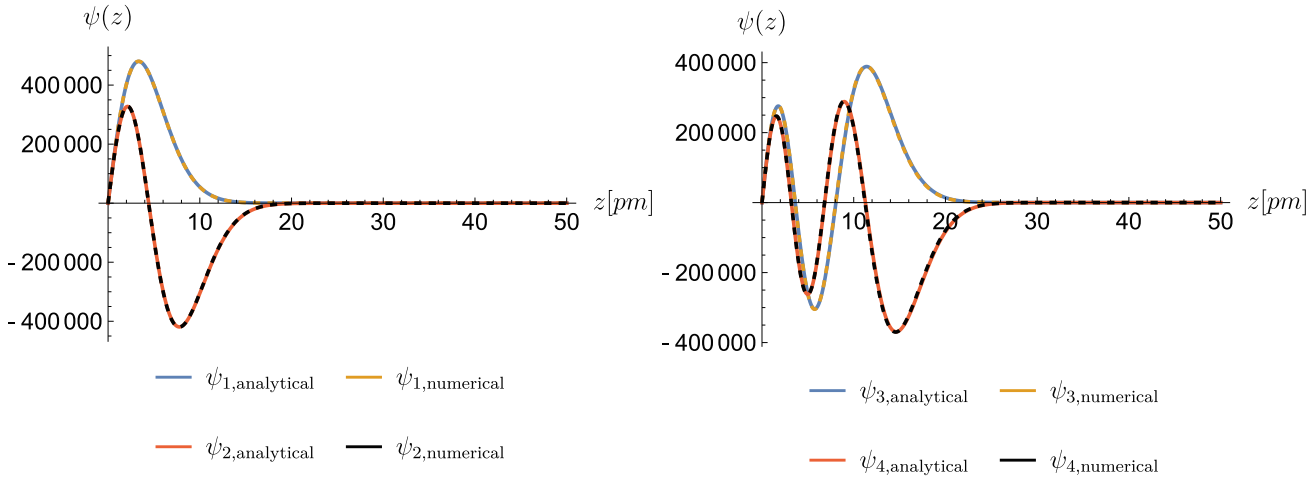

Fig. 4.6.2: The diagram depicts the results obtained from a numerical algorithm directly derived from a simulation of the potential of a dilaton field, utilizing specific parameters: $V_0 = 10$ MeV^4, $A_2 = 10^{40}$, and $\lambda = 10^{23}$. Under these parameter settings, the dilaton field yields an effective g value of 2.7×10^{-10} MeV $(= 1.23 \times 10^{20} \frac{\text{m}}{\text{s}})$, as long as $z < z_{\text{max}} = 1.5 \times 10^{-10}$m. This threshold surpasses the range of the perturbed wave function, thereby rendering the effective g approach valid. A comparison is made with the exact solution corresponding to $g_{\text{eff}} = 2.7 \times 10^{-10}$ MeV. In terms of energy differences, the following comparisons are observed: $|(\Delta E_{13,\text{analytical}} - \Delta E_{13,\text{numerical}})/\Delta E_{13,\text{analytical}}| = 5.1 \times 10^{-3}$, $|(\Delta E_{14,\text{analytical}} - \Delta E_{14,\text{numerical}})/\Delta E_{14,\text{analytical}}| = 6.2 \times 10^{-3}$, for a uniform mesh with cut-off 50 pm and 500 points.

Subsequently, the performance of the code in accurately reproducing solutions of the Schrödinger equation in the presence of a dilaton field was evaluated. This assessment was carried out within parameter ranges where the effective g approach, grounded on known exact solutions, remains valid. Despite being confined to a narrow segment of the parameter space characterized by intense perturbations, the numerical algorithm exhibited remarkable accuracy, even under extreme conditions, as illustrated in Fig. 4.6.2.

In the concluding examination, the algorithm's performance within domains characterized by slight perturbations induced by the dilaton field was analyzed, with perturbations of $\text{pert}(n) \lesssim 0.1$ for $n = 1, ..., 4$ as outlined in Eq. (4.6.157). In this context, a close correspondence with results derived from perturbation theory was anticipated. Below, a tabulated comparison across diverse parameters is presented, revealing a notable concurrence between the numerical algorithm and perturbation theory within the perturbative regime.

$\log_{10}[\lambda]$	$\log_{10}[A_2]$	$\log_{10}[\frac{V_0}{\text{MeV}^4}]$	$\lvert\frac{\Delta E_{13,\text{analytical}}-\Delta E_{13,\text{numerical}}}{\Delta E_{13,\text{analytical}}}\rvert$	$\lvert\frac{\Delta E_{14,\text{analytical}}-\Delta E_{14,\text{numerical}}}{\Delta E_{14,\text{analytical}}}\rvert$	pert(4)
31.3	41	1	1.8×10^{-4}	1.5×10^{-4}	0.02
30.5	36	1	1.4×10^{-4}	1.7×10^{-4}	0.04
30.5	20	10^{18}	1.6×10^{-4}	1.3×10^{-4}	0.08
31	24	10^{18}	1.8×10^{-4}	1.5×10^{-4}	0.03

Table 4: This is a comparison of the energies obtained from perturbation theory (subscript analytical) and the numerical algorithm.

These tests collectively affirm the reliability and adaptability of the numerical algorithm across a diverse array of scenarios and parameter ranges.

The next Section introduces the experiments investigated in this thesis and elucidates the theoretical framework for computing the impacts of scalar fields within the said experiments. The results are then combined with the numerical methods to enable the derivation of parameter constraints for the models under consideration.

5. Theoretical methods and derivation of parameter constraints

This Section aims to introduces the experiments considered in this thesis and to establish the theoretical framework necessary for deriving parameter constraints for screened scalar fields within these experiments.

Subsections 5.1-5.4 present the investigated experiments along with the necessary theoretical background to derive parameter constraints. Subsection 5.5 explains the process by which theoretical and numerical findings, coupled with the actual measurement results of the experiments, are used to derive of parameter constraints for the dilaton, symmetron, and chameleon models.

The combined constraints of all models and experiments are provided and discussed in Section 6.

5.1. Lunar Laser Ranging

5.1.1. Summary of the experiment

Lunar Laser Ranging (LLR) stands as a precise method for determining the Earth-Moon distance. This technique involves directing a laser beam towards a retroreflector array positioned on the lunar surface, a legacy of the Apollo missions. The retroreflectors comprise an arrangement of small mirrors that reflect the laser beam back towards Earth [86, 87]. By measuring the time it takes for the laser pulse to travel to the Moon and return, the distance between the Earth and the Moon can be determined with a high level of accuracy, reaching down to a few centimeters. This data has been instrumental in achieving a highly precise measurement of the Moon's orbit, enabling rigorous testing of GR and imposing stringent constraints on alternative theories. Presently, the collected data aligns with the predictions of GR. This alignment suggests that if scalar fields with a non-minimal coupling to matter exist, they must exhibit a screening mechanism to remain consistent with the observed results from LLR.

LLR has previously been employed to constrain the parameter space of chameleon and symmetron fields [117–119], yet the dilaton field has not been similarly investigated. Here, the focus shifts to the particular aspects of LLR that will be employed to derive experimental constraints.

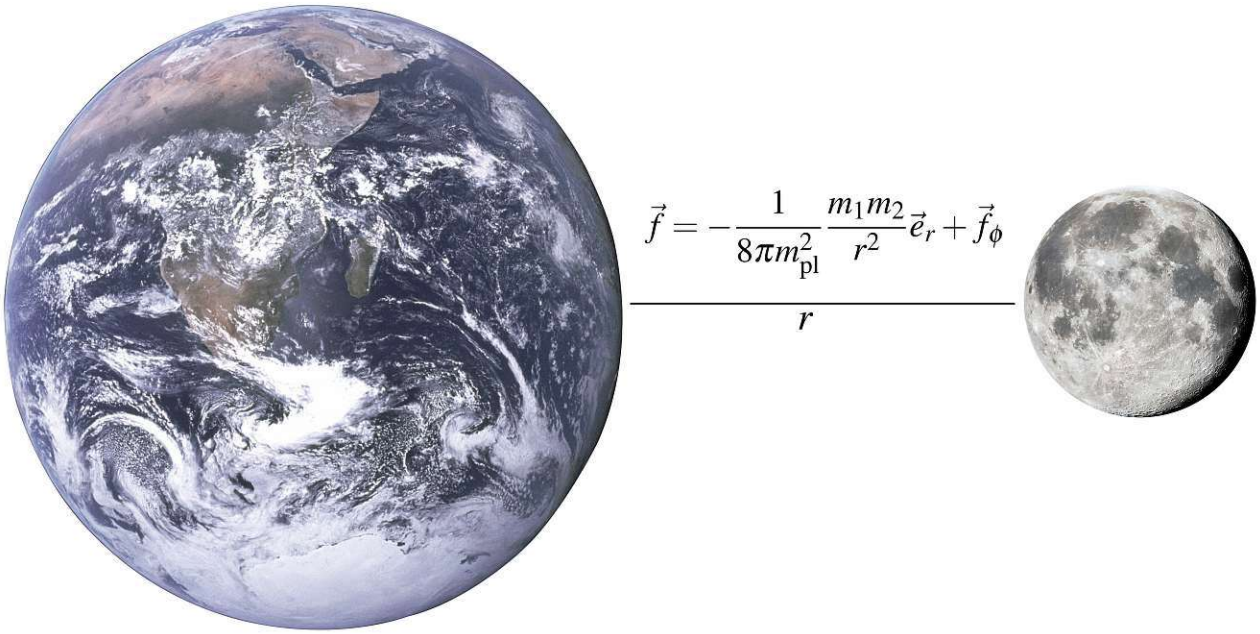

Fig. 5.1.1: Sketch of LLR

5.1.2. Violations of the strong equivalence principle - The Nordtvedt effect

In Newtonian physics, the inertial mass m_I of an object is defined by the Newtonian force law:

$$m_I \vec{a} = \vec{F}, \tag{5.1.175}$$

while the gravitational mass m_G is defined by how the object responds to a gravitational force:

$$\vec{F}_1 = -\frac{1}{8\pi m_{\rm pl}^2}\frac{m_{G,1} m_{G,2}}{r^2}\vec{e}_r, \tag{5.1.176}$$

where

$$\vec{e}_r = \frac{\vec{r}_1 - \vec{r}_2}{\left|\vec{r}_1 - \vec{r}_2\right|}. \tag{5.1.177}$$

If $m_I = m_G$, the acceleration of a point particle is independent of its mass:

$$\vec{a} = -\frac{1}{8\pi m_{\rm pl}^2}\frac{m_{G,2}}{r^2}\vec{e}_r, \tag{5.1.178}$$

where $m_{G,2}$ is the point mass causing the force. As known from special relativity, any form of energy also contributes to the mass of the object via $m = E$. The following discussion for the different types of equivalent principles follows references [41,120]. The equivalent principle comes in two forms:

The weak equivalence principle (WEP) The WEP states that $m_I = m_G$, taking all energy contributions from the strong and electro-weak force into account. The WEP can be tested in laboratory settings, and measurements of the differential accelerations result in the constraint [121]

$$\frac{\Delta a}{a} = 2\frac{a_1 - a_2}{a_1 + a_2} = 2\frac{\left[\frac{m_G}{m_I}\right]_1 - \left[\frac{m_G}{m_I}\right]_2}{\left[\frac{m_G}{m_I}\right]_1 + \left[\frac{m_G}{m_I}\right]_2} = (0.3 \pm 1.8) \times 10^{-13}, \tag{5.1.179}$$

where a uniform gravitational field has been assumed such that $\vec{a}_i = \left[\frac{m_G}{m_I}\right]_i \vec{g} = a_i \frac{\vec{g}}{|\vec{g}|}$.

The strong equivalence principle (SEP) states that $m_I = m_G$ even taking into account objects with considerably gravitational self-energy. The ratio of the gravitational to inertial masses can be parameterized by the Nordtvedt parameter η:

$$\left[\frac{m_G}{m_I}\right] = 1 + \eta\frac{U}{m}, \tag{5.1.180}$$

where U is the gravitational self-energy of the body, and m the mass corresponding to its mass-energy, given by:

$$U = \frac{1}{8\pi m_{\text{pl}}^2}\frac{1}{2}\int \frac{\rho(\vec{x})\rho(\vec{x}')}{|\vec{x} - \vec{x}'|} d^3x d^3x', \tag{5.1.181}$$
$$m = \int \rho(\vec{x}) d^3x,$$

with the bodies energy density ρ. In GR $\eta = 0$ [41, 87, 120]. To test the SEP, objects with a considerable gravitational self-energy are required. LLR tests the SEP by measuring the differential acceleration of the Earth and Moon towards the sun. For the Earth (♁) and Moon (☾) one finds [87]:

$$\left(\frac{U}{m}\right)_{♁} = -4.64 \times 10^{-10},$$
$$\left(\frac{U}{m}\right)_{☾} = -1.90 \times 10^{-11}, \tag{5.1.182}$$

which is a large enough fraction of the total energy content to test the SEP.

The Nordtvedt effect
In Ref. [122, 123] it was shown that a difference between the Earth's and Moon's acceleration towards the sun:

$$\delta\vec{a} := \delta\vec{a}_{☾} - \delta\vec{a}_{♁}, \tag{5.1.183}$$

would change the shape of the orbit of the Moon around the Earth, where $\delta\vec{a} = 0$ in GR. Here, $\delta\vec{a}_{☾}$ and $\delta\vec{a}_{♁}$ refer to a scalar field contribution, assuming the SEP holds. The change of the Earth-Moon distance $\delta r(t)$ is approximately given by [93, 123]:

$$\delta r(t) \simeq \delta a \frac{1 + 2\frac{\omega_0}{\Omega_f}}{\omega_0^2 - \Omega_f^2}\cos(\Omega_f t), \tag{5.1.184}$$

with the Moon's orbital frequency ω_0, $\Omega_f := \omega_0 - \omega_S$, and the sun's frequency ω_S. Since LLR measures $r(t)$, it can be be used to constrain deviations from the SEP [41]. In Section 5.1.5, δa is computed in the presence of a dilaton field, which can be used to constrain the dilaton's parameters.

5.1.3. Violations of the inverse square law

LLR serves as a valuable tool to investigate potential deviations from the gravitational inverse square law. Any Earth-induced force on the Moon deviating from an inverse square law would manifest itself as a precession of the lunar perigee—the point closest to Earth in the Moon's orbit. Isaac Newton calculated this precession in Propositions XLIII-XLV of [124] as is further detailed in [93, 125]:

$$\frac{\delta\Omega_f}{\Omega_f} \simeq -\frac{8\pi m_{\mathrm{pl}}^2 R_{\mathrm{EM}}^2}{M_{\text{ð}}}(\delta f(R_{\mathrm{EM}}) + \frac{R_{\mathrm{EM}}}{2}\frac{d\delta f}{dr}(R_{\mathrm{EM}})). \tag{5.1.185}$$

Here, the angle $\varphi(t)$ of the Moon on the unperturbed orbit is given by $\varphi(t) = \Omega_f t$, assuming a circular orbit of the Moon. $\delta f(R_{\mathrm{EM}})$ is the additional acceleration at the maximum Earth-Moon separation R_{EM}, caused by the dilaton field of the Earth with mass $M_{\text{ð}}$, and the induced precession of the orbit is characterized by $\Delta\varphi(t) = \delta\Omega_f t$. A brief calculation reveals that

$$\frac{\delta\Omega_f}{\Omega_f} = 0, \tag{5.1.186}$$

if

$$\delta f(r) \propto \frac{1}{r^2}, \tag{5.1.187}$$

indicating that LLR can effectively probe forces deviating from an inverse square law, such as those caused by a dilaton field. Both tests of LLR necessitate the computation of the dilaton force on a spherical object, a task undertaken in the subsequent Subsection.

5.1.4. The dilaton force between spheres and the thin-shell effect

A consequence of the screening mechanism is the thin-shell effect [53]. Fig. 5.1.2 illustrates an example of the thin-shell effect. A comparison of the outer field of a solid sphere with a hollow sphere reveals that the outer fields of both objects are practically identical[7]:

Notably, not all of the mass (or volume) of the solid sphere contributes to its outer field for a screened object; only a thin shell below the surface of the object does. This is because the screening mechanism quickly pushes the dilaton field towards its potential minimum inside the object, and the field remains constant once this minimum is reached.

Hence, the force between two spheres generally cannot be accurately approximated by the force between two point particles, for which the thin-shell effect is never present. The next step involves approximately computing the dilaton field of a sphere to quantify the extent to which a sphere's volume contributes to its outer field.

[7] To be more precise, this statement depends on the parameters of the model. A parameter-dependent quantification of the actual thin-shell effect is necessary, given by the screening charge $\mathfrak{Q}$.

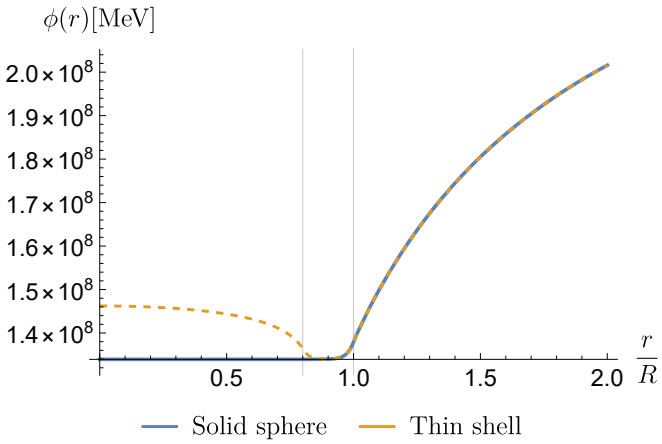

Fig. 5.1.2: This is a comparison of the dilaton field of a hollow sphere with a thin shell indicated by the vertical lines, alongside a solid sphere. The experimental parameters are taken from the Earth, the dilaton parameters are $V_0 = 10$ MeV^4, $\lambda = 10^{15}$ and $A_2 = 10^{10}$. The fields were computed by numerically solving $\frac{d^2\phi}{dr^2} + \frac{2}{r}\frac{d\phi}{dr} = V_{\text{eff},\phi}(\phi;\rho)$, as described in Section 4.

The dilaton field of a sphere and the screening charge

The following derivation follows Refs. [1, 93]. The dilaton field of a sphere is the solution to:

$$\frac{d^2\phi}{dr^2} + \frac{2}{r}\frac{d\phi}{dr} = V_{\text{eff},\phi}(\phi;\rho)\,,$$
$$\rho(r) := \begin{cases} \rho_V & r > R \\ \rho_M & r \leq R. \end{cases} \tag{5.1.188}$$

The boundary conditions are:

$$\phi(r) \to \phi_V, \text{ for } r \to \infty \tag{5.1.189}$$

and

$$\text{and } \frac{d\phi}{dr}|_{r=0} = 0. \tag{5.1.190}$$

Inside the sphere, the field equations pushes ϕ towards its potential minimum ϕ_M, while outside the sphere, the field approaches its asymptotic value ϕ_V. Hence, the effective potential is expanded around these values. To second order, this results in the following approximation:

$$\begin{aligned} \frac{d^2\phi}{dr^2} + \frac{2}{r}\frac{d\phi}{dr} &\simeq V_{\text{eff},\phi\phi}(\phi_M;\rho_M)\,(\phi-\phi_M) = \mu_M^2\,(\phi-\phi_M)\,, && r < R\,, \\ \frac{d^2\phi}{dr^2} + \frac{2}{r}\frac{d\phi}{dr} &\simeq V_{\text{eff},\phi\phi}(\phi_V;\rho_V)\,(\phi-\phi_V) = \mu_V^2\,(\phi-\phi_V)\,, && r \geq R\,. \end{aligned} \tag{5.1.191}$$

Under the transformations:

$$\begin{aligned} \phi - \phi_M &= \frac{\varphi}{r}, \text{ for } r < R, \\ \phi - \phi_V &= \frac{\varphi}{r}, \text{ for } r \geq R \end{aligned} \tag{5.1.192}$$

the equations of motion for the field φ become:

$$\begin{aligned}\frac{d^2\varphi}{dr^2} &= \mu_M^2\varphi, \text{ for } r < R \\ \frac{d^2\varphi}{dr^2} &= \mu_V^2\varphi, \text{ for } r \geq R.\end{aligned} \tag{5.1.193}$$

Using the boundary conditions, one obtains:

$$\begin{aligned}\phi(r) &= \phi_M + \mathfrak{C}_1\frac{\sinh(\mu_M r)}{r}, \text{ for } r < R \\ \phi(r) &= \phi_V + \mathfrak{C}_0\frac{e^{-\mu_V(r-R)}}{r}, \text{ for } r \geq R,\end{aligned} \tag{5.1.194}$$

where $\mathfrak{C}_0$ and $\mathfrak{C}_1$ have to be determined from

$$\begin{aligned}\phi(R_-) &= \phi(R_+) \\ \frac{d\phi}{dr}(R_-) &= \frac{d\phi}{dr}(R_+).\end{aligned} \tag{5.1.195}$$

After some algebraic manipulations one obtains:

$$\begin{aligned}\mathfrak{C}_1 &= \frac{\phi_V - \phi_M}{\cosh(\mu_M R)}\frac{1+\mu_V R}{\mu_M + \mu_V \tanh\,(\mu_M R)}, \\ \mathfrak{C}_0 &= -R\frac{1-\frac{\tanh(\mu_M R)}{\mu_M R}}{1+\frac{\mu_V}{\mu_M}\tanh\,(\mu_M R)}(\phi_V - \phi_M).\end{aligned} \tag{5.1.196}$$

Unlike a Newtonian gravitational potential, $\delta\phi(r) = \phi(r) - \phi_\rho(r)$ does not only fall off with $\frac{1}{r}$ but additionally by either:

$$\sinh(\mu_M r) = \sinh\left(\frac{r}{R_I(\rho_M)}\right), \text{for } r \leq R, \tag{5.1.197}$$

or

$$e^{-\mu_V r} = e^{-\frac{r}{R_I(\rho_V)}}, \text{for } r > R, \tag{5.1.198}$$

where the interaction range of the field is defined by:

$$R_I(\rho) := \frac{1}{\mu_\rho}. \tag{5.1.199}$$

Thus, for a strongly screened sphere, one has $R_I(\rho_M) \ll R$ (the field reaches its minimum closely behind the surface of the sphere) while for an unscreened sphere, one finds $R_I(\rho) \gg R$. Thus $\mathfrak{C}_0$ is expanded in powers of $\mu_M R$. For an unscreened sphere (the lowest order of $\mu_M R$):

$$\mathfrak{C}_0^u = -\frac{\mu_M^2 R^3}{3}(\phi_V - \phi_M). \tag{5.1.200}$$

More generally, defining:

$$\mathfrak{Q} := \frac{\mathfrak{C}_0}{\mathfrak{C}_0^u} = \frac{3}{\mu_M^2 R^3}\frac{1 - \frac{1}{\mu_M R}\tanh(\mu_M R)}{1 + \frac{\mu_V}{\mu_M}\tanh(\mu_M R)}, \tag{5.1.201}$$

as the screening charge, $\mathfrak{Q}$ quantifies the amount of screening of a sphere, with

$$\mathfrak{Q} \to \begin{cases} 0, & \text{for screened bodies with } \mu_M R \to \infty \\ 1, & \text{for unscreened bodies with } \mu_M R \to 0. \end{cases} \tag{5.1.202}$$

An example of the screening charge is shown in Fig. 5.1.3

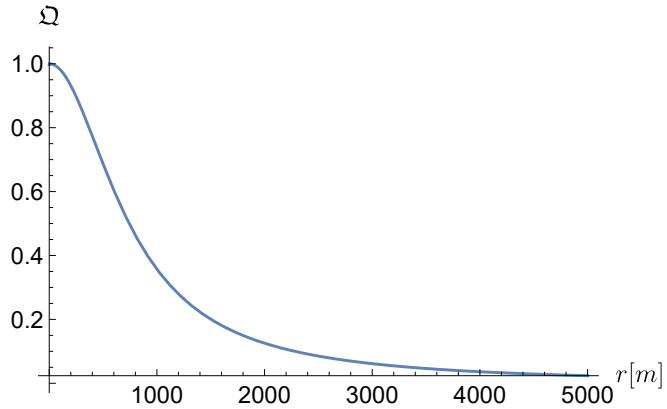

Fig. 5.1.3: The screening charge $\mathfrak{Q}$ is plotted for $A_2 = 10^{15}$, $\lambda = 10^{15}$ and $V_0 = 10$ MeV^4, with $\rho_V = 7.21 \times 10^{-29}$ MeV^4 and $\rho_M = 2.37 \times 10^{-5}$ MeV^4.

Finally, the solution is given by:

$$\phi(r) = \begin{cases} \phi_M + \frac{\phi_V - \phi_M}{\cosh(\mu_M R)}\frac{1+\mu_V R}{\mu_S + \mu_V \tanh(\mu_M R)}\frac{\sinh(\mu_M r)}{r} & , \text{for } r \le R \\ \phi_V - \mathfrak{Q}\frac{\mu_M^2 R^3}{3}(\phi_V - \phi_M)\frac{e^{-\mu_V(r-R)}}{r} & , \text{for } r \ge R. \end{cases} \tag{5.1.203}$$

For large r the acceleration of a point particle in the outer field of the sphere is derived from $A(\phi) = 1 + \frac{A_2}{2m_{pl}^2}\phi^2$ and (2.2.32):

$$\begin{aligned} \vec{a}_\phi &= -\frac{A_2}{m_{pl}^2}\phi\vec{\nabla}\phi \\ &\simeq -\mathfrak{Q}\frac{A_2}{m_{pl}^2}\frac{\mu_V \mu_M^2 R^3}{3}\phi_V(\phi_V - \phi_M)\frac{e^{-\mu_V(r-R)}}{r}\frac{\vec{r}}{r}, \end{aligned} \tag{5.1.204}$$

once again justifying the definition of the screening charge. Notably, μ_M and ϕ_M do not contain any information about the size of the sphere, only its density, and the radius R in $\frac{e^{-\mu_V(r-R)}}{r}\frac{\vec{r}}{r}$ does

not distinguish between a solid sphere or a thin-shell (it only guarantees that at $r = R$ the field starts being suppressed by the vacuum range of the field). Hence, the entire information about the volume of the sphere is contained in the factor R^3, which is however multiplied by $\mathfrak{Q}$. Hence, $\mathfrak{Q}$ quantifies how much of the volume (or mass) of the sphere actually contributes to the acceleration on a point particle far away from the sphere.

5.1.5. Hypothetical dilaton induced effects in Lunar Laser Ranging

Taking the thin-shell effect into account, the force on a sphere with screening charge $\tilde{\mathfrak{Q}}$ and mass M in an external dilaton field ϕ is approximated by

$$\vec{f}_\phi \simeq -\beta(\phi)\tilde{\mathfrak{Q}}\frac{M}{m_{\rm pl}}\vec{\nabla}\phi \tag{5.1.205}$$

where

$$\beta(\phi) = A_2\frac{\phi}{m_{\rm pl}}. \tag{5.1.206}$$

The dilaton-induced violation of the equivalence principle is hence given by

$$\delta_{\rm em} \simeq -\frac{A_2}{2m_{\rm pl}^2|\vec{a}_G|}\left(\mathfrak{Q}_{\sun} - \mathfrak{Q}_{\leftmoon}\right)\frac{d\phi^2(r)}{dr}\bigg|_{r=1\,\rm AU}, \tag{5.1.207}$$

where $\phi(r)$ is the dilaton field of the Sun and $\vec{a}_G$ the Newtonian acceleration towards the Sun. Likewise, the centripetal acceleration experienced by the Moon due to the dilaton field of the Earth is approximated as

$$\delta f(r) \simeq \frac{A_2}{2m_{\rm pl}^2}\,\mathfrak{Q}_{\leftmoon}\,\frac{d\phi^2(r)}{dr}\,. \tag{5.1.208}$$

5.2. Neutron interferometry

5.2.1. Summary of the experiment

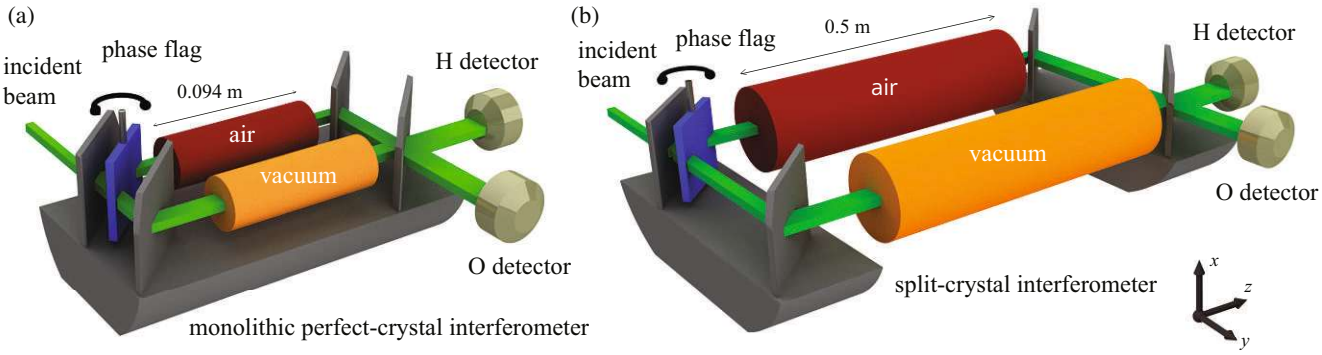

Fig. 5.2.1: Illustrative diagrams of neutron interferometric configurations (not drawn to scale) are presented for probing different prominent dark energy models. The setups involve vacuum and air chambers designed in a cylinder format. **(a)** Depicts a monolithic interferometer similar to the one utilized in [66], while **(b)** illustrates a suggested split-crystal interferometer arrangement with an extended interaction region and increased beam separation, facilitating the use of larger cylinder diameters. Figure published in [3] and provided by Stephan Sponar.

In a neutron interferometer, illustrated in Fig. 5.2.1, a neutron beam undergoes interference [126, 127]. A beam splitter, utilizing Bragg diffraction on a silicon crystal, divides the neutron wave function into two paths, enabling self-interference for each neutron.

The precise alignment of beam splitters, requiring nanoradian precision, often necessitates constructing interferometers from a single crystal, as depicted in Fig. 5.2.1 (a). Introducing chambers into either path, represented as cylinders in Fig. 5.2.1, can introduce a phase difference affecting the count rate of H and O detectors (Fig. 5.2.1, O measures the forward direction and H the refracted direction). Specifically, inserting identical chambers into both paths, one vacuum and one filled with air, would induce a relative phase difference due to the reduced suppression of screened scalar fields in vacuum regions.

In Refs. [79, 128], it has been argued that neutrons are particularly sensitive to screened scalar fields. This sensitivity arises from their lack of experiencing a thin-shell effect due to the relatively large extent of the neutron wave function, making neutron interferometry an effective tool to probe scalar fields.

However, as neutrons are quantum objects and scalar fields are treated classically, a fully consistent treatment is currently unavailable, necessitating further theoretical work. One semi-classical approach suggested in Refs. [129, 130] assumes that the neutron can be treated as a particle with density $\rho(\vec{x}) := m_n|\psi(\vec{x})|^2$, with the neutron's wave function denoted as $\psi(\vec{x})$. For a wave function extending over several millimeters, the neutron's density would be so low that screening effects are expected to be negligible.

However, an alternative semi-classical approach treats the neutron as an object with a well-defined size of about 1 fm, consistent with QCD. Both approaches have been pursued in [63, 64], and it is unclear which is more accurate. In the latter approach, the neutron might still be screened due to its high density, despite its small extent. Nevertheless, an independent motivation for neutron interferometry lies in the fact that neutrons lack electrical charge and have minimal polarizability, rendering them highly insensitive to experimental background disturbances and

making them valuable tools to search for new physics [131,132]. This makes neutron experiments an interesting way to probe screened scalar fields. Following these theoretical motivations, a neutron interferometer was realized in Ref. [66] and used to constrain parts of the parameter space of the chameleon field.

Remarkably, a recent proof-of-principle demonstration in Ref. [133] showcases a split-crystal interferometer built from two crystals (Fig. 5.2.1 (b)). This innovation allows for the insertion of longer chambers into either path, enhancing the interaction time of neutrons with hypothetical scalar fields and consequently increasing the interferometer's sensitivity.

In both configurations, the incident neutron beam, characterized by a mean wavelength of $\lambda_n = 2.72$ Å, with a relative wavelength spread of $\delta\lambda_n/\lambda_n \sim 0.043$ is divided and traverses either an air or vacuum chamber. Following recombination at the final interferometer plate, detectors with an efficiency exceeding 99 percent measure the intensity in the outgoing beams.

The original goal of this research project was for the experimental physicists to replicate the existing experiment in [66] with an improved experimental setup and to extend the theoretical and numerical analysis to a larger part of the chameleon parameter space, as well as the symmetron and dilaton field. Unfortunately, due to time constraints, this analysis relies on the already published experiment [66] and only extends the constraints derived in this reference to other models. Additionally, the analysis here also considers the screening of the neutron, which was neglected in [66]. Moreover, the investigation involves exploring the potential increase in sensitivity achievable through a split-crystal interferometer and computing prospective parameter constraints on an experiment currently in assembly. In the next Subsection, the necessary theoretical framework is derived to compute the phase shift induced by a scalar field in a neutron interferometer.

5.2.2. Scalar field induced phase shifts

The cylinder mantle of the chambers would suppress a scalar field, as shown in Fig. 5.2.2 .

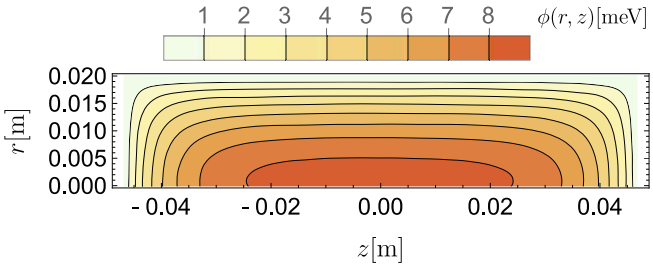

Fig. 5.2.2: Simulated dilaton field for $V_0 = 10$ MeV^4, $A_2 = 10^{37}$ and $\lambda = 10^{-9}$ with $\rho_V = 7.08 \times 10^{-17}$ MeV^4. Figure published in [3].

This scalar field can be computed by solving its static equation of motion:

$$\left[\frac{1}{r}\frac{\partial}{\partial r}\left(r\frac{\partial}{\partial r}\right) + \frac{\partial^2}{\partial z^2}\right]\phi(r,z) = V_{\text{eff},\phi}(\phi;\rho)\,, \tag{5.2.209}$$

as elaborated on in Section 4.5

The presence of a scalar field would induce a phase shift. The formula for this phase shift is derived below. The following derivation is an adaption of [134] (see also [93]) to screened scalar

fields. The starting point is the free Schrödinger equation governing neutrons:

$$\begin{aligned} H_0\phi_0 &= -\frac{1}{2m_n}\,\Delta\phi_0 \\ &= E_0\phi_0\,, \end{aligned} \tag{5.2.210}$$

where $\phi_0 \propto e^{i\vec{k}\cdot\vec{x}}$. Introducing the Ansatz $\phi = \phi_0\chi$ and $E = E_0$ the full Schrödinger equation is given by:

$$\big(H_0 + U\big)\phi = E\phi\,. \tag{5.2.211}$$

A straightforward calculation shows:

$$\phi_0\Delta\chi + 2i\phi_0\vec{k}_0\cdot\vec{\nabla}\chi = 2m_nU\phi_0\chi\,. \tag{5.2.212}$$

In the semi-classical limit ($|\vec{\nabla}\chi| \ll k_0|\chi|$), the first term is negligible. Defining $k_0 := |\vec{k}_0| = 2\pi/\lambda$ and a length parameter s along the direction of $\vec{k}_0$, where $\vec{k}_0\cdot\vec{\nabla} = k_0\,\frac{d}{ds}$ and

$$\chi = e^{-i\frac{m_n}{k_0}\int ds\,U}\,, \tag{5.2.213}$$

results in the phase shift:

$$\delta\varphi = -\frac{m_n}{k_0}\int ds\,U\,. \tag{5.2.214}$$

For neutrons propagating through a cylindrical cavity of length L along the symmetry z-axis at constant radius r_c the phase shift is given by:

$$\delta\varphi = -\frac{m_n}{k_0}\int_{-L/2}^{L/2} dz\,U(r_c,z)\,. \tag{5.2.215}$$

Next, the conditions for the validity of the semi-classical limit are derived. From

$$\vec{\nabla}\chi = -i\frac{m_n}{k_0}\,U(r_c,z)\,\chi\,\vec{e}_z\,, \tag{5.2.216}$$

and considering $|\chi| = 1$, it follows:

$$|\vec{\nabla}\chi| = \frac{m_n}{k_0}\,|U(r_c,z)|\,. \tag{5.2.217}$$

Thus, the condition for the validity of the semiclassical limit is:

$$\frac{|\vec{\nabla}\chi|}{k_0} = \frac{m_n}{k_0^2}\,|U(r_c,z)| \ll 1\,. \tag{5.2.218}$$

Finally, the derivation assumes $U = 0$ outside both chambers, i.e. in air. Nevertheless, scalar fields in air generally exhibit a non-zero value. However, for parameter values allowing constraints, the field ranges in air are small compared to the dimensions of the experimental setup. Consequently, the field can be approximated as nearly constant outside the chambers, maintaining its air expectation value. To adhere to the assumption that $U = 0$ outside the chambers, the potentials for the dilaton (D), symmetron (S), and chameleon (C) are established as follows [8]:

$$U_X(\vec{x}) = m_n\big[A_X\big(\phi(\vec{x})\big) - A_X\big(\phi_{\text{Air}}\big)\big], \tag{5.2.219}$$

where $X \in \{\mathrm{D}, \mathrm{S}, \mathrm{C}\}$.

The provided potentials hold true under the condition that the neutron can be treated as a test particle within a scalar field background, rather than serving as the source of the field. This assumption becomes applicable when the screening of the neutron can be disregarded. To incorporate the screening effect, the above potentials are multiplied with a screening charge,

$$U_X(\vec{x}) \to \mathfrak{Q}_X U_X(\vec{x})\,, \tag{5.2.220}$$

hence, the criteria determining the applicability of the semiclassical limit can be expressed as follows:

$$\mathfrak{Q}_X \frac{m_n^2}{k_0^2}\big[A_X\big(\phi(\vec{x})\big) - A_X\big(\phi_{\mathrm{Air}}\big)\big] \ll 1. \tag{5.2.221}$$

Since screening charges are only applicable for classical spheres, the neutron is treated as such. For the dilaton, the screening charge derived in Section 5.1.4 was utilized, while for the symmetron and chameleon fields, the definitions provided in [3, 61, 62] were employed.

For extremely short scalar field ranges, accurately resolving the slopes of scalar fields poses numerical challenges. However, in such scenarios, the following approximation is employed:

$$\int_{-L/2}^{L/2} dz\big[A_X\big(\phi(0,z)\big) - A_X\big(\phi_{\mathrm{Air}}\big)\big] \simeq L\big[A_X\big(\phi_V\big) - A_X\big(\phi_{\mathrm{Air}}\big)\big] \tag{5.2.222}$$

which allows defining

$$\begin{aligned}
\delta_{\mathrm{sim}} &:= -\mathfrak{Q}_X \frac{m_n^2}{k_0} \int_{-L/2}^{L/2} dz\big[A_X\big(\phi(0,z)\big) - A_X\big(\phi_{\mathrm{Air}}\big)\big], \\
\delta_{\mathrm{approx}} &:= -\mathfrak{Q}_X \frac{m_n^2}{k_0} L\big[A_X\big(\phi_V\big) - A_X\big(\phi_{\mathrm{Air}}\big)\big].
\end{aligned} \tag{5.2.223}$$

Here, δ_{sim} represents the actual phase shift computed from a simulation for a neutron propagating through the chamber's center ($r = 0$), while δ_{approx} denotes an approximation valid solely for extremely short-ranged fields. For the dilaton field, small interaction ranges correspond to large values of A_2. Fig. 5.2.3 demonstrates that the error in the approximation diminishes continuously for larger A_2 values, and the field increasingly adopts its VEV over a broader region inside the cylinder.

[8] The potentials are obtained from the force on a test particle $\vec{f}_\phi(\vec{x}) \simeq -m_n \vec{\nabla} A_X\big(\phi(\vec{x})\big) = -\vec{\nabla} U_X(\vec{x})$, which implies $U_X(\vec{x}) = m_n A_X\big(\phi(\vec{x})\big) + \text{constant}$.

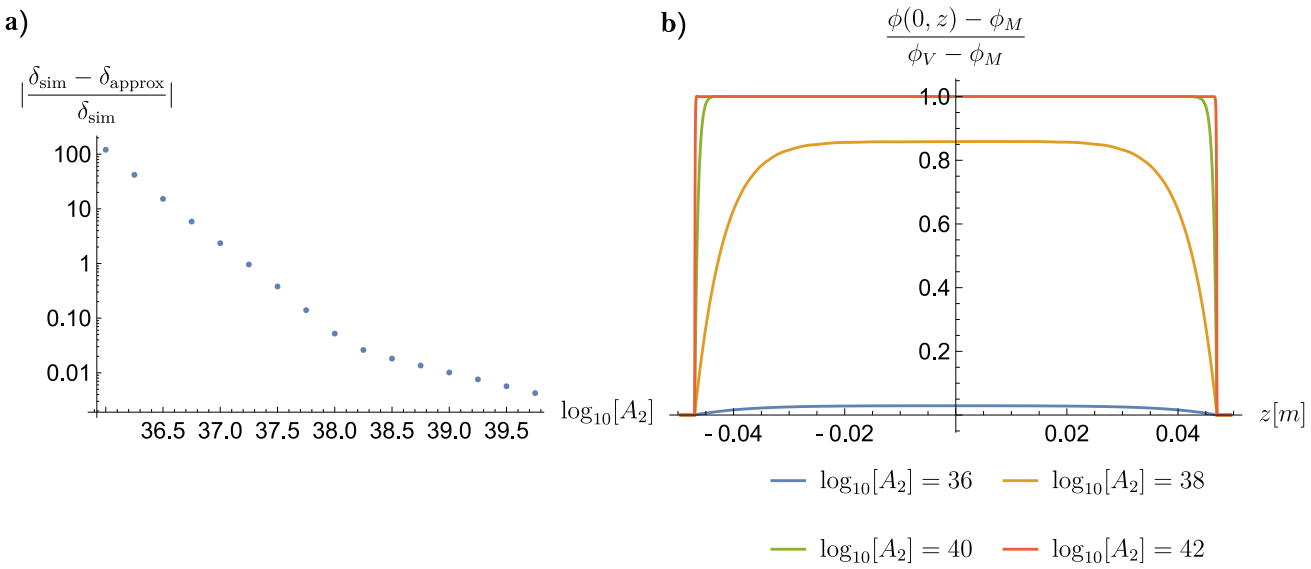

Fig. 5.2.3: The calculations assumed $\lambda = 10^{-9}$ and $V_0 = 10$ MeV^4. **a)** illustrates the relative error of the approximation with respect to A_2 and **b)** the normalized field profiles along the z axis for $r = 0$. Here, the value 1 represents $\phi(0, z) = \phi_V$, while 0 corresponds to $\phi(0, z) = \phi_M$. The steep slopes are observed at the chamber walls. Figure published in [3].

The next Subsection provides a brief explanation on neutron screening.

5.2.3. The fermi and micron screening approximation

In the existing analysis of the symmetron field within the *q*BOUNCE experiment, which is also a neutron experiment, two screening approximations were compared: fermi and micron screening [63,64]. The fermi screening approximation treats the neutron as a classical sphere with a radius of 0.5 fm, inspired by QCD, while the micron screening approximation considers the neutron as a sphere with a radius of 5.9 μm. The latter is motivated by the well-defined analytical length scale $z_0 = 5.9$ μm in *q*BOUNCE, determining the wave function's vertical extent (see Section 5.3). This approximation stems from interpreting the neutron's density as $\rho(\vec{x}) = m_n|\psi(\vec{x})|^2$.

In this thesis, the focus is exclusively on the fermi screening approximation for both experiments. The rationale for the neutron interferometry experiment is provided below:

Firstly, in neutron interferometry, the wave function is non-spherical, extending a few nm in one direction and a few mm in another [3]. Applying the same approach as in *q*BOUNCE (extracting a sphere's radius from the wave function's z-direction extent) raises the question of which direction to choose. Assuming a radius of 1 mm results in a density that is 18 orders of magnitude lower than assuming 1 nm. Given the intrinsic sensitivity of scalar fields to matter densities, selecting one direction fails to provide a valid order of magnitude estimate for neutron screening. It is more appropriate to acknowledge the inability to estimate the neutron's coupling to the scalar field, assuming it couples to the square modulus of the wave function, given that only the screening charge for spheres is known.

Secondly, fermi screening limits are generally more reliable. Assuming a neutron radius of 0.5 fm results in a much higher density than the density given by the wave function. Therefore, the fermi screening approximation consistently implies a much stronger neutron screening compared

to the micron screening approximation[9] and is hence more conservative.

5.3. qBOUNCE

5.3.1. Summary of the experiment

In qBOUNCE [74–76], ultracold neutrons, exhibiting total reflection from most materials, traverse the gravitational field of the Earth. The analysis presented in this thesis is grounded in the Rabi setup [135], as illustrated in Fig. 5.3.1.

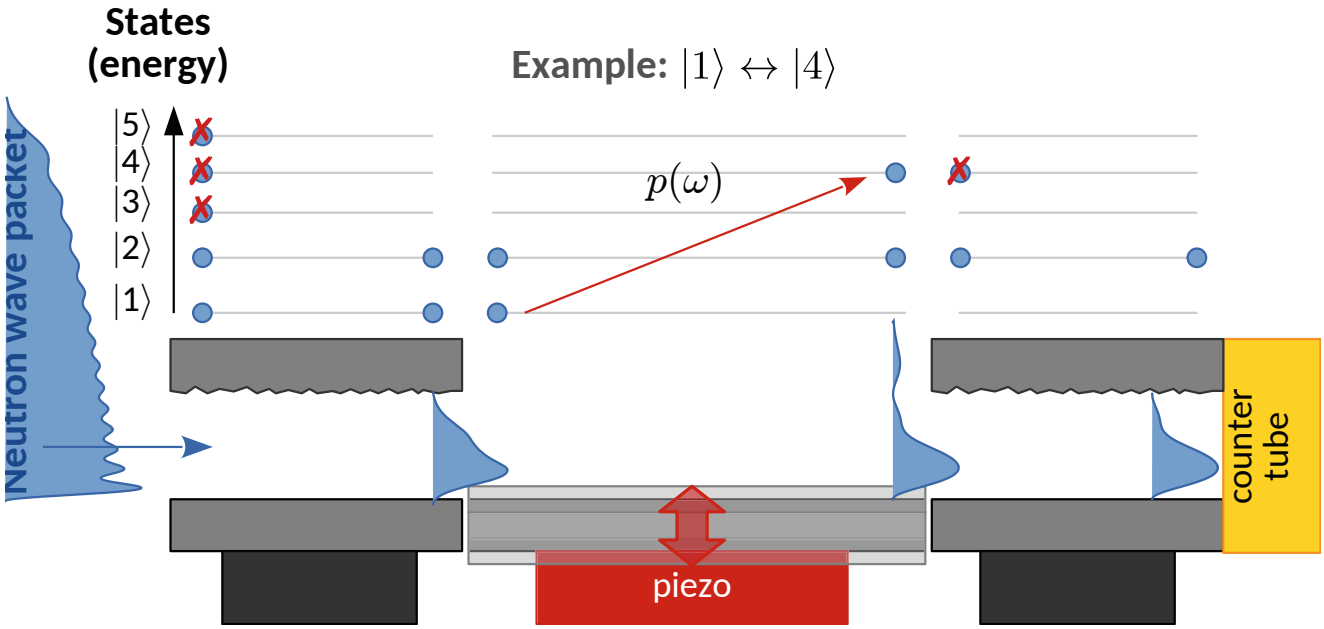

Fig. 5.3.1: Sketch of the qBOUNCE experiment. Figure published in [2] and provided by René Sedmik.

The neutron wave packet encounters three distinct regions:

In the initial region, serving as an effective state selector spanning approximately 15 cm, a polished mirror at the base and a rough scatterer positioned 20 μm above ensure that only neutrons in the lowest states can traverse. Undesired higher energy states are scattered out of the system.

The subsequent region introduces a vibrating mirror with a tunable frequency ω, capable of driving the neutron towards a higher energy state. This region extends for a length of 20 cm.

The final region mirrors the characteristics of the first region. If the energy ω linked to the mirror's frequency closely aligns with the energy difference $\Delta E_n = E_n - E_1$, where E_n refers to the n'th eigenenergy of the neutron, required to transition the neutron to a specific higher energy state, the system enters a coherent superposition of the ground state and the excited state. In instances where the neutron is no longer in one of the lowest ~ 2 states upon entering the last region, a decrease in transmission is observed.

[9] The neutron is assumed to be smaller in the fermi screening approximation. One might wonder if the weaker thin shell effect due to the smaller size can compensate for the much higher density. I have thoroughly examined this and confirmed that for all models under consideration, the effect of the higher density is much larger than the effect of the reduced size. Parameter constraints of the fermi screening approximation are thus always more conservative than micron screening constraints.

The qBOUNCE experiment draws inspiration from Rabi spectroscopy, originally developed to measure nuclear magnetic moments [136]. In Rabi's original work, a homogeneous magnetic field leads to Zeeman splitting[10] [137] of a nucleus with nuclear spin-$\frac{1}{2}$. This splitting defines a frequency $\omega = \Delta E$ associated with the two different energy levels of the system. A second, much weaker, orthogonal magnetic field tuned to this frequency periodically induces transitions between the two states, with a frequency known as the Rabi frequency.

In analogy to Zeeman splitting, qBOUNCE measures different energy levels of ultracold neutrons based on the Earth's gravitational field. The first few eigenenergies are given by

$$\begin{aligned} E_1 &= 1.40672 \text{ peV}, \\ E_2 &= 2.45951 \text{ peV}, \\ E_3 &= 3.32144 \text{ peV}, \\ E_4 &= 4.08321 \text{ peV}. \end{aligned} \tag{5.3.224}$$

Since the gravitational energy levels in qBOUNCE are not equidistant, any two energy states can be treated as an effective two-level system, analogous to a spin-$\frac{1}{2}$ system. The unique transition frequency ω_{pq} between states p and q is given by

$$\omega_{pq} = E_p - E_q. \tag{5.3.225}$$

Similar to the weak magnetic field in Rabi spectroscopy, the oscillating mirror acts as a repulsive potential for the neutrons of ~ 100 neV [138]. Since qBOUNCE is also a neutron experiment, motivations to search for screened scalar fields with qBOUNCE as mentioned for neutron interferometry, also apply. Additionally, qBOUNCE can test Newtonian gravity at the micrometer scale, making it suitable for probing gravity-like interactions at this scale. Consequently, qBOUNCE has already been employed to constrain hypothetical interactions such as the chameleon field, the symmetron field, and axion-like particles [63, 64, 76, 139, 140].

5.3.2. Newtonian theory

In the absence of other forces, the energy eigenstates of neutrons can be obtained by solving the Schrödinger equation within the Earth's gravitational potential. Upon separation into free transversal and bound vertical states, this equation yields [93]

$$\psi_n(\vec{x}, t) = \frac{e^{i(\vec{p}_\perp \cdot \vec{x}_\perp - E_\perp t)}}{2\pi v_\perp} \psi_n(z) e^{-iE_n t}, \tag{5.3.226}$$

and

$$-\frac{1}{2m_n}\frac{d^2\psi_n(z)}{dz^2} + m_n g z \psi_n(z) = E_n \psi_n(z), \tag{5.3.227}$$

where m_n is the neutron's mass, and g the gravitational acceleration. Analytical solutions are provided as follows [78]:

[10] The Zeeman effect occurs when spectral lines split into multiple components in the presence of a stationary magnetic field.

$$\psi_n(z) = \frac{\mathrm{Ai}(\frac{z-z_n}{z_0})}{\sqrt{z_0}\mathrm{Ai}'(-\frac{z_n}{z_0})},$$
$$E_n = \sqrt[3]{\frac{m_n g^2}{2}}\mathrm{Ai}(0,n). \tag{5.3.228}$$

In this context, ψ_n symbolizes the energy state labeled as the n-th state with energy E_n. The parameter $z_0 = 1/\sqrt[3]{2m^2g} = 5.9$ μm defines the extent of the wave functions. Additionally, $z_n = E_n/mg$, and Ai represents the Airy functions (refer to [141]), and $\mathrm{Ai}(0,n)$ denotes the n-th root of the Airy function. Fig. 5.3.2 shows the first few energy states.

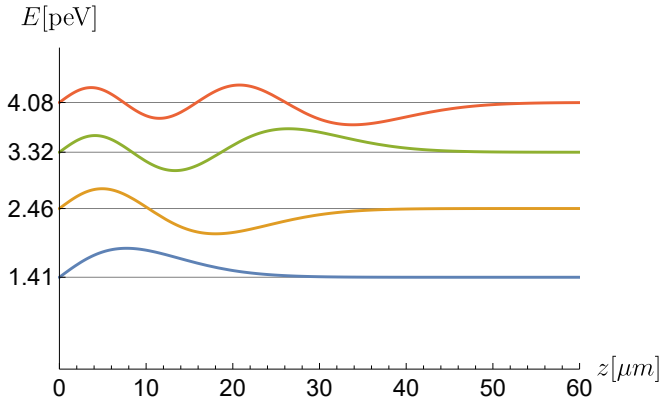

Fig. 5.3.2: The figure depicts the four lowest energy states of neutrons within the gravitational potential of the Earth.

5.3.3. Scalar field induced energy shifts

In addition to Earth's gravitational potential, neutron mirrors would suppress a scalar field, illustrated in Fig. 5.3.3.

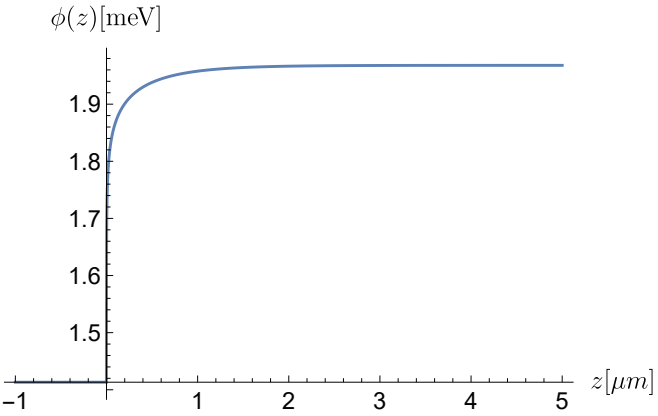

Fig. 5.3.3: The dilaton field above a mirror placed at $z < 0$ is plotted for the parameters $V_0 = 10$ MeV^4, $A_2 = 10^{43}$, $\lambda = 10^{32}$. The mirror density was assumed to be $\rho_M = 1.082 \times 10^{-5}$ MeV^4, the vacuum density is $\rho_V = 10^{-15}$ MeV^4

Treating the mirrors as infinitely extended in the x and y directions, the scalar field is determined by solving:

$$\frac{d^2}{dz^2}\phi(z) = V_{\text{eff},\phi}(\phi;\rho)\,, \tag{5.3.229}$$

for a mirror placed at $z < 0$ with density ρ_M and a vacuum region of density ρ_V above. The boundary conditions are:

$$\begin{aligned} \phi(z) &\to \phi_M, \text{ for } z \to -\infty, \\ \phi(z) &\to \phi_V, \text{ for } z \to +\infty. \end{aligned} \tag{5.3.230}$$

Numerical solutions are obtained as described in Section 4. The scalar field induces an additional potential on a test particle given by[11]

$$U_X(z) := m_n\big[A_X\big(\phi(z)\big) - 1\big], \tag{5.3.231}$$

with $X \in \{\mathrm{D}, \mathrm{S}, \mathrm{C}\}$, for the dilaton, symmetron and chameleon field respectively. Proceeding analogously to neutron interferometry, the screening of the neutron is taken into account by replacing the above definitions with

$$U_X(\vec{x}) \to \mathfrak{Q}_X U_X(\vec{x})\,, \tag{5.3.232}$$

where $\mathfrak{Q}_X$ is the neutron's screening charge. The same definitions of the screening charge as for neutron interferometry are employed.

In this thesis, only the fermi screening approximation is employed, as elaborated in Section 5.2.3. It is noteworthy that, although the shape of the wave function differs between qBOUNCE and neutron interferometry, the precise dimensions in the x and y directions remain uncertain in the context of qBOUNCE. The wave function shape in qBOUNCE significantly deviates from a spherical form. Consequently, the approach presented in [64], which treats the wave function as a sphere in the micron screening approximation, is not adopted. Instead, the micron screening approximation is completely dropped, opting for the more conservative fermi screening approximation.

Hence, in the presence of a scalar field, the eigenfunctions and eigenenergies of the neutron above the mirror satisfy:

$$-\frac{1}{2m_n}\frac{d^2\psi_n(z)}{dz^2} + \big(m_n g z + \mathfrak{Q}_X U_X(z)\big)\psi_n(z) = E_n\psi_n(z). \tag{5.3.233}$$

Since qBOUNCE has an energy resolution of approximately $\Delta E = 2 \times 10^{-15}$ eV it can probe or constrain hypothetical scalar fields. The solution to the stationary Schrödinger equation is described in Section 4.

[11] The derivation is the same as for the neutron interferometry experiment, but the additional constant was chosen differently, which has no physical effect. In neutron interferometry this constant was kept to keep track of the assumption $U_X = 0$ inside air, since this assumption influences the validity conditions for the semi-classical limit.

5.4. CANNEX

5.4.1. Summary of experiment

The Casimir And Non-Newtonian force EXperiment (CANNEX) is currently undergoing reconstruction at the Conrad Observatory in Austria, as detailed in a comprehensive report in Ref. [81]. This experiment has been intricately designed to achieve unparalleled precision in measuring both the Casimir force and potential fifth forces arising from gravity-like interactions, in addition to gravity.

The experimental setup involves two closely situated plane parallel plates with a tunable distance of 3-30 μm. A visual representation is provided in Fig. 5.4.1. As outlined in Ref. [81] (Table 1), CANNEX exhibits a remarkable pressure sensitivity of approximately 0.1 $\frac{\text{pN}}{\text{cm}^2}$, surpassing a sphere-sphere configuration by four orders of magnitude and a sphere-plane configuration by three orders of magnitude. This heightened sensitivity positions CANNEX ideally for probing Casimir forces and fifth forces at small distances.

From its inception, one of the goals of CANNEX was to investigate the chameleon field [80, 82]. The presence of this field (or any other screened scalar field) would result in an additional pressure on the plates. The lower plate is kept fixed, while the upper plate is movable. The experiment is capable of eliciting the distinctive dependence on the matter density of screened scalar fields by adjusting the Xe gas pressure in the chamber between 5.3×10^{-12} kg/m^3 and 2.6 kg/m^3.

The first projective constraints of CANNEX on the chameleon field have already been provided in [82]. Projective constraints from CANNEX on the parameters of the Symmetron field and axion-like particles can be found in [81]. The next Subsection provides a derivation of the pressure induced by a screened scalar field on the upper plate of CANNEX.

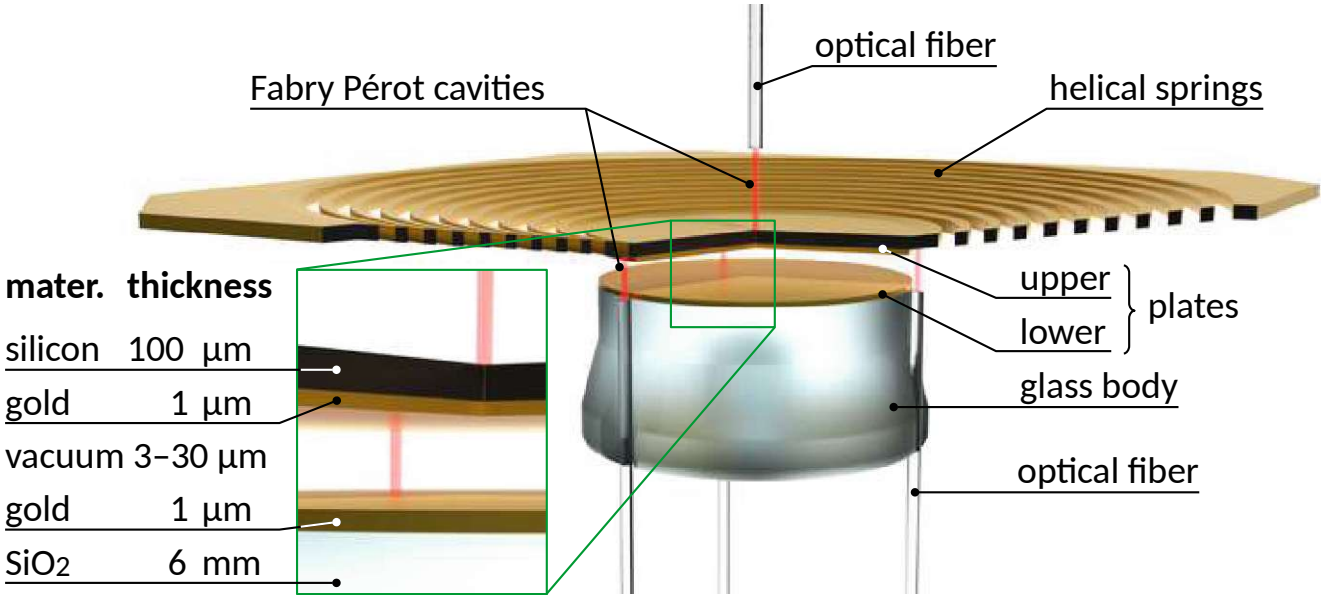

Fig. 5.4.1: A cutaway illustration of the CANNEX setup is provided in the schematic view. Forces within the system are identified through Fabry-Pérot interferometers, which detect the elongation of the mass-spring system formed by helical springs and an upper plate. The inset on the left specifies the material and thickness of different layers. Figure published in [2] and provided by René Sedmik.

5.4.2. Derivation of scalar field induced pressure

In the one-dimensional configuration, the setup can be effectively approximated as a half-space with a density of $\rho_M = 2514\text{kg/m}^3$ for $z \leq -d$, a vacuum region with density ρ_V for $-d < z < d$, an upper plate with a density of ρ_M for $d < z < d + D$, and a vacuum region with density ρ_V for $z > d + D$[12].

The upper plate has a thickness of $D = 100\ \mu$m and is movable, such that $1.5\ \mu\text{m} < d < 15\ \mu$m. If screened scalar fields indeed exist, the mirrors would suppress a scalar field that can be computed by solving

$$\frac{d^2\phi}{dz^2} = V_{\text{eff},\phi}(\phi;\rho)\,, \tag{5.4.234}$$

with boundary conditions

$$\begin{aligned} \phi(z) &\to \phi_M, \text{ for } z \to -\infty, \\ \phi(z) &\to \phi_V, \text{ for } z \to +\infty. \end{aligned} \tag{5.4.235}$$

The formula for the induced scalar field pressure is derived next.

Original formula

Starting with the force on a point particle (2.2.32), the force on the upper plate is:

$$\vec{f}_\phi = -\rho_M \int_{-\infty}^{\infty} dx \int_{-\infty}^{\infty} dy \int_{d}^{d+D} dz \frac{dA(\phi)}{dz} \vec{e}_z. \tag{5.4.236}$$

Consequently, the pressure in the z direction is given by:

$$P = \rho_M \Big[A\Big(\phi(d)\Big) - A\Big(\phi(d+D)\Big) \Big]. \tag{5.4.237}$$

This formula has been used to compute prospective CANNEX symmetron limits in Ref. [81]. The initial intention was to utilize a numerical solution of Eq. (5.4.234) to extract the field values $\phi(d)$ and $\phi(d + D)$ and compute the pressure. However, this approach proved to be unsuitable for general numerical evaluation.

[12] While the actual setup consists of distinct layers with varying densities, the choice of a uniform density for the entire setup simplifies both theoretical and numerical treatments significantly. As demonstrated in Appendix B.2, this approximation proves highly accurate, introducing only negligible errors in calculations. The specific value of ρ_M is derived in Appendix D.

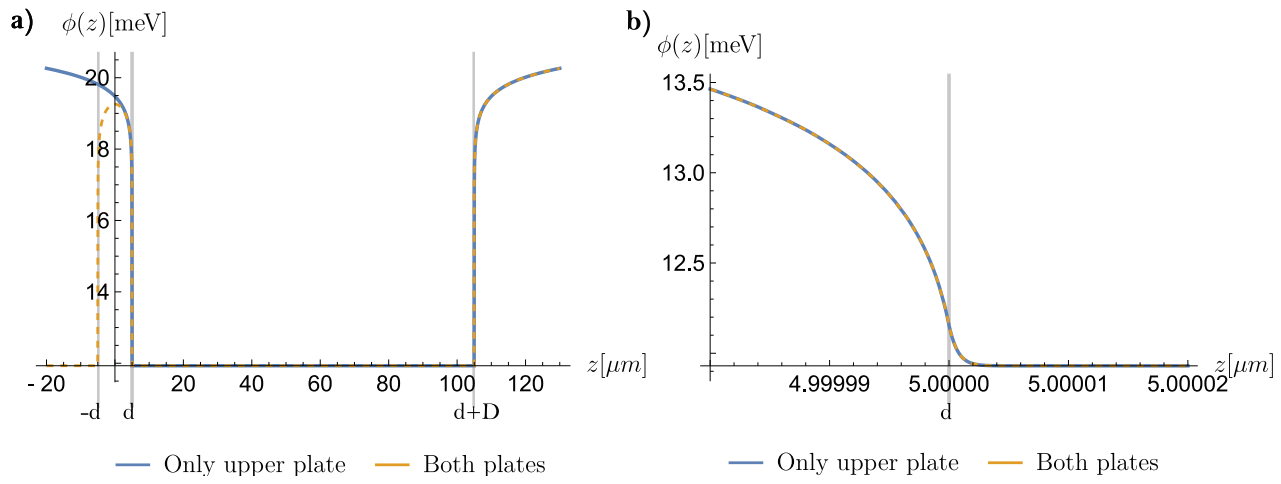

Fig. 5.4.2: **a)** Only the upper plate surrounded by vacuum is simulated and compared to the full CANNEX set up with both plates. **b)** Zooming into the lower surface of the upper mirror demonstrates that both geometries lead to an indistinguishable field close to the mirror surface. The parameters are given by V_0 =10 MeV^4, $\lambda = 10^{31}$, $A_2 = 10^{45}$, and $\rho_V = 2.28 \times 10^{-20}$ MeV^4.

To elucidate the issues encountered, consider Fig. 5.4.2, where a numerical solution of Eq. (5.4.234) is depicted for the specified plate geometries. A comparison is made between the full CANNEX setup with both plates and a simulation involving only the upper plate surrounded by vacuum. Both solutions are indistinguishable above the upper plate, but deviations become visible below the surface of the lower plate (see Fig. 5.4.2 a). Strikingly, very close to the lower surface of the upper mirror (Fig. 5.4.2 b), both solutions are indistinguishable.

This observation implies that, as the solution approaches the surfaces of the upper mirror, it is predominantly influenced by the upper mirror alone, rendering the impact of the lower mirror negligible. Consequently, the values directly at the surfaces of the upper mirror (used as input to (5.4.237)) can be expressed as:

$$\begin{aligned}\phi(d) &= \phi_{\text{one plate}}(d) + \delta_1,\\ \phi(d+D) &= \phi_{\text{one plate}}(d+D) + \delta_2 = \phi_{\text{one plate}}(d) + \delta_2,\end{aligned}$$

where $\phi_{\text{one plate}}(d)$ represents the solution in the presence of only the upper mirror, and due to symmetry, $\phi_{\text{one plate}}(d) = \phi_{\text{one plate}}(d+D)$. Substituting these expressions into Eq. (5.4.237), one obtains:

$$P = \rho_M\big(A(\phi_{\text{one plate}}(d) + \delta_1) - A(\phi_{\text{one plate}}(d) + \delta_2)\big). \tag{5.4.238}$$

The crucial insight here is that the values at the mirror surfaces are predominantly influenced by the upper mirror alone, leading to the conditions:

$$\begin{aligned}\delta_1 &\ll \phi_{\text{one plate}}(d),\\ \delta_2 &\ll \phi_{\text{one plate}}(d).\end{aligned} \tag{5.4.239}$$

Unfortunately, the challenge arises in accurately determining the values of δ_1 and δ_2, which contain all information about the pressure induced by the lower plate. Numerically computing the scalar field results in correct leading digits, but the higher digits are dominated by rounding errors. This poses a serious computational challenge, as extracting accurate values for δ_1 and δ_2 requires an impractical level of precision in solving ϕ, as δ_1 and δ_2 only influence the higher digits of ϕ due to (5.4.239).

In the symmetron analysis conducted in Ref. [81], Mathematica [108] was employed, allowing for arbitrary precision calculations. René Sedmik, the author of the calculations, utilized hundreds of digits in these computations to ensure sufficent precision[13].

This approach was feasible because an analytically exact solution for Eq. (5.4.234) exists for symmetron fields [61, 62]. However, for the dilaton field, no such analytical solution is available, rendering this approach unfeasible. I addressed this challenge by deriving an analytically equivalent and more computationally tractable formula for the pressure, as detailed in the following.

Refined formula

Numerical calculations where based on the formula:

$$P = \frac{\rho_M}{\rho_M - \rho_V} \left(V_{\text{eff}}(\phi_V, \rho_V) - V_{\text{eff}}(\phi_0, \rho_V) \right) . \tag{5.4.240}$$

Here, $\phi_0 = \phi(0)$ represents the scalar field value at the midpoint between the plates, and the effective potential is defined as:

$$V_{\text{eff}}(\phi; \rho) = V(\phi) + \rho\big(A(\phi) - 1\big) . \tag{5.4.241}$$

Due to the screening mechanism, it is assumed that the field reaches its minimum value, denoted as ϕ_M, within the upper mirror with a thickness of D. This assumption holds true across all models and parameter values for which constraints were imposed in this thesis. Consequently, the value of $\phi(d)$ closely aligns with the surface value of a two mirror configuration, where both plates extend infinitely with a vacuum region between them.

Likewise, the value of $\phi(d + D)$ can be obtained from the surface value of a configuration in which one plate extends infinitely, accompanied by an infinitely extended vacuum region above it. Multiplying Eq. (5.4.234) by ϕ' and integrating with respect to z results in:

$$\frac{1}{2}\left(\frac{d\phi}{dz}\right)^2 - \frac{1}{2}\left(\frac{d\phi}{dz}\right)^2 \Bigg|_{z=z_0} = V_{\text{eff}}(\phi; \rho) - V_{\text{eff}}(\phi; \rho)\big|_{z=z_0} . \tag{5.4.242}$$

Considering the one mirror case with boundary conditions $\phi(z) \to \phi_M$ for $z \to -\infty$ and $\phi(z) \to \phi_V$ for $z \to \infty$, in the limit $z \to \infty$ one obtains:

$$-\frac{1}{2}\left(\frac{d\phi}{dz}\right)^2 \Bigg|_{z=z_0} = V_{\text{eff}}(\phi_V; \rho_V) - V_{\text{eff}}(\phi; \rho)\big|_{z=z_0} . \tag{5.4.243}$$

Subtracting Eq. (5.4.243) from Eq. (5.4.242) results in

$$\frac{1}{2}\left(\frac{d\phi}{dz}\right)^2 = V_{\text{eff}}(\phi; \rho_V) - V_{\text{eff}}(\phi_V; \rho_V) . \tag{5.4.244}$$

[13] While not documented in the paper, René Sedmik shared these details in personal conversations.

Inside the mirror, the following relationship holds:

$$\frac{1}{2}\left(\frac{d\phi}{dz}\right)^2 = V_{\text{eff}}(\phi;\rho_M) - V_{\text{eff}}(\phi_M;\rho_M)\,. \tag{5.4.245}$$

The continuity of the derivative at $z = d + D$ implies

$$A\big(\phi(d+D)\big) - 1 = \frac{1}{\rho_M - \rho_V}\left(V_{\text{eff}}(\phi_M;\rho_M) - V_{\text{eff}}(\phi_V;\rho_V)\right)\,. \tag{5.4.246}$$

For the case of two infinitely extended mirrors one can use $d\phi/dz|_{z=0} = 0$ due to the symmetry of the setup and conclude

$$A(\phi(d)) - 1 = \frac{1}{\rho_M - \rho_V}\left(V_{\text{eff}}(\phi_M;\rho_M) - V_{\text{eff}}(\phi_0;\rho_V)\right)\,. \tag{5.4.247}$$

Substituting these equations into Eq. (5.4.237) proves Eq. (5.4.240). In Ref. [68] the formula

$$P \simeq V_{\text{eff}}(\phi_V,\rho_V) - V_{\text{eff}}(\phi_0,\rho_V) \tag{5.4.248}$$

has been derived with a similar derivation, albeit assuming $\rho_V \ll \rho_M$. For the actual vacuum density in CANNEX

$$\frac{\rho_M}{\rho_M - \rho_V} \simeq 1 \tag{5.4.249}$$

and hence the difference between both formulas is negligible. This formula excels in achieving accurate numerical evaluations. Instead of computing $\phi(d)$ and $\phi(d+D)$, which minimally incorporate the influence of the lower mirror, the calculation now focuses on the value ϕ_0, situated between the upper and lower mirrors. As illustrated in Fig. 5.4.2, it becomes apparent that the disparity in scalar fields between the upper mirror alone and both mirrors is substantial and visually discernible. This difference significantly contributes to the leading digits of ϕ and is therefore much more straightforward to compute. Appendix B provides a formal analysis to demonstrate the superiority of this formula.

Finally, it's worth noting that this derivation can be extended to calculate the values $\phi(0)$, $\frac{d\phi}{dz}(0)$, and $\frac{d^2\phi}{dz^2}(0)$ for the one mirror solution scenario applicable to qBOUNCE, where a mirror with density ρ_M is positioned at $z < 0$, and a vacuum region exists at $z > 0$. Taking the dilaton field as an example, Equation (5.4.246) implies:

$$\phi(0) = \sqrt{\frac{2m_{\text{pl}}^2}{A_2(\rho_M - \rho_V)}\Big(V_{\text{eff}}(\phi_M;\rho_M) - V_{\text{eff}}(\phi_V;\rho_V)\Big)}. \tag{5.4.250}$$

Here, the positivity of the dilaton field has been utilized. Similarly, the values of $\frac{d\phi}{dz}(0)$ and $\frac{d^2\phi}{dz^2}(0)$ can be directly derived from equations (5.4.244) and (5.4.234):

$$\begin{aligned}\frac{d\phi}{dz}(0) &= \sqrt{2\Big(V_{\text{eff}}(\phi(0);\rho_V) - V_{\text{eff}}(\phi_V;\rho_V)\Big)},\\ \frac{d^2\phi}{dz^2}(0) &= V_{\text{eff},\phi}(\phi(0),\rho_V).\end{aligned} \tag{5.4.251}$$

These computed values enable the exact determination of energy shifts caused by a scalar field in the parameter region where it acts as effective renormalization of g within the framework of the qBOUNCE experiment. Further elaboration on this topic can be found in Section 4.6.2.

5.5. Derivation of parameter constraints

In this Section, the outcomes from prior Sections are used to establish constraints on the parameters of the chameleon, symmetron, and dilaton models. The methodology involves comparing the theoretical predictions of measured quantities for each model against empirical measurements. Prior derivations of parameter constraints from neutron interferometry [66] and qBOUNCE [63,64] used a statistical technique known as χ^2-analysis.

However, these analyses only considered experimental measurement sensitivities and errors, but did not take theoretical uncertainties into account. Notably, two major sources of theoretical uncertainties include:

1. The fermi screening approximation simplifies the neutron to a classical sphere with a radius of 0.5 fm. However, as detailed in Appendix B.3, this approximation can result in significant discrepancies in the predicted energy shifts in qBOUNCE (or equivalently, the predicted phase shift in neutron interferometry). These discrepancies may diverge by several orders of magnitude from the actual values, leading to substantial errors in the computed constraints.

2. The screening charge employed to characterize neutron screening is heuristic and derived from linearizing spherical equations of motion. However, the accuracy of this approximation remains largely uncertain.

Since not all errors can be quantified, we deemed elaborate statistical analyses assuming negligible theoretical errors to be inappropriate and used simplified constraint criteria that will be explained in more detail in the following Subsections.

It has to be stressed, however, that within these uncertainties, significant progress has been made in enhancing theoretical predictions through numerical and analytical methods in this thesis. Two examples of this progress concerning the qBOUNCE and CANNEX analysis are provided in Sections 6.2.2-6.2.3, by comparing results obtained in this thesis to results that have been published prior to this thesis. Nevertheless, the resulting constraints must be regarded as the current best estimate given the available theoretical and numerical tools, underscoring the necessity for further theoretical advancements.

It is imperative to emphasize that in the CANNEX experiment, the calculations are very accurate. Since computing pressure involves classical calculations devoid of any heuristic screening charge, one can typically compute the pressure accurately to the percent level, rendering a statistical analysis meaningful for this experiment. However, as the experiment is currently under construction, measurement data remains unavailable at this point, and the analysis will hence rely on the expected measurement sensitivity.

In order to validate the theoretical assumptions underlying constraint calculations, several cut-off criteria have been implemented, thereby excluding parameters from the analysis that contravened any of the following conditions:

1. $\frac{\phi}{M_c}, \frac{\phi^2}{2M^2}, \frac{A_2}{2}\frac{\phi^2}{m_{\rm Pl}^2} < 0.1$, indicating that higher-order couplings between the matter density and the scalar field can be neglected. The necessity of this condition has been discussed in Section 3.

2. For qBOUNCE and CANNEX, only parameters for which the interaction range of the field in vacuum is at most 1 mm are considered, to justify the neglect of the influence of the vacuum chamber. Additionally, parameters are excluded for CANNEX for which the scalar field does not fully decay to its minimum ϕ_M inside the upper mirror, to ensure the applicability of Eq. (5.4.240). This latter assumption also ensures that it is feasible to model the mirrors as one dimensional.

3. For neutron interferometry, only parameters for which the interaction range of the field does not exceed 0.25 mm inside the cylinder shell are considered, ensuring that the boundary condition $\phi = \phi_M$ inside the cylinder shell is physically sensible.

Demanding these conditions leads to sharp cuts in the derived constraints. The following Subsection provides a brief summary of how constraints have been derived for each experiment.

5.5.1. Lunar Laser Ranging

In this Section the theoretical results from 5.1 and numerical results from Section 4 are applied to derive parameter constraints of the dilaton model in the context of LLR. The LLR analyis is restricted to the dilaton field, for a LLR analysis in the context of the symmetron or chameleon field see [117–119].

Constraints from equivalence principle violations

The measured value for violations of the equivalence principle is [41]

$$\delta_{\rm em} \simeq \frac{a_{\phi ☿} - a_{\phi ☾}}{a_G} = (-3 \pm 5) \times 10^{-14}\,, \tag{5.5.252}$$

where $a_{\phi ☿}$, $a_{\phi ☾}$ refer to the scalar field induced acceleration of the Earth and Moon towards the sun, whereas a_G is the regular Newtonian acceleration towards the sun. Parameters are constrained for which the scalar field contribution leads to an at least two sigma deviation of the measured value. Parameter constraints are hence placed for

$$\delta_{\rm em} \notin (-1.3 \times 10^{-13}, 7 \times 10^{-14})\,. \tag{5.5.253}$$

The dilaton field of the Sun has been computed by solving the nonlinear differential Eq. (5.1.188). The procedure to compute the constraint volume was analogous for all experiments and screened scalar field models, and is hence only detailed and visualized for the two most complex cases[14], neutron interferometry and qBOUNCE.

Notably, constraints in the small λ region employed the analytical field solution derived in Appendix C, since the dilaton field equations are effectively linear inside this parameter region and the analytical solution - based on a linearization - hence exact. In the large λ region the spherical differential equation was solved numerically. The cutoff for large r was always chosen to ensure that the field naturally relaxes to ϕ_V within the cutoff. The FDM mesh was always checked for its accuracy by ensuring that further refinement marginally influences (5.5.252).

Constraints from violations of the inverse square law

The constraint for violations of the inverse square law is taken from Ref. [142] and is given by:

$$\left|\frac{\delta\Omega_f}{\Omega_f}\right| \simeq \frac{8\pi m_{\rm pl}^2 R_{\rm EM}^2}{M_{☉}} \left|\delta f(R_{\rm EM}) + \frac{R_{\rm EM}}{2}\frac{d\delta f}{dr}(R_{\rm EM})\right| \leq 1.6 \times 10^{-11}, \tag{5.5.254}$$

where $R_{\rm EM}$ denotes the maximum Earth-Moon separation. These constraints largely overlap with those obtained from equivalence violations. For this test, I exclusively utilized the analytically approximate solution but ensured that in parameter space regions where this LLR test constrains parameters not already constrained by equivalence principle violations, the constraints align with predictions from a full numerical simulation of the Earth's field.

[14] Neutron interferometry requires a proper integration of the short-range approximation. qBOUNCE does not only require screened scalar field simulations, but also a numerical solution of the Schrödinger equation.

Calculating $\frac{8\pi m_{\rm pl}^2 R_{\rm EM}^2}{M_{\text{ð}}}\left|\delta f(R_{\rm EM})+\frac{R_{\rm EM}}{2}\frac{d\delta f}{dr}(R_{\rm EM})\right|$ poses significant challenges for parameters where the field starts to resemble an inverse square law near the Moon. In the case of an exact inverse square law, this quantity vanishes; for an approximate inverse square law, $|\delta f(R_{\rm EM})| \simeq |\frac{R_{\rm EM}}{2}\delta f'(R_{\rm EM})|$. Consequently, the leading digits of both terms cancel out, and only higher digits dominate this expression. Precise simulations are required to accurately capture this, often proving unfeasible. Given that such parameters yield no novel constraints, the less accurate analytical approximate solution was employed in this case.

5.5.2. Neutron interferometry

In this Section the theoretical results from Section 5.2 and numerical results from Section 4 are applied to derive parameter constraints of the dilaton and symmeron model in the context of neutron interferometry. The analysis herein is based on the experimental setup described in Ref. [66], which initially investigated chameleon-induced phase shifts, for a fixed value of $\Lambda = 2.4$ meV. This analysis is extended to encompass the symmetron and dilaton fields and to a larger part of the chameleon parameter space.

If a scalar field does indeed exist, the neutron would undergo distinct phase shifts along each of its paths. In the semi-classical approximation, this shift is given by Eq. (5.2.215), expressed as:

$$\delta\varphi_{X;P}(r) = -\frac{m_n}{k_0}\int_{-L/2}^{L/2} U_{X;P}(r,z)\,dz\,. \tag{5.5.255}$$

Here, X represents three possible scenarios $\{\mathrm{D},\mathrm{S},\mathrm{C}\}$, k_0 denotes the neutron's wave number, r signifies the radius, L stands for the length of the vacuum chamber, $U_{X;P}(r,z) := \mathfrak{Q}_X m_n\big(A_X(\phi) - A_X(\phi_{\rm Air})\big)$ represents the scalar field potential within the vacuum or air chamber at pressure P, and the integration over z extends along the classical flight path (CFP) within the respective vacuum chamber. The experiment employed two measurement modes:

Constraint calculation profile mode

In this operational mode, the vacuum chamber pressure remained fixed at 10^{-4} mbar, while the position of the beam was varied. Initially, both beams traversed through the respective central region of the corresponding chamber, after which they were adjusted closer to the chamber walls, reaching a displacement of approximately 1.5 cm from the center. This mode demonstrates heightened sensitivity towards long-ranged fields, showcasing substantial variations in the field across several centimeters, as illustrated in Fig. 5.2.3 ($A_2 = 10^{36}$, $A_2 = 10^{38}$). Conversely, very short-ranged fields, as exemplified in Fig. 5.2.3 ($A_2 = 10^{42}$), tend to attain their VEV near the chamber wall, while maintaining relative constancy within the chamber. Consequently, the profile mode is deemed unsuitable for investigating such parameters.

Experimental constraints for scalar fields were derived by measuring the phase difference for both beam positions. The computation of the phase shift utilized the expression:

$$\Delta\varphi_{X;P} = \delta\varphi_{X;P}(0) - \delta\varphi_{X;P}(0.015\ \mathrm{m})\,, \tag{5.5.256}$$

for both the vacuum and air chamber. The experiment measured

$$\alpha := \Delta\varphi_{X;\rm Vacuum} - \Delta\varphi_{X;\rm Air} < 0\,. \tag{5.5.257}$$

This quantity is negative due to the increased suppression of the potential near the chamber walls, coupled with $|\Delta\varphi_{X;\text{Air}}| < |\Delta\varphi_{X;\text{Vacuum}}|$. The experimentally determined value is denoted as $\alpha = (0.56 \pm 2.50)°$. To establish a 95% CL, the error is assumed to conform to a normal distribution and $\alpha < 0$ is taken into account. Accordingly, the normal distribution is modeled with a mean of 0.56° and a standard deviation of 2.5°. Given the anticipated negativity of α, the objective is to identify x such that the probability of measuring α within the interval $(-\infty, x)$ is only 5%, allowing to constrain α values in this interval with a 95% CL. Therefore, x has to be determined by solving:

$$\frac{1}{2.5°\sqrt{2\pi}} \int_{-\infty}^{x} e^{-\frac{1}{2}\left(\frac{s-0.56°}{2.5°}\right)^2} ds = 0.05\,, \tag{5.5.258}$$

which yields $x \simeq -3.55°$ allowing to constrain parameters for which

$$\alpha < -3.55°\,. \tag{5.5.259}$$

Constraint calculation pressure mode

In this mode, both beams traversed through the center of each chamber, while the pressure within the vacuum chamber was adjusted. Initially, the phase shift resulting from the highest pressure of $P_0 = 10^{-2}$ mbar served as a reference, after which the pressure was decreased to $P_1 = 2.4 \times 10^{-4}$ mbar.

This mode exhibits heightened sensitivity towards very short-ranged fields, as depicted in Fig. 5.2.3 ($A_2 = 10^{42}$), where the field essentially maintains its VEV throughout the chamber. Given that the VEV relies on the vacuum density in the considered models, comparing phase shifts at different gas pressures introduces a relative phase difference for short-ranged fields.

Thus, the measured quantity is expressed as:

$$\xi := \delta\varphi_{X,P_1}(0) - \delta\varphi_{X,P_0}(0) < 0, \tag{5.5.260}$$

with a vacuum pressure of $P_1 = 2 \times 10^{-4}$ mbar and a reference pressure $P_0 = 10^{-2}$ mbar. The experimentally determined result is $\beta = (0.37 \pm 3.53)°$. Accounting for $\xi < 0$ and assuming a normal distribution for the error, y is computed such that:

$$\frac{1}{3.53°\sqrt{2\pi}} \int_{-\infty}^{y} e^{-\frac{1}{2}\left(\frac{s-0.37°}{3.53°}\right)^2} ds = 0.05, \tag{5.5.261}$$

yielding $y \simeq -5.44°$. Consequently, parameters are constraint if

$$\xi < -5.44°. \tag{5.5.262}$$

Projective constraints for the split interferometer were derived using the same equations and experimental parameters, except that the second beam position was assumed to be 4 cm displaced from the center.

Dilaton constraints calculation

The existing experiment deviated from a perfect cylindrical shape, instead featuring a rectangular design with rounded edges. Due to the substantial computational expense associated with conducting 3D simulations, the actual geometry is approximated using cylinders. These cylinders were configured to match the length of the real chambers, which measured 0.094 m in the

experiment and 0.5 m for the split interferometer. They were either designed to fit within the actual chamber (with a radius of $r = 2$ cm for both chambers) or to encompass the chamber entirely (with a radius of $r = \sqrt{8}$ cm for the vacuum chamber and $r = \sqrt{3.25^2 + 2^2}$ cm for the air chamber). Extensive verification confirmed that the disparities between the two geometries were negligible, allowing me to proceed with computing the final constraints while assuming $r = 2$ cm.

The constraints were derived as follows: Starting with a fixed V_0 and commencing from the smallest permissible value of A_2 (dictated by the long-range cutoff to ensure field decay to ϕ_M within the vacuum chamber's shell), a systematic search for the contour of the constrained region along the λ-axis was conducted. This search involved employing a step width of 0.1 in a logarithmic plot. Subsequently, A_2 was incremented by a factor of 10, and the iterative process continued until reaching a regime where the pressure mode exerted dominance, rendering the short-range approximation in Eq. (5.2.223) indistinguishable from the simulations. For larger values of A_2, only the short-range approximation was used to compute the remainder of the constrained region. Finally, the points located at the edge of the constrained region were connected. The FEM mesh was always refined to the point where further refinement has negligible influence on the computed phase shift.

An illustrative example of this methodology is presented in Fig. 5.5.1

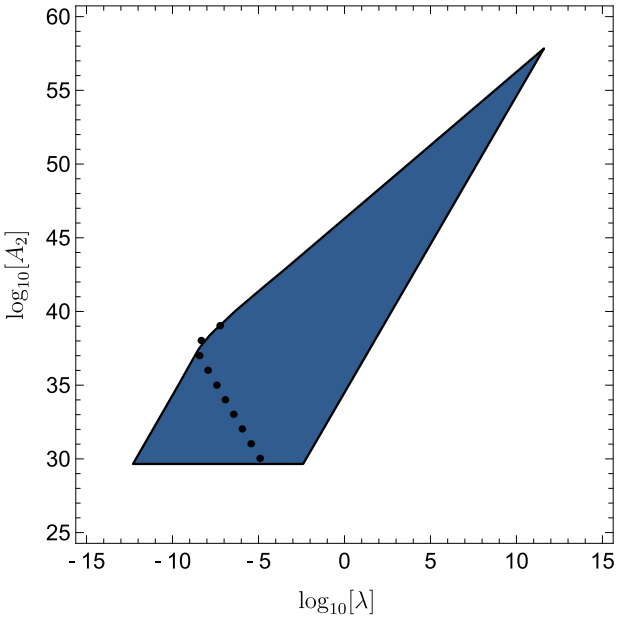

Fig. 5.5.1: The shaded blue region represents constraints derived from the short-range approximation given by Eq. (5.2.223). The bullet points denote positions along the real contour of the constrained region, obtained from simulations with $V_0 = 10$ MeV^4. Figure published in [3].

Symmetron constraints calculation and domain wall solutions

The behavior of the symmetron field is dictated by its effective potential, which takes the form:

$$V_{\text{eff}}(\phi) = \frac{1}{2}\left(\frac{\rho}{M^2} - \mu^2\right)\phi^2 + \frac{\lambda_S}{4}\phi^4. \tag{5.5.263}$$

This potential permits spontaneous symmetry breaking. In high-density regions where $\frac{\rho}{M^2} - \mu^2 > 0$, the potential has a single real minimum at $\phi = 0$, indicating a symmetric phase and resulting in the absence of fifth forces. Conversely, in low-density regions where $\frac{\rho}{M^2} - \mu^2 <$

0, the field undergoes symmetry breaking, acquiring a non-zero VEV and giving rise to fifth forces. Additionally, owing to the symmetry $\phi \to -\phi$ of the potential, the differential equation Eq. (4.0.77) may have multiple solutions, as discussed in [61, 62] for the case of the two mirror geometry. This property is further elucidated below.

Constraint calculations employed solutions exhibiting a single node, typically corresponding to the lowest energy solution (as illustrated in the top of Fig. 5.5.2). Numerical simulations revealed that for sufficiently small μ values, no solution exists[15]. This observation aligns with findings from [61,62], which established that between two infinitely extended mirrors, no solution can exist for small μ. Consequently, given the dimensions of the vacuum and air chambers, symmetron ranges of approximately 1 mm or larger preclude the existence of field solutions satisfying the boundary conditions.

This inherent limitation of the symmetron field confines the parameter space accessible to short-ranged fields. Notably, it was determined that employing the short-range approximation (5.2.223) proves sufficiently accurate across the parameter space where new constraints can be established.

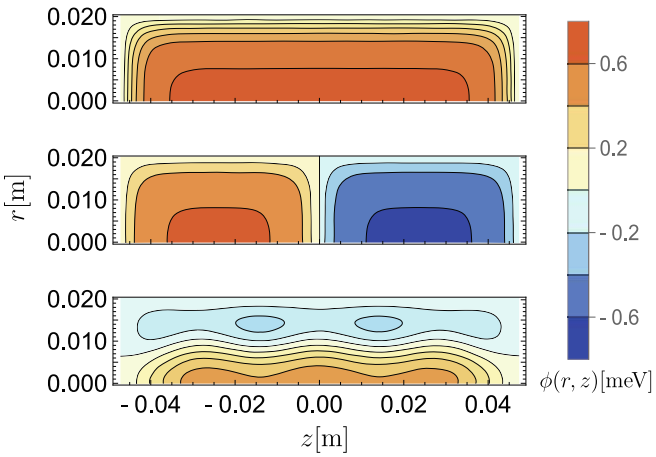

Fig. 5.5.2: The field profiles of the three solutions listed in Table 5 are displayed. It's noteworthy that for the specified parameters, $\phi_V = 0.61$ meV is maintained. Figure published in [3].

Domain walls and multiple node solutions

In the symmetry-broken phase, the symmetron field may settle into distinct VEVs, potentially leading to the formation of domains where the field adopts either VEV. The boundaries separating these domains are termed domain walls (as discussed in [143]). Although domain walls may be unstable on cosmological time scales [144], they could produce observable effects on ultra-cold neutrons by causing their deflection towards the domain wall [145]. Moreover, Ref. [146] has proposed to deliberately induce such domain walls by manipulating gas within a vacuum chamber.

However, these domain walls may also be unstable over experimental time scales. Ensuring their stability within a cavity can be achieved by introducing appropriate matter distributions at the experiment's center, providing anchoring points for the walls [145, 146]. The decay time and required matter distribution for stability depend on the specific model parameters, necessitating thorough investigations through time-dependent simulations across various setups, which extend beyond the current thesis scope but remain the focus of future studies. Nonetheless, the

[15] The trivial solution $\phi(r, z) = 0$ is not considered a solution, since it does not induce any phase shift.

present investigation highlights the existence of diverse static solutions in principle. It's crucial to acknowledge that detecting these solutions may demand specific stabilization procedures.

A search for static domain walls within a realistic cylindrical vacuum chamber involved testing numerous plausible initial guesses using Newton's method to solve Eq. (4.0.77). The spectrum of solutions obtained for a fixed parameter combination is depicted in Fig. 5.5.2.

Among these solutions, the top one exhibits a single domain with a sole local extremum at the chamber's center. In contrast, the middle solution features two domains, with the field assuming its positive VEV for $z < 0$ and its negative VEV for $z > 0$. Notably, this latter solution demonstrates anti-symmetry $\phi(r, -z) = -\phi(r, z)$, illustrating that in the symmetry-broken phase, the field need not adhere to the chamber's symmetries. Instead of the anticipated three-domain solution along the z-axis, a different configuration, depicted at the bottom, is found. While this solution displays multiple local extrema along each axis, none closely approaches any VEV. This implies that static solutions can exist without the field assuming its VEV within the vacuum chamber. Despite employing numerous seeds for Newton's method, no additional solutions were identified. However, it's suspected that solutions without cylinder symmetry also exist, given that symmetron field solutions need not conform to their environment's symmetry. Discovering such solutions would necessitate solving the full 3D differential equation, exceeding the scope of this thesis. It's further speculated that solutions containing more domains may emerge only for larger parameter values of μ, allowing for increased field curvature. This behavior, including the absence of solutions for excessively small μ values, has been observed in [61,62] for a one-dimensional setup with two parallel mirrors. The energies of these field solutions and their interaction with matter density can be evaluated using the Hamilton density,

$$\begin{aligned}\mathcal{H} &= \frac{1}{2}\left(\vec{\nabla}\phi\right)^2 + V_{\text{eff}}(\phi) \\ &= \frac{1}{2}\left\{\left(\frac{\partial\phi}{\partial r}\right)^2 + \left(\frac{\partial\phi}{\partial z}\right)^2\right\} + V_{\text{eff}}(\phi)\,,\end{aligned} \tag{5.5.264}$$

where cylinder symmetry is assumed. The energy E inside the cylinder is hence given by:

$$E = \int_{\text{cylinder}} d^3x\, \mathcal{H}(\vec{x}) = 2\pi \int_0^d dr\, r \int_{-L/2}^{L/2} dz\, \mathcal{H}(r, z)\,, \tag{5.5.265}$$

where d and L represent the cylinder's radius and length, respectively. The obtained energies are listed in Table 5.

Mode	E [eV]
0	-2.097
1	-1.710
2	-0.06

Table 5: The table shows energies E corresponding to the three obtained solutions, with the mode number enumerating the solutions with increasing energy. Numerical values used include $\rho_M = 1.16 \times 10^{-5}$ MeV^4, $\rho_V = 7.08 \times 10^{-17}$ MeV^4, $\lambda_S = 10^{-2}$, $M = 10^3$ GeV, and $\mu = 6.1 \times 10^{-5}$ eV.

Constraint calculation chameleon field

Currently, neutron interferometry lacks the capability to impose new limits for $n = 1$ and varying Λ, as well as for the scenario $1 \leq n \leq 10$ and $\Lambda = 2.4$ meV. This conclusion was drawn not from precise constraint computations, but rather from the following rationale:

A static chameleon field obeys the inequality (see Appendix A):

$$\phi_M \leq \phi(x) \leq \phi_V \,. \tag{5.5.266}$$

The quantity $\Delta_{\max}\varphi_C$ is defined as

$$\Delta_{\max}\varphi_C := \mathfrak{Q}_C \frac{m_n^2 L}{k_0 M_c} \max\{(|\phi_V - \phi_{\text{Air}}|)\,, (|\phi_M - \phi_{\text{Air}}|)\}\,, \tag{5.5.267}$$

and can be used to bound the maximal expected phase shift:

$$\begin{aligned} \left|\alpha\right| &\leq 4\Delta_{\max}\varphi_C\,, \\ |\xi| &\leq 2\Delta_{\max}\varphi_C\,. \end{aligned} \tag{5.5.268}$$

Over all unconstrained parts of the parameter space one has

$$4\Delta_{\max}\varphi_C \ll 1^\circ\,. \tag{5.5.269}$$

Thus, neutron interferometry cannot yield new constraints. Any obtained limits would be significantly weaker than existing ones, rendering a more detailed analysis of this experiment redundant for chameleons.

5.5.3. qBOUNCE

This Section applies theoretical results from 5.3 and numerical results from Section 4 to derive parameter constraints of the dilaton, symmetron and chameleon model in the context of qBOUNCE. In the experiment in Ref. [63], the transition energies $\Delta E_{13} := E_3 - E_1$ and $\Delta E_{14} := E_4 - E_1$ were measured. The experimentally observed values are $\Delta E_{13} = (1.9222 \pm 0.0054)$ peV and $\Delta E_{14} = (2.6874 \pm 0.0074)$ peV, which align with the transition energies anticipated from a Newtonian gravitational potential alone.

Scalar field parameters are constrained if they would result in a deviation of at least two standard deviations from the measured values. Therefore, parameters are considered constrained if:

$$\begin{gathered} \Delta E_{13} \notin (1.9114, 1.933)\ \text{peV}, \\ \text{or} \\ \Delta E_{14} \notin (2.6726, 2.7022)\ \text{peV}. \end{gathered} \tag{5.5.270}$$

Here, ΔE_{13} and ΔE_{14} denote the solutions for the eigenenergies of the stationary Schrödinger equation in the presence of a scalar field, as elaborated in Section 5.3.3.

The procedure for deriving the constraint volume was akin to the case of neutron interferometry depicted in Fig. 5.5.1 and is elucidated using the example of the dilaton field:

- For a fixed V_0, the analysis began from the smallest permissible value of A_2 determined by a cutoff. Subsequently, the boundary of the constraint region was sought with a step width of 0.1 in a log-log plot in the λ direction.
- A_2 was incremented by a factor of 10.
- This process was reiterated until the entire non-trivial boundary (not arising from cutoffs) was identified, and the points along the boundary of the constraint region were connected.

Each step comprised two sub-steps: Firstly, the one mirror solution was computed numerically to determine the scalar field-induced potential of the neutron. Subsequently, the stationary Schrödinger equation was solved to calculate the energy shifts induced by the scalar field. Perturbation theory was used in parameter regions where it was evidently applicable, due to its lower computational cost. Otherwise, the entire Schrödinger equation was solved numerically. An illustration of this process is presented in Fig. 5.5.3.

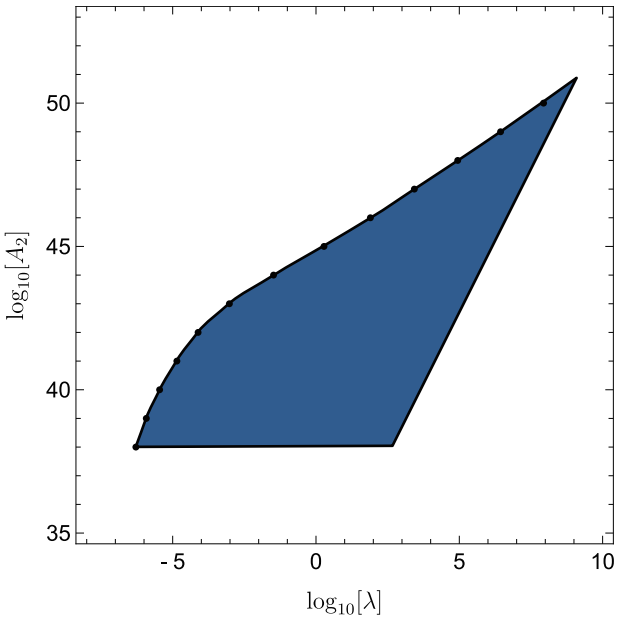

Fig. 5.5.3: This is an illustration of how parameter constraints for *q*BOUNCE were derived. V_0 was set to 10 MeV^4. The bullet points represent the actual boundary of the parameter region constrained by *q*BOUNCE. The dots were connected, and the cutoffs were added to obtain the complete constrained region.

While previous studies have computed *q*BOUNCE constraints for the symmetron field [63, 64], this thesis undertakes a reevaluation of these constraints. The new analysis employs the following refinements:

- Previous works [63, 64] assumed a residual gas density of $\rho_V = 0$ in the vacuum chamber surrounding the experiment. However, the re-analysis incorporates the actual experimental density of $\rho_V = 2.32 \times 10^{-7}$ kg/m^3. This adjustment significantly alters constraints since assuming $\rho_V = 0$ could erroneously allow the symmetron to exist in its symmetry-broken phase in situations where it is not.

- A non-perturbative solution of the stationary Schrödinger equation is employed.
- The new analysis acknowledges the possibility that the symmetron within the neutron mirror used in *q*BOUNCE may exist in its symmetry-broken phase [62].
- To ensure theoretical rigor, appropriate cut-offs are applied.

Section 6.2.2 demonstrates that each refinement significantly enhances the resultant constraints.

Similarly, constraints for the chameleon model have already been published in [54, 135, 147] assuming $\rho_V = 0$ and either neglecting neutron screening altogether [135, 147] or using a different definition of the screening charge [54] sometimes treating the neutron as a test particle even when $\mu_M R \gg 1$, leading to significantly larger constraints. This disparity underscores the imperative for further theoretical advancements to transcend heuristic approximations and accurately determine the true coupling of neutrons to the individual scalar field. These chameleon analyses are also updated in this thesis, to have a consistent treatment for all models using the same methodologies.

For the case of the symmetron field, the analytically exact one mirror solutions derived in Refs. [61, 62] has been used, rather than a numerical solution.

The FDM cutoff was always chosen to ensure that the field naturally relaxes to ϕ_V within the cutoff, and the FDM mesh refined to the point where further refinement has negligible effect on the computed energy shifts.

5.5.4. CANNEX

In this Section the theoretical results from 5.4 and numerical results from Section 4 are applied to derive prospective parameter constraints of the dilaton, symmetron and chameleon model in the context of CANNEX. A recent publication [4] has examined the anticipated measurement sensitivity at one σ for both pressure and pressure gradient measurements as a function of the plate separation d, illustrated in Fig. 5.5.4. Constraints have been established for parameters where

$$|P(d)| > 2\sigma(d), \quad \text{or} \quad \left|\frac{\partial P}{\partial d}(d)\right| > 2\sigma(d). \tag{5.5.271}$$

The scalar field-induced pressure has been calculated from Eq. (5.4.240), where ϕ_0 is computed by numerically determining the two mirror solution. Pressure gradients have been computed using

$$\frac{\partial P}{\partial d}(d) \simeq \frac{P(d+\delta) - P(d-\delta)}{2\delta} \tag{5.5.272}$$

for sufficiently small δ.

It is noteworthy that prospective constraints for the symmetron field have been previously outlined in [81], along with constraints for the chameleon with $\Lambda = 2.4$ meV and small values of n [82]. However, these analyses are revisited due to their reliance on analytical approximations and their lack of consideration for the variability of plate separation and vacuum pressure variation. Additionally, none of the existing analyses accounted for pressure gradient measurements. The constraint determination closely parallels the *q*BOUNCE case in Fig. 5.5.3, with two notable adjustments:

Firstly, the analysis incorporates the variability of plate separation between 3-30 μm and vacuum density 5.3×10^{-12} kg/m^3 $< \rho_V <$ 2.6 kg/m^3 within the experimental setup.

Secondly, for the chameleon with $n = 1$, the analytically exact solution presented in Ref. [111] is utilized. For the symmetron field, only solutions with a single node, akin to the neutron interferometry analysis, have been employed.

The FDM mesh was always refined to the point where further refinement has negligible effect on the computed pressure.

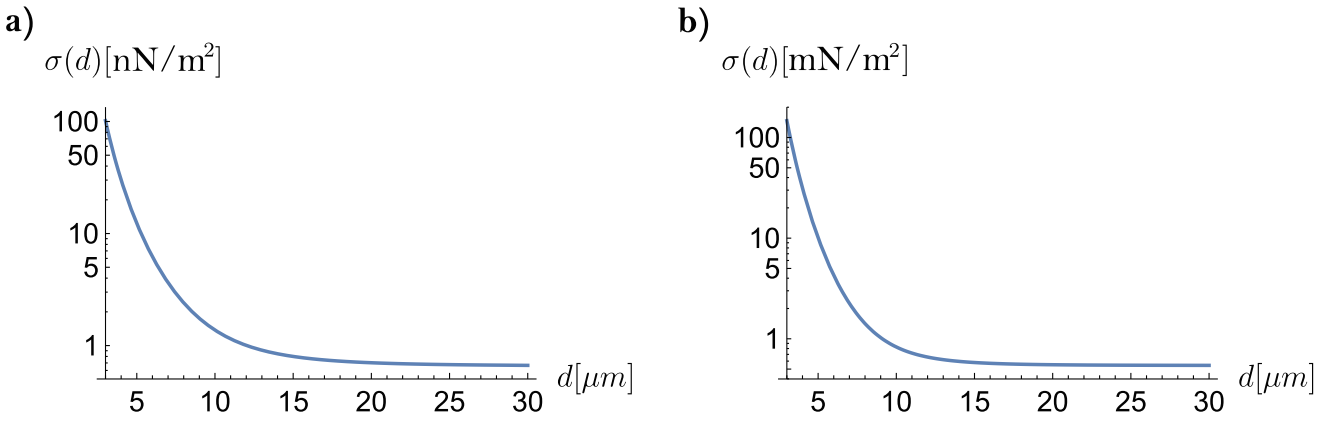

Fig. 5.5.4: The potential sensitivity of the forthcoming CANNEX measurements, displayed at a one σ confidence level is depicted for both **a)** pressure and **b)** pressure gradient measurements. The sensitivity is presented as a function of plate separation d.

6. Results and discussion

This Section offers an in-depth discussion and interpretation of the derived constraints, along with the theoretical and numerical advancements achieved in scalar field calculations.

Section 6.1 provides an exploration of the combined dilaton constraints emerging from the considered experiments, spanning the entire three-dimensional parameter space. Additionally, constraints arising if the dilaton field is considered as the source of dark energy are explored. Subsection 6.1.3 elaborates on potential enhancements achievable through a split-crystal interferometer, while Subection 6.1.4 delves into the interpretation of constraints derived from LLR.

Moving forward, Section 6.2 focuses on the collective constraints concerning the symmetron field, offering a comprehensive comparison with constraints obtained from experiments not directly related to this thesis. Within Subsection 6.2.2, a comparative analysis between the pre-existing *q*BOUNCE symmetron constraints, predating this thesis [63, 64], and the results derived from this thesis is undertaken. This comparison serves to highlight the substantial improvements achieved in both theoretical frameworks and numerical analyses throughout the duration of this thesis. Similarly, a comparison of the old CANNEX analysis and the new results is provided in Subsection 6.2.3.

Lastly, Section 6.3 provides an extensive discussion on chameleon constraints.

6.1. Constraints for the environment-dependent dilaton field

6.1.1. Combined constraints for the three dimensional parameter space

The dilaton constraints naturally segregate into two regions: the small λ region (Fig. 6.1.1 a)) and the large λ region (Fig. 6.1.1 b)) region. The intermediate λ region violates the cutoff in Eq. (3.1.38), rendering the model undefined. This violation manifests as diagonal cuts in the constraint regions.

In the small λ region, the shape of the constraint areas remains constant as V_0 increases, shifting only towards lower values of λ due to the $V_0\lambda$ symmetry discussed in Section 3.1.2, illustrated by arrows in Fig. 6.1.1 a).

In the large λ region, constraint areas systematically shift towards lower values of A_2 as V_0 increases, in accordance with the approximate $A_2\ln\left(V_0/\rho\right)$ symmetry, indicated by a downward vertical arrow. Notably, this symmetry applies solely to the fifth force, not to the cutoff in Eq. (3.1.38), which progressively reduces the size of constraint regions for larger V_0, as shown by diagonal arrows.

LLR is sensitive to dilaton ranges of approximately 1 AU and larger; shorter ranges render the dilaton force weak. Tabletop experiments, however, can constrain parameters close to dilaton ranges of 1 μm.

Notably, neutron interferometry can probe extremely small ranges of $\sim$ 1 pm (it can set constraints for substantially larger values of A_2 than the other experiments). The physical reason is that very small dilaton ranges simply mean that the field reaches its VEV very close to the cylindrical vacuum chamber walls, as shown, e.g. in Fig. 5.2.3 ($A_2 = 10^{42}$). The potential is roughly constant inside the vacuum chamber, but the VEV still induces a phase shift, according to Eq. (5.2.223). Since the VEV is contingent on the vacuum density, the phase shift induced in the air and vacuum chamber is not the same, even for extremely small dilaton ranges. Hence, even very short-ranged dilaton fields still induce a relative phase difference in neutron interferometry, which is one the substantial advantages of this experiment.

The lower edge of neutron interferometry constraints acts as a cutoff to ensure the dilaton field decay within the cylinder shell, which allows to neglect influences from outside the chamber.

The lower edge of *q*BOUNCE is a vacuum range cut-off (1 mm) to ensure that the influence of the vacuum chamber can be neglected, and using the one mirror solution is appropriate.

At the lower edge of CANNEX, two cutoffs overlap: parameters exceeding a 1 mm vacuum range are disregarded, similar to *q*BOUNCE. However, since CANNEX can increase the vacuum density up to $\sim$2.6 kg/m^3, it effectively weakens this cutoff by suppressing screened scalar fields in dense environments, enabling analysis of lower A_2 values. Additionally, a second cutoff ensures the field decays to ϕ_M within the upper plate, justifying the use of Eq. (5.4.240) to calculate the pressure and the treatment of the mirror as infinitely extended.

For significantly lower values of V_0 than those depicted in Fig. 6.1.1, constraints from both the large and small λ regions converge, leading to a rapid disappearance of constraints due to weakened physical effects. The specific point of convergence depends on the experiment and vacuum density but is generally around $\sim 10^{-20}$ MeV^4 qualitatively.

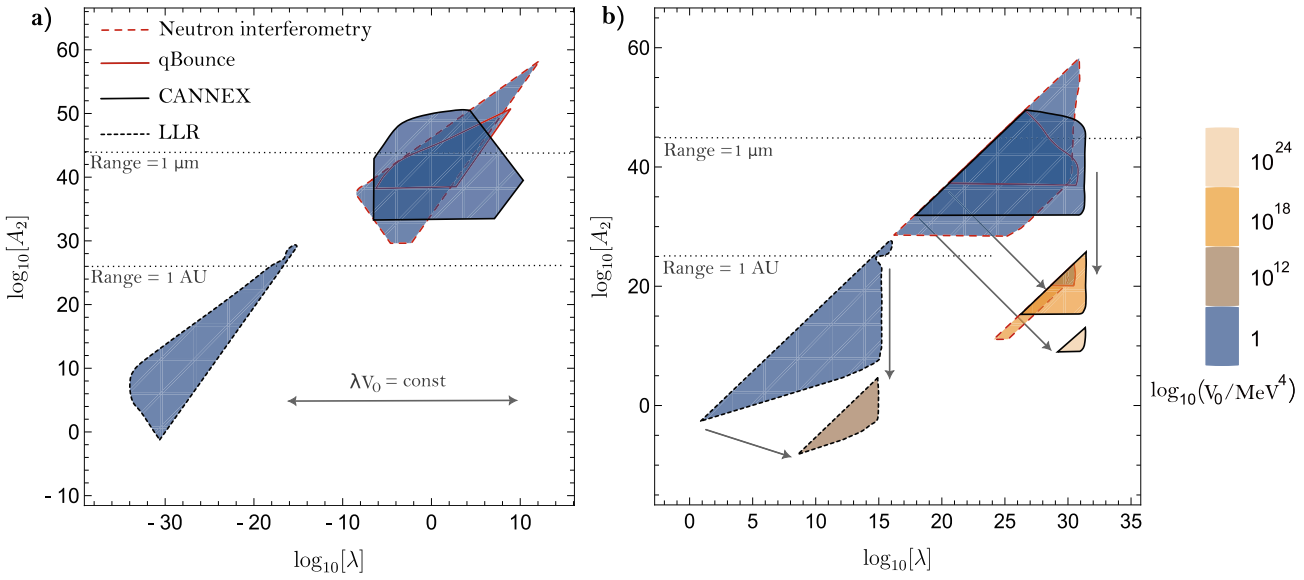

Fig. 6.1.1: The constraint plots typically exhibit two distinct regimes: **a)**: Illustrating constraints for small values of the parameter λ. **b)**: Depicting constraints for large values of λ. Further explanations are available in the main text.
LLR: For LLR, the combined constraints from violations of the equivalence principle and violations of the inverse square law are represented by filled areas located in the bottom-left of each region.
Neutron interferometry: Constraint are filled areas surrounded by dashed red lines.
*q*BOUNCE: Constraints are filled areas surrounded by solid red lines.
CANNEX: Prospective constraints are surrounded by solid black lines.
The interaction range of the dilaton is illustrated for $\log_{10}(V_0/\text{MeV}^4) = 1$, considering two distinct values: The 1 μm and 1 AU contours correspond to vacuum densities of $\rho_V = 2.32 \times 10^{-7}$ kg/m^3 (for *q*BOUNCE) and $\rho_V = 1.67 \times 10^{-20}$ kg/m^3 (pertaining to the interplanetary medium). Figure published in [5].

6.1.2. Constraints for the dilaton as a source of dark energy

Ensuring the dilaton's exclusive role as the primary source of dark energy is feasible solely within the small λ region. Within this domain, the effective potential is approximated as:

$$V_{\text{eff}}\left(\phi_M, \rho_M\right) \simeq V_0, \tag{6.1.273}$$

as elaborated in Section 3.1.3. Consequently, the examination of the dilaton as a source of dark energy involves enforcing $V_0 = 3\Omega_{\Lambda_0} m_{\text{pl}}^2 H_0^2 \simeq 2.51 \times 10^{-35}$ MeV^4, as depicted in Fig. 6.1.2. LLR remains the sole experimental method discussed in this thesis capable of setting constraints in this scenario, given the exceedingly low value of V_0, which nullifies constraints from other experiments.

It's worth mentioning that in Ref. [1], it was demonstrated that the dilaton parameter space can be effectively reduced to two dimensions by stipulating $V_{\text{eff}}\left(\phi_M, \rho_M\right) = 3\Omega_{\Lambda_0} m_{\text{pl}}^2 H_0^2$. This allows the expression of V_0 as a function of A_2 and λ. However, the constraints depicted in Fig. 6.1.2 remain identical, as the condition $V_0 = 3\Omega_{\Lambda_0} m_{\text{pl}}^2 H_0^2$ suffices within the small λ region.

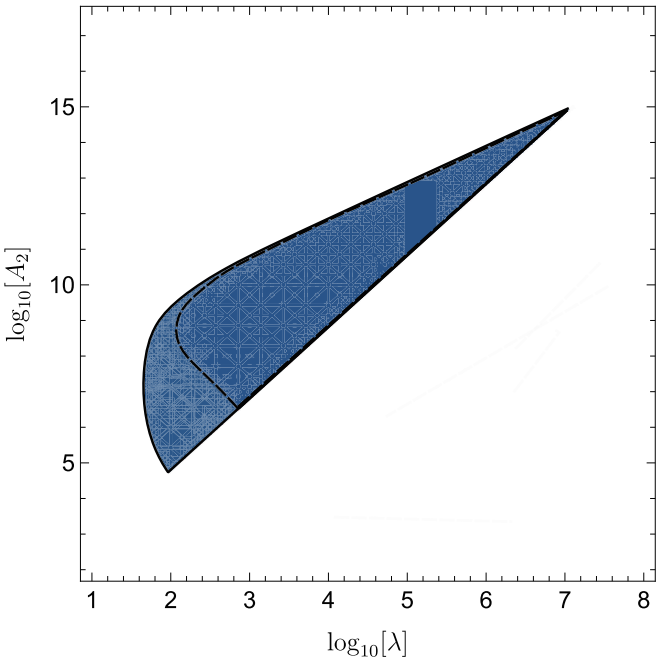

Fig. 6.1.2: Constraints regarding the dilaton field's role as the source of dark energy are primarily established by LLR. Within the illustrated region, V_0 is defined as $V_0 = 3\Omega_{\Lambda_0} m_{\text{pl}}^2 H_0^2$. Constraints pertaining to violations of the equivalence principle are shown in blue, while constraints from violations of the inverse square law are surrounded by dashed lines. Figure published in [2].

6.1.3. Improvements from a split-crystal interferometer

Figure 6.1.3 compares the actual constraints derived from neutron interferometry, as depicted in Fig. 6.1.1, with those that would arise from a split-crystal interferometer. The split-interferometer analysis presumed identical experimental parameters—vacuum density, measurement sensitivity, etc.—except for variations in the dimensions of the vacuum chamber: a longer chamber (0.5 m instead of 0.0094 m) and widened chamber (radius of 4.75 cm instead of 2 cm). This comparison illuminates the impact of differing vacuum chamber sizes on the resultant constraints.

Evidently, the enhanced size yields negligible improvements in the parameter space available for probing the dilaton using neutron interferometry. A more promising avenue for enhancing the sensitivity of neutron interferometry to screened scalar fields lies in reducing the vacuum pressure, which stood at approximately 10^{-4} mbar during the experiment. Given that screened scalar fields

are inherently sensitive to ambient matter density, decreasing the vacuum density by several orders of magnitude would exert a far more pronounced effect. For instance, the CANNEX project aims for a vacuum pressure as low as 10^{-9} mbar. The improvements of the split-interferometer in the context of the symmetron field would be too small to be visible in a log-log plot and are hence not plotted.

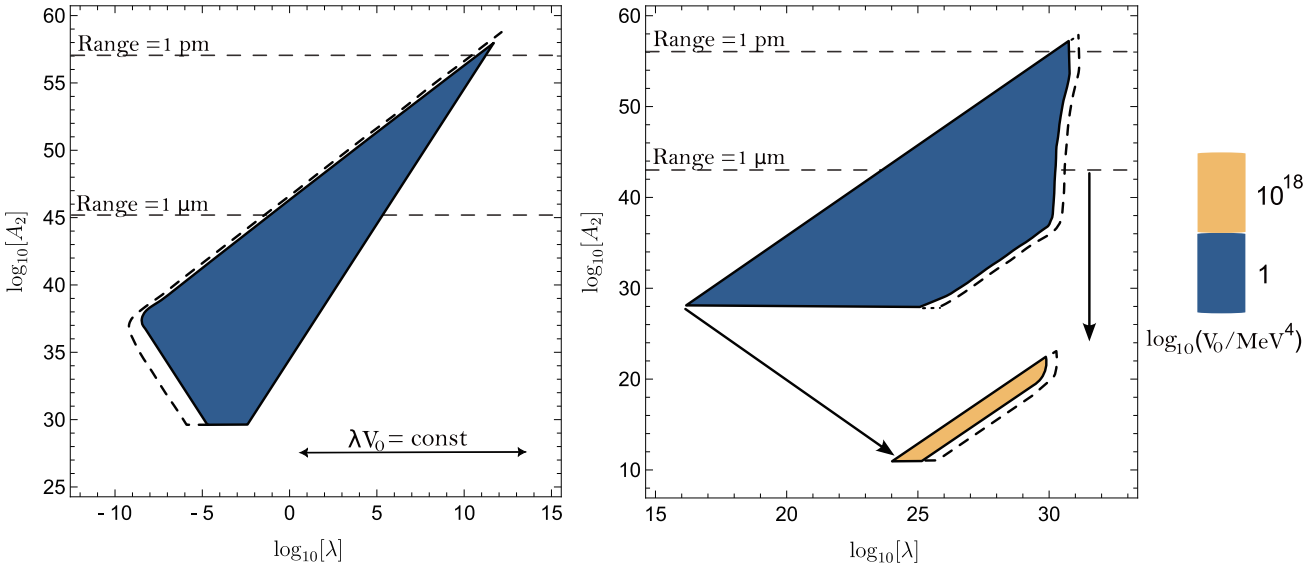

Fig. 6.1.3: This figure presents a comparison of neutron interferometry constraints derived from the experiment in Ref. [66], depicted in color, alongside the split-crystal interferometer geometry delineated by dashed lines, as explained in the text.

6.1.4. Interpretation of LLR constraints

This Subsection delves into the contributions of two distinct LLR tests: the tests of the equivalence principle (LLR I) and those concerning the inverse square law (LLR II), to the combined LLR constraints, as illustrated in Figure 6.1.4. Notably, constraints originating from LLR II deviate from the approximate $A_2 \ln(V_0/\rho)$ symmetry derived in Section 3.1.2.

This example underscores that the approximate parameter symmetry isn't universally applicable and cannot be reliably exploited to treat the model as having two parameters in the large λ region.

The physical reason for LLR II to deviate from this approximate symmetry is the following:
The force exerted by the Earth on the Moon can be expressed as follows (see Eq. (5.1.205)):

$$\vec{f}_\phi = -\beta(\phi)\mathfrak{Q}_{\leftmoon} \frac{M_{\leftmoon}}{m_{\rm pl}} \vec{\nabla}\phi = -\beta(\phi)\mathfrak{Q}_{\leftmoon} \frac{M_{\leftmoon}}{m_{\rm pl}} \vec{\nabla}\delta\phi, \tag{6.1.274}$$

where ϕ represents the Earth's field and $\delta\phi := \phi - \phi_V$. For long-ranged dilaton fields defined by $\mu_V r \ll 1$, with μ_V denoting the dilaton mass in vacuum and r the distance between the Earth and the Moon, one can approximate (using Eq. (5.1.203)):

$$\delta\phi \propto \frac{e^{-\mu_V r}}{r} \simeq \frac{1}{r}\,. \tag{6.1.275}$$

Consequently, the dilaton force on the Moon can be approximated by

$$\vec{f}_\phi \propto -\beta(\phi)\mathfrak{Q}_{\leftmoon}\,\frac{M_{\leftmoon}}{m_{\rm pl}}\vec{\nabla}\frac{1}{r}. \tag{6.1.276}$$

Since $\beta(\phi)$ generally retains spatial dependence, long-ranged dilaton fields do not generally mimic an inverse square law akin to Newtonian gravity, where the coupling to matter lacks spatial dependence. Thus, the dilaton field still induces a precession of the lunar perigee, as evident from Equation (5.1.185). However, for very large values of V_0, one can approximate $\beta(\phi) \approx \beta(\phi_V)$, as discussed in Section 3.1.2. Consequently, the spatial dependence of $\beta(\phi)$ diminishes significantly for large V_0 values, causing long-range dilaton fields to precisely mimic an inverse square law, thereby nullifying the precession of the lunar perigee. This understanding, coupled with the observation that the cutoff in Eq. (3.1.38) eliminates short-ranged fields as V_0 increases[16],

elucidates why these constraints weaken swiftly for increasing V_0 values, in contrast to constraints from other experiments detailed in this thesis.

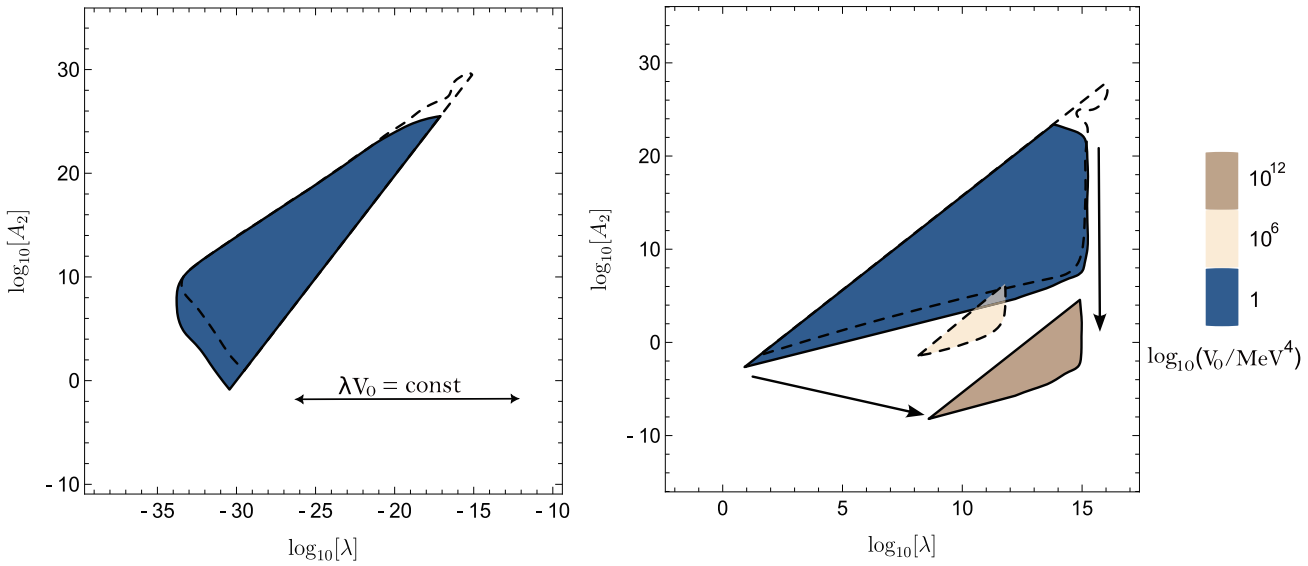

Fig. 6.1.4: This figure illustrates the distinct contributions of constraints pertaining to the equivalence principle, marked by solid lines, and deviations from the inverse square law, delineated by dashed lines, towards the cumulative constraints derived from LLR, as depicted in Fig. 6.1.1. While the constraints originating from equivalence principle violations exhibit systematic shifts for increasing V_0 in the large λ region, in accordance with the explanations detailed in Fig. 6.1.1, constraints from deviations of the inverse square law deviate from this shifting behavior.

[16] This is visually illustrated in the computed constraint regions shown in Fig.6.1.1. The cutoff truncates the upper portions of these regions as the values of V_0 increase, which corresponds to large values of A_2. These truncated regions represent short dilaton ranges, as indicated in Tab.2. Therefore, as V_0 increases, only the constraint regions associated with long-range fields persist.

6.2. Constraints for the symmetron field

6.2.1. Combined constraints from all experiments

The comprehensive set of constraints derived in this thesis is illustrated in Fig. 6.2.1, alongside a comparison with existing constraints from other studies. Below follows a detailed breakdown of the obtained constraints:

a) Tabletop experiments predominantly target the μ values depicted here, given the symmetron's range proximity to 1 mm which roughly corresponds to the smallest distances probed by several experiments.

b) CANNEX is anticipated to yield robust constraints, as the range aligns closely with 1 μm, akin to the plate separation. Eöt-Wash and atom interferometry currently lack the capability to establish limits for these μ values.

c) Certain quantum experiments can still impose constraints despite the symmetron's range being close to 1 nm, which is beyond the reach of current experiments relying on the classical force of the symmetron field. Similar to dilaton field constraints, neutron interferometry can probe extremely small ranges effectively. Similarly, qBOUNCE can explore these ranges as the neutron's wave function would be significantly compressed by the steep slope of the symmetron potential, resulting in measurable effects.

d) At these μ values, roughly corresponding to a symmetron range of 1 pm, neutron screening becomes highly pronounced, challenging the limits of neutron-probing capabilities. However, muonium remains a potent tool for setting substantial constraints due to its composition solely comprising fundamental particles. Reference [65] suggests that treating an anti-muon and an electron within muonium as pointlike test particles explains the absence of screening observed in muonium spectroscopy compared to hydrogen spectroscopy.

It is important to note that once the symmetron range approaches the dimensions of the vacuum chamber, it completely vanishes, as elaborated in Section 5.5.2. Since $\mu = 0.1$ meV corresponds to a range of approximately 1 cm, tabletop experiments cannot effectively probe much smaller values of μ than those displayed.

The lower diagonal cuts in the constraints stem from Eq. (3.3.69), while the left vertical cut denotes the threshold where the symmetron enters its symmetric phase inside the vacuum chamber. For even smaller values of M, it remains globally in its symmetric phase, with classical forces and potentials completely vanishing.

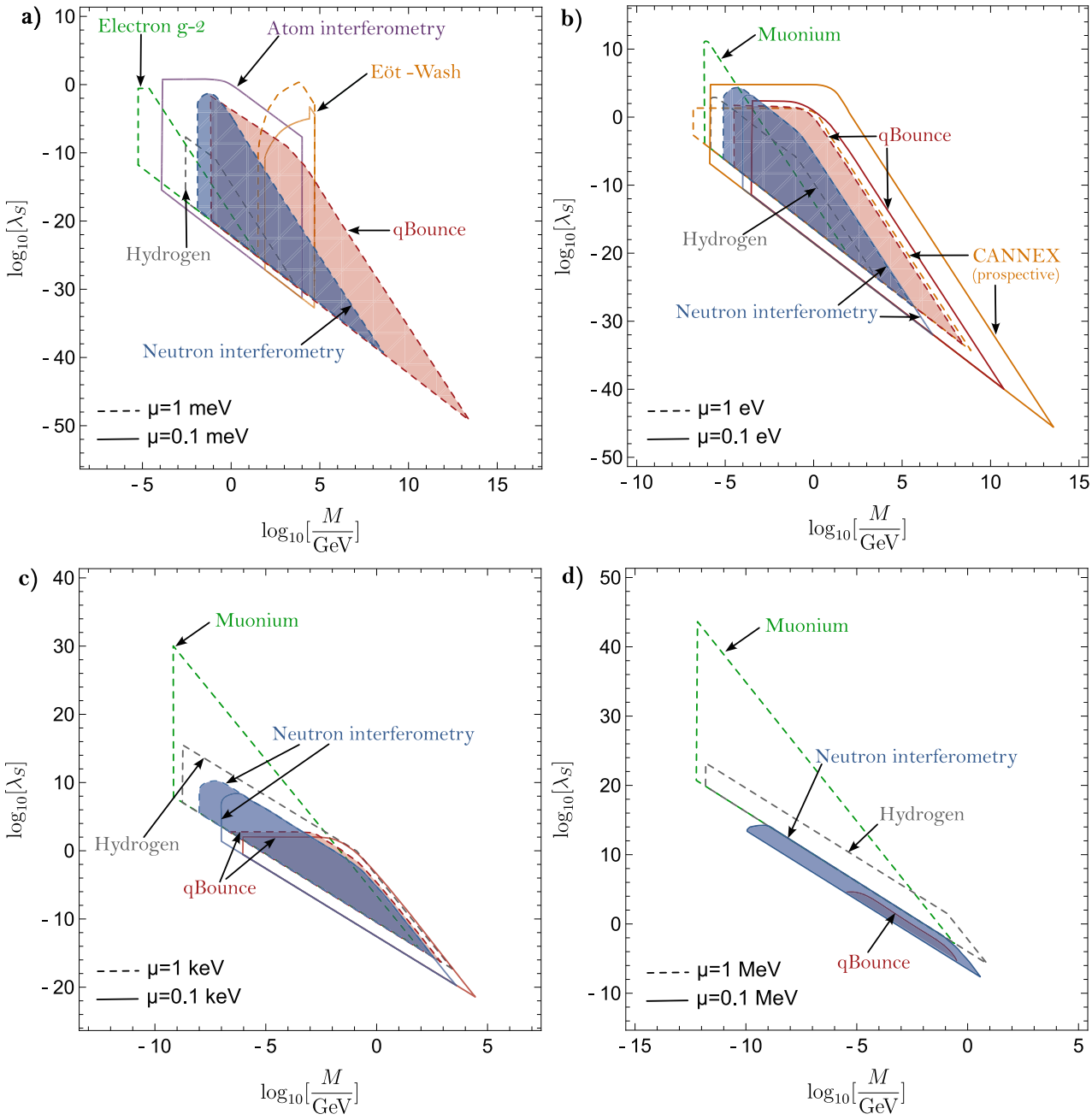

Fig. 6.2.1: Constraints on the parameter space of the symmetron model for different values of the parameter μ based on the review in Ref. [53]; the Eöt-Wash results from Ref. [59]; the atom interferometry analysis in Ref. [58] (see Ref. [99] for an earlier analysis); the investigations of hydrogen, muonium and the electron (g-2) in Ref. [65]; and the analysis in this article for qBOUNCE, neutron interferometry, and CANNEX (only prospective). A full explanation is given in the main text. Figure published in [5].

6.2.2. Comparison of the old qBOUNCE analysis and this work

This Section illustrates the advancements made in theoretical and numerical analyses within this thesis compared to prior work. Focusing on the qBOUNCE framework and the derivation of symmetron constraints, the improvement in each aspect is demonstrated, enhancing the calculation of experimental constraints. This enhancement is showcased through a direct comparison between

the symmetron constraints computed in this thesis and those computed previously [63, 64].

It's noteworthy that in [64], a χ^2 analysis was employed to derive constraints, which differs from the approach in this thesis. To ensure the meaningfulness of the subsequent comparisons despite this difference, I repeated the calculations in the existing analysis with the exact same assumptions as that reference ($\rho_V = 0$, neglecting the possibility of the mirror being in the symmetry-broken phase, assuming perturbation theory to first order is always applicable, and applying the same cut-offs as in the existing analyses).

The only difference was that I employed the conditions in Eq. (5.5.270) rather than a χ^2- data analysis, aiming to isolate how strongly a throrough statistical analysis affects the computed constraints. The results of this comparison are shown in Fig. 6.2.2, demonstrating that the difference in constraint criteria is negligible.

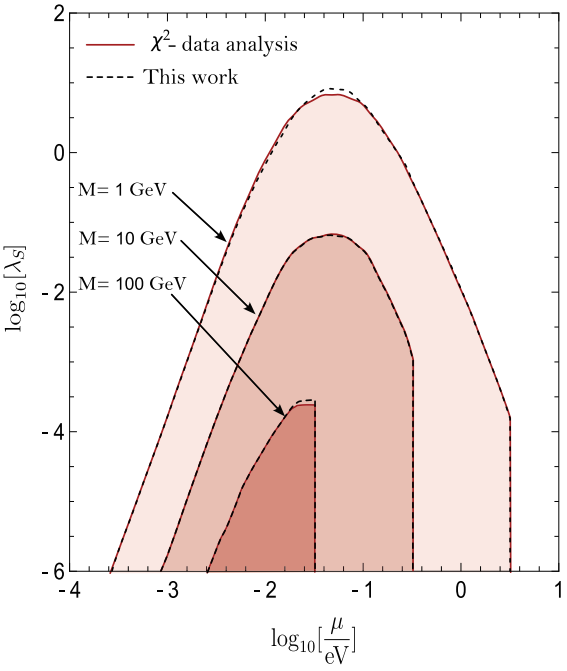

Fig. 6.2.2: This is a comparison between symmetron constraints computed in Ref. [64] using a χ^2 analysis and constraints obtained with the criteria established in this work, while adopting all other theoretical assumptions from Ref. [64]. The colored filled areas represent the constrained regions from Ref. [64] for different values of M. The dashed line depicts the edge of the constrained region from my calculation, nearly overlapping with the published result.

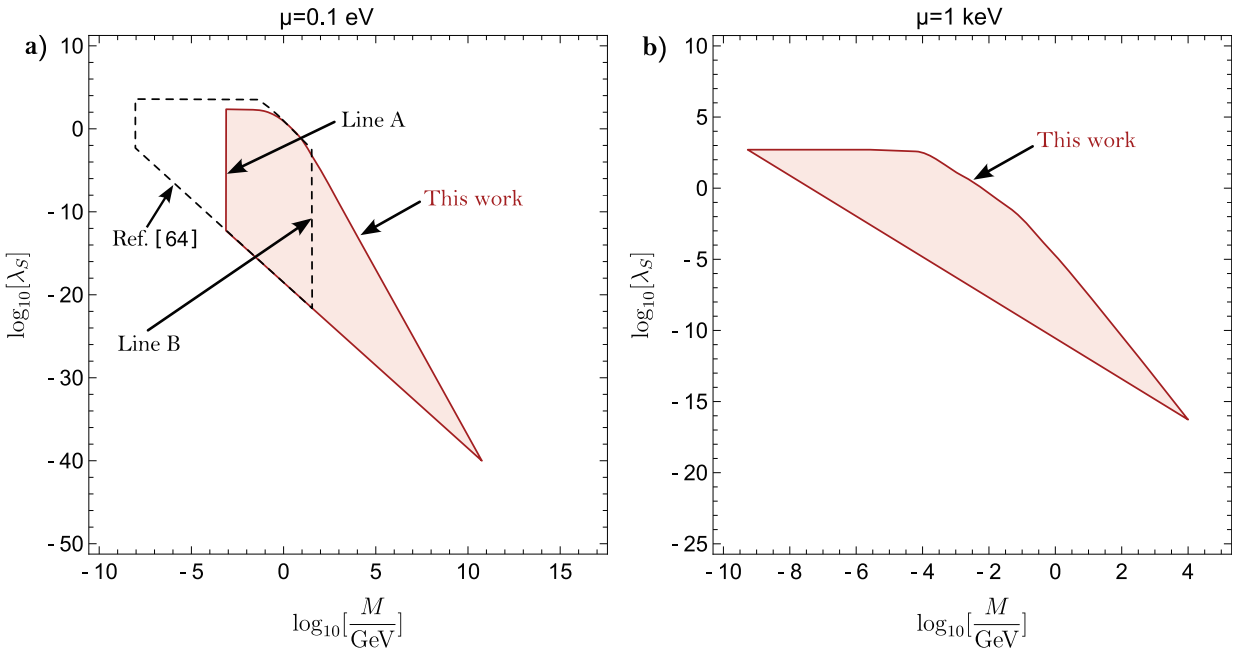

Fig. 6.2.3: Comparison between the *q*BOUNCE constraints derived in Ref. [64] and those computed in this work. **a)** The symmetron parameter μ is set to 0.1 eV. To the left of *line A*, no symmetron solutions exist because the symmetron remains in its symmetric phase within both the vacuum and mirror regions. To the right of *line B*, the symmetron is in its symmetry-broken phase within the mirror. **b)** Here, μ is set to 1 keV, a parameter value for which Ref. [64] provides no constraints.

Fig. 6.2.3 illustrates that the old analysis deviates from the improved analysis by many orders of magnitude. Each of the improvements, including applying the correct vacuum density, considering the symmetry-broken phase of the mirror, and employing non-perturbative techniques to compute the energy alone, corrects the existing analysis by several orders of magnitude.

It is noteworthy that according to perturbation theory, *q*BOUNCE cannot effectively constrain the symmetron field for values of $\mu \gtrsim 10$ eV. However, my numerical calculations demonstrate substantial constraints can be obtained up to $\mu = 0.1$ MeV. This considerable discrepancy arises because perturbation theory computes energy shifts by integrating the symmetron potential multiplied by the modulus squared of the unperturbed wave function, which spans approximately 100 μm:

$$\delta E_{pq} = \mathfrak{Q}_X \int_{-\infty}^{\infty} dz U_X(z) \left(|\Psi_p^{(0)}(z)|^2 - |\Psi_q^{(0)}(z)|^2 \right), \tag{6.2.277}$$

At $\mu = 10$ eV, the vacuum range of the symmetron field is approximately 0.1 μm. Consequently, the field rapidly reaches its VEV, leading the unperturbed wave function to perceive a nearly constant potential shift (except for the initial 0.1 μm above the mirror, contributing minimally to the integral), resulting in:

$$\delta E_{pq} = \mathfrak{Q}_X \int_{-\infty}^{\infty} dz U_X(z) \left(|\Psi_p^{(0)}(z)|^2 - |\Psi_q^{(0)}(z)|^2 \right)$$
$$\simeq \mathfrak{Q}_X U_X^{VEV} \int_{-\infty}^{\infty} dz \left(|\Psi_p^{(0)}(z)|^2 - |\Psi_q^{(0)}(z)|^2 \right) = 0, \tag{6.2.278}$$

where U_X^{VEV} is the value of $U_X(z)$ corresponding to the VEV. However, the actual behavior of strong scalar fields at such short ranges is to distort the wave functions of the neutron, resulting in vastly different energy shifts for various energy states, which would be readily observable in experiments and thus, constrainable. An example of the real behavior of wave functions is given in Appendix B.6.

In essence, a non-perturbative treatment is indispensable for accurately determining the parameter regions that can be constrained with qBOUNCE.

6.2.3. Comparison of the old CANNEX analysis and this work

Prospective CANNEX constraints for the symmetron model, published in Ref. [81], have vastly underestimated the potential of CANNEX to search for the symmetron field. The primary reason is that existing analyses did not take into account that the plate separation can be varied.

For too small values of μ the field vanishes entirely and with it the induced pressure as well. This happens approximately for [61]

$$\sqrt{\mu^2 - \frac{\rho_V}{M^2}}\, d < \frac{\pi}{2}\,, \tag{6.2.279}$$

where d refers to half the plate separation. For too large μ values, however, the force between the plates gets very weak. Hence, CANNEX can only probe a small interval of μ values. It has been found that in some cases pressure gradients provide better constraints than the pressure itself and that the plate separation has a large impact on the limits. The analysis herein significantly improves on the previous analysis in [81]. Specifically, for $\mu = 1$ eV, corresponding roughly to an interaction range of 0.2 μm, the CANNEX constraints have previously been underestimated by a factor of $\sim 10^{20}$ on the λ_S axis, since a plate separation of 10 μm was assumed. Clearly, a smaller plate separation of 3 μm yields an enormously stronger pressure and consequently better constraints. Due to the same reason, previous limits for $\mu = 0.1$ eV have also been underestimated by several orders of magnitude. Based on Eq. (6.2.279), in combination with a value of $d = 10$ μm, the conclusion was drawn in [81], that CANNEX can probe only parameter values $M > 10^{-4}$ GeV for $\mu = 0.1$ eV. However, increasing d to 20 μm removes this constraint, and more substantial limits with $M > 10^{-6}$ GeV can be obtained, resulting in significant improvements with respect to existing constraints.

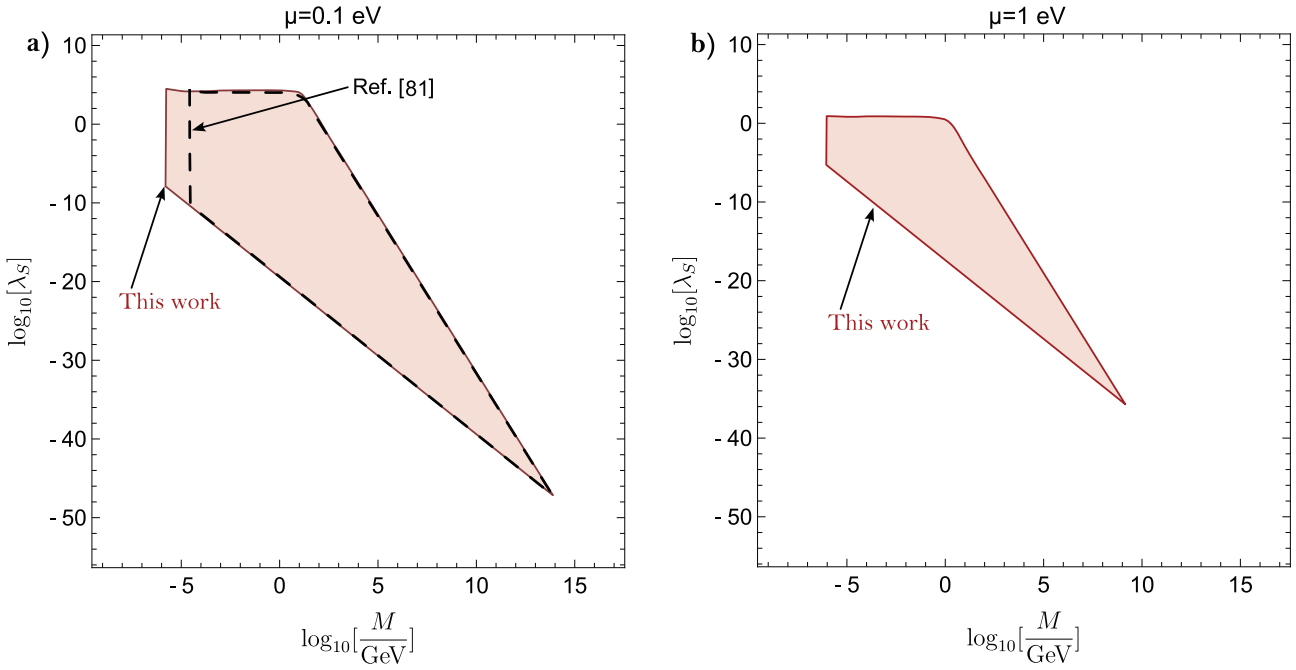

Fig. 6.2.4: The prospective CANNEX constraints derived in Ref. [81] are compared to constraints computed in this thesis. **a)** The value μ is fixed to 0.1 eV. The constraints largely overlap, however, constraints in Ref. [81] have underestimated the potential of CANNEX by around two orders of magnitude on the M axis. **b)** The value μ is fixed to 1 eV. The constraints computed in Ref. [81] are far below the lower cut-off (they violate Eq. (3.3.69)), resulting in a null result. The constraints have been vastly underestimated.

6.3. Constraints for the chameleon field

The combined constraints from qBOUNCE and CANNEX on the parameters of the chameleon model are illustrated in Fig. 6.3.1.

Each value of the chameleon parameter n typically corresponds to a different chameleon model. This thesis focused on the most commonly studied models: either the parameter Λ is fixed to the dark energy scale of 2.4 meV (Fig. 6.3.1 a)), where models for small n are considered, or $n = 1$, while allowing the other parameters to vary (Fig. 6.3.1 b)).

In Fig. 6.3.1 a), only CANNEX is anticipated to probe new regions of the parameter space. qBOUNCE and neutron interferometry are unable to constrain this portion of the parameter space. The contour from CANNEX (indicated by the black arrow) arises from a cutoff (it is required that the field decays to ϕ_M inside the upper mirror, as explained for dilaton constraints in Section 6.1.1). However, the pressure at the contour only slightly exceeds the measurement sensitivity. Even if the necessity of this cutoff was eliminated by simulating the entire vacuum chamber, the contour would only marginally shift.

No new constraints have been found for the case of $n = 1$ and varying Λ, as shown in Fig. 6.3.1 b). Neutron interferometry constraints have not been thoroughly analyzed, as justified in Section 5.5.2, while qBOUNCE constraints are relatively weak. The diagonal cuts in Fig. 6.3.1 b) (the cutoff pointed to by the CANNEX arrow and the parallel qBOUNCE cutoff) ensure that the vacuum range cannot exceed 1 mm for either experiment, and for CANNEX, the field must decay to ϕ_M inside the upper mirror, as explained for the dilaton constraints in Section 6.1.1. The upper qBOUNCE cutoff and the parallel CANNEX cutoff stem from Eq. (3.2.64).

The primary reason that *q*BOUNCE and neutron interferometry yield relatively weak constraints compared to symmetron and dilaton constraints is that the mass of the chameleon field scales with $\rho^{3/2}$ for $n = 1$ (see Eq. (3.2.66)), where ρ is the matter density, while for the dilaton field, the mass approximately scales with $\sqrt{\rho}$ (see Table 1 and 2). For the symmetron, the mass is either dominated by the parameter μ for the symmetry-broken phase or approximately scales with $\sqrt{\rho}$ in the symmetric phase, see Eq. (3.3.71) and Eq. (3.3.73).

Due to the extremely high density of the neutron, its screening (quantified by the screening charge) is usually much more pronounced in chameleons. However, this interpretation relies on the fermi screening approximation.

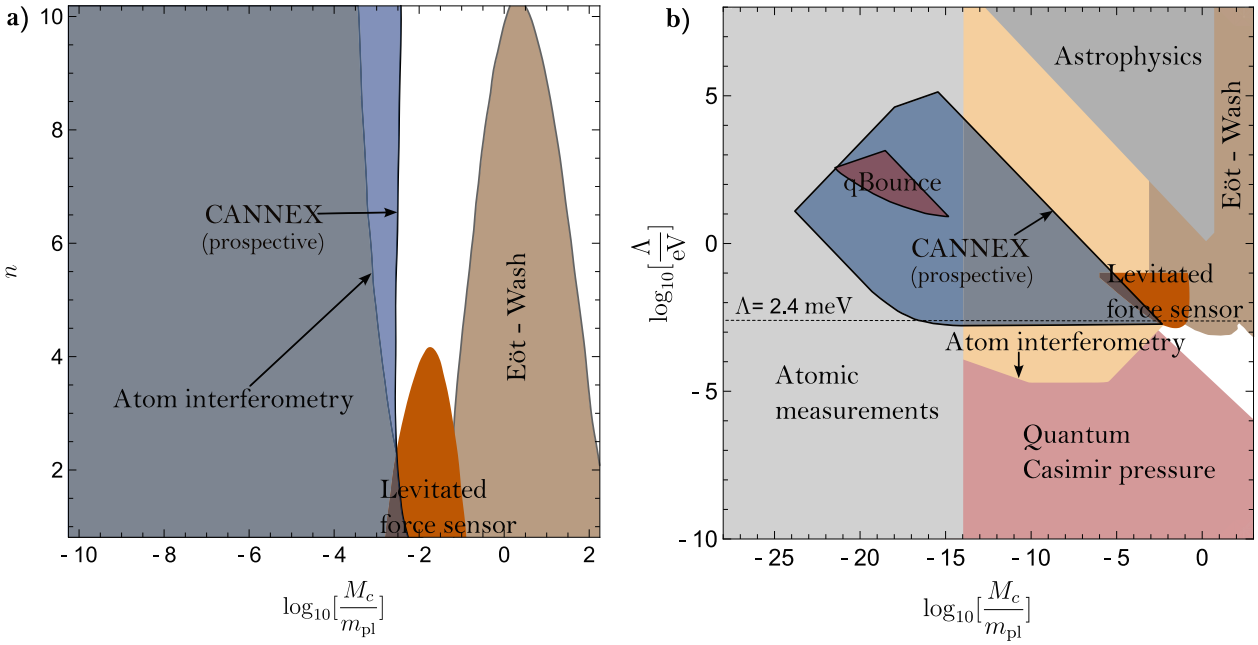

Fig. 6.3.1: Constraints on the parameter space of chameleon models, as elucidated in Ref. [53], are further refined with considerations of quantum Casimir pressure [148], constraints from levitated force sensor measurements [149], atom interferometry [58], and the analyses conducted herein for *q*BOUNCE and CANNEX. **a)** In this context, the parameter Λ is held constant at the dark energy scale of 2.4 meV. The shaded blue region delineates the combined prospective constraints arising from pressure and pressure gradient measurements on chameleon interactions, as inferred from CANNEX. Conversely, neither *q*BOUNCE nor neutron interferometry yield discernible constraints. **b)** Specifically for the chameleon model with $n = 1$, the shaded blue area represents anticipated constraints from CANNEX, which are expected to coincide with existing limits. Meanwhile, the compact dark red region denotes constraints from *q*BOUNCE, overlapping with atomic measurements and the CANNEX-derived constraints. Further explanations are provided in the main text. Figure published in [5].

7. Conclusion

The research conducted for this PhD thesis has yielded several outcomes:

The investigation of the dilaton model has provided detailed insights into its parameter-

dependent behavior, distinguishing between small and large λ regions. This includes exploring screening mechanisms, parameter symmetries (Section 3.1.2), and its potential role as a candidate for dark energy (Section 3.1.3). Additionally, the first exact solution, assuming $\rho_V = 0$, has been derived (Section 4.1), along with detailed solutions addressing intrinsic numerical precision issues (Section 4.2). Techniques for numerical simulation across arbitrary parameters have been developed (Sections 4.4 and 4.5), leading to the derivation of first parameter constraints.

The algorithms devised for dilaton simulations have been generalized to apply to scalar-tensor theories beyond the dilaton model, exhibiting reliability across chameleon and symmetron models as well (Section 4.4.4 and Section 4.5.4).

A thorough examination of equivalence principle violations and deviations from the inverse square law in the context of LLR has led to the establishment of parameter constraints for the dilaton model (Section 5.1 and 6.1).

The analysis of neutron interferometry has refined the phase shift formula (Section 5.2.2), offering a more realistic approach compared to the previous chameleon investigation (cf. Ref. [66]), particularly in considering neutron screening effects. Consequently, this analysis has yielded novel parameter constraints for both the dilaton and symmetron fields (Sections 6.1 and 6.2). Moreover, neutron interferometry has been validated as a potent tool for probing scalar fields with classical ranges as minute as 1 pm, surpassing experiments reliant on classical effects for such parameters. Notably, the examination also revealed the potential formation of domain walls within the vacuum chamber, prompting further investigation (Section 5.5.2).

The analysis of *q*BOUNCE has resulted in a robust numerical method (Section 4.6.3) to solve the stationary Schrödinger equation even in the strongly perturbed regime. The equations of motion for screened scalar fields (Section 4.4) can now be solved numerically for various models, eliminating the need for additional assumptions such as a vanishing vacuum density to find analytical solutions (as was the case in Ref. [77] for the chameleon model). In total, constraints for the dilaton, symmetron, and chameleon model have been derived, constraining previously unconstrained parts of the parameter space for the symmetron and dilaton model. Similarly to neutron interferometry, a fully non-perturbative treatment has revealed that *q*BOUNCE is also able to probe extremely small scalar field ranges, sometimes as low as 1 pm (Section 6.2).

The CANNEX analysis has clearly highlighted the numerical unsuitability of the original analytical formula for the pressure (Section 5.4.2 and Appendix B.1) and provided a solution by bringing the original formula into a numerically more suitable form. The results have been utilized for the first complete analysis of CANNEX, including variations of vacuum density, plate separation, and pressure gradients to derive the best prospective constraints possible for the dilaton, symmetron, and chameleon model (Section 6). Section 6.2.3 has shown that the analysis in this thesis provides significant improvements compared to previous analyses.

In summary, significant strides have been made in the analysis of screened scalar fields within the contexts of LLR, neutron interferometry, *q*BOUNCE, and CANNEX.

8. Contributions of Collaborators

This research was funded by the FWF project P 34240-N. I extend my sincere gratitude to my collaborators for their invaluable contributions to this work:

Mario Pitschmann:[1]

- Acquisition of funding, supervision, conceptualization.

- Reviewed all analytical calculations, simplifying them if possible.
- Provided several influential working notes:
  - Lecture notes on "gravitation and cosmology II" / working notes on scalar-tensor theory, serving as the primary reference for Section 2.
  - Dilaton working notes, including formulas for mass and potential minimum (Section 3.1) and idea to investigate the dilaton field as a source of dark energy according to Eq. (3.1.54); approximate one and two mirror solutions (Appendix C); approximate spherical field profile with screening charge, detailed derivation and motivation for analytical formulas for hypothetically induced dilaton effects for LLR, first CANNEX pressure formula (as in Eq. (5.4.237)), utilization of perturbation theory and the effective g approach for qBOUNCE (Section 4.6.1-4.6.2).
  - Working notes on the Lloyd interferometer, providing a similar phase shift derivation as needed for neutron interferometry (Section 5.2.2).
  - All these notes, excepting the lecture notes on "gravitation and cosmology II" are collected in his habilitation thesis [93].

René Sedmik:[1]

- Offered guidance on numerical techniques.
- Contributed to the ideas of avoiding overflows in Section 4.2.2, as well to the ideas on mesh construction in Section 4.4.2.
- Provided experimental parameters and sensitivities, as well as figures for qBOUNCE and CANNEX experiments.

Christian Käding:[1]

- Provided essential references related to scalar fields in the context of dark matter, enriching the theoretical background of this research.

Philippe Brax:[2]

- Suggested investigating the environment-dependent dilaton model.
- Suggested to search for a parameter symmetry in the large λ region after seing the systematic shifting behavior of constraints in this region. (see Section 3.1.2)

Stephan Sponar:[1]

- Provided figures illustrating neutron interferometry setups.
- Offered a summary of neutron interferometry, adapted for inclusion in this work.

Hartmut Lemmel:[1,3]

- Provided experimental parameters for neutron interferometry.
- Offered dimensions for the vacuum chamber in the projective split interferometer.

Tobias Jenke:[3]

- Provided constraint criteria and their derivation in the context of neutron interferometry, as detailed in Section 5.5.2.

Hartmut Abele:[1]

- Confirmed the accuracy of employed *q*BOUNCE parameters provided in Appendix D.

Affiliations:
[1]: Atominstitut, Technische Universität Wien, Stadionallee 2, A-1020 Vienna, Austria
[2]: Institut de Physique Théorique, Université Paris-Scalay, CEA, CNRS, F-91191 Gif/Yvette Cedex, France
[3]: Institut Laue Langevin, 38000 Grenoble, France

A. Bounds on Stationary Scalar Fields

The aim of this Section is to establish the following theorem:

Theorem
Let ϕ be a scalar field with the following properties:

- $\rho_1 < \rho_2 \Rightarrow \phi_{\rho_1} > \phi_{\rho_2}$
- $V_{\mathit{eff},\phi\phi}(\phi;\rho) > 0$ *for all* ϕ *and* ρ,

then the scalar field obeys the following bounds: Let $\hat{\Omega} \subset \mathbb{R}^3$, and ϕ be a stationary scalar field on $\hat{\Omega}$ with Dirichlet boundary conditions $\phi(\vec{x}) = \phi_\rho(\vec{x})$ on $\partial\hat{\Omega}$, where $\phi_\rho(\vec{x})$ has been defined in Eq. (4.5.151). Moreover, assume the density is bounded by

$$\rho_{min} \leq \rho(\vec{x}) \leq \rho_{max} \text{ for all } \vec{x} \in \hat{\Omega}, \tag{A.0.280}$$

then the scalar field is bounded by

$$\phi_{\rho_{max}} \leq \phi(\vec{x}) \leq \phi_{\rho_{min}}, \quad \text{for all } \vec{x} \in \hat{\Omega}. \tag{A.0.281}$$

All stationary scalar field calculations in this thesis employed the Dirichlet boundary conditions stated in this theorem. This inequality is frequently referenced throughout this thesis, and a proof is provided in this Section. The discussion commences with the following observation:

Lemma
Let $\hat{\Omega} \subset \mathbb{R}^3$, and ϕ be a scalar field on $\hat{\Omega}$ with the same properties as in the theorem and Dirichlet boundary conditions $\phi(\vec{x}) = \phi_\rho(\vec{x})$ on $\partial\hat{\Omega}$. Then ϕ cannot have any local minima with $\phi(\vec{x}) < \phi_\rho(\vec{x})$, nor can it have local maxima with $\phi(\vec{x}) > \phi_\rho(\vec{x})$.

Proof of the Lemma
Only the first statement is proved; the second statement follows similarly. From

$$V_{\mathrm{eff},\phi\phi}(\phi(\vec{x});\rho(\vec{x})) > 0 \tag{A.0.282}$$

follows that $V_{\mathrm{eff},\phi}$ is a strictly increasing function of $\phi(\vec{x})$ with

$$V_{\text{eff},\phi}(\phi(\vec{x});\rho(\vec{x})) < 0, \text{ for } \phi(\vec{x}) < \phi_\rho(\vec{x}),$$
$$V_{\text{eff},\phi}(\phi(\vec{x});\rho(\vec{x})) > 0, \text{ for } \phi(\vec{x}) > \phi_\rho(\vec{x}). \tag{A.0.283}$$

From the differential equation, one obtains

$$\Delta\phi(\vec{x}) = V_{\text{eff},\phi}(\phi(\vec{x});\rho(\vec{x})) < 0, \text{ for } \phi(\vec{x}) < \phi_\rho(\vec{x}). \tag{A.0.284}$$

Next, assume a local minimum at $\vec{x}_0 = (x_0, y_0, z_0)$ with $\phi(\vec{x}_0) < \phi_\rho(\vec{x}_0)$. I will show that this leads to a contradiction. From

$$\Delta\phi(\vec{x}_0) < 0, \tag{A.0.285}$$

follows that at least one second partial derivative is smaller than 0. Without loss of generality, assume

$$\frac{\partial^2\phi}{\partial z^2}(\vec{x}_0) < 0. \tag{A.0.286}$$

The function

$$f(z) := \phi(x_0, y_0, z) \tag{A.0.287}$$

is a 1D slice of ϕ and thus also has a local minimum at z_0. Since $\phi(\vec{x}) = \phi_\rho(\vec{x})$ at the boundary of $\hat{\Omega}$, this minimum cannot be at the boundary, and the first partial derivatives of ϕ have to vanish.

However, the above considerations imply

$$\frac{df}{dz}(z_0) = \frac{\partial\phi}{\partial z}(\vec{x}_0) = 0,$$
$$\frac{d^2f}{dz^2}(z_0) = \frac{\partial^2\phi}{\partial z^2}(\vec{x}_0) < 0. \tag{A.0.288}$$

These conditions are well known to imply a local maximum of f at z_0, which is a contradiction. Hence local minima with $\phi(\vec{x}) < \phi_\rho(\vec{x})$ are impossible. □

This Lemma is used to prove the theorem:

Proof of the theorem

Since ϕ is continuous with finite boundary conditions, it has a (possibly not unique) global minimum and global maximum[17]. Assume that the global minimum at $\vec{x}_0$ fulfills

$$\phi(\vec{x}_0) < \phi_{\rho_{\max}}. \tag{A.0.289}$$

Trivially, the global minimum is also a local minimum. However, since $\rho_2 > \rho_1$ implies $\phi_{\rho_1} > \phi_{\rho_2}$, it follows

$$\phi(\vec{x}_0) < \phi_{\rho_{\max}} \leq \phi_\rho(\vec{x}_0). \tag{A.0.290}$$

Thus, $\phi(\vec{x}_0)$ is a local minimum with $\phi(x_0) < \phi_\rho(\vec{x}_0)$, which contradicts the last lemma. Hence one finds

$$\phi_{\rho_{\max}} \leq \phi(\vec{x}), \text{ for all } \vec{x} \in \hat{\Omega}. \tag{A.0.291}$$

The proof for the upper bound follows analogous reasoning. □

Applications to the dilaton and chameleon field

The chameleon and dilaton field both fulfill the assumptions of the theorem, as can easily be checked. This theorem, however, does not apply to the symmetron field. For example, in the symmetry-broken phase, the potential has a local maximum at $\phi = 0$, hence $V_{\text{eff},\phi\phi}(0;\rho) < 0$.

B. Additional numerical investigations

B.1. Comparisons of the two pressure formulas

This Section formally demonstrates the numerical superiority of the pressure formula in CANNEX, given by Eq. (5.4.240), over the previous formulation, Eq. (5.4.237), with a focus on the dilaton model. Notably, the value at the upper surface of the upper plate is given by (5.4.250):

$$\phi^2(d+D) = \frac{2m_{\text{pl}}^2}{A_2(\rho_M - \rho_V)}\Big(V_{\text{eff}}(\phi_M;\rho_M) - V_{\text{eff}}(\phi_V;\rho_V)\Big). \tag{B.1.292}$$

This leads to two analytically equivalent methods for computing the pressure:

$$P_1\big(\phi_d\big) := \rho_M \frac{A_2}{2m_{\text{pl}}^2}\Big[\phi_d^2 - \phi^2(d+D)\Big], \tag{B.1.293}$$

$$P_2\big(\phi_0\big) := \frac{\rho_M}{\rho_M - \rho_V}\Big(V_{\text{eff}}(\phi_V;\rho_V) - V_{\text{eff}}(\phi_0;\rho_V)\Big), \tag{B.1.294}$$

with $\phi_0 := \phi(0)$ and $\phi_d := \phi(d)$.

The primary objective is to assess the amplification of relative errors in the arguments ϕ_d and ϕ_0 by their respective formulas. A standard approach involves calculating the condition number [151]. For a given function $f(x)$, the aim is to determine the relative error of $f(x)$ given a relative error in x. Assuming uncertainty in the real value of x and using $\tilde{x}$ as an approximation, one employs a Taylor expansion:

$$\begin{aligned} f(\tilde{x}) &\simeq f(x) + \frac{df}{dx}(x)(\tilde{x}-x), \\ \Rightarrow \Big|\frac{f(\tilde{x})-f(x)}{f(x)}\Big| &\simeq \Big|\frac{\frac{df}{dx}(x)}{f(x)}x\Big|\,\Big|\frac{(\tilde{x}-x)}{x}\Big|, \\ K &:= \Big|\frac{\frac{df}{dx}(x)}{f(x)}x\Big|. \end{aligned} \tag{B.1.295}$$

Here, K is the condition number, where $K > 1$ signifies error amplification, while $K < 1$ indicates error dampening. For the pressure formulas, these values are given by

[17] The Extreme Value Theorem [150] proofs that for any continuous function defined on a compact set (which means bounded sets containing their boundary, such as spheres), the function is bounded and attains both a global maximum and minimum. In unbounded domains, a continuous function may grow arbitrarily large as $|\vec{x}| \to \infty$, and therefore, it may not possess a global maximum or minimum. However, the focus is solely on the physically relevant scenario, where $\phi(\vec{x})$ approaches its potential minimum as $|x| \to \infty$, ensuring it remains bounded even in $\mathbb{R}^3$ with a finite global maximum and minimum.

$$K_{P_1} = |\frac{\frac{\partial P_1}{\partial \phi_d}}{P_1}\phi_d| = |\frac{\rho_M \frac{A_2}{m_{pl}^2}\phi_d}{P_1}\phi_d|,$$
$$K_{P_2} = |\frac{\frac{\partial P_2}{\partial \phi_0}}{P_2}\phi_0| = |\frac{\frac{\lambda V_0}{m_{pl}} e^{-\lambda\phi_0/m_{pl}} - \rho_V A_2 \frac{\phi_0}{m_{pl}^2}}{P_2}\phi_0|. \tag{B.1.296}$$

The ratio

$$\alpha := \frac{K_{P_1}}{K_{P_2}} = |\frac{\rho_M \frac{A_2}{m_{pl}^2}\phi_d}{\frac{\lambda V_0}{m_{pl}} e^{-\lambda\phi_0/m_{pl}} - \rho_V A_2 \frac{\phi_0}{m_{pl}^2}} \frac{\phi_d}{\phi_0}|, \tag{B.1.297}$$

quantifies how much worse the error propagation properties of the old formula P_1 are compared to the new formula P_2, utilizing $P_1 = P_2$ and $\frac{\rho_M}{\rho_M - \rho_V} \simeq 1$, which holds to an extremely good approximation for the CANNEX setup. Fig. B.1.1 plots α close to the contour of the CANNEX constraint region. The error propagation properties of the original formula worsen significantly for large values of A_2, reaching $\alpha > 10^{500}$ at $A_2 = 10^{52}$, rendering the original formula numerically unusable.

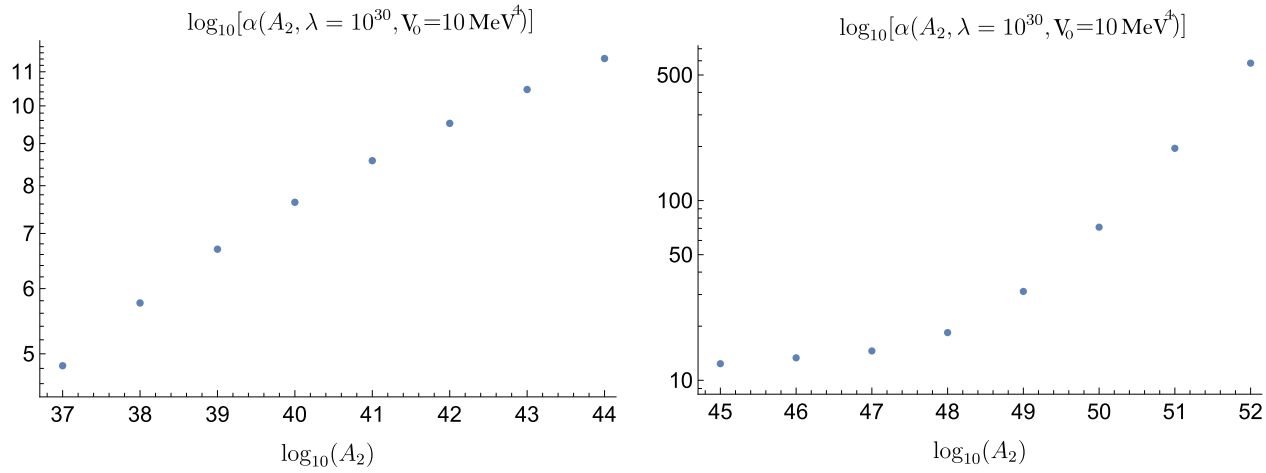

Fig. B.1.1: B.1.297 is plotted close to the contour of the CANNEX exclusion region. At the upper edge, the relative error propagation of the old formula is worse by roughly a factor 10^{500} and hence completely unusable numerically.

Another analysis confirms the above observation. With an exact two mirror solution derived in Section 4 for $\rho_V = 0$, which remains practically exact even for $\rho_V \neq 0$ at $A_2 \leq 10^{45}$ and $V_0 = 10$ MeV^4, one can compute the pressure analytically in two equivalent ways.

Performing the following consistency checks involves computing the pressure using either formula for the analytically exact solution and for numerical simulations, which align well with the analytical solution for these parameters. The results are shown in Fig. B.1.2 **a)**, where, as expected, both formulas yield practically the same result with the analytical solution. Discrepancies start appearing at the percent level near $A_2 = 10^{45}$ due to the solution no longer approximating the case $\rho_V \neq 0$.

The situation is starkly different for simulations. Even at $A_2 = 10^{44}$, both results disagree by a factor of roughly 10^7.

To ensure the reliability of using simulations with the new formula, a comparison is made between results obtained using the analytical solution and numerical solution with the new formula, finding agreement within a few percent, as shown in B.1.2 **b)**.

The discovery of the new formula for the pressure was hence instrumental in obtaining reliable parameter constraints, due to the absence of analytically exact solutions. For similar reasons, it is also very useful for computing the pressure for the chameleon field, where the exact two mirror solution is only known for the case $n = 1$, and the exact one mirror solution for no parameters.

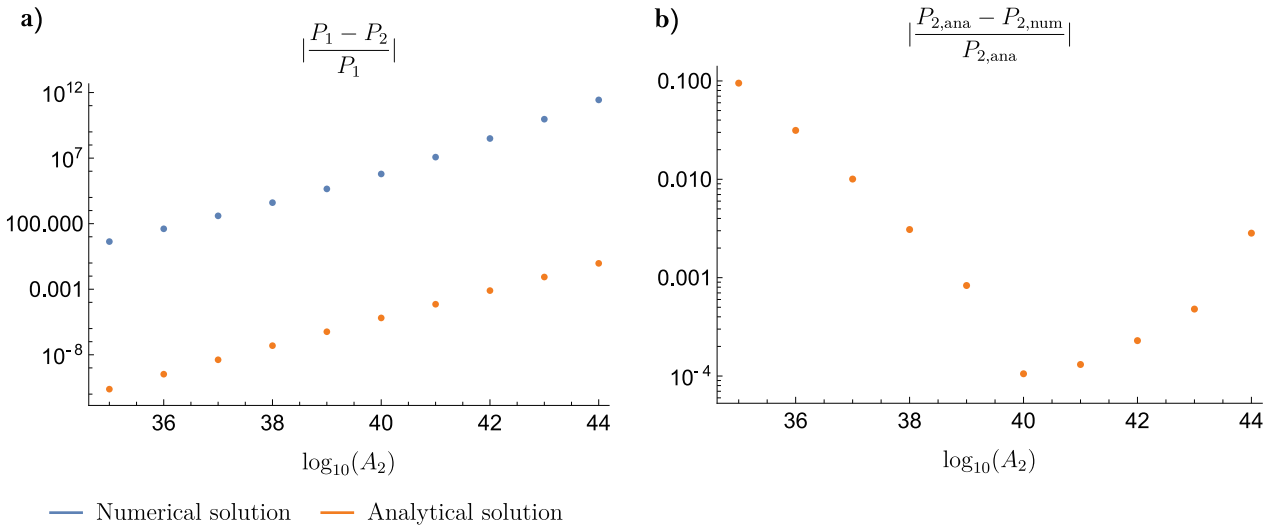

Fig. B.1.2: **a)** A consistency check is shown for the two equivalent pressure formulas for numerical simulations and the analytically exact solution with $\rho_V = 0$. **b)** A comparison of the pressure obtained from the analytical solution and from numerical simulations with the new formula is shown. $V_0 = 10$ MeV^4 and $\lambda = 10^{31.5}$ were kept fixed, these values lie very close to the contour of the exclusion region, and are hence very relevant.

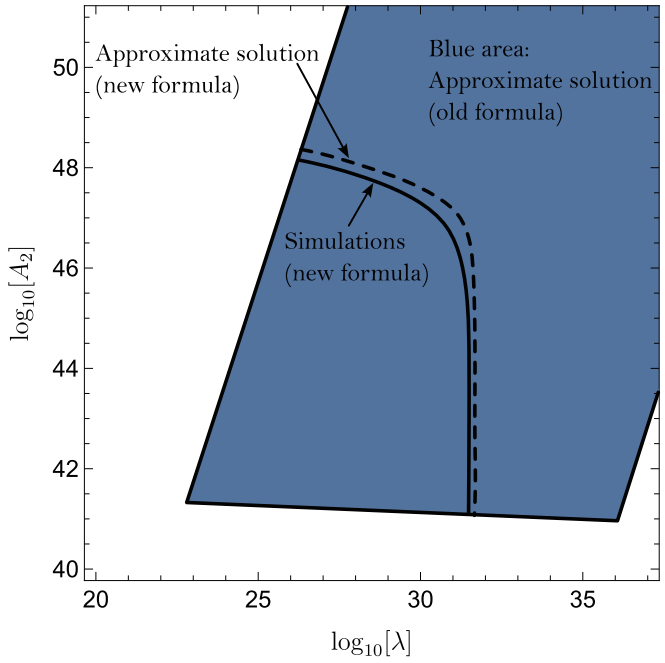

Fig. B.1.3: This figure shows a comparison between constraints obtained from P_1 (B.1.293) computed from the approximate two mirror solution in Appendix C (blue area without clear bounds), the constraint computed from P_2 (B.1.294) with the same solution and constraints computed from P_2 with simulations. The parameter V_0 was fixed to 10 MeV^4 and $\rho_V = 2.28 \times 10^{-20}$ MeV^4.

In Fig. B.1.3, the efficacy of the new formula Eq. (B.1.294) is presented. Even when derived from the crude analytical two mirror approximation in Appendix C and compared against much more accurate simulations, the deviations between constraints are minimal in a log-log plot when computed with the new formula, as expected for a formula with good error propagation properties.

Conversely, utilizing the exact value at the upper surface of the upper mirror alongside the two mirror approximation with the old pressure formula Eq. (B.1.293) yields constraints lacking clear bounds. The errors are so pronounced that the resulting data is effectively numerical garbage. Constraints from simulations solely with the old formula were not computed due to persistent numerical challenges encountered when attempting this method. However, it's worth noting that significant disparities in pressure between the approximate solution and simulations were encountered when initially pursuing this approach.

B.2. CANNEX error in using a homogeneous mirror density

This Section demonstrates that the approximation of treating all mirrors in CANNEX with the same average density ($\rho_M = 2514$ kg/m^3), results in a negligible error on the derived prospective constraints. Figure B.2.1 illustrates a comparison of constraints computed for the dilaton model, assuming mirrors are entirely composed of gold ($\rho_M = 19320$ kg/m^3), the densest layer, and silica ($\rho_M = 2329$ kg/m^3), the layer with the lowest density. Remarkably, the constraints exhibit identical behavior in a log-log plot, indicating that the pressure is highly insensitive to the specific value of the material density.

This consistent behavior holds true for both the chameleon and symmetron models as well. Consequently, the error introduced by treating all mirrors with the same average density is deemed

entirely negligible. In the context of CANNEX, my findings indicate that only the vacuum density significantly influences the computed constraints.

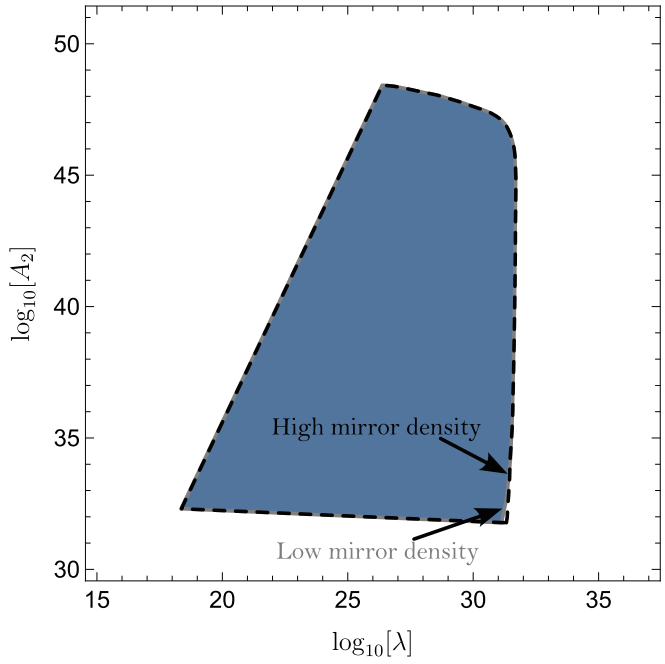

Fig. B.2.1: The prospective constraints from CANNEX are compared for two mirror densities: $\rho_M = 19320$ kg/m^3 and $\rho_M = 2329$ kg/m^3, considering $V_0 = 10$ MeV^4. Remarkably, both densities yield nearly identical constraints, with only a minuscule mismatch observed near the arrows. It's noteworthy that there is no discernible mismatch whatsoever in the small λ region. The symmetron and chameleon models exhibit comparable insensitivity to the precise values of the mirror densities. Given the substantial computational effort required to execute numerous simulations, this plot was generated based on the approximate two mirror setup outlined in Appendix C. Nevertheless, the simulations consistently demonstrate the same insensitivity to the mirror density.

B.3. qBOUNCE error of the fermi screening approximation

This Section highlights the potential significant error associated with the fermi screening approximation. The existing symmetron analysis [64] considered both the micron screening approximation (modeling the neutron as a sphere with a radius of 5.9 μm) and the fermi screening approximation (modeling the neutron as a sphere with a radius of 0.5 fm). The resulting constraints on the parameters of the symmetron field exhibited deviations spanning several orders of magnitude.

The micron screening calculation underscored the profound theoretical uncertainties inherent in the qBOUNCE symmetron calculations. To illustrate this point, the first dilaton constraints published in [2] are provided in Fig. B.3.1 that included the micron screening approximation for qBOUNCE.

The large discrepancy between both approximations shows how uncertain either approximation is, while confirming that the fermi screening approximation is the more conservative estimate.

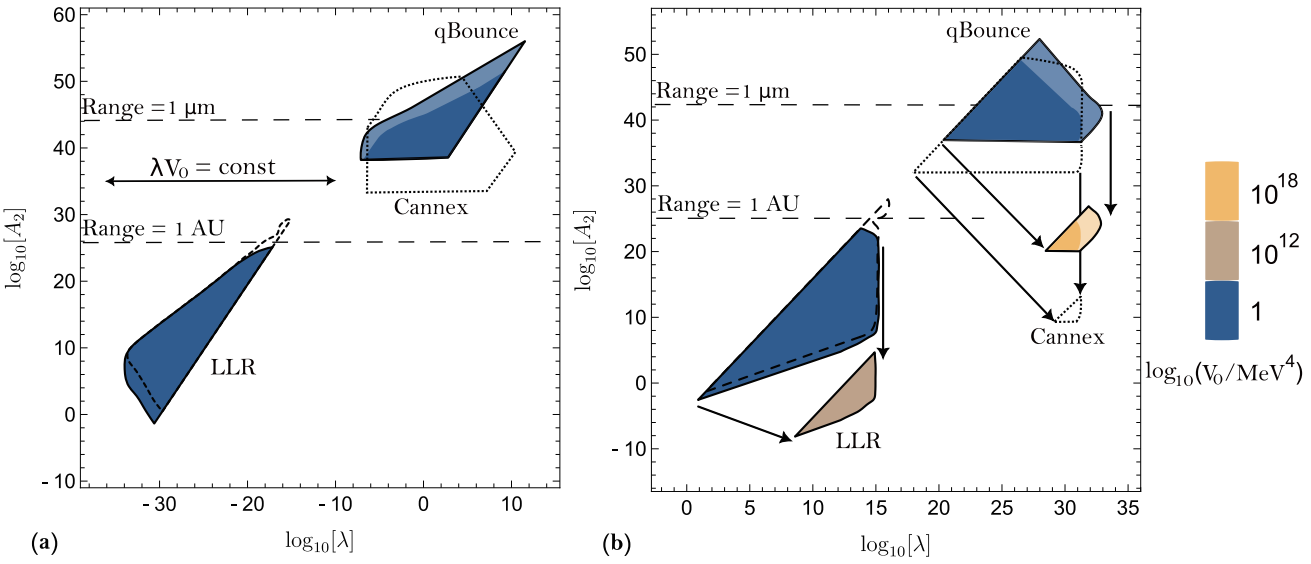

Fig. B.3.1: This figure has been published in [2], and constraints have been computed as explained in this reference. The explanation of this figure matches the explanations of Fig. 6.1.1 in Section 6.1 with two notable differences: First, two *q*BOUNCE constraints are presented: Lighter areas correspond to the micron screening approximation, while darker areas correspond to the fermi screening approximation. Second the individual contributions of LLR I (filled blue areas) and LLR II (dashed LLR area) are shown. The main text provides a more detailed explanation.

B.4. Newton's method for the finite difference scheme

The method that was used to solve the discretized differential equation (4.4.122) is outlined in the following.

The definition

$$\begin{aligned} F &: \mathbb{R}^N \to \mathbb{R}^N \\ F_i(\phi_1, ..., \phi_N) &= \frac{2(\phi_{i+1} - \phi_i)}{h_i(h_i + h_{i-1})} - \frac{2(\phi_i - \phi_{i-1})}{h_{i-1}(h_i + h_{i-1})} + \Gamma \frac{2}{s_i}\left[\frac{h_i(\phi_i - \phi_{i-1})}{h_{i-1}(h_i + h_{i-1})} + \frac{h_{i-1}(\phi_{i+1} - \phi_i)}{h_i(h_i + h_{i-1})}\right] \\ &\quad - V_{\text{eff},\phi}(\phi_i, \rho_i), \end{aligned} \tag{B.4.298}$$

results in an N-dimensional root-finding problem for F. The values ϕ_0 and ϕ_{N+1} must be fixed to set the boundary conditions. The equation

$$F(\phi_1, ..., \phi_N) = (0, ..., 0)^T \tag{B.4.299}$$

can be solved using Newton's method (refer to [151]). Starting from an initial guess $\phi^{(0)} = (\phi_1^{(0)}, ..., \phi_N^{(0)})$, F is linearized around that guess and the following equation solved:

$$F(\phi^{(0)}) + J_F(\phi^{(0)})(\phi^{(1)} - \phi^{(0)}) = 0, \tag{B.4.300}$$

with the Jacobi Matrix $(J_F)_{ij} := \frac{\partial F_i}{\partial \phi_j}$. This defines the improved guess $\phi^{(1)}$, and the procedure is iterated. In the n'th iteration, the linear system

$$
\begin{aligned}
A^{n-1}\phi^{(n)} &= b^{n-1},\\
A^{n-1} &:= J_F(\phi^{(n-1)}),\\
b^{n-1} &:= -F(\phi^{(n-1)}) + J_F(\phi^{(n-1)})\phi^{(n-1)},
\end{aligned}
\tag{B.4.301}
$$

needs to be solved. For $i = 2, ..., N-1$, A^{n-1} and b^{n-1} are given by

$$
A_{ij}^{n-1} = \begin{cases}
\frac{2}{h_i(h_i+h_{i-1})} + \Gamma\frac{2}{s_i}\frac{h_{i-1}}{h_i(h_i+h_{i-1})} & , \text{if } j = i+1\\
\frac{2}{h_{i-1}(h_i+h_{i-1})} - \Gamma\frac{2}{s_i}\frac{h_i}{h_{i-1}(h_i+h_{i-1})} & , \text{if } j = i-1,\\
-\frac{2}{h_i(h_i+h_{i-1})} - \frac{2}{h_{i-1}(h_i+h_{i-1})} + \Gamma\frac{2}{s_i}\left[\frac{h_i}{h_{i-1}(h_i+h_{i-1})} - \frac{h_{i-1}}{h_i(h_i+h_{i-1})}\right] - V_{\text{eff},\phi\phi}(\phi_i^{(n-1)}, \rho_i) & , \text{if } j = i,\\
0 & , \text{else },
\end{cases}
\tag{B.4.302}
$$

and

$$
b_i^{n-1} = V_{\text{eff},\phi}(\phi_i^{(n-1)}; \rho_i) - V_{\text{eff},\phi\phi}(\phi_i^{(n-1)}; \rho_i)\phi_i^{(n-1)}. \tag{B.4.303}
$$

The remaining values must account for the boundary conditions.

B.4.1. Boundary conditions for the one and two mirror case

The fields minimize their effective potential at the boundary, hence $\phi_0 = \phi_M$, and $\phi_{N+1} \in \phi_V, \phi_M$ for the one and two mirror cases, respectively. This results in

$$
\begin{aligned}
A_{1,1}^{n-1} &= -\frac{2}{h_1^2} - V_{\text{eff},\phi\phi}(\phi_1^{(n-1)}; \rho_1),\\
A_{1,2}^{n-1} &= \frac{1}{h_1^2},\\
A_{N,N-1}^{n-1} &= \frac{1}{h_{N-1}^2},\\
A_{N,N}^{n-1} &= -\frac{2}{h_{N-1}^2} - V_{\text{eff},\phi\phi}(\phi_N^{(n-1)}, \rho_N),\\
b_1^{n-1} &= V_{\text{eff},\phi}(\phi_1^{(n-1)}; \rho_1) - V_{\text{eff},\phi\phi}(\phi_1^{(n-1)}; \rho_1)\phi_1^{(n-1)} - \frac{\phi_0}{h_1^2},\\
b_N^{n-1} &= V_{\text{eff},\phi}(\phi_N^{(n-1)}; \rho_N) - V_{\text{eff},\phi\phi}(\phi_N^{(n-1)}; \rho_N)\phi_N^{(n-1)} - \frac{\phi_{N+1}}{h_{N-1}^2},
\end{aligned}
\tag{B.4.304}
$$

where $h_0 := h_1$, $h_N := h_{N-1}$.

B.4.2. Boundary conditions for a sphere and the cross section of a cylinder

r=0:

In the context of spherical geometry and the cross section of a cylinder, ensuring $\frac{d\phi}{dr}|_{r=0} = 0$ is imperative to address the coordinate singularity at $r = 0$ in Eq. (4.4.117).

To overcome this singularity, a ghost point at $r_0 := -r_1 < 0$ with no physical significance is introduced and ϕ_0 defined as

$$\phi_0 := \phi_1. \tag{B.4.305}$$

Although $\phi_{1/2} := \phi(0)$ is excluded from discretization to circumvent the singularity, the condition $\frac{d\phi}{dr}|r = 0$ is guaranteed by Eq. (4.4.121) if the neighboring points of $\phi_{1/2}$ are chosen to be ϕ_0 and ϕ_1. This avoidance strategy for the singularity has been proposed in [152]. Utilizing (B.4.305) for $i = 1$ and $r_1 = h_0/2$ yields

$$\begin{aligned} A_{1,1} &:= -\frac{6}{h_1(h_1+h_0)} - V_{\text{eff},\phi\phi}(\phi_1^{(n-1)}, \rho_1), \\ A_{1,2} &:= \frac{6}{h_1(h_1+h_0)}, \\ b_1 &:= V_{\text{eff},\phi}(\phi_1^{(n-1)}; \rho_1) - V_{\text{eff},\phi\phi}(\phi_1^{(n-1)}; \rho_1)\phi_1^{(n-1)}. \end{aligned} \tag{B.4.306}$$

$r =$ **cutoff**:

By setting $h_N := h_{N-1}$ and using $\phi_{N+1} = \phi_B$, with $\phi_B = \phi_M$ for the cross section of a cylinder, and $\phi_B = \phi_V$ for a sphere, it follows

$$\begin{aligned} A_{N,N-1}^{n-1} &= \frac{1}{h_{N-1}^2} - \frac{1}{r_N h_{N-1}}, \\ A_{N,N}^{n-1} &= -\frac{2}{h_{N-1}^2} - V_{\text{eff},\phi\phi}(\phi_N^{(n-1)}, \rho_N), \\ b_N^{n-1} &= V_{\text{eff},\phi}(\phi_N^{(n-1)}; \rho_N) - V_{\text{eff},\phi\phi}(\phi_N^{(n-1)}; \rho_N)\phi_N^{(n-1)} - \frac{\phi_B}{h_{N-1}^2} - \frac{\phi_B}{r_N h_{N-1}}. \end{aligned} \tag{B.4.307}$$

B.4.3. Convergence

The euclidean norm

$$||\phi^{(n)}||_2 := \sqrt{\sum_{i=0}^{N+1} (\phi_i^{(n)})^2}, \tag{B.4.308}$$

is used to monitor convergence and iterations are stopped when

$$\frac{||\phi^{(n)} - \phi^{(n-1)}||_2}{||\phi^{(n-1)}||} < \varepsilon, \tag{B.4.309}$$

where ε is sufficiently small. Mathematica's LinearSolve function was utilized for solving the linear systems of equations. The remaining task involves determining an initial guess.

B.4.4. Initial guess

The success of Newton's method in achieving convergence relies on selecting an appropriate initial guess, denoted as $\phi^{(0)}$. Three reliable seeds consistently leading to convergence have been identified.

For the dilaton and chameleon models, convergence is guaranteed with either of the following trivial guesses:

- $\phi_i^{(0)} := \phi_M$
- $\phi_i^{(0)} := \phi_{\rho(s_i)}$

In the symmetron model, the effective potential is expanded around its potential minimum, resulting in a linear differential equation:

$$\frac{d^2\phi}{ds^2} + \Gamma\frac{2}{s}\frac{d\phi}{ds} = V_{\text{eff},\phi\phi}(\phi_\rho(s))\,(\phi(s) - \phi_\rho(s))\,. \tag{B.4.310}$$

This equation can be solved with the same method outlined above using $V_{\text{eff,approx}} := \frac{1}{2}V_{\text{eff},\phi\phi}(\phi_\rho(s))\,(\phi(s) - \phi_\rho(s))^2$. As the linearization of an already linear equation has no impact, Newton's method concludes after a single iteration for an arbitrary initial guess.

B.5. FDMs as a special case of the FEM in one dimension

This Section demonstrates that the non-uniform FDM employed in this thesis is a specialized instance of the FEM for the one and two mirror geometries (this result has not been established for the spherical and cylindrical geometries), achieved through a proper selection of FEM basis functions. The one-dimensional equation of motion is given by

$$\frac{d^2\phi}{dz^2} - V_{\text{eff},\phi}(\phi;\rho) = 0, \tag{B.5.311}$$

which has to be solved over a domain $z \in [a,b]$, subject to appropriate Dirichlet boundary conditions that depend on the geometry under consideration. Starting from a mesh $z_1,\ ...,\ z_N$ with $h_i := h_{i+1} - h_i$, the standard piece-wise linear basis functions for the FEM are defined as

$$\varphi_i(z) := \begin{cases} \frac{z-z_i}{h_{i-1}}, & z \in [z_{i-1}, z_i] \\ \frac{z_{i+1}-z}{h_i}, & z \in [z_i, z_{i+1}] \\ 0, & \text{else.} \end{cases} \tag{B.5.312}$$

It's worth noting that this definition ensures $\varphi_i(z_j) = \delta_{ij}$. Following the procedure outlined in Section 4.5.1, $\mathbf{F}_i$ (see (Eq. 4.5.133)) is given by

$$\mathbf{F}_i(\phi_1,\ ...,\ \phi_N) = -\sum_{j=1}^{N}\phi_j\Big(\int_{z_1}^{z_N}\frac{d\varphi_i}{dz}\frac{d\varphi_j}{dz}dz\Big) - \int_{z_1}^{z_N}V_{\text{eff},\phi}(\sum_{k=1}^{N}\phi_k\varphi_k;\rho)\varphi_i dz, \tag{B.5.313}$$

where the term associated with Neumann boundary conditions has been omitted[18].

The integrals are numerically evaluated in the FEM. A common choice is the trapezoidal rule [151], applied to each subdomain separately:

$$\int_{z_1}^{z_n} f dz = \sum_{i=1}^{N-1} \int_{z_i}^{z_{i+1}} f dz \simeq \sum_{i=1}^{N-1} h_i \frac{f(z_{i+1}) + f(z_i)}{2}. \tag{B.5.314}$$

The trapezoidal rule exactly integrates polynomials up to the first order. A straightforward calculation yields

$$\int_{z_1}^{z_N} \frac{d\varphi_i}{dz} \frac{d\varphi_j}{dz} dz = \begin{cases} \frac{1}{h_{i-1}} + \frac{1}{h_i}, & i = j \\ -\frac{1}{h_{i-1}}, & j = i-1 \\ -\frac{1}{h_i}, & j = i+1 \\ 0, & \text{else.} \end{cases} \tag{B.5.315}$$

Applying the trapezoidal rule to the second integral in Eq. (B.5.313) yields

$$\begin{aligned} \mathbf{F}_i(\phi_1, \ ..., \ \phi_N) &\simeq \frac{\phi_{i-1}}{h_{i-1}} - \phi_i\Big(\frac{1}{h_{i-1}} + \frac{1}{h_i}\Big) + \frac{\phi_{i+1}}{h_i} - \frac{h_i + h_{i-1}}{2} V_{\text{eff},\phi}(\phi_i, \rho_i) \\ &= \frac{h_i + h_{i-1}}{2}\Big[\frac{2(\phi_{i+1} - \phi_i)}{h_i(h_i + h_{i-1})} - \frac{2(\phi_i - \phi_{i-1})}{h_{i-1}(h_i + h_{i-1})} - V_{\text{eff},\phi}(\phi_i, \rho_i)\Big]. \end{aligned} \tag{B.5.316}$$

The final algorithm is based on this approximation. Therefore, the objective of the FEM is to determine $(\phi_1, ..., \phi_N)$ that solves the nonlinear system of equations

$$\frac{2(\phi_{i+1} - \phi_i)}{h_i(h_i + h_{i-1})} - \frac{2(\phi_i - \phi_{i-1})}{h_{i-1}(h_i + h_{i-1})} - V_{\text{eff},\phi}(\phi_i, \rho_i), \ \text{for } i = 1, ..., N, \tag{B.5.317}$$

where the factor $\frac{h_i + h_{i-1}}{2}$ has been omitted since it doesn't affect the root finding problem. Notably, this system of equations is identical to the one derived from the non-uniform FDM, as seen in Eq. (B.4.298) and Eq. (B.4.299). Therefore, the non-uniform FDM can be interpreted as a special case of the FEM.

B.6. The inappropriateness of perturbation theory for the dilaton and symmetron field

This Section shows that perturbation theory is inappropriate to derive constraints for the dilaton or symmetron model and briefly outlines the reason. Fig. B.6.1 shows a direct comparison between constraints computed by always applying perturbation theory to first order and constraints computed from a numerical solution of the Schrödinger equation.

[18] This term evaluates to precisely 0 for the one and two mirror geometries since we require the field to asymptotically minimize its potential, implying that the derivative specified by Neumann boundary conditions vanishes. In practice, we introduce a cut-off while ensuring that the field naturally relaxes to its minimum at the boundary condition, consistent with homogeneous Neumann boundary conditions.

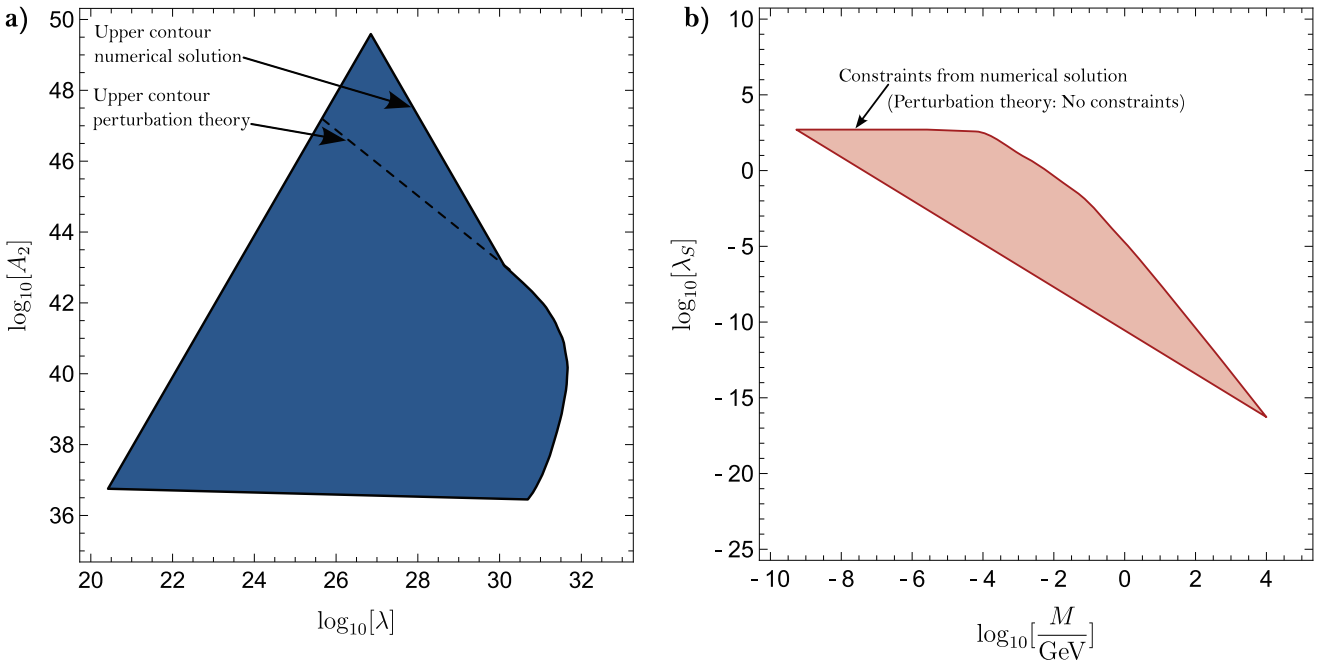

Fig. B.6.1: Examples are presented for comparing dilaton constraints for *q*BOUNCE derived from perturbation theory with those obtained via numerical calculations in the large λ region. **a)** In the investigation of the large λ region of the dilaton field with $V_0 = 10$ MeV^4, the approximate two mirror solution derived in Appendix C was utilized for comparison. It's important to note that the constraints applied here required $|\delta E_{14}| > 2 \times 10^{-15}$ eV. These assumptions slightly deviate from the treatment outlined in the main text, as this comparison predates the completion of this thesis and certain assumptions have been refined subsequently. Due to time constraints and the illustrative nature of this example this analysis was not repeated with the updated constraint criteria. Nevertheless, this doesn't alter the qualitative insight gained, indicating that numerical and perturbative calculations can diverge significantly in magnitude. **b)** Contrasting *q*BOUNCE constraints derived from perturbation theory with those obtained via numerical calculations for the symmetron model with $\mu = 1$ keV reveals that perturbation theory results in *no constraints at all!*

The results disagree by several orders of magnitude. The reason is outlined in the following.

The main task is to compute the outer edge of the constraint area, which is the parameter region where the scalar field effects are just large enough to be still detectable with the current measurement sensitivity of $\sim 10^{-15}$ eV. Since the Newtonian energy states have energies in the 10^{-12} eV regime, one could naivley assume that perturbation theory should be appropriate to compute the correct edge of the constraint volume, where energy differences are at the order of 10^{-15} eV.

Its also possible, for example, that perturbation theory yields the following result:

$$\begin{aligned} \delta E_1 &= 2 \times 10^{-15}\ \text{eV} + 1\ \text{GeV}, \\ \delta E_4 &= 1\ \text{GeV}, \\ \Rightarrow |\delta E_{14}| &= |\delta E_1 - \delta E_4| = 2 \times 10^{-15}\ \text{eV}. \end{aligned} \tag{B.6.318}$$

Despite perturbation theory asserting $|\delta E_{14}| = 2 \times 10^{-15}$ eV—considerably smaller than the individual Newtonian energies—this outcome lacks credibility. The use of perturbation theory necessitates both energy shifts to be individually much smaller than the Newtonian contribution, thereby questioning its reliability. Hence, generally, determining the surface of the constraint volume necessitates non-perturbative techniques.

The following example illustrates the real behavior of wave functions at the edge of the constraint region, assuming the strongly perturbed regime.

Wave Function Perturbation Analysis:

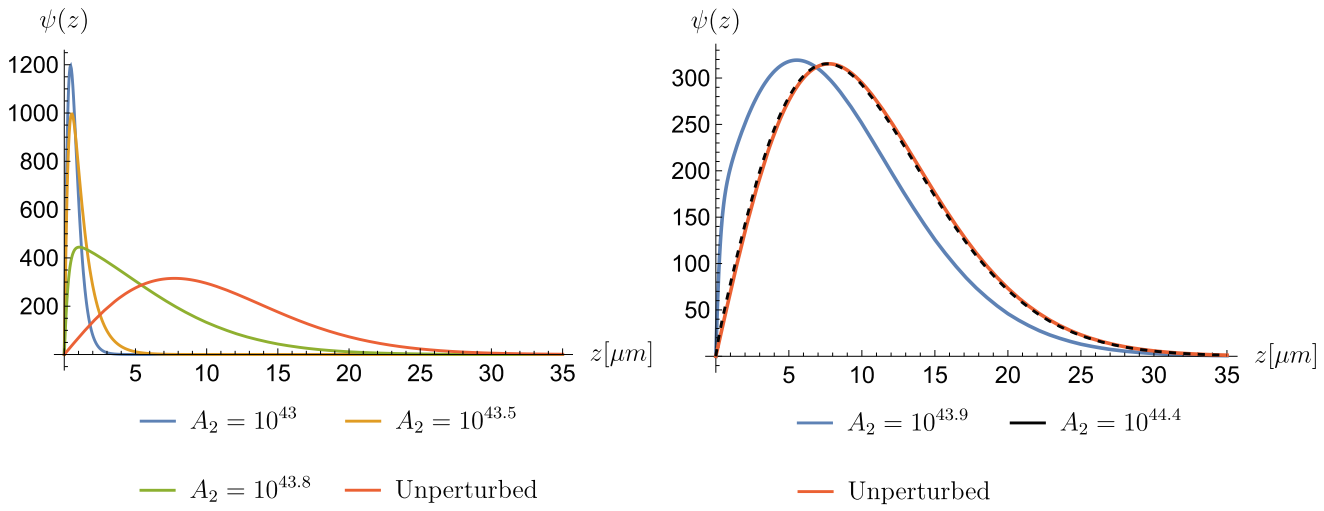

Fig. B.6.2: The ground state wave function in the presence of a dilaton field for the fixed paramters $V_0 = 10$ MeV^4 and $\lambda = 8 \times 10^{28}$ is shown. The parameter A_2 was varied as indicated in the figure. The unperturbed Newtonian case is shown in red.

Fig. B.6.2 illustrates that the dilaton potential squashes the ground state wave function of the neutron for $A_2 < 10^{44.4}$, $\lambda = 8 \times 10^{28}$ and $V_0 = 10$ MeV^4. Increasing A_2 while keeping other parameters fixed causes the wave function to gradually revert to its original unperturbed Newtonian shape. At $A_2 = 10^{44.4}$, the wave function becomes indistinguishable from the unperturbed case. However, comparing its energy to the unperturbed Newtonian energy yields[19]:

$$\frac{E_1}{E_1^{(0)}} \simeq 2761 \gg 1. \tag{B.6.319}$$

Although the energies are strongly perturbed, the wave function remains largely unaffected. To elucidate this behavior, I offer a physical interpretation.

Fig. B.6.3 shows that the dilaton potential is comparatively short-ranged compared to the unperturbed wave function's extent. To evade the higher potential above the mirror, the neutron compresses itself into the region where the dilaton potential is lower. However, as the neutron compresses further, its kinetic energy increases. With increasing A_2, the potential steepens, necessitating further compression to avoid the dilaton field's potential energy. Eventually, a threshold

is reached where it becomes more energetically favorable to expand into the high potential region. This threshold can be estimated analytically.

Considering the dilaton field's decreasing range, when the neutron fully enters the high potential region, its energy would be approximately:

$$\alpha := E_1^{(0)} + \mathfrak{Q}_D\big(m_n \frac{A_2}{2} \frac{\phi_V^2 - \phi(0)^2}{m_{\text{pl}}^2}\big), \tag{B.6.320}$$

since the dilaton is mostly sitting at its VEV. Once the neutron's energy approaches this threshold, it becomes more economical to expand into the potential rather than increasing the kinetic energy further. The approximately constant dilaton potential no longer significantly affects the neutron's wave function shape in this case. This explanation's validity has been confirmed numerically, as depicted in Fig. B.6.3.

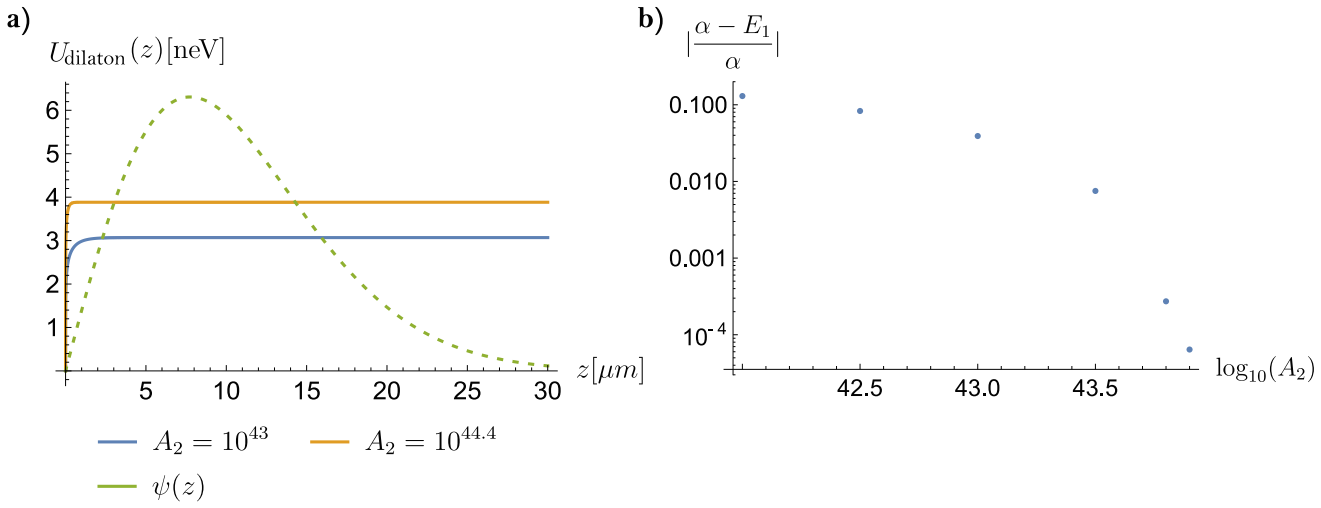

Fig. B.6.3: **a)** The dilaton potential for the neutron is shown for two different value of A_2, the unperturbed ground state of the neutron is shown in dashed green. **b)** The neutrons ground state energy in the presence of a dilaton field is compared to B.6.320.

The threshold where the wave function reverts back to its original shape is exactly the behavior of the wave functions at the edge of the constraint region. Once the wave functions are reverted back to their original shape, the dilaton field gives the same energy contribution to all energy states, which results in no energy differences. The exact threshold can only be computed numerically, and cannot be obtained from perturbation theory.

[19] For the comparisons presented in this Subsection, $E_1^{(0)}$ is defined as the lowest energy state of the neutron in the presence of only the Newtonian potential $U(z) = m_n g z$. E_1 is the lowest energy state in the presence of both the Newtonian potential and the dilaton potential defined by $U_{\text{dilaton}}(z) := \mathfrak{Q}_D(U_D(z) - U_D(0))$. It's important to recognize that potentials are inherently defined with an indeterminate constant term. To align with the convention of the Newtonian potential, which is set to 0 at the mirror surface, I imposed the same condition on the dilaton field.

C. Additional approximate dilaton field solutions

In this Section, additional approximate dilaton field solutions are explored, employed either in the small λ region for constraint computations, where the equations of motion exhibit linearity, or for testing numerical methods within this specific region. The derivations of the approximate one and two mirror solutions presented below closely resemble those of the spherical field profile or the exact two mirror solution with $\rho_V = 0$ in the main text, and therefore, concise formulations are provided. Detailed derivations for these two approximations can be found in Ref. [1].

C.1. Approximate one mirror solution

The approximate one mirror solution has originally been derived by Mario Pitschmann, with his derivation published in [1].

Initially, an approximate dilaton field solution for a mirror located at $z \leq 0$ and vacuum for $z > 0$ is derived. Assuming that the field does not vary in the $x-y$ plane, the stationary equation of motion for ϕ becomes:

$$\frac{d^2\phi}{dz^2} = V_{\text{eff},\phi}(\phi;\rho). \tag{C.1.321}$$

As a boundary condition for $z \to \infty$ it is assumed that ϕ minimizes its potential and takes on the value ϕ_V. Similarly, for $z \to -\infty$, the boundary condition ϕ_M is adopted. Except near the surface of the mirror at $z = 0$, the field approaches ϕ_M inside the mirror and ϕ_V inside the vacuum region. The following approximation is made:

$$\begin{aligned}\frac{d^2\phi}{dz^2} &\approx V_{\text{eff},\phi\phi}(\phi_V)(\phi-\phi_V) = \mu_V^2(\phi-\phi_V),\\ \frac{d^2\phi}{dz^2} &\approx V_{\text{eff},\phi\phi}(\phi_M)(\phi-\phi_M) = \mu_M^2(\phi-\phi_M),\end{aligned} \tag{C.1.322}$$

inside the vacuum region and inside the mirror, respectively. Obtaining the solution is straightforward: First, the general homogeneous solution is computed in either region, and a particular solution is added. Then, the free parameters are determined by demanding continuity of ϕ and $\frac{d\phi}{dz}$ at $z = 0$. The final solution reads:

$$\phi(z) = \theta(z)(\phi_V + (\phi_0 - \phi_V)e^{-\mu_V z}) + \theta(-z)(\phi_M + (\phi_0 - \phi_M)e^{\mu_M z}), \tag{C.1.323}$$

with

$$\phi_0 = \frac{\mu_V\phi_V + \mu_M\phi_M}{\mu_V + \mu_M}. \tag{C.1.324}$$

C.2. Approximate two mirror solution

The approximate two mirror solution has originally been derived by Mario Pitschmann, with his derivation published in [1].

The exact two mirror solution derived in the main text assumes $\rho_V = 0$. However, in the small λ region, it is more accurate to relax this assumption and solve the linearized equations of motion assuming $\rho_V > 0$. The differential equation is given by

$$\frac{d^2\phi}{dz^2} = V_{\text{eff},\phi}(\phi;\rho), \tag{C.2.325}$$

assuming two mirrors: One located at $z \geq d$ and one at $z \leq -d$. For $-d \leq z \leq d$, there is vacuum with density ρ_V. The boundary conditions are $\phi(z) \to \phi_M$ for $|z| \to \infty$. Unlike in the one mirror case, ϕ will never fully reach ϕ_V due to the finite extent of the vacuum region. Thus, the potential is expanded around $\phi_0 := \phi(0)$ in the vacuum region, which is the highest value ϕ can take, and for which $\frac{d\phi}{dz}(0) = 0$ has to hold due to the symmetric setup. One approximates

$$\begin{aligned}\frac{d^2\phi}{dz^2} &\approx V_{\text{eff},\phi}(\phi_0) + V_{\text{eff},\phi\phi}(\phi_0)(\phi-\phi_0) = -D_0 + \mu_0^2(\phi-\phi_0),\\ \frac{d^2\phi}{dz^2} &\approx V_{\text{eff},\phi\phi}(\phi_M)(\phi-\phi_M) = \mu_M^2(\phi-\phi_M),\end{aligned} \tag{C.2.326}$$

in the vacuum region and inside the mirrors respectively, with $D_0 = -V_{\text{eff},\phi}(\phi_0)$ and $\mu_0 = \frac{1}{m_{pl}}\sqrt{\lambda^2 V_0 e^{-\lambda\phi_0/m_{pl}} + A_2\rho_V}$. Obtaining the homogenous solutions in the respective regions is straightforward: Due to the symmetric set up, $\phi_h(z) \propto \cosh(\mu_0 z)$ holds in the vacuum region and due to the finite boundary conditions $\phi_h(z) \propto e^{-\mu_M|z|}$ inside the mirrors. Adding the particular solution in the respective regions and demanding that ϕ and $\frac{d\phi}{dz}$ are continuous at $z = \pm d$, one easily obtains

$$\phi(z) = \theta(d-|z|)\left\{\phi_0 + \frac{D_0}{\mu_0^2}(1-\cosh(\mu_0 z))\right\} + \theta(|z|-d)\left\{\phi_M + (\phi_d - \phi_M)e^{-\mu_M(|z|-d)}\right\}, \tag{C.2.327}$$

where ϕ_0 is defined implicitly by

$$\phi_M + \frac{D_0}{\mu_0\mu_M}\sinh(\mu_0 d) = \phi_0 + \frac{D_0}{\mu_0^2}(1-\cosh\,(\mu_0 d)). \tag{C.2.328}$$

C.3. Approximate solution for the cross section of a cylinder

In this section, we calculate the field of the cross section of an infinitely extended cylinder, where the field shows no dependence on the direction of the cylinder's symmetry axis, denoted as the z- direction. The equation of motion for ϕ simplifies to

$$\frac{d^2\phi}{dr^2} + \frac{1}{r}\frac{d\phi}{dr} + = V_{\text{eff},\phi}(\phi;\rho). \tag{C.3.329}$$

Vacuum is assumed for $r \leq d$ and an infinitely extended shell with density ρ_M for $r > d$. The boundary conditions are thus

$$\begin{aligned}&\phi(r) \to \phi_M, \text{ for } r \to \infty,\\ &\frac{d\phi}{dr} = 0, \text{ for } r = 0.\end{aligned} \tag{C.3.330}$$

Similarly to the approximate two mirror solution, the following approximations are employed

$$\begin{aligned}
\frac{d^2\phi}{dr^2} + \frac{1}{r}\frac{d\phi}{dr} &\approx -D_0 + \mu_0^2(\phi - \phi_0), \quad r \leq d, \\
\frac{d^2\phi}{dr^2} + \frac{1}{r}\frac{d\phi}{dr} &\approx \mu_M^2(\phi - \phi_M), \quad r > d, \\
D_0 &:= -V_{\text{eff},\phi}(\phi_0, \rho_V), \\
\mu_0 &:= \sqrt{V_{\text{eff},\phi\phi}(\phi_0, \rho_V)}, \\
\phi_0 &:= \phi(0).
\end{aligned} \tag{C.3.331}$$

The equations inside vacuum and inside the shell are formally identical, with different inhomogenous constant, since

$$-D_0 + \mu_0^2(\phi - \phi_0) = \mu_0^2(\phi - \phi_0 - \frac{D_0}{\mu_0^2}). \tag{C.3.332}$$

Thus by the replacement

$$\begin{aligned}
\mu_0^2 &\to \mu_M^2 \\
\phi_0 + \frac{D_0}{\mu_0^2} &\to \phi_M,
\end{aligned} \tag{C.3.333}$$

both equations are formally identical. Therefore only the vacuum equation is discussed in detail. The aim is to reduce Eq. (C.3.331) to an equation with known analytical solutions. The right choice is the modified Bessel equation, which reads (see e.g. [153], [154])

$$x^2\frac{d^2y}{dx^2}(x) + x\frac{dy}{dx}(x) - (x^2 + \alpha^2)y(x) = 0, \tag{C.3.334}$$

where α is an arbitrary complex constant. The modified Bessel functions are two linearly independent solution to this equation. One typically distinguishes between modified Bessel functions of the first kind ($I_\alpha(x)$) and second kind ($K_\alpha(x)$). In this case, only $\alpha = 0$ is relevant. I_0 has a vanishing derivative at $x = 0$, but diverges for $x \to \infty$, while K_0 diverges for $x \to 0$, but converges to 0 for $x \to \infty$, see Fig. C.3.1.

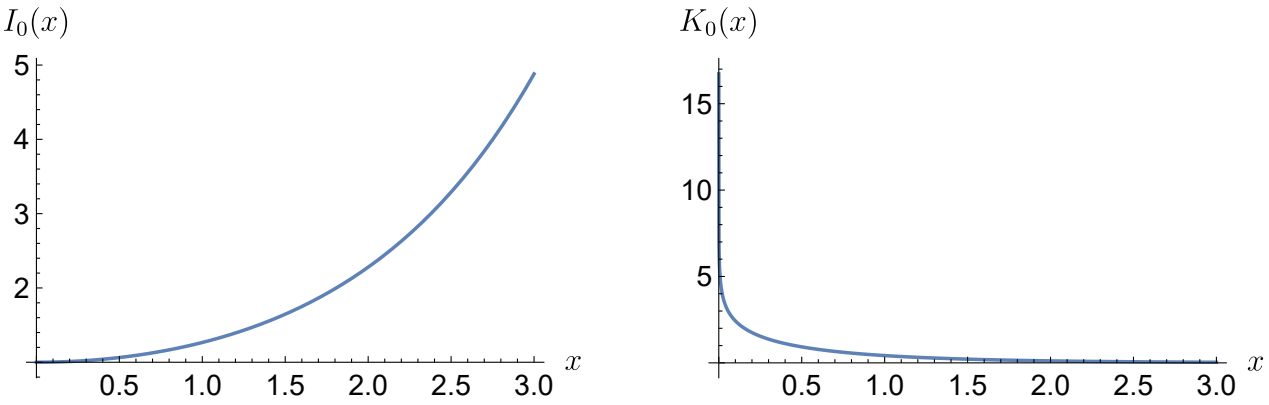

Fig. C.3.1: The two modified Bessel functions are plotted for $\alpha = 0$.

The homogeneous equation is given by

$$\frac{d^2\phi}{dr^2} + \frac{1}{r}\frac{d\phi}{dr} = \mu_0^2\phi, \tag{C.3.335}$$

and transforms to

$$\tilde{r}^2\frac{d^2\tilde{\phi}}{d\tilde{r}^2} + \tilde{r}\frac{d\tilde{\phi}}{d\tilde{r}} - \tilde{r}^2\tilde{\phi}(\tilde{r}) = 0, \tag{C.3.336}$$

where $\tilde{r} := \mu_0 r$ and $\tilde{\phi}(\tilde{r}) := \phi(r) = \phi(\frac{\tilde{r}}{\mu_0})$. The last equation is the modified Bessel equation for the case $\alpha = 0$, and the general homogeneous solution is

$$\begin{aligned}\tilde{\phi}_{h,\text{general}}(\tilde{r}) &= c_1 I_0(\tilde{r}) + c_2 K_0(\tilde{r}) \\ &= c_1 I_0(\mu_0 r) + c_2 K_0(\mu_0 r).\end{aligned} \tag{C.3.337}$$

Thus

$$\phi_{h,\text{general}}(r) = c_1 I_0(\mu_0 r) + c_2 K_0(\mu_0 r). \tag{C.3.338}$$

Inside the vacuum region, fulfilling the boundary condition $\frac{d\phi}{dr}(0) = 0$ implies that $c_2 = 0$, since K_0 diverges for $x = 0$. A particular solution inside the vacuum region is given by

$$\phi_{\text{particular}}(r) = \phi_0 + \frac{D_0}{\mu_0^2}. \tag{C.3.339}$$

Lastly, c_1 can be determined from $I_0(0) = 1$. Thus, in the vacuum region the solution is given by

$$\phi_{\text{vacuum}}(r) = \phi_0 + \frac{D_0}{\mu_0^2}(1 - I_0(\mu_0 r)). \tag{C.3.340}$$

Similarly, inside the shell $c_1 = 0$ is necessary, since I_0 diverges for large arguments, but the field approaches a finite boundary condition for $r \to \infty$. Since $K_0(r) \to 0$ for $r \to \infty$, it follows

$$\phi(r) = \phi_M + c_2 K_0(\mu_M r). \tag{C.3.341}$$

Demanding continuity of $\frac{d\phi}{dr}$ at $r = d$, results in

$$-\frac{D_0}{\mu_0}\frac{dI_0}{dr}(\mu_0 d) = c_2 \mu_M \frac{dK_0}{dr}(\mu_M d), \tag{C.3.342}$$

which implies

$$c_2 = -\frac{D_0}{\mu_0 \mu_M}\frac{\frac{dI_0}{dr}(\mu_0 d)}{\frac{dK_0}{dr}(\mu_M d)}. \tag{C.3.343}$$

Hence,

$$\phi_{\text{shell}}(r) = \phi_M - \frac{D_0}{\mu_0 \mu_M}\frac{\frac{dI_0}{dr}(\mu_0 d)}{\frac{dK_0}{dr}(\mu_M d)} K_0(\mu_M r). \tag{C.3.344}$$

The only remaining unknown is ϕ_0. An implicit equation for ϕ_0 can be derived by demanding continuity of $\phi(r)$ at $r = d$, which can be solved numerically:

$$\phi_0 + \frac{D_0}{\mu_0^2}(1 - I_0(\mu_0 d)) = \phi_M - \frac{D_0}{\mu_0 \mu_M}\frac{\frac{dI_0}{dr}(\mu_0 d)}{\frac{dK_0}{dr}(\mu_M d)} K_0(\mu_M d). \tag{C.3.345}$$

In conclusion, the full solution is given by

$$\phi(r) = \begin{cases} \phi_{\text{vacuum}}(r), & \text{for } r \leq d, \\ \phi_{\text{shell}}(r), & \text{else} \end{cases} \tag{C.3.346}$$

where ϕ_0 is the solution to (C.3.345).

D. Experimental parameters

This Section provides all experimental parameters utilized in numerical calculations, followed by succinct derivations for parameters derived from other values.

Parameters for LLR

The analysis of LLR utilized the astrophysical parameters given in Ref. [7]. When calculating field profiles and screening charges for the Sun, Moon, and Earth, their respective average densities where employed. The density of the interplanetary medium is assumed to be $\rho_V = 1.67 \times 10^{-20}$ kg/m^3, roughly equivalent to 10 hydrogen atoms per cubic centimeter. It's worth noting that the actual density varies, ranging from 5 to 40 atoms per cubic centimeter [155]. Nevertheless, my analyses showed that altering the vacuum density by a factor of 10 had only a marginal impact on the computed constraints.

Parameters for neutron interferometry

Description	Value
Inner radius vacuum chamber	2 cm
Inner length of vacuum chamber	9.4 cm
Inner radius vacuum chamber	2 cm
Inner length chamber	9.4 cm
Thickness of chamber walls	0.5 cm
Density of cylinder shells ρ_M	2700 kg/m^3
Lowest vacuum pressure profile-mode	10^{-4} mbar
Lowest vacuum pressure pressure-mode	2.4×10^{-4} mbar
ρ_V profile-mode	1.64×10^{-8} kg/m^3
ρ_V pressure-mode	3.92×10^{-8} kg/m^3
Air density	1.18 kg/m^3
Temperature	293 K
Beam separation	5 cm
Wavelength of the neutron	2.72×10^{-10} m
Neutron mass m_n	939.565 MeV
cut-off to ensure field decays to ϕ_M inside cylinder shell	$R_I(\rho_M) < 0.25$ mm

Table 6: This is a summary of the experimental parameters used for computing constraints based on the already existing neutron interferometry experiment in Ref. [66].

Description	Value
Inner radius vacuum chamber	4.75 cm
Inner length of vacuum chamber	0.5 m
Inner radius vacuum chamber	4.75 cm
Inner length chamber	0.5 m
Thickness of chamber walls	0.5 cm
Density of cylinder shells ρ_M	2700 kg/m^3
Lowest vacuum pressure profile-mode	10^{-4} mbar
Lowest vacuum pressure pressure-mode	2.4×10^{-4} mbar
ρ_V profile-mode	1.64×10^{-8} kg/m^3
ρ_V pressure-mode	3.92×10^{-8} kg/m^3
Air density	1.18 kg/m^3
Temperature	293 K
Beam separation	10 cm
Wavelength of the neutron	2.72×10^{-10} m
Neutron mass m_n	939.565 MeV
cut-off to ensure field decays to ϕ_M inside cylinder shell	$R_I(\rho_M) < 0.25$ mm

Table 7: This is a summary of the experimental parameters used for computing prospective constraints for the split-interferometer.

Parameters for qBOUNCE

Description	Value
Mirror density ρ_M	2510 kg/m^3
Vacuum pressure	2×10^{-4} mbar
Vacuum density ρ_V	2.32×10^{-7} kg/m^3
Temperature	300 K
Gravitational acceleration g	9.806 m/s^2
Neutron mass m_n	939.565 MeV
cut-off to neglect influence of the vacuum chamber	$R_I(\rho_V) < 1$ mm

Table 8: This is a summary of the experimental parameters used for computing constraints for qBOUNCE.

Parameters for CANNEX

Description	Value
Mean mirror density ρ_M	2514 kg/m^3
Lowest vacuum pressure	10^{-9} mbar
Highest vacuum pressure	500 mbar
Lowest vacuum density ρ_V	5.3×10^{-12} kg/m^3
Highest vacuum density ρ_V	2.6 kg/m^3
Lowest plate separation	3 μm
Highest plate separation	30 μm
cut-off to ensure field decays to ϕ_M inside upper mirror	$R_I(\rho_M) < 2.5$ μm
cut-off to neglect influence of the vacuum chamber	$R_I(\rho_V) < 1$ mm

Table 9: This is a summary of the experimental parameters used for computing prospective constraints for CANNEX.

Pressure density conversion

In experiments such as qBOUNCE, CANNEX, and neutron interferometry, the measurement typically focuses on vacuum pressure rather than its density. To convert pressure into density, the ideal gas law is applied in the following form [156]:

$$p = \rho \frac{N_A k_B T}{M}$$
$$\Rightarrow \rho = \frac{Mp}{N_A k_B T},$$

where p denotes pressure, ρ represents gas density, N_A stands for Avogadro's number, k_B for Boltzmann's constant, M for molar mass (mass in kg per mole), and T for gas temperature.
The neutron interferometry analysis assumed helium with a molar mass of $M_{\mathrm{He}} \approx 4 \times 10^{-3}$ kg/mol and a temperature of $T = 293$ K.
For qBOUNCE, a composition of 80% nitrogen (N_2) and 20% oxygen (O_2), having molar masses $M_{O_2} \approx 31.9988 \times 10^{-3}$ kg/mol, $M_{N_2} \approx 28.0134 \times 10^{-3}$ kg/mol and a temperature of $T = 300$ K

was assumed.
The CANNEX analsis assumed Xenon with a molar mass of $M_{\text{Xe}} \approx 131.293 \times 10^{-3}$ kg/mol and a temperature of $T = 300$ K.

CANNEX mirror density

For CANNEX, a mean mirror density (for both the upper and lower mirrors) of $\rho_M = 2514$ kg/m^3 was utilized, initially provided by René Sedmik and derived from the following considerations:
During the inception of my PhD, the envisaged design for CANNEX was as follows:
The lower plate, several millimeters thick, was intended to be composed of SiO_2 with a density of 2642 kg/m^3, overlaid with a thin gold layer 200 nm thick, possessing a density of 19320 kg/m^3.
Conversely, the upper plate was designed with three layers. The main layer, 100 μm in thickness, comprised of Si with a density of 2329 kg/m^3, coated on both top and bottom with a 70 nm thick layer of gold.
To ensure symmetry in the setup, an average plate density for both plates was determined, assuming the SiO_2 layer to also be 100 μm thick. This assumption was reasonable given that all calculations assumed the scalar field could not penetrate deeper than 100 μm into the material. Consequently,

$$\rho_M = \frac{340 \times 19320 + 10^5 \times 2329 + 10^5 \times 2642}{2 \times 10^5 + 340} \text{kg/m}^3 \simeq 2514 \text{kg/m}^3. \tag{D.0.347}$$

It's important to note that the actual layers implemented differed slightly, a decision made later in my PhD journey, after all calculations were completed. However, rigorous checks confirmed that the constraint regions were highly insensitive to minor changes in ρ_M, as demonstrated in Section B.2. Consequently, the constraint regions calculated in this thesis remain applicable to the updated experiment.

List of Figures

List of Tables

Bibliography

[1] Philippe Brax, Hauke Fischer, Christian Käding, and Mario Pitschmann. The environment dependent dilaton in the laboratory and the solar system. *Eur. Phys. J. C*, 82(10):934, 2022.

[2] Hauke Fischer, Christian Käding, René I. P. Sedmik, Hartmut Abele, Philippe Brax, and Mario Pitschmann. Search for environment-dependent dilatons. *Phys. Dark Univ.*, 43:101419, 2024.

[3] Hauke Fischer, Christian Käding, Hartmut Lemmel, Stephan Sponar, and Mario Pitschmann. Search for dark energy with neutron interferometry. *PTEP*, 2024(2):023E02, 2024.

[4] Hamid Haghmoradi, Hauke Fischer, Alessandro Bertolini, Ivica Galić, Francesco Intravaia, Mario Pitschmann, Raphael Schimpl, and René I. P. Sedmik. Force metrology with plane parallel plates: Final design review and outlook. *Physics*, 6:690–741, 3 2024.

[5] Hauke Fischer, Christian Käding, and Mario Pitschmann. Screened Scalar Fields in the Laboratory and the Solar System. *Universe*, 10:297, 2024.

[6] Hauke Fischer and René IP Sedmik. Numerical methods for scalar field dark energy in table-top experiments and lunar laser ranging. *arXiv:2401.16179*, 2024.

[7] R. L. Workman and Others. Review of Particle Physics. *PTEP*, 2022:083C01, 2022.

[8] Vera C. Rubin and W. Kent Ford, Jr. Rotation of the Andromeda Nebula from a Spectroscopic Survey of Emission Regions. *Astrophys. J.*, 159:379–403, 1970.

[9] F. Zwicky. Die Rotverschiebung von extragalaktischen Nebeln. *Helv. Phys. Acta*, 6:110–127, 1933.

[10] A. Arbey and F. Mahmoudi. Dark matter and the early Universe: a review. *Prog. Part. Nucl. Phys.*, 119:103865, 2021.

[11] Volker Springel, Simon DM White, Adrian Jenkins, Carlos S Frenk, Naoki Yoshida, Liang Gao, Julio Navarro, Robert Thacker, Darren Croton, John Helly, et al. Simulations of the formation, evolution and clustering of galaxies and quasars. *nature*, 435(7042):629–636, 2005.

[12] Julien Billard et al. Direct detection of dark matter—APPEC committee report*. *Rept. Prog. Phys.*, 85(5):056201, 2022.

[13] S. Perlmutter et al. Discovery of a supernova explosion at half the age of the Universe and its cosmological implications. *Nature*, 391:51–54, 1998.

[14] Adam G. Riess et al. Observational evidence from supernovae for an accelerating universe and a cosmological constant. *Astron. J.*, 116:1009–1038, 1998.

[15] Brian P. Schmidt et al. The High Z supernova search: Measuring cosmic deceleration and global curvature of the universe using type Ia supernovae. *Astrophys. J.*, 507:46–63, 1998.

[16] P. de Bernardis et al. A Flat universe from high resolution maps of the cosmic microwave background radiation. *Nature*, 404:955–959, 2000.

[17] Andrew E. Lange et al. Cosmological parameters from the first results of BOOMERANG. *Phys. Rev. D*, 63:042001, 2001.

[18] G. Hinshaw et al. Nine-Year Wilkinson Microwave Anisotropy Probe (WMAP) Observations: Cosmological Parameter Results. *Astrophys. J. Suppl.*, 208:19, 2013.

[19] Max Tegmark et al. Cosmological parameters from SDSS and WMAP. *Phys. Rev. D*, 69:103501, 2004.

[20] Uros Seljak et al. Cosmological parameter analysis including SDSS Ly-alpha forest and galaxy bias: Constraints on the primordial spectrum of fluctuations, neutrino mass, and dark energy. *Phys. Rev. D*, 71:103515, 2005.

[21] Daniel J. Eisenstein et al. Detection of the Baryon Acoustic Peak in the Large-Scale Correlation Function of SDSS Luminous Red Galaxies. *Astrophys. J.*, 633:560–574, 2005.

[22] Brian Albert Robson et al. Introductory chapter: Standard model of cosmology. *Redefining Standard Model Cosmology*, pages 1–4, 2019.

[23] Alan H. Guth. The Inflationary Universe: A Possible Solution to the Horizon and Flatness Problems. *Phys. Rev. D*, 23:347–356, 1981.

[24] Steven Weinberg. *Cosmology*. 2008.

[25] Dragan Huterer. Growth of cosmic structure. *Astron. Astrophys. Rev.*, 31(1):2, 2023.

[26] Alan H Guth, David I Kaiser, Andrei D Linde, Yasunori Nomura, Charles L Bennett, J Richard Bond, François Bouchet, Sean Carroll, George Efstathiou, Stephen Hawking, et al. A cosmic controversy. *Scientific American*, 317(1):5–7, 2017.

[27] P. A. R. Ade et al. Planck 2015 results. XIII. Cosmological parameters. *Astron. Astrophys.*, 594:A13, 2016.

[28] Joan Sola. Cosmological constant and vacuum energy: old and new ideas. *J. Phys. Conf. Ser.*, 453:012015, 2013.

[29] Austin Joyce, Bhuvnesh Jain, Justin Khoury, and Mark Trodden. Beyond the Cosmological Standard Model. *Phys. Rept.*, 568:1–98, 2015.

[30] P. J. E. Peebles and Bharat Ratra. The Cosmological Constant and Dark Energy. *Rev. Mod. Phys.*, 75:559–606, 2003.

[31] G. S. Guralnik, C. R. Hagen, and T. W. B. Kibble. Global Conservation Laws and Massless Particles. *Phys. Rev. Lett.*, 13:585–587, 1964.

[32] Gerald S. Guralnik. The History of the Guralnik, Hagen and Kibble development of the Theory of Spontaneous Symmetry Breaking and Gauge Particles. *Int. J. Mod. Phys. A*, 24:2601–2627, 2009.

[33] Tom W. B. Kibble. Englert-Brout-Higgs-Guralnik-Hagen-Kibble mechanism (history). *Int. J. Mod. Phys. A*, 24:6001–6009, 2009.

[34] Georges Aad et al. Observation of a new particle in the search for the Standard Model Higgs boson with the ATLAS detector at the LHC. *Phys. Lett. B*, 716:1–29, 2012.

[35] Karl Schwarzschild. Über das gravitationsfeld eines massenpunktes nach der einsteinschen theorie. *Sitzungsberichte der königlich preussischen Akademie der Wissenschaften*, pages 189–196, 1916.

[36] Claus Kiefer. *Quantum gravity*, volume 124. Clarendon, Oxford, 2004.

[37] J. M. Overduin and P. S. Wesson. Kaluza-Klein gravity. *Phys. Rept.*, 283:303–380, 1997.

[38] Daniel Z. Freedman and Antoine Van Proeyen. *Supergravity*. Cambridge Univ. Press, Cambridge, UK, 5 2012.

[39] H. A. Buchdahl. Non-Linear Lagrangians and Cosmological Theory. *Mon. Not. Roy. Astron. Soc.*, 150(1):1–8, 1970.

[40] C. Brans and R. H. Dicke. Mach's principle and a relativistic theory of gravitation. *Phys. Rev.*, 124:925–935, 1961.

[41] F. Hofmann and J. Müller. Relativistic tests with lunar laser ranging. *Class. Quant. Grav.*, 35(3):035015, 2018.

[42] Justin Khoury and Amanda Weltman. Chameleon cosmology. *Phys. Rev. D*, 69:044026, 2004.

[43] Kurt Hinterbichler and Justin Khoury. Symmetron Fields: Screening Long-Range Forces Through Local Symmetry Restoration. *Phys. Rev. Lett.*, 104:231301, 2010.

[44] A. I. Vainshtein. To the problem of nonvanishing gravitation mass. *Phys. Lett. B*, 39:393–394, 1972.

[45] Clare Burrage and David Seery. Revisiting fifth forces in the Galileon model. *JCAP*, 08:011, 2010.

[46] Clare Burrage, Edmund J. Copeland, Christian Käding, and Peter Millington. Symmetron scalar fields: Modified gravity, dark matter, or both? *Phys. Rev. D*, 99(4):043539, 2019.

[47] Christian Käding. Lensing with Generalized Symmetrons. *Astronomy*, 2(2):128–140, 2023.

[48] Clare Burrage, Edmund J. Copeland, and Peter Millington. Radial acceleration relation from symmetron fifth forces. *Phys. Rev. D*, 95(6):064050, 2017. [Erratum: Phys.Rev.D 95, 129902 (2017)].

[49] Ciaran A. J. O'Hare and Clare Burrage. Stellar kinematics from the symmetron fifth force in the Milky Way disk. *Phys. Rev. D*, 98(6):064019, 2018.

[50] M. Milgrom. A Modification of the Newtonian dynamics as a possible alternative to the hidden mass hypothesis. *Astrophys. J.*, 270:365–370, 1983.

[51] Riccardo Scarpa. Modified newtonian dynamics, an introductory review. *AIP Conf. Proc.*, 822(1):253–265, 2006.

[52] Jacob D. Bekenstein. Modified gravity vs dark matter: Relativistic theory for MOND. *PoS*, JHW2004:012, 2005.

[53] Clare Burrage and Jeremy Sakstein. Tests of Chameleon Gravity. *Living Rev. Rel.*, 21(1):1, 2018.

[54] Clare Burrage, Edmund J. Copeland, and E. A. Hinds. Probing Dark Energy with Atom Interferometry. *JCAP*, 03:042, 2015.

[55] Clare Burrage and Edmund J. Copeland. Using Atom Interferometry to Detect Dark Energy. *Contemp. Phys.*, 57(2):164–176, 2016.

[56] Clare Burrage, Andrew Kuribayashi-Coleman, James Stevenson, and Ben Thrussell. Constraining symmetron fields with atom interferometry. *JCAP*, 12:041, 2016.

[57] Philippe Brax and Anne-Christine Davis. Atomic Interferometry Test of Dark Energy. *Phys. Rev. D*, 94(10):104069, 2016.

[58] Cristian D Panda, Matthew J Tao, Miguel Ceja, Justin Khoury, Guglielmo M Tino, and Holger Müller. Measuring gravitational attraction with a lattice atom interferometer. *Nature*, pages 1–6, 2024.

[59] Amol Upadhye. Symmetron dark energy in laboratory experiments. *Phys. Rev. Lett.*, 110(3):031301, 2013.

[60] Amol Upadhye. Dark energy fifth forces in torsion pendulum experiments. *Phys. Rev. D*, 86:102003, 2012.

[61] Philippe Brax and Mario Pitschmann. Exact solutions to nonlinear symmetron theory: One- and two-mirror systems. *Phys. Rev. D*, 97(6):064015, 2018.

[62] Mario Pitschmann. Exact solutions to nonlinear symmetron theory: One- and two-mirror systems. II. *Phys. Rev. D*, 103(8):084013, 2021. [Erratum: Phys.Rev.D 106, 109902 (2022)].

[63] Gunther Cronenberg, Philippe Brax, Hanno Filter, Peter Geltenbort, Tobias Jenke, Guillaume Pignol, Mario Pitschmann, Martin Thalhammer, and Hartmut Abele. Acoustic Rabi oscillations between gravitational quantum states and impact on symmetron dark energy. *Nature Phys.*, 14(10):1022–1026, 2018.

[64] Tobias Jenke, Joachim Bosina, Jakob Micko, Mario Pitschmann, Rene Sedmik, and Hartmut Abele. Gravity resonance spectroscopy and dark energy symmetron fields: qBOUNCE experiments performed with Rabi and Ramsey spectroscopy. *Eur. Phys. J. ST*, 230(4):1131–1136, 2021.

[65] Philippe Brax, Anne-Christine Davis, and Benjamin Elder. Screened scalar fields in hydrogen and muonium. *Phys. Rev. D*, 107(4):044008, 2023.

[66] H. Lemmel, Ph. Brax, A. N. Ivanov, T. Jenke, G. Pignol, M. Pitschmann, T. Potocar, M. Wellenzohn, M. Zawisky, and H. Abele. Neutron Interferometry constrains dark energy chameleon fields. *Phys. Lett. B*, 743:310–314, 2015.

[67] Benjamin Elder, Valeri Vardanyan, Yashar Akrami, Philippe Brax, Anne-Christine Davis, and Ricardo S. Decca. Classical symmetron force in Casimir experiments. *Phys. Rev. D*, 101(6):064065, 2020.

[68] Philippe Brax and Anne-Christine Davis. Casimir, Gravitational and Neutron Tests of Dark Energy. *Phys. Rev. D*, 91(6):063503, 2015.

[69] Ana Lucía Báez-Camargo, Daniel Hartley, Christian Käding, and Ivette Fuentes-Guridi. Dynamical Casimir effect with screened scalar fields. 4 2024.

[70] Philippe Brax, Carsten van de Bruck, Anne-Christine Davis, David Fonseca Mota, and Douglas J. Shaw. Detecting chameleons through Casimir force measurements. *Phys. Rev. D*, 76:124034, 2007.

[71] Daniel Hartley, Christian Käding, Richard Howl, and Ivette Fuentes. Quantum-enhanced screened dark energy detection. *Eur. Phys. J. C*, 84(1):49, 2024.

[72] Daniel Hartley, Christian Käding, Richard Howl, and Ivette Fuentes. Quantum simulation of dark energy candidates. *Phys. Rev. D*, 99(10):105002, 2019.

[73] Philippe Brax, Clare Burrage, and Anne-Christine Davis. Laboratory constraints. *Int. J. Mod. Phys. D*, 27(15):1848009, 2018.

[74] H. Abele, T. Jenke, H. Leeb, and J. Schmiedmayer. Ramsey's method of separated oscillating fields and its application to gravitationally induced quantum phase shifts. *Phys. Rev. D*, 81:065019, Mar 2010.

[75] Tobias Jenke, Peter Geltenbort, Hartmut Lemmel, and Hartmut Abele. Realization of a gravity-resonance-spectroscopy technique. *Nature Phys.*, 7:468–472, 2011.

[76] T. Jenke et al. Gravity Resonance Spectroscopy Constrains Dark Energy and Dark Matter Scenarios. *Phys. Rev. Lett.*, 112:151105, 2014.

[77] A. N. Ivanov, R. Hollwieser, T. Jenke, M. Wellenzohen, and H. Abele. Influence of the chameleon field potential on transition frequencies of gravitationally bound quantum states of ultracold neutrons. *Phys. Rev. D*, 87(10):105013, 2013.

[78] Gunther Cronenberg, Hanno Filter, Martin Thalhammer, Tobias Jenke, Hartmut Abele, and Peter Geltenbort. A gravity of earth measurement with a qbounce experiment. *arXiv preprint arXiv:1512.09134*, 2015.

[79] Philippe Brax, Guillaume Pignol, and Damien Roulier. Probing Strongly Coupled Chameleons with Slow Neutrons. *Phys. Rev. D*, 88:083004, 2013.

[80] Ph. Brax, C. van de Bruck, A. C. Davis, D. J. Shaw, and D. Iannuzzi. Tuning the Mass of Chameleon Fields in Casimir Force Experiments. *Phys. Rev. Lett.*, 104:241101, 2010.

[81] René I. P. Sedmik and Mario Pitschmann. Next Generation Design and Prospects for Cannex. *Universe*, 7(7):234, 2021.

[82] Attaallah Almasi, Philippe Brax, Davide Iannuzzi, and René I. P. Sedmik. Force sensor for chameleon and Casimir force experiments with parallel-plate configuration. *Phys. Rev. D*, 91(10):102002, 2015.

[83] T. Damour and Alexander M. Polyakov. The String dilaton and a least coupling principle. *Nucl. Phys. B*, 423:532–558, 1994.

[84] Philippe Brax, Carsten van de Bruck, Anne-Christine Davis, and Douglas Shaw. The Dilaton and Modified Gravity. *Phys. Rev. D*, 82:063519, 2010.

[85] M. Gasperini, F. Piazza, and G. Veneziano. Quintessence as a runaway dilaton. *Phys. Rev. D*, 65:023508, 2002.

[86] Jürgen Müller, Thomas W Murphy, Ulrich Schreiber, Peter J Shelus, Jean-Marie Torre, James G Williams, Dale H Boggs, Sebastien Bouquillon, Adrien Bourgoin, and Franz Hofmann. Lunar laser ranging: a tool for general relativity, lunar geophysics and earth science. *Journal of Geodesy*, 93:2195–2210, 2019.

[87] Stephen M. Merkowitz. Tests of Gravity Using Lunar Laser Ranging. *Living Rev. Rel.*, 13:7, 2010.

[88] Mario Pitschmann. Lecture notes, gravitation and cosmology 2. *unpublished*, 2023.

[89] LD Landau and EM Lifschitz. Klassische Feldtheorie (Lehrbuch der theoretischen Physik, Bd. II. *Berlin: Akademie-Verlag.[Erstpublikation: 1939]*, 1989.

[90] Shinji Tsujikawa. Quintessence: A Review. *Class. Quant. Grav.*, 30:214003, 2013.

[91] Takeshi Chiba. Slow-Roll Thawing Quintessence. *Phys. Rev. D*, 79:083517, 2009. [Erratum: Phys.Rev.D 80, 109902 (2009)].

[92] Takeshi Chiba, Masaru Siino, and Masahide Yamaguchi. Slow-roll Extended Quintessence. *Phys. Rev. D*, 81:083530, 2010.

[93] Mario Pitschmann. *The High Precision Frontier: Search for New Physics with "Tabletop Experiments" & Beyond*. habilitation, TU Wien, 2023.

[94] Yasunori Fujii and Kei-ichi Maeda. *The Scalar-Tensor Theory of Gravitation*. Cambridge Monographs on Mathematical Physics. Cambridge University Press, 2003.

[95] David Hilbert. Die grundlagen der physik.(erste mitteilung.). *Nachrichten von der Gesellschaft der Wissenschaften zu Göttingen, Mathematisch-Physikalische Klasse*, 1915:395–408, 1915.

[96] R. M. Corless, G. H. Gonnet, D. E. G. Hare, D. J. Jeffrey, and D. E. Knuth. On the LambertW function. *Adv. Comput. Math.*, 5:329–359, 1996.

[97] Benjamin Elder, Justin Khoury, Philipp Haslinger, Matt Jaffe, Holger Müller, and Paul Hamilton. Chameleon Dark Energy and Atom Interferometry. *Phys. Rev. D*, 94(4):044051, 2016.

[98] Chad Briddon, Clare Burrage, Adam Moss, and Andrius Tamosiunas. Selcie: a tool for investigating the chameleon field of arbitrary sources. *Journal of Cosmology and Astroparticle Physics*, 2021(12):043, 2021.

[99] Matt Jaffe, Philipp Haslinger, Victoria Xu, Paul Hamilton, Amol Upadhye, Benjamin Elder, Justin Khoury, and Holger Müller. Author Correction: Testing sub-gravitational forces on atoms from a miniature in-vacuum source mass [doi: 10.1038/nphys4189]. *Nature Phys.*, 13:938, 2017.

[100] Paul Hamilton, Matt Jaffe, Philipp Haslinger, Quinn Simmons, Holger Müller, and Justin Khoury. Atom-interferometry constraints on dark energy. *Science*, 349:849–851, 2015.

[101] Philippe Brax, Anne-C. Davis, Baojiu Li, Hans A. Winther, and Gong-Bo Zhao. Systematic simulations of modified gravity: chameleon models. *JCAP*, 04:029, 2013.

[102] Philippe Brax, Anne-Christine Davis, Baojiu Li, Hans A. Winther, and Gong-Bo Zhao. Systematic Simulations of Modified Gravity: Symmetron and Dilaton Models. *JCAP*, 10:002, 2012.

[103] Anne-Christine Davis, Baojiu Li, David F. Mota, and Hans A. Winther. Structure Formation in the Symmetron Model. *Astrophys. J.*, 748:61, 2012.

[104] Marvin F. Silva, Hans A. Winther, David F. Mota, and C. J. A. P. Martins. Spatial variations of the fine-structure constant in symmetron models. *Phys. Rev. D*, 89(2):024025, 2014.

[105] Claudio Llinares and David F. Mota. Cosmological simulations of screened modified gravity out of the static approximation: effects on matter distribution. *Phys. Rev. D*, 89(8):084023, 2014.

[106] Claudio Llinares, David F. Mota, and Hans A. Winther. ISIS: a new N-body cosmological code with scalar fields based on RAMSES. Code presentation and application to the shapes of clusters. *Astron. Astrophys.*, 562:A78, 2014.

[107] Philippe Brax, Carsten van de Bruck, Anne-Christine Davis, Baojiu Li, and Douglas J. Shaw. Nonlinear Structure Formation with the Environmentally Dependent Dilaton. *Phys. Rev. D*, 83:104026, 2011.

[108] Wolfram Research, Inc. Mathematica, Version 13.1.

[109] Hans Petter Langtangen and Kent-Andre Mardal. *Introduction to numerical methods for variational problems*, volume 21. Springer Nature, 2019.

[110] Randall J LeVeque. *Finite difference methods for ordinary and partial differential equations: steady-state and time-dependent problems*. SIAM, 2007.

[111] A. N. Ivanov, G. Cronenberg, R. Höllwieser, M. Pitschmann, T. Jenke, M. Wellenzohn, and H. Abele. Exact solution for chameleon field, self-coupled through the Ratra-Peebles potential with $n = 1$ and confined between two parallel plates. *Phys. Rev. D*, 94(8):085005, 2016.

[112] Joachim Schöberl. Numerical methods for partial differential equations. *Script, http:\\www. asc. tuwien. ac. at\ schoeberl\wiki\index. php\numpde12*, 2009.

[113] Peter Deuflhard. *Newton methods for nonlinear problems: affine invariance and adaptive algorithms*, volume 35. Springer Science & Business Media, 2005.

[114] Hans Petter Langtangen. Solving nonlinear ode and pde problems. *Center for Biomedical Computing, Simula Research Laboratory and Department of Informatics, University of Oslo*, 2016.

[115] Lev D Landau and Evgenii M Lifshitz. Quantenmechanik, lehrbuch der theoretischen physik iii, 1991.

[116] I-H Tan, Gregory L Snider, LD Chang, and Evelyn L Hu. A self-consistent solution of schrödinger–poisson equations using a nonuniform mesh. *Journal of applied physics*, 68(8):4071–4076, 1990.

[117] Jeremy Sakstein. Tests of Gravity with Future Space-Based Experiments. *Phys. Rev. D*, 97(6):064028, 2018.

[118] Lucila Kraiselburd, Susana J. Landau, Marcelo Salgado, Daniel Sudarsky, and Héctor Vucetich. Equivalence Principle in Chameleon Models. *Phys. Rev. D*, 97(10):104044, 2018.

[119] Xing Zhang, Rui Niu, and Wen Zhao. Constraining the scalar-tensor gravity theories with and without screening mechanisms by combined observations. *Phys. Rev. D*, 100(2):024038, 2019.

[120] James G. Williams, Slava G. Turyshev, and Dale Boggs. Lunar Laser Ranging Tests of the Equivalence Principle. *Class. Quant. Grav.*, 29:184004, 2012.

[121] Stephan Schlamminger, K. Y. Choi, T. A. Wagner, J. H. Gundlach, and E. G. Adelberger. Test of the equivalence principle using a rotating torsion balance. *Phys. Rev. Lett.*, 100:041101, 2008.

[122] Clifford M Will. Theoretical frameworks for testing relativistic gravity. ii. parametrized post-newtonian hydrodynamics, and the nordtvedt effect. *Astrophysical Journal, vol. 163, p. 611*, 163:611, 1971.

[123] K. Nordtvedt. Testing relativity with laser ranging to the moon. *Phys. Rev.*, 170:1186–1187, 1968.

[124] Isaac Newton. Philosophiae naturalis principia mathematica, mathematical principles of natural philosophy, translated by i. bernard cohen and anne whitman with the assistance of julia budenz, preceded by a guide to newton's principia by i. bernard cohen, 1999.

[125] Subrahmanyan Chandrasekhar. *Newton's Principia for the common reader*. Oxford University Press, 2003.

[126] H. Rauch, W. Treimer, and U. Bonse. Test of a single crystal neutron interferometer. *Phys. Lett.*, 47A(5):369 – 371, 1974.

[127] H. Rauch and S. A. Werner. *Neutron Interferometry*. Clarendon Press, Oxford, 2000.

[128] Yu. N. Pokotilovski. Strongly coupled chameleon fields: Possible test with a neutron Lloyd's mirror interferometer. *Phys. Lett. B*, 719:341–345, 2013.

[129] L. Diósi. Gravitation and quantummechanical localization of macroobjects. *Phys. Lett. A*, 105:199–202, 1984.

[130] Roger Penrose. Quantum computation, entanglement and state reduction. *Phil. Trans. Roy. Soc. Lond. A*, 356:1927–1938, 1998.

[131] Martin Suda, Manfried Faber, Joachim Bosina, Tobias Jenke, Christian Käding, Jakob Micko, Mario Pitschmann, and Hartmut Abele. Spectra of neutron wave functions in Earth's gravitational field. *Z. Naturforsch. A*, 77(9):875–898, 2022.

[132] Christian Käding, Mario Pitschmann, and Hartmut Abele. Green's function analysis of the neutron Lloyd interferometer. *Z. Naturforsch. A*, 78(7):651–658, 2023.

[133] Hartmut Lemmel, Michael Jentschel, Hartmut Abele, Fabien Lafont, Bruno Guerard, Carlo P. Sasso, Giovanni Mana, and Enrico Massa. Neutron interference from a split-crystal interferometer. *J. Appl. Cryst.*, 55:870–875, 2022.

[134] Daniel M Greenberger and AW Overhauser. Coherence effects in neutron diffraction and gravity experiments. *Reviews of Modern Physics*, 51(1):43, 1979.

[135] G. Cronenberg, H. Filter, M. Thalhammer, T. Jenke, H. Abele, and P. Geltenbort. A Gravity of Earth Measurement with a qBOUNCE Experiment. *PoS*, EPS-HEP2015:408, 2015.

[136] Isidor Isaac Rabi, Sidney Millman, Polykarp Kusch, and Jerrold Reinach Zacharias. The molecular beam resonance method for measuring nuclear magnetic moments. the magnetic moments of li 6 3, li 7 3 and f 19 9. *Physical review*, 55(6):526, 1939.

[137] Pieter Zeeman. *Ueber einen Einfluss der Magnetisirung auf die Natur des von einer Substanz emittirten Lichtes*. 1896.

[138] H. Abele, T. Jenke, H. Leeb, and J. Schmiedmayer. Ramsey's Method of Separated Oscillating Fields and its Application to Gravitationally Induced Quantum Phaseshifts. *Phys. Rev. D*, 81:065019, 2010.

[139] Stephan Sponar, René I. P. Sedmik, Mario Pitschmann, Hartmut Abele, and Yuji Hasegawa. Tests of fundamental quantum mechanics and dark interactions with low-energy neutrons. *Nature Rev. Phys.*, 3(5):309–327, 2021.

[140] Tobias Jenke et al. Testing gravity at short distances: Gravity Resonance Spectroscopy with qBOUNCE. *EPJ Web Conf.*, 219:05003, 2019.

[141] Vallee Olivier et al. *Airy functions and applications to physics*. World Scientific, 2010.

[142] E. G. Adelberger, Blayne R. Heckel, and A. E. Nelson. Tests of the gravitational inverse square law. *Ann. Rev. Nucl. Part. Sci.*, 53:77–121, 2003.

[143] Tanmay Vachaspati. *Kinks and domain walls: An introduction to classical and quantum solitons*. Cambridge University Press, 2007.

[144] Øyvind Christiansen, Farbod Hassani, Mona Jalilvand, and David F Mota. Asevolution: a relativistic n-body implementation of the (a) symmetron. *Journal of Cosmology and Astroparticle Physics*, 2023(05):009, 2023.

[145] Claudio Llinares and Philippe Brax. Detecting coupled domain walls in laboratory experiments. *Physical Review Letters*, 122(9):091102, 2019.

[146] Kate Clements, Benjamin Elder, Lucia Hackermueller, Mark Fromhold, and Clare Burrage. Detecting dark domain walls. *arXiv preprint arXiv:2308.01179*, 2023.

[147] Philippe Brax and Guillaume Pignol. Strongly Coupled Chameleons and the Neutronic Quantum Bouncer. *Phys. Rev. Lett.*, 107:111301, 2011.

[148] Philippe Brax and Sylvain Fichet. Quantum Chameleons. *Phys. Rev. D*, 99(10):104049, 2019.

[149] Peiran Yin, Rui Li, Chengjiang Yin, Xiangyu Xu, Xiang Bian, Han Xie, Chang-Kui Duan, Pu Huang, Jian-hua He, and Jiangfeng Du. Experiments with levitated force sensor challenge theories of dark energy. *Nature Phys.*, 18(10):1181–1185, 2022.

[150] Walter Rudin et al. *Principles of mathematical analysis*, volume 3. McGraw-hill New York, 1976.

[151] William H Press. *Numerical recipes 3rd edition: The art of scientific computing*. Cambridge university press, 2007.

[152] Kamran Mohseni and Tim Colonius. Numerical treatment of polar coordinate singularities. *Journal of Computational Physics*, 157(2):787–795, 2000.

[153] Frank E Harris. *Mathematics for physical science and engineering: symbolic computing applications in Maple and Mathematica*. Academic Press, 2014.

[154] George B Arfken and Hans J Weber. Mathematical methods for physicists, 1999.

[155] Leonard F Burlaga. Micro-scale structures in the interplanetary medium. *Solar Physics*, 4:67–92, 1968.

[156] August Karl Krönig. *Grundzüge einer theorie der gase*. AW Hayn, 1856.

Abbreviations and Symbols

List of Abbreviations

CANNEX	Casimir And Non-Newtonian force EXperiment, see Section 5.4
chameleon	chameleon field model defined in Section 3.2
CMB	Cosmic microwave background radiation
dilaton	environment-dependent dilaton field model defined in Section 3.1
Eq.	Equation
FEM	Finite Element Method. Numerical method to solve PDEs.
Fig.	Figure
FLRW metric	Friedmann-Lemaître-Robertson-Walker metric, describes a universe obeying the cosmological principle of homogeneity and isotropy
FWF	Fonds zur Förderung der wissenschaftlichen Forschung, Österreichs zentrale Einrichtung zur Förderung der Grundlagenforschung.
GR	general relativity
intermediate λ region	parameter region of the dilaton defined in Section 3.1.2
large λ region	parameter region of the dilaton defined in Section 3.1.2
LLR	Lunar Laser Ranging
LLR I	LLR tests of the SEP
LLR II	LLR tests of the inverse square law
Mathematica	Wolfram Mathematica software, see Ref. [108]
MOND	Modifield Newtonian Dynamics
PDE	partial differential equation
qBOUNCE	gravity-resonance-spectroscopy experiment, see Section 5.3
RS	relative residual, defined in Eq. (4.1.96) and (4.5.146)
small λ region	parameter region of the dilaton defined in Section 3.1.2
SEP	Strong equivalence principle
symmetron	symmetron field model defined in Section 3.3
VEV	vacuum expectation value, classically: ϕ_ρ
WEP	weak equivalence principle
ΛCDM	Standard model of cosmology, with a cosmological constant Λ_0 and cold dark matter

List of Symbols

$\vec{a}$	acceleration
$\vec{a}_G$	Newtonian acceleration of the Earth and Moon towards the Sun
$A(\phi)$	Weyl-rescaling
A_2	dilaton parameter $A(\phi) \simeq 1 + A_2 \frac{\phi^2}{m_{\text{pl}}^2}$
Ai	Airy function
a_S	scale factor of the universe
C	when used as subscript it refers to the chameleon field
c	speed of light in vacuum
D	mesh construction parameters defined in Section 4.4.2 when used as subscript it refers to the dilaton field in the context of CANNEX this refers to the thickness of the upper plate
d	either radius of inner cylinder in neutron interfeometry, or half the plate separation in the CANNEX experiment

dl	line element ($g_{\mu\nu}dx^\mu dx^\nu$)
E_n	n'th energy of the neutron
$\vec{f}_\phi$	fifths force associated with a scalar field
$\mathbf{F}, \mathbf{F}_i$	The FEM seeks to finds roots to $\mathbf{F} = (\mathbf{F}_1, ..., \mathbf{F}_N)$, see Section 4.5.1
F, F_i	The FDM seeks to finds roots to $F = (F_1, ..., F_N)$, see Appendix B.4
G	Gravitational constant
GM(i)	Meshes defined in Section 4.4.2
g	determinant of the space-time metric, or $g \simeq 9.8 \frac{\mathrm{m}}{\mathrm{s}^2}$
$g_{\mu\nu}$	Einstein Metric
$\tilde{g}_{\mu\nu}$	Jordan Metric
g_{eff}	effective gravitational acceleration of the neutron including scalar field effects
$\hbar$	reduced planck constant
H	Hubble parameter
H_0	current value of the Hubble parameter
h_i	defined as $s_{i+1} - s_i$, where $s_1, ..., s_N$ refers to a 1D mesh
I_α	modified Bessel function of the first kind
J_F	Jacobi matrix of F
k	$k \in \{-1, 0, 1\}$ for a negatively curved, flat or positively curved universe
K_α	modified Bessel function of the second kind
k_0	wave number of the neutron in neutron interferometry
L	chamber length in neutron interferometry
$\mathcal{L}_{\mathrm{SM}}$	Lagrange density of standard model particles
M	Symmetron parameter $A(\phi) \simeq 1 + \frac{\phi^2}{2M^2}$
m	mass or meter
$M_\oplus$	mass of the Earth
M_c	Chameleon parameter $A(\phi) = e^{\phi/M_c}$
m_G	gravitational mass
m_I	intertial mass
m_n	mass of a neutron
m_{pl}	reduced Planck mass $\sqrt{\frac{\hbar c}{8\pi G}}$
n	Chameleon parameter $V(\phi) = \frac{\Lambda^{n+4}}{\phi^n}$
$\vec{n}$	normal vector
N_1, N_2, N_3	mesh construction parameters defined in Section 4.4.2
p	pressure
pert(n)	heuristic criterion for the validity of perturbation theory, defined in Eq. (4.6.157)
P	scalar field induced pressure in the z- direction on the upper plate of CANNEX
R	Radius of a sphere / in Section 2: Ricci scalar
r	radial coordinate for spherical of cylindrical coordinates
$R_I(\rho)$	$\frac{1}{\mu_\rho}$
$R_{\mu\nu}$	Ricci tensor
R_{EM}	Maximum Earth-Moon separation
S	when used as subscript it refers to the symmetron field
s	$s = r$ for the cross section of a cylinder or a sphere, $s = z$ for the one and two mirror geometries
t	time

$T_{\mu\nu}$	energy-momentum tensor
$T^{\phi}_{\mu\nu}$	$T_{\mu\nu}$ of a scalar field: $\partial_\mu\phi\partial_\mu\phi - g_{\mu\nu}\left(\frac{1}{2}\partial_\alpha\partial^\alpha\phi - V(\phi)\right)$
U	gravitational self-energy ($\frac{1}{8\pi m_{\text{pl}}^2}\frac{1}{2}\int\frac{\rho(\vec{x})\rho(\vec{x}')}{\lvert\vec{x}-\vec{x}'\rvert}d^3xd^3x'$)
U_X	Scalar field induced potential of a neutron, defined in Eq. (5.2.219) (neutron interferometry) and Eq. (5.3.231) (qBOUNCE)
UM(i)	Meshes defined in Section 4.4.2
$U_{X;P}(r,z)$	represents the scalar field potential within the vacuum or air chamber at pressure P
u_μ	four-velocity
$V(\phi)$	self-interaction potential of scalar fields
$V_{,\phi}$	$\frac{\partial V}{\partial\phi}$
V_0	dilaton parameter $V(\phi) = V_0 e^{-\lambda\phi/m_{\text{pl}}}$
V_{eff}	effective scalar field potential $V_{\text{eff}} = V(\phi) + \big(A(\phi)-1\big)\rho$
$V_{\text{eff},\phi}$	$\frac{\partial V_{\text{eff}}}{\partial\phi}$
W	Lambert W function, defined as inverse function of xe^x
w	pressure-to-energy-density ratio
X	used to distinguish between dilaton (D), chameleon (C) and symmetron (S) models
$x,\ y,\ z$	Cartesian coordinates
$\vec{x}$	position vector in three dimensions
z_0	$\sqrt[3]{\frac{1}{2m^2g}} \sim 5.9\ \mu$m, length-scale associated with neutron wave functions
z_{max}	maximum value of z up to which we can linearize a scalar field potential of a neutron, see Eq. (4.6.160)

α	$\Delta\varphi_{X;\text{Vacuum}} - \Delta\varphi_{X;\text{Air}}$
$\beta(\phi)$	full coupling to matter $\beta(\phi) \simeq m_{\text{pl}}\frac{dA}{d\phi}(\phi)$
Γ	Paramteter that takes the value 0 for one and two mirror geometries, 0.5 for cylindrical geometries and 1 for spherical geometries
γ	dilaton parameter $\gamma := \log_{10}\big(V_0/\text{MeV}^4\big)$
$\Gamma^\alpha_{\mu\nu}$	Christophel Symbol
Δ	Laplace operator
ΔE_{pq}	Difference between p'th and q'th energy state
$\Delta\varphi_{X;P}$	$= \delta\varphi_{X;P}(0) - \delta\varphi_{X;P}(0.015\text{ m})$
$\delta\phi$	redefined dilaton field $\phi = \phi_M + \delta\phi$
$\delta f(r)$	centripetal acceleration of the Moon caused by the dilaton field of Earth
$\delta\varphi_{X;P}(r)$	Scalar field induced phase shift for a neutron flying in a cylinder at radius r, with gas pressure P
δE_{pq}	difference between scalar field induced energy shifts between states p and q computed using perturbation theory to first order
δ_{em}	$\frac{a_{\phi♃} - a_{\phi☾}}{a_G}$, where $a_{\phi♃}$, $a_{\phi☾}$ refer to the scalar field induced acceleration of the Earth and Moon towards the sun, whereas a_G is the regular Newtonian acceleration towards the sun.
δ_{sim}	$:= -\mathfrak{Q}_X\frac{m_n^2}{k_0}\int_{-L/2}^{L/2}dz\big[A_X\big(\phi(0,z)\big) - A_X\big(\phi_{\text{Air}}\big)\big]$
δ_{approx}	$:= -\mathfrak{Q}_X\frac{m_n^2}{k_0}L\big[A_X\big(\phi_V\big) - A_X\big(\phi_{\text{Air}}\big)\big]$
η	Nodtvedt parameter for violations of the SEP ($n=0$) in GR

$\eta_{\mu\nu}$	Minkowski metric
Λ_0	Cosmological constant
Λ	Chameleon field parameter $V(\phi) = \frac{\Lambda^{n+4}}{\phi^n}$
λ	dilaton parameter $V(\phi) = V_0 e^{-\lambda\phi/m_{\text{pl}}}$
λ_S	Symmetron parameter $V(\phi) = -\frac{mu^2}{2}\phi^2 + \frac{\lambda_S}{4}\phi^4$
λ_n	wavelength of the neutron in neutron interferometry ($= 2.72$ Å)
μ	Symmetron parameter $V(\phi) = -\frac{\mu^2}{2}\phi^2 + \frac{\lambda_S}{4}\phi^4$, or 10^{-6}
μ_ρ	scalar field mass at material density ρ
ξ	$\delta\varphi_{X,P_1}(0) - \delta\varphi_{X,P_0}(0)$
ρ	density
ρ_M	material density
ρ_V	vacuum density
ρ_{Λ_0}	density of dark energy
ρ_c	critical density to make the universe flat
$\sigma(d)$	Measurement sensitivity of CANNEX at a CL of 68 %, as function of d
Σ	symbol for sums
ϕ	Symbol for scalar fields
$\phi_\rho(\vec{x})$	positive solution of $V_{\text{eff},\phi}\big(\phi_\rho(\vec{x}), \rho(\vec{x})\big) = 0$
ϕ_0	value of ϕ at $z = 0$
ϕ_V	potential minimum inside vacuum
ϕ_M	potential minimum inside material
ϕ_ρ	potential minimum at material density ρ
$\phi^{(n)}$	n'th guess of ϕ in Newton's method
φ_i	FEM basis functions
φ_{ij}	Kronecker Delta symbol
χ	Original string dilaton not investigated in this work, see Section 3.1
χ_0	value of χ for which the coupling to matter is minimized
ψ	neutron wave function
ψ_i	Standard Model fields, or value of ψ at z_i
ψ_n	n'th energy state of the neutron
Ω	(average density of the universe) / (density to make the universe flat)
Ω_f	$= \omega_0$-ω_S
$\hat{\Omega}$	Domain over which a PDE is solved
Ω_{Λ_0}	contribution of dark energy density to Ω
Ω_{matter}	contribution of matter energy density to Ω
ω_0	Moon's orbital frequency
ω_S	Sun's orbitan frequency

$\partial\hat{\Omega}_D$	Boundary of domain where Dirichlet boundary conditions apply
$\partial\hat{\Omega}_N$	Boundary of domain where Neumann boundary conditions apply
$\partial_\alpha\phi$	partial derivative of ϕ with respect to x_α, notation used in relativistic context
$\frac{\partial}{\partial x_i}$	partial derivative with respect to coordinate x_i, notation used in non-relativistic context
∇_ν	covariant derivative
$\vec{\nabla}$	gradient
$\mathfrak{Q}_X$	screening charge, definitions in Eq. (5.1.201) for the dilaton

	and for the chameleon and symmetron we used the definitions provided in [3, 61, 62]
$\Box$	D'Alembert operator $n^{\mu\nu}\partial_\mu\partial_\nu$
$\dot{f}$	time derivative of f
$\frac{df}{du}$	derivative of function f that only depends on u
$\|\|\phi\|\|_2$	Euclidean norm of ϕ
☾	quantitity associated with the Moon
♁	quantity associated with the Earth
$\tilde{}$	A $\tilde{}$ above a quantity refers to the corresponding Jordan frame expression
$\ll$, $\gg$	much smaller, much greater
$\wedge$	logical and
$\vee$	logical or
$\int_{\hat{\Omega}} f(u)du$	integral of $f(u)$ over $\hat{\Omega}$

Hauke Fischer

Curriculum Vitae

hauke.fischer@tuwien.ac.at

Scientific Career

6/2021 - current **Project assistant**
In the group of Privatdoz. Dipl.-Ing. Dr.techn. Mario Pitschmann,
at the Atominstitut of the Technische Universität Wien.

Education

6/2021 - current **PhD** in Physics, Technische Universität Wien
Thesis: *Search for Dark Energy and Modified Gravity with Tabletop Experiments*
Supervisor: Privatdoz. Dipl.-Ing. Dr.techn. Mario Pitschmann

10/2018 - 2/2021 **Master of Science** in Physics (average grade 1.0), Universität Wien
Thesis: *Investigation of the phase transition from low- to high chalcocite in nanorods using High-Dimensional Neural Network Potentials*
Supervisor: Univ.-Prof. Mag. Dr. Christoph Dellago

10/2016 - 11/2018 **Bachelor of Science** in Physics (average grade 1.2), Universität Wien
Thesis: *A general review on dark matter, culminating in possible detection methods using molecule interferometry*
Supervisors: Univ.-Prof. Dr. Markus Arndt, Dipl.-Ing. Dr. Armin Shayeghi

10/2012 - 7/2015 **Bachelor of Science** in Mathematics (average grade 1.1), Universität Wien
Thesis 1: *The Central Limit Theorem, Following a Method by J.W. Lindeberg*
Supervisor: Assoz. Prof. Mag. Dr. Roland Zweimüller
Thesis 2: *Differentiation on normed spaces*
Supervisor: Univ.-Prof. Dipl.-Ing. Dr. Gerald Teschl

Publications & preprints

2024 **Hauke Fischer**, Christian Käding, René I.P. Sedmik, Hartmut Abele Philippe Brax and Mario Pitschmann.
Search for environment-dependent dilatons.
Phys. Dark Univ., 43:101419, 2024.

2024 **Hauke Fischer**, Christian Käding, Hartmut Lemmel, Stephan Sponar and Mario Pitschmann.
Search for dark energy with neutron interferometry.
PTEP, 2024(2):023E02, 2024.

2024 Hamid Haghmoradi, **Hauke Fischer**, Alessandro Bertolini, Ivica Galić, Francesco Intravaia, Mario Pitschmann, Raphael Schimpl, and René I.P. Sedmik.
Force metrology with plane parallel plates: Final design review and outlook.
Physics, 6:690–741, 3 2024.

2024 **Hauke Fischer,** and René I.P. Sedmik.
Numerical methods for scalar field dark energy in table-top experiments and lunar laser ranging.
arXiv:2401.16179, 2024.

2024 **Hauke Fischer,** Christian Käding and Mario Pitschmann.
Screened Scalar Fields in the Laboratory and the Solar System.
Universe, 10:297, 2024.

2022 Philippe Brax, **Hauke Fischer**, Christian Käding, and Mario Pitschmann.
The environment dependent dilaton in the laboratory and the solar system.
Eur. Phys. J. C, 82(10):934, 2022.

Conferences

2023	XVIII International Conference on Topics in Astroparticle and Underground Physics 2023 (TAUP) *Parallel Talk*
2022	16th Central European Seminar on Particle Physics and Quantum Field Theory (VCES) *Poster presentation*

Teaching & Supervision

2023	Supervision of two project thesis at the TU Wien
2017-18	Group leader: Begleitseminar Studieneingangsphase I-II

Honors & Awards

2021	**DEAN'S LIST AWARD** for academic excellence, Universität Wien
2017 - 2021	**Merit based scholarship** Universität Wien Physics
2013 - 2015	**Merit based scholarship** Universität Wien Mathematics
2010	**DMV-Abiturpreis** for outstanding performance in Mathematics, issued by the Deutsche Mathematiker Vereinigung